Title

Hubble Constant and Strong Gravitational Lensing

ISBN

9798293831005

Author

Schmidt, Thomas

Publication Date

2025-09-11

Peer reviewed|Thesis/dissertation

UNIVERSITY OF CALIFORNIA

Los Angeles

Hubble Constant and Strong Gravitational Lensing

A dissertation submitted in partial satisfaction
of the requirements for the degree of
Doctor of Philosophy
in Astronomy and Astrophysics

by

Thomas Schmidt

2025

ABSTRACT OF THE DISSERTATION

Hubble Constant

and Strong Gravitational Lensing

by

Thomas Schmidt

Doctor of Philosophy in Astronomy and Astrophysics

University of California, Los Angeles, 2025

Professor Tommaso L. Treu, Chair

The persistent tension between early and late universe measurements of the Hubble constant (H_0) represents one of the most significant challenges in modern cosmology, with implications for our understanding of fundamental physics. Strong gravitational lensing of variable sources offers a unique pathway to independent H_0 measurements that bypass systematic uncertainties inherent in traditional methods that rely on the distance ladder. However, high-precision strong lens modeling has been computationally expensive and is further limited by extensive human resources required, thus creating bottlenecks for exploiting the wealth of strong lens discoveries expected from current and upcoming surveys.

This dissertation presents advances in strong gravitational lensing that address these challenges while demonstrating the extraordinary potential of complex lensing configurations for high-precision cosmography. I develop and implement an automated modeling pipeline that drastically reduces computational time and investigator input requirements for cosmography-grade lens modeling. Applied to a sample of 31 quadruply imaged quasar systems, observed with the Hubble Space Telescope, this automated approach successfully produces models for 30/31 systems using $<$100 CPU hours and minimal human intervention per system, representing significant improvement over traditional methods typically requiring 10^{5-6} CPU

hours and one ore more years of investigator time.

Complementing this large-scale development in methodology, I present comprehensive analyses of J1721+8842, an extraordinary strong lens system that exemplifies nature's capacity to provide precision laboratories. Initially modeled as an unprecedented dual AGN configuration, subsequent time-delay measurements and James Webb Space Telescope spectroscopic observations reveal J1721+8842 to be the first confirmed Einstein zigzag lens, a single quasar lensed into six images by compound deflection from two nearly perfectly aligned deflectors at redshifts $z_1 = 0.184$ and $z_2 = 1.885$. This remarkable geometry enables percent-level precision in time-delay predictions and provides up to 15 potential time-delay measurements compared to the 6 typically available from quadruply lensed systems, thereby dramatically enhancing both statistical precision and systematic error control.

The work presented in this thesis demonstrates that uniform cosmography-grade modeling of large strong lens samples is achievable through automation, while exceptional individual systems can achieve percent-level precision in H_0 measurements. These advances provide the technical foundation necessary to transform strong gravitational lensing from a specialized technique into a cornerstone for high-precision cosmology, capable of providing independent constraints necessary to resolve the Hubble tension and advancing our understanding of cosmic evolution.

The dissertation of Thomas Schmidt is approved.

Bradley M. Hansen

Steven R. Furlanetto

Matthew Arnold Malkan

Tommaso L. Treu, Committee Chair

University of California, Los Angeles

2025

DEDICATION

To my loving wife, Christine.

TABLE OF CONTENTS

LIST OF FIGURES

LIST OF TABLES

Page

VITA

Thomas Schmidt

EDUCATION

M.S. – Astronomy and Astrophysics **2021**

UCLA *Los Angeles, CA*

B.S. – Physics with Specialization in Astrophysics **2018**

UCI *Irvine, CA*

A.S. – Mathematics, Computer Science **2015**

MCC *Oceanside, CA*

RESEARCH EXPERIENCE

Graduate Student Researcher **2019–2025**

University of California *Los Angeles, CA*

Post-Baccalaureate Researcher **2018–2019**

University of California *Irvine, CA*

Undergraduate Student Researcher **2016–2018**

University of California *Irvine, CA*

TEACHING EXPERIENCE

Learning Coach **2018–2019**

MCC STEM Center *Oceanside, CA*

Facilitated Learning Studies (FLS) Instructor **2014–2015**

MCC STEM Center *Oceanside, CA*

REFEREED JOURNAL PUBLICATIONS

Schmidt, T., Treu, T., and 8 colleagues (2025). TDCOSMO. XVIII. Strong lens model and time-delay predictions for J1721+8842, the first Einstein zigzag lens. *A&A*, 700:A92

Williams, D. M., Treu, T., Birrer, S., Shajib, A. J., Wong, K. C., Morishita, T., Schmidt, T., and Stiavelli, M. (2025). TDCOSMO. XX. WFI2033–4723, the First Quadruply-Imaged Quasar Modeled with JWST Imaging. *Submitted to MNRAS (2025) and arXiv e-prints*, page arXiv:2503.00099

Gonzalez-Buitrago, D., Barth, A. J., Edelson, R., Hernández Santisteban, J. V., Horne, K., Schmidt, T., and 39 colleagues (2025). Departures from Standard Disk Predictions in Intensive Ground-Based Monitoring of Three AGN. *MNRAS*, 542(3):2572–2596

Dux, F., Millon, M., Lemon, C., Schmidt, T., and 15 colleagues (2025a). J1721+8842: The first Einstein zigzag lens. *A&A*, 694:A300

Erickson, S., Wagner-Carena, S., Marshall, P., Millon, M., Birrer, S., Roodman, A., Schmidt, T., 4 colleagues, and The LSST Dark Energy Science Collaboration (2025). Lens Modeling of STRIDES Strongly Lensed Quasars Using Neural Posterior Estimation. *AJ*, 170(1):44

Roberts-Borsani, G., Treu, T., Mason, C., Ellis, R. S., Laporte, N., Schmidt, T., and 4 colleagues (2023). Nature and Nurture? Comparing Lyα Detections in UV-bright and Fainter [O III]+Hβ Emitters at z 8 with Keck/MOSFIRE. *ApJ*, 948(1):54

Ertl, S., Schuldt, S., Suyu, S. H., Schmidt, T., Treu, T., Birrer, S., Shajib, A. J., and Sluse, D. (2023). TDCOSMO. X. Automated modeling of nine strongly lensed quasars and comparison between lens-modeling software. *A&A*, 672:A2

Schmidt, T., Treu, T., 69 colleagues, and DES Collaboration (2023a). STRIDES: automated uniform models for 30 quadruply imaged quasars. *MNRAS*, 518(1):1260–1300

Chen, G. C. F., Treu, T., Fassnacht, C. D., Ragland, S., Schmidt, T., and Suyu, S. H. (2021a). Point spread function reconstruction of adaptive-optics imaging: meeting the astrometric requirements for time-delay cosmography. *MNRAS*, 508(1):755–761

Birrer, S. and 20 colleagues, including Schmidt, T. (2021). lenstronomy II: A gravitational lensing software ecosystem. *The Journal of Open Source Software*, 6(62):3283

Chapter 1

Introduction

1.1 Hubble tension and ΛCDM model

Modern cosmology rests on the foundation of the Λ Cold Dark Matter (ΛCDM) model, which provides a comprehensive framework for understanding the structure and evolution of our Universe. The ΛCDM cosmology breaks down the cosmic energy budget as $\sim$ 70 percent dark energy with the remaining 30 percent classified as matter, which can be further divided as approximately 5 percent ordinary baryonic matter and radiation and roughly 25 percent attributed to non-visible dark matter, transparent to electromagnetic radiation with interactions limited to the gravitational force (Planck Collaboration et al., 2020). While dark energy, expressed in models as the cosmological constant, Λ, drives the observed acceleration in the Universe's expansion rate, the dark and baryonic matter components are responsible for the gravitational potential necessary in the formation of large-scale structures and galaxy clustering in the Universe (Riess et al., 1998; Perlmutter et al., 1999). Observational evidence for the dark matter component arises from multiple independent sources, including galaxy rotation curves, gravitational lensing by massive galaxies and structures, and large-scale matter distribution patterns (see, e.g., Treu and Koopmans, 2004; Clowe et al., 2004; Heymans et al., 2013).

The ΛCDM framework has proven remarkably successful across a diverse array of cosmological observations over a wide range of different scales and epochs. It accurately reproduces the temperature fluctuations and polarization patterns observed in the cosmic microwave background (CMB) radiation, explains the abundance ratios of primordial elements in the Big Bang nucleosynthesis as well as the characteristic scale imprinted by baryon acoustic oscillations (BAOs), predicts the clustering properties of galaxies on large scales, and characterizes the luminosity-distance relationships of Type Ia supernovae (SNIa) responsible for the discovery of cosmic acceleration (e.g., Riess et al., 1998; Perlmutter et al., 1999; Eisenstein et al., 2005; Planck Collaboration et al., 2020).

Despite these successes, significant challenges have emerged that question the limits of our current understanding. Most notably, perhaps, precision measurements of the Hubble constant, H_0, which represents the current expansion rate of the Universe, have revealed a substantial disagreement between different observational approaches, therefore making the H_0 value a quantity of fundamental importance in the current cosmological debate. Analyses relying on CMB data yield $H_0 = 67.4 \pm 0.5$ km s^{-1} Mpc^{-1} (Planck Collaboration et al., 2020) when interpreted through a flat ΛCDM cosmology and extrapolated to present times. This lower H_0 value represents the current expansion rate inferred from the early Universe. Conversely, local (or late universe) H_0 measurements using Cepheid variable and SNIa light curves as rungs in the cosmic distance ladder consistently produce higher values around $H_0 = 73.04 \pm 1.04$ km s^{-1} Mpc^{-1} (Riess et al., 2022).

This discrepancy in H_0 measurement results, widely known as Hubble Tension currently exceeds 5σ in statistical significance (see, e.g., Di Valentino et al., 2025, and references therein), leading profound implications toward our understanding of fundamental physics. It should be mentioned that the possibility exists that the underlying tension is caused by previously unrecognized systematic uncertainties, affecting one or multiple methods used to measure H_0. However, if systematic effects can be confidently excluded, the tension would point toward new physics beyond the standard ΛCDM model, potentially requiring

modifications to our understanding of dark energy, dark matter, or even the fundamental physics governing cosmic expansion. Proposed theoretical solutions to solve the Hubble tension range from modifications to the sound horizon at the epoch of recombination by incorporating an early form of dark energy or through the addition of currently undiscovered relativistic particle in the ΛCDM model to local void models for which late universe H_0 measurements could be systematically higher than the cosmic average due to our location near the center of a large under-dense region (e.g. Knox and Millea, 2020; Di Valentino et al., 2021; Schöneberg et al., 2022; Vagnozzi, 2023).

To resolve this tension, independent methodologies for measuring H_0 become crucial to distinguish between systematic effects and genuine new physics. Strong gravitational lensing of a variable background source offers a unique and powerful approach to determine the Hubble constant in a single-step measurement, completely avoiding any rungs (and associated systematic uncertainties) in the local distance ladder (Refsdal, 1964; Treu and Marshall, 2016; Treu et al., 2022; Treu and Shajib, 2024; Birrer et al., 2024). In contrast to methods that rely on empirically calibrated standard candles, strong lensing exploits the time-delay differences observed between lensed images of the same variable source that arise as a consequence of photons traveling along geometric paths of different lengths and experiencing distinct gravitational delays in travel time as they traverse the potential of a massive lensing galaxy. When combined with accurate models of the lens mass distribution, the observed differences in a photon's travel time directly constrain the time-delay distance, a specific combination of angular diameter distances that scales inversely with H_0 (see, e.g., Treu and Koopmans, 2002; Suyu et al., 2010, 2014; Treu and Marshall, 2016; Birrer et al., 2016; Bonvin et al., 2017; Birrer et al., 2019; Shajib et al., 2020). This approach has yielded increasingly precise results over the past decade, with recent analyses achieving measurements uncertainties of only a few percent, thereby able to compete with traditional methods of extracting H_0. These strong lens results generally support higher H_0 values that are also measured by traditional methods involving the distance ladder, which strengthens the hypothesis that the Hubble

tension is the result of missing physics in the ΛCDM framework rather than systematic errors.

The path toward resolving the tension in H_0 measurements through strong lensing critically depends on developing robust techniques for accurately modeling the mass distributions of lensing galaxies. Precise lens models, which require sophisticated treatment of both the primary deflector and environmental effects from surrounding structures, are essential for translating observed time delays and measurements of the lens environment into reliable constraints of the time-delay distance and Hubble constant. The following section introduces underlying key concepts necessary for the application of time-delay cosmography.

1.2 Strong lensing fundamentals

Gravitational lensing represents one of the most directly observable confirmations of Einstein's theory of general relativity, demonstrating how mass curves spacetime and consequently bends the path of light. When a massive object lies between a distant source and an observer, the gravitational field of the object acts as a natural lens, bending light rays and, depending on the mass and alignment of the lens, potentially creating multiple images of the lensed background source.

The gravitational lensing classification critically depends on the mass of the lens, i.e. the resulting strength of the gravitational field produced by the deflector. For instance, microlensing occurs when an object, relatively low in mass such as a star or a planetary body, temporarily magnifies a background sources without creating multiple images. This generally produces a characteristic light curve as the lensing object moves across the line of sight. In contrast, strong gravitational lensing occurs when a large-scale foreground deflector, typically a massive galaxy or a galaxy cluster for which the surface mass density exceeds the critical density for multiple image formation, lenses a background source into highly distorted arcs and produces multiple distinct images. This usually requires the deflector and

the lensed source to be nearly perfectly aligned with the observer, and the deflector to be massive enough to create a substantial deflection angle.

Most strong lens scenarios can be accurately described using the thin lens approximation, whereby the mass of the deflector is treated as concentrated or flattened in a single two-dimensional plane perpendicular to the line of sight. This simplification is valid because the physical extent of the deflector along the line of sight is negligible in comparison to the cosmological distances involved in the lensing geometry. Under this approximation, the deflection angle $\hat{\boldsymbol{\alpha}}$ at location $\boldsymbol{\xi}$ depends only on the projected surface mass density $\Sigma(\boldsymbol{\xi})$, which describes the lensing matter distribution of the deflector with a three-dimensional mass density ρ as

$$\Sigma(\boldsymbol{\xi}) = \int \rho(\boldsymbol{\xi}, z) dz. \tag{1.1}$$

For an extended mass distribution, the total deflection angle $\hat{\boldsymbol{\alpha}}$ at impact parameter $\boldsymbol{\xi}$ can then be expressed as the summation of all contributing mass elements $\Sigma(\boldsymbol{\xi'})d^2\boldsymbol{\xi'}$ across the deflector as follows:

$$\hat{\boldsymbol{\alpha}}(\boldsymbol{\xi}) = \frac{4G}{c^2} \int \frac{\boldsymbol{\xi} - \boldsymbol{\xi}'}{|\boldsymbol{\xi} - \boldsymbol{\xi}'|^2} \Sigma(\boldsymbol{\xi'}) d^2\boldsymbol{\xi}' \tag{1.2}$$

(see, e.g., Blandford and Narayan, 1986; Meneghetti, 2021).

Figure 1.1 shows a sketch of a simple gravitational lens system for a background source at position $\boldsymbol{\eta}$ that is imaged by a single deflector located in the lens plane. The trajectory of light rays emitted by the source is altered by the deflection angle $\hat{\boldsymbol{\alpha}}$ at the impact parameter $\boldsymbol{\xi}$ in the lens plane. Under the small-angle approximation, the position of the source, $\boldsymbol{\eta}$, can be expressed as

$$\boldsymbol{\eta} = \boldsymbol{\beta} D_\mathrm{s} = \boldsymbol{\theta} D_\mathrm{s} - \hat{\boldsymbol{\alpha}}(\boldsymbol{\theta}) D_\mathrm{ds}, \tag{1.3}$$

where D_s and D_ds are the angular diameter distances to the source and between the lens

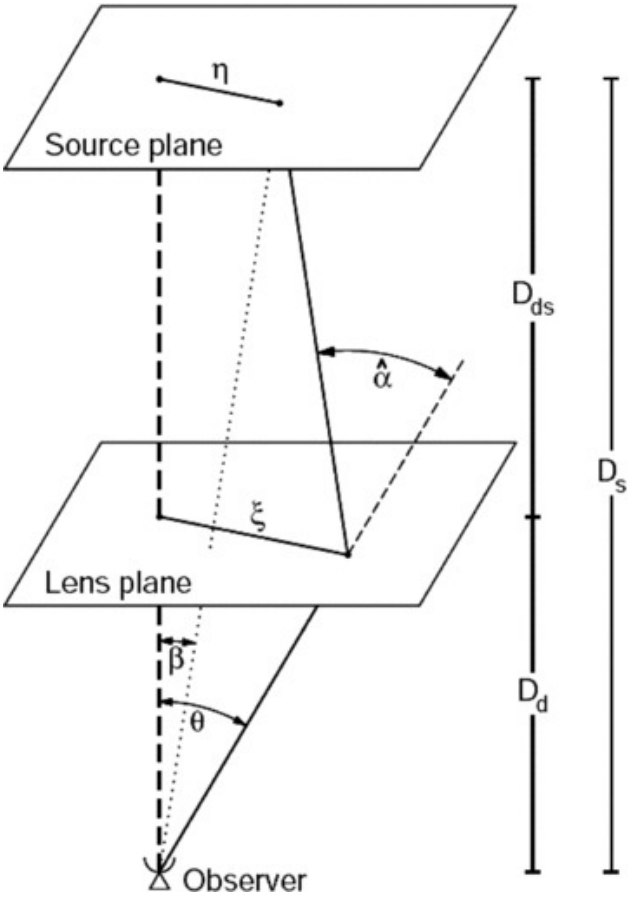

Figure 1.1: Sketch of a typical gravitational lensing system (Schneider et al., 2006)

and source plane, respectively. This expression can be further simplified by incorporating the scaled deflection angle, defined as

$$\boldsymbol{\alpha}(\boldsymbol{\theta}) \equiv \frac{D_{\rm ds}}{D_{\rm s}}\hat{\boldsymbol{\alpha}}(\boldsymbol{\theta}), \tag{1.4}$$

to arrive at

$$\boldsymbol{\beta} = \boldsymbol{\theta} - \boldsymbol{\alpha}(\boldsymbol{\theta}), \tag{1.5}$$

which is known as the lens equation that governs the relationship between the true source position $\boldsymbol{\beta}$ and an observed image position $\boldsymbol{\theta}$. For a given source position, the lens equation may have multiple solutions, corresponding to the multiple images, an above referenced characteristic of strong gravitational lensing. The configuration and the number of lensed images depend on both, the mass distribution of the lens as well as the precise alignment between source and deflector with respect to an observer.

To extract cosmological information from a strong lensing configuration, the lensed background source must exhibit intrinsic variations in luminosity as exhibited by quasars or by a SNIa. When such a source is multiply imaged by a strong lens, any brightness fluctuation observed in one image will also be seen in the remaining images, but with a characteristic and measurable delay in the arrival time. This delay in brightness variations between two images A and B occurs because photons associated with the same emission event traverse paths of different geometrical lengths and cross the lens plane at different points with a distinct gravitational potential, therefore experiencing different gravitationally induced time dilation. This observable time-delay difference is encapsulated in the following expression

$$\Delta t_{\rm AB} = \frac{D_{\Delta t}}{c}\Delta\phi_{\rm AB}, \tag{1.6}$$

where $\Delta\phi_{\rm AB}$ is the Fermat potential difference between the two images and $D_{\Delta t}$ represents the time-delay distance. Expressed in terms of image position, $\boldsymbol{\theta}$, and source position, $\boldsymbol{\beta}$,

the Fermat potential difference between images A and B is given by

$$\Delta\phi_{\rm AB}(\boldsymbol{\theta_{\rm A};\theta_{\rm B};\beta}) = \frac{1}{2}\left[(\boldsymbol{\theta_{\rm A}}-\boldsymbol{\beta})^2-(\boldsymbol{\theta_{\rm B}}-\boldsymbol{\beta})^2\right]-\left[\psi(\boldsymbol{\theta_{\rm A}})-\psi(\boldsymbol{\theta_{\rm B}})\right], \tag{1.7}$$

where the term enclosed in the first bracket encapsulates the geometric path difference and where the term in the second bracket represents the gravitational potential difference between the image locations, responsible for the time dilation effects the traveling photons experience (Shapiro, 1964). In the expression, $\psi(\boldsymbol{\theta})$ denotes the deflection potential at the position of a lensed image, which is related to the scaled deflection angle through $\boldsymbol{\alpha}(\boldsymbol{\theta}) \equiv \nabla\psi(\boldsymbol{\theta})$.

Measured time delays, extracted by long-term observations at high cadence, combined with precise lens models allow us to solve for the time-delay distance, a specific combination of angular diameter distances defined as

$$D_{\Delta t} \equiv (1+z_{\rm d})\frac{D_{\rm d}D_{\rm s}}{D_{\rm ds}}. \tag{1.8}$$

Here, $z_{\rm d}$ is the redshift of the deflector and $D_{\rm d}$, $D_{\rm s}$, and $D_{\rm ds}$ represent the angular diameter distance to the deflector, to the source, and between the deflector and the source, respectively. This time-delay distance encodes fundamental cosmological information, in particular the expansion rate H_0, since each angular diameter distance depends inversely on the Hubble constant.

To be more precise, the expression for an angular diameter distances D_A is given by

$$D_A(z_1,z_2) = \frac{c}{H_0(1+z_2)}\int_{z_1}^{z_2} f(z)dz, \tag{1.9}$$

where the cosmology, $f(z)$, is defined as

$$f(z) = \left[\frac{\Omega_{m,0}}{(1+z)}+\frac{\Omega_{k,0}}{(1+z)^2}+\frac{\Omega_{\Lambda,0}}{(1+z)^4}\right]^{-1/2}. \tag{1.10}$$

$\Omega_{m,0}$, $\Omega_{k,0}$, and $\Omega_{\Lambda,0}$, denote the present-day parameters for matter density, curvature

density, and the cosmological constant, respectively. It should be noted that in the expression for the cosmology, the present-day parameter for the radiation density, $\Omega_{r,0}$, is omitted as $\Omega_{r,0} \ll \Omega_{m,0}$.

This inverse relationship between $D_{\Delta t}$ and H_0 makes time-delay cosmography a powerful tool to measure the current expansion rate of the universe. Unlike other methods that use the distance ladder and therefore require multiple calibration steps, or CMB analyses that depend on early universe physics, strong gravitational lensing of variable sources provide a direct, one step distance measurement for targets at low to intermediate redshifts.

Achieving a subpercent precision in H_0 measurements through time-delay cosmography requires continued progress in both sample size and accuracy. Upcoming wide-field surveys are expected to discover hundreds to thousands of new lensed quasars, however, analyzing such large samples will require automated modeling techniques and careful systematic error control. The ultimate goal of strong lens measurements is to provide independent constraints on cosmological parameters to resolve the current Hubble tensions and with it deepen our understanding of cosmic evolution.

1.3 Dissertation overview

In this dissertation, I present significant advances in the modeling approach for large samples of strong gravitational lenses, with particular focus on the measurement of the Hubble constant. My work spans from developing efficient automated strong lens modeling pipeline, able to process a variety of strong lens configurations, to the detailed analyses of an extraordinary individual system that promises unprecedented precision in time-delay cosmography.

In Chapter 2, I describe the development of an automated modeling pipeline and how it is applied to a sample of 31 strong lens systems observed by the Hubble Space Telescope. This automated approach is able to produce models for 30 out of the 31 lenses with few hours of human time and <100 CPU hours in computing time per system — a dramatic improvement

over traditional methods, which typically require 6 months to 1 year of investigator time and 10^{5-6} CPU hours. In my results, I find that 10/30 lens models produced by the pipeline achieve cosmography or nearly cosmography grade precision (<3% and 3-5% variations in time-delay predictions) and 6/30 lens models approach this standard (5-10% variations). This represents a crucial step toward exploiting the large number of lenses forecast to be discovered over the current and upcoming decade.

In Chapters 3 and 4, I present detailed lens models for J1721+8842, an extraordinary strong lens system that exemplifies the remarkable potential of complex lensing configurations for high-precision cosmology. Due to incomplete spectroscopic observations at the start of the analysis, I model this system under two different scenarios: first as an unprecedented dual AGN system (one AGN quadruply imaged and the second AGN as a double) consisting of four separate lensed galaxies (Chapter 3), with the completion and submission of the analysis for publication prior to measured time delays and prior to spectroscopic measurements with the James Webb Space Telescope, which revealed that all images in the lens configuration belong to the same quasar source. Subsequently, after a spectroscopic analysis with the James Webb Space Telescope revealed that one of the lensed galaxies, previously assumed to be the host of the doubly imaged quasar, turned out to be a galaxy at a different redshift, I model the system as the first-ever confirmed Einstein zigzag lens involving a single quasar lensed into six images by two, nearly perfectly aligned, deflectors at redshifts $z_1 = 0.184$ and $z_2 = 1.885$ (Chapter 4). This unique geometry observed in J1721+8842 provides exceptional constraints on lens mass profiles and enables percent-level precision in time-delay predictions. Unlike typical quadruply imaged quasars, which provide 6 measurable delays, this configuration offers up to 15 potential time-delay measurements, dramatically enhancing both statistical precision and systematic uncertainties. The system's extraordinary configuration makes it an extremely promising candidate for a high-precision strong lens measurement of H_0.

Lastly, I conclude the dissertation in Chapter 5 by providing a brief summary of the

main results. The work presented in this dissertation demonstrates that strong gravitational lensing is now a reliable tool to extract high-precision measurements of H_0 as well as other cosmological parameters and is destined to become a foundational cornerstone in the field of cosmology. By addressing both, the scalability challenges through automated lens modeling and showcasing the extraordinary precision achievable with an exceptional system like J1721+8842, this research establishes the transformation into using strong lensing as capable method to answer fundamental cosmological questions. The following chapters present the detailed methodologies, analyses, and results that substantiate these advances.

Chapter 2

Automated uniform models for 30 quadruply imaged quasars

2.1 Background

Our most successful cosmological model to date, the Λ Cold Dark Matter (ΛCDM) model, has been able to accurately explain a plethora of cosmological observations in the early and late universe, including observations of the cosmic microwave background (CMB) radiation, the Big Bang nucleosynthesis, the formation of large scale structures and galaxy clustering, and the acceleration in the expansion of our universe (e.g., Planck Collaboration et al., 2020; Eisenstein et al., 2005; Riess et al., 1998; Perlmutter et al., 1999). However, over the last few years, the tension in the measurements of the Hubble constant, which quantifies the Universe's current expansion rate, has been increasing between probes of the early Universe, i.e. measurements using the information contained within the CMB, and the probes of the late Universe, such as methods using the local distance ladder. Early-Universe measurements of the CMB give a Hubble constant of 67.4 ± 0.5 km s^{-1} Mpc^{-1} (Planck Collaboration et al., 2020) while observations of the late Universe measure H_0 at a higher value of 73.0 ± 1.4 km s^{-1} Mpc^{-1} (Riess et al., 2021), resulting in a currently 5-6 σ tension between the two

measurements (Verde et al., 2019; Wong et al., 2020). Solving this tension, if confirmed, would require new Physics, for example changing the sound horizon at recombination via the introduction of a new relativistic particle or a form of early dark energy (Knox and Millea, 2020; Di Valentino et al., 2021). Given the importance of the tension, it is imperative to develop multiple independent methods with sufficiently high precision to confirm the H_0 tension or possibly rule it out.

Strong gravitational lensing, where the lensed source is a multiply-imaged quasar, provides a powerful cosmological probe that can be used to determine the Hubble constant, independent of measurements relying on the local distance ladder (Refsdal, 1964). Light rays from a variable point source, the quasar, traverse the gravitational potential of a foreground galaxy, the lens or deflector, with paths of different lengths and through different points in the gravitational field of the deflector. Therefore, we observe different images of the same quasar in the plane of the lens, the image plane. High cadence, long-term observations of the lensed source allow us to use the intrinsic quasar variability to measure the time delay of the variations between the four observed images in the plane of the lens (Tewes et al., 2013). Since the angular diameter distances from the observer to the main deflector, $D_{\rm d}$, from the observer to the source, $D_{\rm s}$, and from the deflector to the source, $D_{\rm ds}$, are much greater than the physical extent of the lensing galaxy, we can simplify the geometry of the problem by considering a two dimensional deflector, which leads to the following expression for the measurable time-delay distance between two images A and B:

$$\Delta t_{\rm AB} = \frac{D_{\Delta t}}{c} \Delta\Phi_{\rm AB}, \tag{2.1}$$

where the time-delay distance, $D_{\Delta t}$, is related to the angular diameter distances and the main deflector's redshift, $z_{\rm d}$, by

$$D_{\Delta t} = (1 + z_{\rm d}) \frac{D_{\rm d} D_{\rm s}}{D_{\rm ds}}. \tag{2.2}$$

$\Delta\Phi_{\rm AB}$ represents the difference in the Fermat potential of the lens at the position of the images A and B, and c is the speed of light. The Fermat potential for an image position, $\boldsymbol{\theta}$, and source position, $\boldsymbol{\beta}$, is given by

$$\Phi(\boldsymbol{\theta};\boldsymbol{\beta}) = \frac{1}{2}(\boldsymbol{\theta}-\boldsymbol{\beta})^2 - \psi(\boldsymbol{\theta}), \tag{2.3}$$

where the deflection potential, $\psi(\boldsymbol{\theta})$, is related to the projected surface mass density (or convergence), κ, by

$$\nabla^2\psi = 2\kappa. \tag{2.4}$$

Therefore, if we can recover the Fermat potential for a given lens configuration by reconstructing a model that matches high resolution imaging of the system, we are able use the measured time delays between lensed quasar image positions to determined the time-delay distance, which is inversely proportional to the Hubble constant.

Achieving ~ 1 % precision in the Hubble constant requires a sample size of at least $\sim$40 systems (Treu et al., 2016; Shajib et al., 2018; Birrer and Treu, 2021). Fortunately, ongoing and future wide-field deep-sky surveys are expected to rapidly increase the number of known quadruply imaged quasars (e.g., Oguri and Marshall, 2010; Collett, 2015). Indeed, in recent years, the discovery rate has accelerated owing to the large dataset and the development of automatic detection algorithms (e.g., Agnello et al., 2015; Williams et al., 2017, 2018; Lemon et al., 2018). Thus, the prospect of precise and accurate Hubble constant measurements from strong gravitational lensing is bright, provided sufficient resources can be devoted to follow-up and model the systems. High-precision models of strong lens systems are currently very time consuming, with an approximate 6 to 12 months of investigator time required per lens, depending on the complexity of the deflectors involved. Therefore, major improvements in modeling speed are required to scientifically exploit the anticipated influx of newly discovered strong lenses.

This paper takes an important step towards relieving the bottleneck created by time limitations in the modeling speed. While other approaches focus on machine learning methods to increase lens modeling speeds (e.g., Hezaveh et al., 2017; Pearson et al., 2019, 2021; Schuldt et al., 2021), we use an improved version of the uniform lens modeling framework set forth by Shajib et al. (2019) and build an automated pipeline to model strong gravitational lenses expanded around an elliptical power-law mass profile for a system's central main deflector. To facilitate the reconstruction of a wide array of lenses with varying intricacies, the pipeline makes modeling choices selected from a uniform set of components for mass and light profiles to iteratively increase each lens model's complexity until a good fit is found that accurately matches the observational data for the object. With this automated approach, we are able to process sets of strong lenses that are much larger than in previous studies and reduce the requirement of an investigator's involvement to ancillary tasks, such as data reduction and addressing failure modes. These advantages make the automated pipeline a powerful springboard for the scientific analysis of the expected increase in newly discovered lensed systems.

We apply our automated lens modeling pipeline to a sample of 31 strong gravitational lenses imaged by the Hubble Space Telescope (*HST*) during cycles 25 and 26 between the years 2017 and 2020 in filters F160W, F475X, and F814W. To assess the stability of the difference in the Fermat potential at the position of the lensed quasar in the image plane, we introduce a new metric that allows us to visualize and test the impact of the pipeline's modeling choices on the Fermat potential at the population level. To demonstrate its usefulness, we further use this new metric to address the impact of the source complexity level in a model by introducing small perturbations in the source light structure and evaluate if, and by how much, the introduced perturbations change the stability of the Fermat potential difference between image positions. Of course, a full cosmographic error budget will have to consider other sources of uncertainty, such as those arising from line of sight effects (Suyu et al., 2010; Rusu et al., 2017), time delay measurements (Millon et al., 2020), and the

mass sheet degeneracy (Falco et al., 1985; Schneider and Sluse, 2013; Birrer et al., 2020), in addition to the modeling errors considered here.

The paper is organized in the following manner: Section 2.2 gives a description of our sample, highlights the data reduction, and discusses *HST* cycle 26 lenses. Detail on our lens modeling procedures, along with the parameterization of mass and light profiles, are listed in Section 2.3, uniform lens modeling. The results of our analysis are presented in Section 2.4, results. We address the impact of modeling choices and underlying systematic uncertainties in source complexity in Section 2.5 and conclude with a summary in Section 2.6. Magnitudes are reported in the AB system and whenever necessary we use a cosmological concordance model with parameters $H_0 = 70$ km s^{-1} Mpc^{-1}, $\Omega_{\mathrm{m},0} = 0.3$, and $\Omega_{\Lambda,0} = 0.7$.

2.2 *HST* Sample

Our sample consists of 31 lenses from *HST* cycle 25 and cycle 26, with the cycle 25 lenses consisting of the same sample as modelled by Shajib et al. (2019). The targets that were observed during *HST* cycle 26 consist of 16 quads and two five-image systems with two main deflectors for a total of 18 lenses. While information about cycle 25 targets are listed in Shajib et al. (2019), a brief description of the main characteristics and respective discovery of the cycle 26 sample can be found below in Section 2.2.2.

2.2.1 Data and Data Reduction

The observations of the lenses in our sample were taken by the Hubble Space Telescope under cycle 25 and cycle 26 programs HST-GO-15320 and HST-GO-15652 (PI: Treu), respectively, using the Wide Field Camera 3 (WFC3). With the exception of one lens, W2M J1042+1641, exposures for each lens were taken in three filters, F160W for infrared (IR) data and F475X, as well as F814W, for ultraviolet-visual (UVIS) data. For W2M J1042+1641

the two programs did not obtain data in the IR channel and restricted the observation to the UVIS bands, as IR images are available from a previous *HST* visit as explained in the description of the lens below. In order to improve the sampling of the data, we adopted a 4-point dither pattern in the IR channel, while for the UVIS channel observations we adopted a 2-point dither pattern. To properly sample the full dynamic range of the data, including areas around the bright quasar images, we took a long and short exposure at each dither point. The total exposure times per filter band are comparable to the exposure times of the 13 lenses listed in Table 1 of Shajib et al. (2019), since observations took place with the same instrument under an identical strategy. For our data reduction, as well as alignment and combination of the various exposures in each filter, we use the Python package AstroDrizzle (Avila et al., 2015). The pixel size in the final reduced and combined images is 0.08″/pix for IR exposures and 0.04″/pix for exposures in the UVIS bands.

2.2.2 Notes on individual quads

This section gives a brief description of each quadruply imaged quasar in our sample, regardless of whether it was successfully modeled by the automated pipeline or whether a model needs further work.

2.2.2.1 J0029-3814

J0029-3814 was discovered among extragalactic objects with astrometric anomalies between the optical and infrared in VEXAS (Spiniello and Agnello, 2019), further prioritized as a "naked cusp" candidate from model-based deblending of its image cutouts (following Morgan et al., 2004), and its spectroscopic confirmation at the 3.5m ESO-NTT (PI T. Anguita) determined a preliminary source redshift z=2.821, while the deflector redshift needs deeper follow-up with larger facilities (Schechter et al. in prep).

2.2.2.2 PS J0030-1525

This lens was discovered by Lemon et al. (2018) by cross-matching multiple catalogued detections in *Gaia* Data Release 1 (DR1) against photometric quasar candidates from the Wide-field Infrared Spectroscopic Explorer. The imaging in Pan-STARRS shows just two blue point sources offset from a galaxy, and follow-spectroscopy confirmed these to both be quasars at z=3.36. An archival VST-ATLAS r-band image revealed a likely counterimage, and Lemon et al. (2018) suggested that this system is likely a fold quad, with image A composed of a merging pair. They modeled the system as an SIE + shear, predicting flux ratios of 7:7:3:1 (ABCD), yet only measuring 7:0.5:4:1, suggesting a strong demagnification of image B. They report a particularly large best-fit total model magnification of 71.

2.2.2.3 DES J0053-2012

DES J0053-2012 was discovered and confirmed by Lemon et al. (2020), after being selected in *Gaia* DR1 as a double detection associated to a red *WISE* detection. The source redshift is ≈3.8, however this is uncertain due to absorption and possible blueshift of the broad quasar emission lines. Lemon et al. (2020) find that a SIE + shear model is insufficient to reproduce the image positions, but including an SIE for the galaxy 4 arcseconds to the South-East provides a good fit to the system.

2.2.2.4 WG0214-2105

WG0214-2105 was discovered by Agnello (2018) as a *Gaia* multiplet corresponding to an extragalactic candidate from its *WISE* magnitudes. It has a high UV deficit and "blue" *WISE* colours, which are more similar to those of known white dwarfs and may explain why it was discovered only once the ESA-*Gaia* mission pipeline resolved it into multiple source detections. Its source redshift is 3.229±0.004, and the deflector's photometric redshit is 0.22±0.09, as it was too faint to obtain a secure spectroscopic redshift on the 10m SALT follow-up (PI L. Marchetti; Spiniello et al., 2019).

2.2.2.5 DES J0530-3730

This system was discovered using the method described by Ostrovski et al. (2017), and by Lemon et al. (in prep) as a triple detection in *Gaia* DR2 around a photometric quasar candidate. The coordinates are RA=05:30:36.984, DEC=-37:30:11.16 (J2000). It was confirmed as a quasar at z=2.838 from spectra obtained at the NTT in December 2016 during the run described by Anguita et al. (2018).

2.2.2.6 J0659+1629

This system was discovered by Lemon et al. in prep as a triple detection in *Gaia* DR2 around a photometric quasar candidate. They confirm the source redshift to be 3.09, and an SIE + shear model requires only a modest shear of 0.06, however the predicted flux of image D is 60% fainter than observed, suggesting variability over the time delay as a possible cause for this discrepancy. The system was also independently selected by Delchambre et al. (2019) using the astrometry of the three *Gaia* DR2 detections, and Stern et al. (2021) also spectroscopically confirm that the source redshift is 3.083, and the lens redshift is 0.766. Stern et al. (2021) model the system as an SIS + shear, however their flux ratios are poorly reproduced and the ellipticity is unrealistic. Stern et al. (2021) suggest this is indicative of a missing nearby galaxy.

2.2.2.7 J0818-2613

This system was discovered by Lemon et al. in prep as four detections in *Gaia* DR2 around a photometric quasar candidate. They confirm the source redshift to be a BAL quasar at z=2.155. Their SIE + shear model recovers the image positions, but is highly unphysical with perpendicular shear and mass ellipticity, suggesting that the system is likely lensed by a complex mass distribution composed of several galaxies. The system was also independently confirmed by Stern et al. (2021) who measure a source redshift of 2.164. They reach the same conclusion as Lemon et al. in prep. regarding the likely presence of a galaxy group or

cluster.

2.2.2.8 W2M J1042+1641

Information about the discovery, main characteristics, and measured redshifts for this system can be found in the paper by Glikman et al. (2018). For this target we obtained UVIS data only. The IR data used to model this lens was observed with *HST* Proposal 14706 (PI: E. Glikman), which is publicly available from the *HST* archive.

2.2.2.9 J1131-4419

This system was found using *Gaia* catalogue positions as potential quad configurations using extremely randomized trees by Krone-Martins et al. (2018) and Delchambre et al. (2019) as GRAL113100-441959. It was spectroscopically confirmed by Wertz et al. (2019), who measure a source redshift of 1.09, and present models in the absence of the lensing galaxy position.

2.2.2.10 2M1134-2103

This bright quad was discovered serendipitously by Lucey et al. (2018) while visually inspecting the target catalogue of the Taipan Galaxy Survey. Rusu et al. (2019) obtained spectra for this system, confirming the source to be at 2.77. Both papers confirm that a large shear is required to model the system. Rusu et al. (2019) detect a companion object in the Pan-STARRS r and i PSF-subtracted images $\approx$ 4 arcseconds South-East of the system, which they suggest could be partly responsible for the shear. The strong shear could also be due to a galaxy group $\approx$1 arcminute North-West of the system.

2.2.2.11 J1537-3010

This system was discovered by Lemon et al. (2019), who obtained a source redshift of 1.72. They are able to fit the system well with an SIE + shear model. The system was also inde-

pendently selected using *Gaia* astrometry by Delchambre et al. (2019) and spectroscopically confirmed by Stern et al. (2021), who corroborate a source redshift of 1.721.

2.2.2.12 J1721+8842

The system was originally discovered by Lemon et al. (2019) who confirmed the source to be at z≈2.37, with strong absorption features. *Gaia* DR2 catalogues 5 detections, and an in-depth study of this system by Lemon et al. (2022) show that there are two quasar sources at similar redshifts, with one being lensed into four images, and one into two images. They provide several mass models for the system, which we will compare to in Section 2.4.2. The source is also unique in that the bright images A and C are confirmed to have a proximate damped Lyman alpha absorber.

2.2.2.13 J1817+2729

This system was discovered by Lemon et al. (2018) as a *Gaia* quartet associated with a photometric quasar candidate in *WISE*. Only three of these detections were due to the images of the system, with the fourth due to a nearby star. They measure a source redshift of 3.07. The system was independently selected by (Delchambre et al., 2019) and confirmed spectroscopically by Stern et al. (2021), who measured a source redshift of 3.074. Rusu and Lemon (2018) present a detailed model of this system based on Subaru-FOCAS *i*-band imaging, showing that the lens is an edge-on disk galaxy.

2.2.2.14 WG2100-4452

WG2100-4452 was discovered[1] by Agnello and Spiniello (2019) as an extragalactic candidate with astrometric anomalies between the optical and infrared in VEXAS (Spiniello and Agnello, 2019). Its source redshift is 0.920±0.002 and its deflector redshift is 0.203±0.002 (Spiniello et al., 2019).

[1]This discovery was first reported in 05/2018, arxiv:1805.11103

2.2.2.15 J2145+6345

J2145+6345 was discovered by Lemon et al. (2019) as a quartet in *Gaia* associated with a *WISE* photometric quasar candidate. The images are particularly bright (*Gaia* magnitudes of 16.86, 17.26, 18.34, 18.56) and has X-ray (ROSAT) and radio (VLASS) detections. Lemon et al. (2019) did not report the lensing galaxy position, as it was not detected in the Pan-STARRS PSF subtracted images; either since it was too faint or the PSF model was not sufficient to correctly subtract the four nearby bright PSFs.

2.2.2.16 J2205-3727

This quad was discovered by Lemon et al. in prep. by searching photometric quasar candidates from *WISE* for multiple *Gaia* detections following Lemon et al. (2019). They confirm the source to be at redshift 1.848.

2.2.3 Notes on individual Five-image systems

This section gives a brief description of the quads in our sample that hold a fifth image due to a lens configuration that includes two primary deflectors.

2.2.3.1 J0343-2828

This system was discovered by Lemon et al. in prep. by searching for single *Gaia* detections offset from galaxies, as possible lensed quasars, following Lemon et al. (2017). The system was selected for *HST* follow-up imaging due to the image colours and point-source nature, however follow-up spectroscopy reveals no quasar emission lines, but absorption features of a galaxy at z=1.655. The lens redshift is 0.385.

2.2.3.2 2M1310-1714

This system was discovered serendipitously by Lucey et al. (2018) while visually inspecting the target catalogue of the Taipan Galaxy Survey. They report the presence of two lensing

galaxies at z=0.293, and the source to be at z=1.975. Their mass model of two SIEs fixed to the galaxy positions with position angles both matching that of the extended halo light, and a shear fixed at 45 deg to this, predicts a fifth image five magnitudes fainter than the outer images. They also note the presence of a possible Einstein ring in VISTA Hemisphere Survey K_s band imaging.

2.3 Uniform Lens Modeling

We develop and apply an automated pipeline (see Figure 2.3 for general overview) that is based on the uniform lens modeling process that was originally set forth by Shajib et al. (2019) and further improved as detailed in Section 2.3.4. Except for the initial setup of a lens, outlined in step a. of Section 2.3.4, all model component decisions, e.g. to increase necessary model complexity, are made during runtime by the automated pipeline.

Our pipeline is based on the gravitational lens modeling software Lenstronomy (Birrer and Amara, 2018) [2], which is a publicly available open source distribution written in Python. Lenstronomy is the foundation in many strong lens analyses and is also used in time-delay cosmography (Birrer et al., 2016; Birrer and Treu, 2019; Shajib et al., 2020). Additionally, Lenstronomy is an Astropy (Astropy Collaboration et al., 2013, 2018) affiliated package. Explicit details on the modeling choices and analysis procedures to probe the parameter space for our models are presented in Section 2.3.4, modeling procedure. We refer to e.g. Shajib et al. (2021); Etherington et al. (2022) for automated pipelines analysing galaxy-galaxy lenses without lensed quasars.

[2] https://github.com/sibirrer/lenstronomy

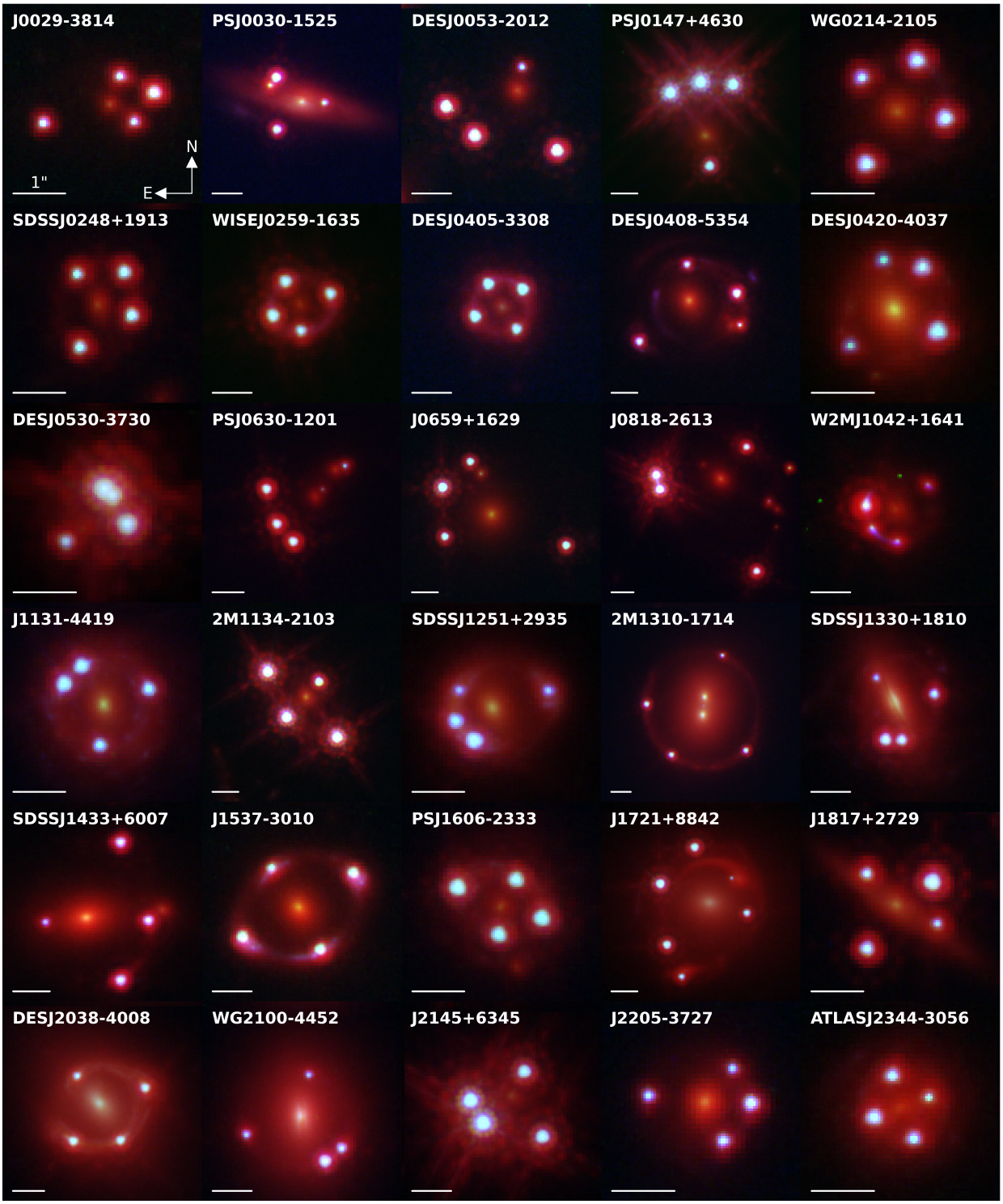

Figure 2.1: Sample of quadruply lensed quasar used in our analysis. The figure shows a composite red-green-blue (RGB) image for each lens, generated from *HST* observation in bands F160W (red channel), F475X (blue channel), and F814W (green channel). For visualization purposes, the intensities for each band vary between systems and are adjusted to emphasize each lens' individual configuration.

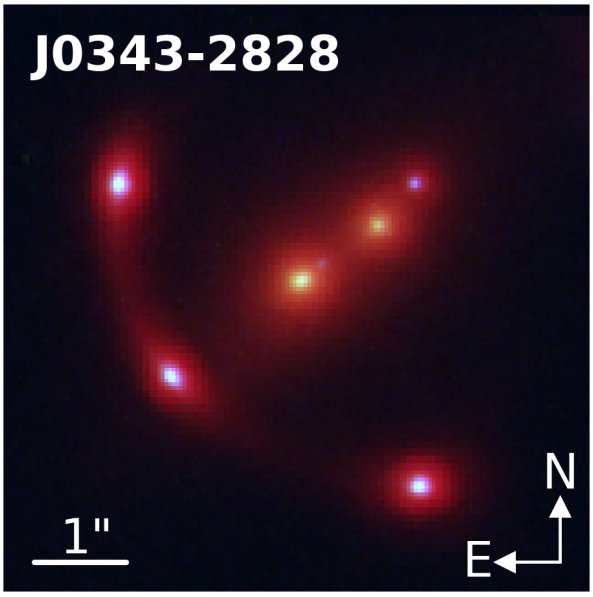

Figure 2.2: Quintuply lensed galaxy J0343-2828 used in our analysis. The figure shows a composite red-green-blue (RGB) image for each lens, generated from *HST* observation in bands F160W (red channel), F475X (blue channel), and F814W (green channel). For visualization purposes, the intensities for each band is adjusted to emphasize the system's configuration.

2.3.1 Mass profile parameterization

The mass profile of the main deflector is modeled with a power-law elliptical mass distribution (PEMD), which corresponds to a radial mass density profile of $\rho \propto r^{-\gamma}$, where γ is the power-law slope. The convergence, or dimensionless projected surface mass density, for the profile at position θ is parameterized as

$$\kappa(\theta_1, \theta_2) = \frac{3-\gamma}{2} \left(\frac{\theta_E}{\sqrt{q\theta_1^2 + \theta_2^2/q}} \right)^{\gamma-1} \tag{2.5}$$

where θ_1 and θ_2 are aligned along the semi-major and semi-minor axis through the rotational position angle $\phi = \arctan(\theta_2, q\theta_1)$, and where q is the corresponding axis ratio.

If our data show a second main deflector, resulting in a fifth image, or a satellite to the main deflector, we model the secondary object using a Singular Isothermal Sphere (SIS), which is a PEMD with a fixed power-law slope, γ, of 2.0 and an axis ratio, q of 1.0. Any

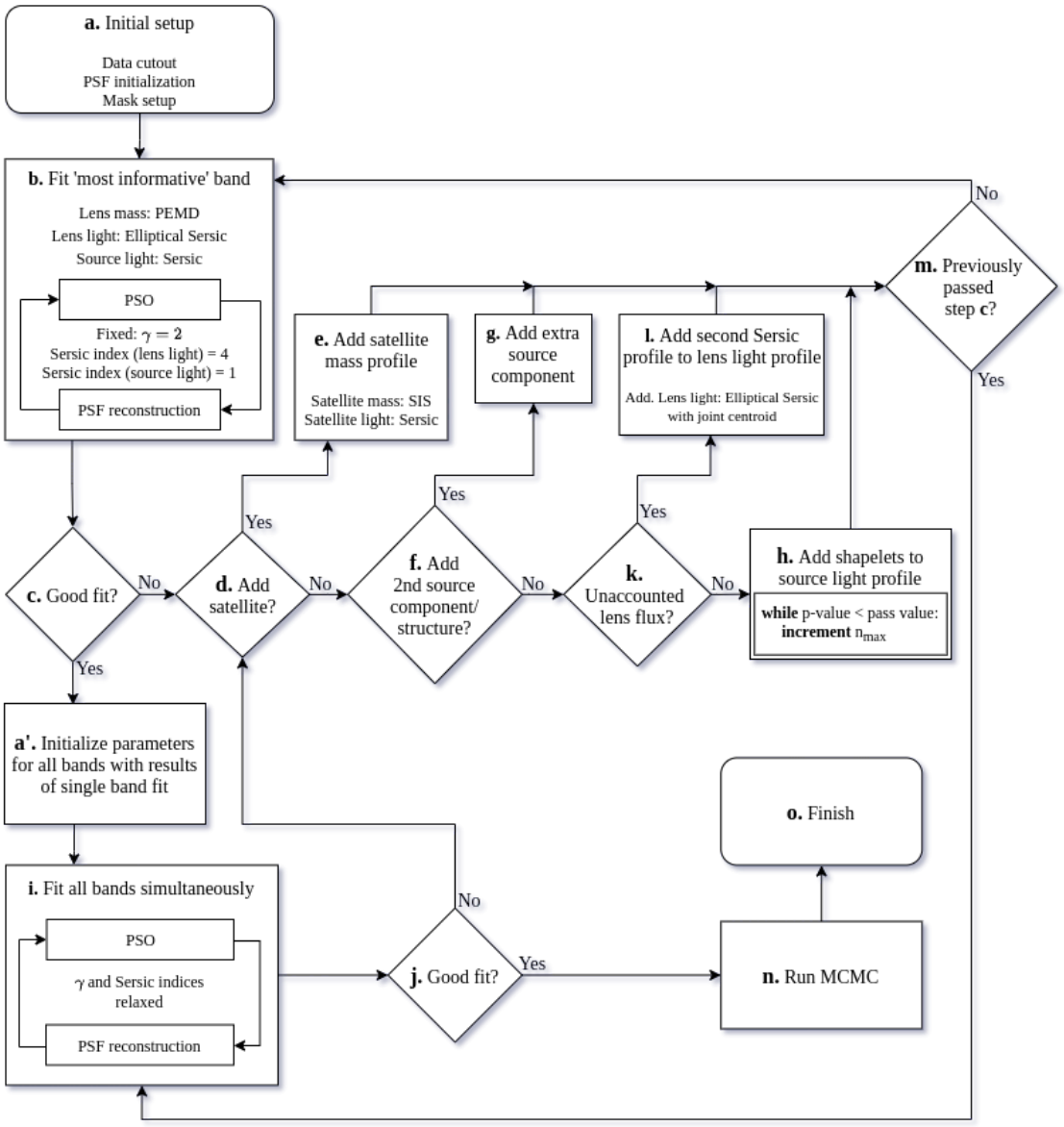

Figure 2.3: Flowchart illustrating individual modeling choices that are made by the pipeline along the process of lens model reconstruction. After being set up in node a., the pipeline traverses this decision tree, iteratively adding model complexity until the adopted minimum acceptance threshold for the p-value or associated reduced χ^2-value is achieved. Steps c., j., and h., initially use the mask that includes the lens light. For these three steps (c., j., h.), the lens light flux is only excluded if there are remaining residuals in the lens light after a second light profile was added in step l. In the last step, node n., the pipeline probes the posterior distribution of each free model parameter until convergence is reached.

additional linear distortions to the lensed structure, resulting from line-of-sight perturbers, are modelled through an external shear profile with strength

$$\gamma_{\rm ext} = \sqrt{\gamma_{\rm ext,1}^2 + \gamma_{\rm ext,2}^2}, \tag{2.6}$$

and position angle

$$\phi_{\rm ext} = \frac{1}{2} \arctan\left(\gamma_{\rm ext,2}, \gamma_{\rm ext,1}\right). \tag{2.7}$$

2.3.2 Light profile parameterization

The light profile of the main deflector is modeled with an elliptical Sérsic function (Sérsic, 1968), which is parameterized as:

$$I(\theta) = I(\theta_{\rm e})\ \exp\left\{-C(n)\left[\left(\frac{(q_{\rm L}\theta_1)^2 + \theta_2^2}{q_{\rm L}\theta_{\rm e}^2}\right)^{\frac{1}{2n}} - 1\right]\right\}, \tag{2.8}$$

where $C(n)$ is a normalization constant so that at the effective radius, $\theta_{\rm e}$, the profile includes half of the deflector's light. n represents the Sérsic index, θ_1 and θ_2 are the angular coordinates aligned along the semi-major and semi-minor axis through the rotational position angle $\phi_{\rm L} = \arctan(\theta_2, q\theta_1)$ of the light profile, and $q_{\rm L}$ represents the corresponding axis ratio. Each main deflector in our sample is initially modeled with one elliptical Sérsic, however, as further detailed in node l. of the modeling procedure below, the pipeline adds an additional Sérsic with a fixed Sérsic index in the case of unaccounted lens flux.

If the main deflector is accompanied by a satellite, or if the lens has a secondary main deflector, the light of the additional perturber is modelled as a circular Sérsic function, which corresponds to an elliptical Sérsic function (2.8) with a fixed axis ratio at $q_{\rm L} = 1.0$. We restrict our analysis to circular secondary light distributions in order to limit the number of free parameters in our models. In nearly all cases the circular Sérsic function models the light of the additional perturber with sufficient precision.

The images of the lensed quasar are modeled by a point spread function (PSF) in the

image plane. To model the light of the lensed source, or host galaxy of the lensed quasar, we choose a circular Sérsic function in the source plane as described in the light profile parameterization of additional perturbers above. If additional lensed source light is identified that is not part of the primary source hosting the quasar, we adopt a second circular Sérsic to model the extra source light separately from light profile of the host galaxy. If the Sérsic functions are insufficient to describe the complexity of the source, we add a set of two-dimensional Cartesian shapelets (Refregier, 2003; Birrer et al., 2015). The shapelet number, or number of basis functions which form an orthonormal basis, is given by

$$N_{\rm shapelet} = \frac{(n_{\rm max}+1)(n_{\rm max}+2)}{2}, \tag{2.9}$$

where $n_{\rm max}$ represents the highest shapelet order, or maximum source complexity, and is linked to the maximum spatial scale, $l_{\rm max}$, and the characteristic scale, β, by $l_{\rm max} = \beta\sqrt{n_{\rm max}+1}$. Increasing the parameter $n_{\rm max}$ corresponds to the reconstruction of additional smaller features in the lensed source.

2.3.3 Priors

A number of well known degeneracies affect lens modeling (see, e.g., Falco et al., 1985; Schneider and Sluse, 2014). To avoid non-physical results, we impose priors on the axis ratio, q, and the position angle, ϕ, of the primary deflector's mass profile, motivated by the analysis of 63 lenses from the SLACS sample (Bolton et al., 2006, 2008; Auger et al., 2010b). For each SLACS lens we compare the axis ratio of the deflector's mass profile to the corresponding axis ratio of the light profile, with the results of this comparison shown in Figure 2.4. Given a 5% error and a requirement that 95% of the sample to fall within the constraint, we then determine a linear prior whereby the lower limit of the mass profile's axis ratio is given by $q \geq q_{\rm L} - 0.1$. If during the fitting process a model instance produces an axis ratio below this limit, the pipelines discards the likelihood of the model. This prior avoids

nonphysical solutions, such as extreme ellipticity in a deflector's mass profile, and guides the model to increase the strength in the external shear instead.

To find a suitable restriction on the convergence's position angle, we plot the absolute difference between the position angles of the mass and light profiles, $\Delta_{\rm PA}$, as a function of the light profile's axis ratio, $q_{\rm L}$, for the 63 lenses in the SLACS sample. Due to symmetry, any position angle difference greater or less than 90 degrees is shifted by 180 degrees with the results shown in Figure 2.5. Following a requirement for 95% of the sample to fall within the constraint, given an error margin of 10 degrees, we arrive at a prior for the upper limit of the position angle difference given by $\Delta_{\rm PA} \leq 10 - 5/(q_{\rm L} - 1)$. Models with angle difference exceeding this limit are excluded a priori. Although our prior is well justified and prevents unphysical solution, it is of course not a unique choice. It is thus important that this as well as other informative priors adopted in our analysis are to be kept in mind when interpreting our results.

To place a constraint on the centroid of the main deflector's mass profile, we use a Gaussian prior for each axis that depends on the centroid coordinates of the deflector's light profile and a standard deviation of $0.04''$, which corresponds to 1 pixel in UVIS. If a lens model includes a secondary deflector, or satellite, we join the centroid of the sattelilte's mass profile with the centroid of the corresponding light profile.

For some of our targets the lensed host galaxies of the multiply imaged quasars do not a have sufficiently high signal to noise ratio and therefore provide insufficient radial information to constrain the slope of the mass density profile. For that reason, we adopt an informative prior to constrain the power-law slope of the main deflector's mass density profile. Due to a degeneracy between the slope and the characteristic scale, β, in the shapelets used to describe higher source complexity, the prior prevents nonphysical results when the slope is not well constrained by the data (Birrer et al., 2016). In their analysis of early-type galaxy strong gravitational lenses from the SLACS sample, Auger et al. (2010a) find a distribution of the power-law slope with a mean of 2.078 ± 0.027, which agrees with the findings of Koopmans

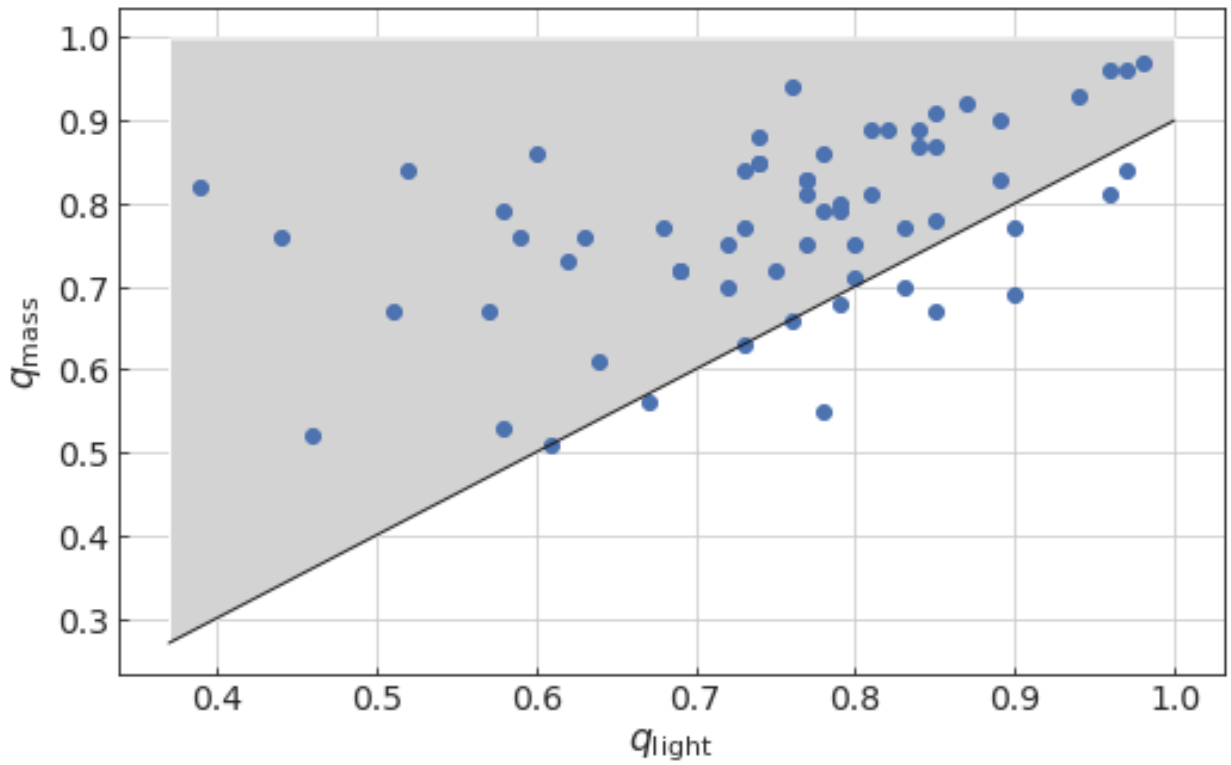

Figure 2.4: Linear prior on axis ratio for main deflector's mass profile (shaded area), motivated by the analysis of 63 lenses from the SLACS sample, and chosen with 95% of the 63 SLACS lenses meeting the constraint, given a 0.05 tolerance in the axis ratio. For each lens, we compare the axis ratio of the mass profile, q_{mass}, to the respective light profile's axis ratio, q_{light}.

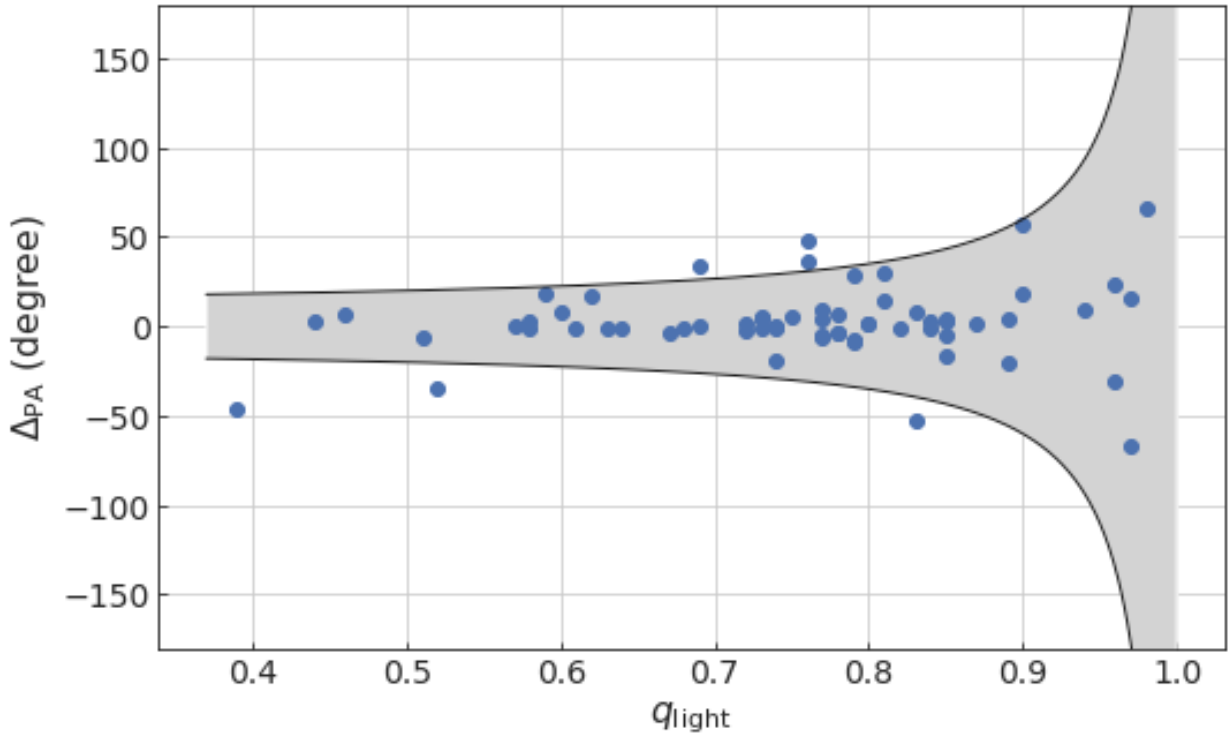

Figure 2.5: Prior on the position angle for main deflector's mass profile (shaded area), based on axis ratio and position angle of the deflector's respective light profile. The y-axis shows the difference in the position angle between the mass and light profile, $\Delta_{\rm PA}$, as a function of the respective light profile's axis ratio, $q_{\rm light}$. The prior is set with 95% of the 63 strong lenses in the SLACS sample meeting the criterion, given a 10 degree tolerance. Values outside the gray shaded are are exluded a priori in our analysis.

et al. (2009). For all lenses in our sample we use these results in a Gaussian distributed prior and additionally reject the likelihood of any model that produces a slope with 12σ above or below the aforementioned mean.

We note that the slope of the radial mass density profile is a key parameter for determining the time delay distance and hence H_0 (e.g., Wucknitz, 2002). Therefore, if one wishes to use the results of this work as a starting point for cosmographic work, the prior needs to be accounted for in order to avoid underestimating the errors or biasing the results.

2.3.4 Modeling procedure

To fit the observed data from all *HST* filters, all lenses in our sample are modeled using LENSTRONOMY's particle swarm optimization (PSO). We probe the posterior distribution of each model via Markov chain Monte Carlo (MCMC) sampling, built on the EMCEE package (Foreman-Mackey et al., 2013), which is an affine-invariant ensemble sampler (Goodman and Weare, 2010). Since the effectiveness of an optimization routine depends the initial starting point, we implemented a three step process to effectively find the global maximum likelihood for our models, with each step in our fitting routine building on the results of the previous optimization. Should an optimization routine produce an unsatisfactory fit to the data, we increase the model complexity to account for additional features. During each step, we evaluate the difference in the Fermat potential at the image positions in order to track the lens model's evolution. Using LENSTRONOMY's PSO, we first find the best fit for a single band (F814W), which we deem the most informative band as most or all features that are visible in other bands also appear in the F814W filter, and as it has a higher resolution than WFC3-IR. Once an acceptable model has been established, we fit all three bands simultaneously using the results from the previous fitting routine for each model parameter, again using LENSTRONOMY's PSO. After an acceptable lens model has been established, we probe the model's posterior probability distribution with LENSTRONOMY's above described MCMC routine.

Figure 2.3 gives a general overview to our uniform modeling procedure while a detailed description of each node in the flow chart can be found in the following subsections:

a. Initial setup: First, we pre-process the images in each filter band. After our data reduction process, as described in Section 2.2.1, we select a cutout for each *HST* filter, large enough to encompass the lens, the lensed quasar images, and any satellite or perturbers that are to be included in the model. We then subtract the mean of the background flux, which is determined by running SourceExtractor (Bertin and Arnouts, 1996) on the full *HST* image. Afterwards, we make preliminary guesses for the position of the lensed quasar images and for the main deflector's centroid. If the model were to include another perturber or additional source components, initial guesses for the location of these features are determined as well. To differentiate additional source components, lensed by the main perturber, we look for structure with conjugate components that are situated near the lensed primary source. We then apply a circular mask to the cutout with a radius appropriate to exclude unwanted nearby features. If we identify additional attributes within the circular mask that are not deemed to be part of the lens model, we exclude them by applying further masking. A second circular mask is separately applied to the cutout to separate the lens flux, which allows the pipeline to determine the goodness of a uniform lens light profile fit. Additionally we estimate a radius up to which neighboring QSO images will be blocked during the iterative PSF fitting process, as described below in step b. Lastly, we select a set of five or more small bright stars in each reduced *HST* image to obtain an initial estimate of the point spread function for each band (Birrer and Treu, 2019; Shajib et al., 2022).

b. Fit the 'most informative' band: For a typical system in our sample, the pollution in the arc and in the lensed images, caused by the lens light contribution, decreases in the bluer bands. At the same time, in the bluer filters the arc light intensity from the lensed source decreases compared the redder bands. We therefore designate the F814W filter as the 'most informative' band, as the signal to noise ratio for the lensed source is typically highest in filter F814W, compared to the other two bands used in our observations.

Since even our simplest starting models include the deflector's mass and light profile in addition to the four point source locations and a light profile for the lensed source, the fitting routines have to traverse a large parameter space to find the maximum likelihood to fit the lens model to our data. We therefore follow the procedure as set forth by Shajib et al. (2019) and fit the most informative band and increase the model's complexity before fitting the data in all filters simultaneously. For this step, we hold the power-law slope of the main deflector's mass profile constant at a value of 2.0, effectively fitting the profile for an isothermal mass distribution. To further limit the number of free parameters in the initial fitting process, and moreover effectively decreasing the computation time, we also hold the Sérsic index of the source and lens light profile fixed at 1.0 and 4.0, representative of an exponential and de Vaucouleurs light profile, respectively. Due to the strong degeneracy between the light profile's effective radius and Sérsic index, holding these settings constant furthermore prevents the half light radii from reaching on nonphysical values. Because we start each model with the same set of initial parameters, we first sample the parameter space with a broad search region. Within the same fitting sequence, after the completion of each PSO run, we optimize the PSF to best fit the model's quasar images after accounting for extended source light. We perform this iterative PSF reconstruction with 90 degree symmetry and update the PSF's error map with each new iteration (see Chen et al., 2016; Birrer et al., 2019; Shajib et al., 2020). In order to avoid corrections that have already been included in the error map of a nearby quasar image, we block any neighboring images around their centroid up to a radius that is determined in the initial setup for the lens (step a.). The alternating PSO/PSF fitting is then repeated with a narrower search region, corresponding to 1/10 of the previous iteration and centered around the results of the maximum likelihood for the previous PSO. This process is continued until the search region has been reduced to probe the parameter space within 1/1000 of the first PSO sampling range. Further details on the iterative approach to reconstructing the PSF and finding the maximum likelihood of models by probing the parameter space with PSOs can be found in the paper by Birrer and

Amara (2018).

c. Good fit? To determine how well our data fit the current model, we compute the p-value for the masked circular region in the most informative band, using the reduced χ^2 value resulting from the best fit and the degree of freedom represented by the pixels in the applied mask. We follow the acceptance criterion as set forth by Shajib et al. (2019) and deem the fit to be acceptable if the computed p-value is greater than 10^{-8}, which, given the diversity of lenses in our sample, should be beyond sufficient to indicate missing features in our models without modeling noise in the data. As an alternative acceptance criterion, we use the reduced χ^2 value and test if it is smaller than 1.1 for the masking region.

If node c. is being visited after a second Sérsic function was added to the description of the main deflector's light profile in step l. and there are remaining residuals in the lens center that would require a higher lens light complexity, then we subtract the lens center mask from the fitting region and re-evaluate the above discussed acceptance criteria to determine the goodness of the fit. This exclusion of the lens light from the fitting mask is necessary, since additional descriptions to the lens light flux would be needed and the pipeline, in its current stage, is limited to a double Sérsic as most complex light profile.

d. & e. Add satellite to mass profile: If the acceptance criteria in the goodness tests of step c. or step j. are not met, indicating the current model is missing components or complexity, and a satellite has been identified in the initial setup (step a.) but is not yet included in the model, we add an SIS profile, as outlined in the mass profile parameterization, to the description of the main deflector's mass profile. The light profile of this additional perturber is modeled by a spherical Sérsic as described in Section 2.3.2 for the light profile parameterization. The joint centroid for both, the satellite's mass and light profile, is initialized with the guess that is made during the model setup (see step a.) and the pipeline returns to the iterative fitting process of step b. or step i., depending on the evaluation of node m.

f. & g. Add additional source component: If steps c. or j. for the current

model indicate missing complexity and an additional source was identified in step a., we add a separate source light profile using a circular Sérsic function as outlined on the section on the light profile parameterization. The centroid for this additional source light profile is initialized with the guess determined in the model setup (node a.) before the iterative fitting process is restarted in steps b. or i. For the centroids location we use LENSTRONOMY's BIJECTIVE mode, whereby the location of the additional source is indentified and constrained in the lens plane and then ray-traced back to its position in the source plane.

k. Check for unaccounted lens flux: To check our models for flux, not captured by the current lens light profile, we again compute the reduced χ^2 and associated p-value for the latest fit, only using the mask that singles out the lens flux as described in the initial setup procedures. We compare this p-value and chi square result, which only pertains to the lens light profile, with the fitting results computed in step c. In the case of a lower p-value, or larger reduced χ^2 result, for the lens light mask, which would indicate missing lens light flux, the pipeline proceeds to step l. and adds an additional Sérsic profile to the description of the lens light, given that node l. has not been previously visited. In all other cases the pipeline proceeds to the next node in the decision tree.

l. Add second Sérsic function to lens light profile: Should node k. call for the addition of a lens light to account for missing flux in the main deflector's light profile, we add a second elliptical Sérsic profile to the existing description of the lens light model, with a joint centroid. We follow Shajib et al. (2019) by setting the Sérsic indices, as described in the light profile parameterization, to constant values of n = 1.0 and n = 4.0, representative of an exponential and de Vaucouleurs light profile, respectively. As discussed by Shajib et al. (2019), we hold the Sérsic indices fixed for numerical stability in our models only; therefore the two light profiles are not to be understood as individual galactic components of the main deflector. If, however, the addition of a second lens light profile results in a fit, after steps b. or i., with a larger overall reduced chi square or smaller associated p-value, the addition of the second Sérsic profile to the lens light description is reversed and the previous fitting

result is used for the remainder of the modeling process.

h. Add shapelets to source light profile: Additional complexity in the source light and not accounted by the source's Sérsic profile is modelled through a basis set of shapelets, which shares the same centroid as the primary source's light profile. To find the proper shapelet order we iteratively increase the maximum order and guess the characteristic scale, β, using the primary source's Sérsic radius. Running a SciPy minimization routine, the pipeline proceeds to find the β value to the current maximum shapelet order that results in the best p-value, and lowest associated chi square number, effectively performing a linear minimization of the shapelet coefficient, and then tests if the acceptance criteria as set forth in step c are reached. If the p-value for the best β scale lies below the threshold, the shapelet order is incremented and the minimization steps are repeated until the shapelet order was raised by 6 for a newly added basis set, or raised by 5 for a previously fitted basis set, in which case the pipeline returns to the PSO/PSF fitting step (b. or i.) that lead to this node. If the χ^2 result, or associated p-value, meets the acceptance threshold, the pipeline proceeds to the simultaneous fitting of all bands with the shapelet order starting values determined from the minimization routine. This iterative approach to raising the source complexity is performed for each band in which the p-value of the corresponding filter's cutout mask lies below our acceptance criterion.

m. Completed fit for most informative band? Since it is possible for nodes e., g., h., and l. to be reached after fitting the single, most informative, band or after fitting all bands simultaneously, we check if a previous iteration has already achieved a good fit for a single filter, in which case we continue with the simultaneous fitting of all bands in step i.

i. Fit all bands simultaneously: On the first visit of this node we align the data from all filters to the data of the most informative band. For this step we use Lenstronomy's iterative alignment routine, as described by Birrer and Amara (2018), to match the coordinate frames of different filters using the astrometric positions of the lensed quasar images. We estimate this alignment to be accurate within 1 milliarcsecond. After the alignment we

initialize each free parameter with the results of the best fit for the most informative band and continue to simultaneously fit all filters using LENSTRONOMY's PSO routine iteratively. For this step, we relax the power-law slope of the main deflector's mass profile as well as the Sérsic indices of the light profiles, as these parameters were held constant during the fitting described by step b. Due to the strong correlation between the effective radius and the Sérsic index in the light profile parameterization and to further avoid nonphysical fitting results, the upper boundaries of the Sérsic indices are set to a limit of 6.0 and 4.0 for the lens light and source light profile, respectively.

We begin the sampling of the parameter space with 1/10 of the initial search region used for fitting the most informative band. As in step b., we continue to optimize the PSF within the same fitting sequence to obtain the best fit for our model's quasar images. Again, this iterative PSF reconstruction is performed for each filter with a 90 degree symmetry in the PSF and the PSF's error map is updated for each band. In each filter we block neighboring images around their centroid position to avoid the double counting of corrections from nearby quasar images. As previously outlined in step c., the alternating PSO/PSF fitting is repeated for all bands simultaneously with 1/10 of the former search region and around the results of the maximum likelihood for the previous PSO iteration. This is continued until the search region has been reduced to probe the parameter space down to 1/100 of the first PSO sampling range in this step. For the simultaneous fitting approach of all bands we follow Shajib et al. (2019) and hold the following lens light, additional perturber light, and source light profile parameters common across all filters: Sérsic radius, Sérsic index, centroid, ellipticity, and position angle. This choice greatly simplifies the computational cost of the fit, and it is commonly adopted in the literature when large dataset need to be fit (e.g. SDSS) - see Stoughton et al. (2002) and Lackner and Gunn (2012). Shajib et al. (2019) find that this common parameter approach across various filters results in fits that are within the estimated uncertainties compared to fits obtained from the fitting using unlinked parameters. Therefore, in our automated uniform approach, we deem this approximation to be acceptable

for the purpose of this work. All other model parameters not specifically mentioned to be held common (e.g. maximum shapelet order) are allowed to vary across filters.

j. Good fit? To test the fit of our model for the bands that have been fit simultaneously, we repeat the procedures described in node c., namely computing the p-value for the masking region in each filter and test of it is above 10^{-8} or if the associated reduced χ^2 meets the acceptance criterion of being lower than 1.1. This acceptance procedure is performed for each filter separately, with the pipeline proceeding to add higher complexity to the model if one of the bands fails these tests. As a third alternative to the two acceptance criteria (outlined immediately above), we also compute the overall reduced χ^2 value for the fit combining all bands and accept the current model if the overall result lies below 1.1. As described in the single band fitness test (step c.), if we detect residuals in the lens flux after a second Sérsic profile has been added to the lens light description, we exclude the masking region that encompasses the lens center for the purpose of calculating the χ^2 and associated p-values.

n. Run MCMC: Once the alternating PSO/PSF fitting routine finds a good model, meeting our acceptance criteria, we probe the posterior distribution for each free model parameter using Lenstronomy's MCMC routine. We first initialize each free parameter with the best fit found by the final PSO run and then run a burn-in cycle for 1500 iterations to assure the chain reaches an equilibrium distribution. The total number of likelihood evaluations corresponding to the burn-in cycle is given by the product of the number of free parameters in the model, the number of walkers per parameter, and the number of iterations. After the burn-in, we stop the MCMC run every 100 iterations to compute the mean as well as the spread in the distribution for each free model parameter, using the corresponding distribution's 16- and 84-th percentiles. The pipeline continues by comparing the current mean of each parameter with the mean computed during the previous 100 iterations. If the change in the mean value is less than 1/100 of the full spread for the respective parameter, we consider the value to be converged. Only if this convergence criterion has been reached simultaneously for all free parameters in our model, the pipeline considers the reconstruction

completed.

o. Finish Given the large diversity of lenses in our sample, we visually inspect each model after the successful completion of the pipeline's reconstruction process, to assess how well the pipeline performed. We also check if model parameters have diverged towards their corresponding upper or lower bounds. Additionally, we track the evolution of the difference in a model's Fermat potential at the position of the quasar images to ensure stability in our models. Further details relating to this stability metric can be found in Section 2.4.5.

2.4 Results

This section provides details on the lens systems that have been successfully processed by the automated pipeline. For each lens, we give a description of the deflector's mass profile parameters as well as details on the corresponding light profile components. For the system that cannot be successfully reconstructed by the framework, we list the reasons in Appendix 2.E and discuss necessary modification that could be implemented in future iterations of the pipeline in order to achieve a fully automated reconstruction. We further show predicted time delays for flux variations between the quasar images, based on measured or assumed redshifts for the main deflector and lensed quasar.

2.4.1 Lens models

For 30 out of 31 lenses (97%), our automated pipeline is able to reconstruct models based on the observational data. As an example, for two of the systems in our sample, we show in Figures 2.6 and 2.7 a comparison between the *HST* observations in each filter (column 1) and the corresponding reconstructed lens model (column 2). To demonstrate how well our models match the data, we include (in column 3) the normalized residuals after the subtraction of observational data from the reconstructed model. Also shown, in the 4th row for each figure, is a reconstruction of the lensed galaxy's light in *HST* band F160W (column

Table 2.1: Model parameters for lens mass distributions, which are median values. The associated uncertainties are statistical in nature and were computed using 84th and 16th percentiles.

Name of Lens System	$\theta_{\rm E}$ (arcsec)	γ	q	ϕ (N of E) (degree)	$\gamma_{\rm ext}$	$\phi_{\rm ext}$ (N of E) (degree)	Area of Inner Caustic (arcsec^2)
J0029-3814	$0.769^{+0.007}_{-0.010}$	$1.99^{+0.02}_{-0.02}$	$0.54^{+0.06}_{-0.03}$	$73.4^{+0.2}_{-0.3}$	$0.252^{+0.017}_{-0.014}$	$-15.2^{+0.1}_{-0.1}$	$0.610^{+0.041}_{-0.059}$
PS J0030-1525	$0.996^{+0.003}_{-0.003}$	$1.97^{+0.02}_{-0.03}$	$0.72^{+0.02}_{-0.02}$	$9.6^{+0.6}_{-0.7}$	$0.071^{+0.004}_{-0.004}$	$-11.0^{+2.1}_{-2.0}$	$0.057^{+0.005}_{-0.005}$
DES J0053-2012	$1.380^{+0.005}_{-0.006}$	$2.03^{+0.02}_{-0.02}$	$0.69^{+0.03}_{-0.02}$	$-58.1^{+0.6}_{-0.4}$	$0.215^{+0.009}_{-0.007}$	$21.7^{+0.2}_{-0.2}$	$0.250^{+0.028}_{-0.030}$
PS J0147+4630	$1.886^{+0.005}_{-0.004}$	$2.08^{+0.02}_{-0.02}$	$0.80^{+0.01}_{-0.01}$	$-85.8^{+0.4}_{-0.4}$	$0.147^{+0.005}_{-0.006}$	$-12.2^{+0.2}_{-0.2}$	$0.463^{+0.005}_{-0.006}$
WG0214-2105	$0.849^{+0.001}_{-0.001}$	$2.08^{+0.02}_{-0.03}$	$0.86^{+0.01}_{-0.01}$	$-17.8^{+2.4}_{-2.5}$	$0.101^{+0.003}_{-0.003}$	$-50.3^{+0.4}_{-0.3}$	$0.029^{+0.002}_{-0.002}$
SDSS J0248+1913	$0.767^{+0.001}_{-0.001}$	$2.01^{+0.06}_{-0.06}$	$0.54^{+0.01}_{-0.01}$	$80.2^{+0.8}_{-0.7}$	$0.222^{+0.003}_{-0.004}$	$-86.8^{+0.6}_{-0.7}$	$0.026^{+0.004}_{-0.004}$
WISE J0259-1635	$0.742^{+0.001}_{-0.001}$	$2.20^{+0.03}_{-0.02}$	$0.79^{+0.01}_{-0.01}$	$78.8^{+0.5}_{-0.5}$	$0.058^{+0.003}_{-0.003}$	$-28.8^{+0.6}_{-0.6}$	$0.038^{+0.002}_{-0.002}$
J0343-2828	$0.900^{+0.002}_{-0.002}$	$1.99^{+0.01}_{-0.01}$	$0.50^{+0.01}_{-0.01}$	$-44.3^{+0.1}_{-0.2}$	$0.150^{+0.002}_{-0.002}$	$46.8^{+0.1}_{-0.1}$	$0.013^{+0.002}_{-0.002}$
DES J0405-3308	$0.705^{+0.001}_{-0.001}$	$2.15^{+0.03}_{-0.03}$	$0.70^{+0.01}_{-0.01}$	$49.4^{+0.4}_{-0.5}$	$0.039^{+0.002}_{-0.001}$	$27.2^{+1.6}_{-2.0}$	$0.015^{+0.001}_{-0.001}$
DES J0420-4037	$0.839^{+0.001}_{-0.001}$	$2.02^{+0.03}_{-0.03}$	$0.78^{+0.01}_{-0.01}$	$61.6^{+0.4}_{-0.5}$	$0.038^{+0.001}_{-0.001}$	$88.1^{+1.7}_{-1.7}$	$0.015^{+0.001}_{-0.001}$
DES J0530-3730	$0.557^{+0.010}_{-0.008}$	$2.07^{+0.03}_{-0.03}$	$0.68^{+0.11}_{-0.11}$	$73.0^{+6.7}_{-20.0}$	$0.107^{+0.039}_{-0.044}$	$76.2^{+5.7}_{-23.7}$	$0.001^{+0.002}_{-0.001}$
PS J0630-1201	$1.574^{+0.004}_{-0.010}$	$2.11^{+0.02}_{-0.02}$	$0.56^{+0.01}_{-0.01}$	$-77.3^{+1.0}_{-1.1}$	$0.209^{+0.002}_{-0.002}$	$85.1^{+0.7}_{-0.7}$	$0.129^{+0.002}_{-0.002}$
J0659+1629	$2.124^{+0.016}_{-0.017}$	$1.89^{+0.03}_{-0.03}$	$0.85^{+0.01}_{-0.01}$	$-59.7^{+1.7}_{-1.9}$	$0.069^{+0.005}_{-0.005}$	$25.8^{+1.0}_{-1.0}$	$0.010^{+0.001}_{-0.001}$
J0818-2613	$2.896^{+0.001}_{-0.001}$	$2.07^{+0.01}_{-0.01}$	$0.60^{+0.01}_{-0.01}$	$76.0^{+0.6}_{-1.1}$	$0.317^{+0.003}_{-0.002}$	$59.7^{+0.1}_{-0.1}$	$0.000^{+0.001}_{-0.000}$
W2M J1042+1641	$0.892^{+0.001}_{-0.001}$	$2.17^{+0.02}_{-0.03}$	$0.68^{+0.01}_{-0.01}$	$65.8^{+0.6}_{-0.7}$	$0.055^{+0.003}_{-0.003}$	$85.9^{+1.7}_{-1.7}$	$0.023^{+0.002}_{-0.002}$
J1131-4419	$0.876^{+0.001}_{-0.001}$	$2.02^{+0.02}_{-0.02}$	$0.58^{+0.01}_{-0.01}$	$81.4^{+0.2}_{-0.2}$	$0.057^{+0.004}_{-0.003}$	$74.0^{+0.7}_{-0.8}$	$0.052^{+0.003}_{-0.003}$
2M1134-2103	$1.264^{+0.003}_{-0.004}$	$2.15^{+0.02}_{-0.02}$	$0.66^{+0.02}_{-0.01}$	$-55.6^{+0.7}_{-0.8}$	$0.338^{+0.008}_{-0.007}$	$45.5^{+0.1}_{-0.1}$	$0.444^{+0.015}_{-0.013}$
SDSS J1251+2935	$0.841^{+0.001}_{-0.001}$	$2.09^{+0.01}_{-0.01}$	$0.81^{+0.01}_{-0.01}$	$63.0^{+0.5}_{-0.5}$	$0.090^{+0.002}_{-0.002}$	$-11.5^{+0.3}_{-0.4}$	$0.077^{+0.001}_{-0.001}$
2M1310-1714	$1.465^{+0.002}_{-0.002}$	$2.01^{+0.01}_{-0.01}$	$0.65^{+0.01}_{-0.01}$	$-72.5^{+0.4}_{-0.1}$	$0.024^{+0.001}_{-0.001}$	$80.5^{+1.6}_{-0.6}$	$0.983^{+0.040}_{-0.027}$
SDSS J1330+1810	$0.996^{+0.007}_{-0.007}$	$2.06^{+0.03}_{-0.03}$	$0.37^{+0.02}_{-0.02}$	$65.7^{+0.2}_{-0.2}$	$0.124^{+0.007}_{-0.006}$	$78.2^{+1.1}_{-1.1}$	$0.184^{+0.022}_{-0.021}$
SDSS J1433+6007	$1.581^{+0.002}_{-0.003}$	$1.92^{+0.03}_{-0.03}$	$0.96^{+0.01}_{-0.01}$	$-28.1^{+4.5}_{-2.6}$	$0.127^{+0.004}_{-0.004}$	$-82.4^{+0.4}_{-0.4}$	$0.002^{+0.002}_{-0.001}$
J1537-3010	$1.408^{+0.001}_{-0.001}$	$2.02^{+0.02}_{-0.02}$	$0.85^{+0.01}_{-0.01}$	$55.3^{+0.2}_{-0.3}$	$0.124^{+0.003}_{-0.004}$	$-28.3^{+0.1}_{-0.1}$	$0.167^{+0.005}_{-0.005}$
PS J1606-2333	$0.700^{+0.003}_{-0.003}$	$1.93^{+0.01}_{-0.01}$	$0.54^{+0.01}_{-0.01}$	$-76.6^{+0.2}_{-0.3}$	$0.088^{+0.005}_{-0.004}$	$39.1^{+1.3}_{-1.1}$	$0.197^{+0.007}_{-0.007}$
J1721+8842	$1.947^{+0.001}_{-0.001}$	$1.97^{+0.01}_{-0.01}$	$0.80^{+0.01}_{-0.01}$	$19.7^{+0.2}_{-0.1}$	$0.075^{+0.001}_{-0.001}$	$-78.8^{+0.1}_{-0.1}$	$0.199^{+0.002}_{-0.002}$
J1817+2729	$0.893^{+0.001}_{-0.001}$	$2.03^{+0.02}_{-0.02}$	$0.84^{+0.01}_{-0.01}$	$14.5^{+1.8}_{-0.9}$	$0.044^{+0.001}_{-0.001}$	$-12.0^{+1.3}_{-1.1}$	$0.008^{+0.001}_{-0.001}$
DES J2038-4008	$1.376^{+0.001}_{-0.001}$	$2.33^{+0.01}_{-0.01}$	$0.64^{+0.01}_{-0.01}$	$52.3^{+0.1}_{-0.1}$	$0.086^{+0.002}_{-0.002}$	$-32.5^{+0.2}_{-0.1}$	$0.297^{+0.005}_{-0.005}$
WG2100-4452	$1.322^{+0.003}_{-0.002}$	$2.19^{+0.03}_{-0.04}$	$0.51^{+0.01}_{-0.01}$	$87.2^{+0.1}_{-0.1}$	$0.012^{+0.003}_{-0.002}$	$30.6^{+25.6}_{-10.5}$	$0.071^{+0.003}_{-0.004}$
J2145+6345	$1.013^{+0.004}_{-0.003}$	$2.03^{+0.03}_{-0.03}$	$0.71^{+0.04}_{-0.03}$	$-64.3^{+1.0}_{-1.3}$	$0.104^{+0.010}_{-0.011}$	$36.8^{+0.6}_{-0.6}$	$0.173^{+0.014}_{-0.014}$
J2205-3727	$0.772^{+0.001}_{-0.001}$	$2.04^{+0.02}_{-0.02}$	$0.66^{+0.01}_{-0.01}$	$-82.9^{+0.5}_{-0.4}$	$0.017^{+0.005}_{-0.005}$	$-5.1^{+4.2}_{-5.7}$	$0.064^{+0.004}_{-0.004}$
ATLAS J2344-3056	$0.501^{+0.001}_{-0.001}$	$2.02^{+0.02}_{-0.03}$	$0.74^{+0.01}_{-0.01}$	$-24.4^{+0.3}_{-0.4}$	$0.028^{+0.003}_{-0.003}$	$89.2^{+2.7}_{-2.2}$	$0.017^{+0.001}_{-0.001}$

Table 2.2: Model parameters for lens light distributions, which are median values. The associated uncertainties are statistical in nature and were computed using 84th and 16th percentiles.

Name of Lens System	$n_{\rm Sérsic}$	$\theta_{\rm e}$ (arcsec)	$q_{\rm L}$	$\phi_{\rm L}$ (N of E) (degree)	$I_{\rm e}$ (F814W) (mag/arcsec^2)	$I_{\rm e}$ (F475X) (mag/arcsec^2)	$I_{\rm e}$ (F160W) (mag/arcsec^2)
J0029-3814	$5.99^{+0.01}_{-0.02}$	$1.07^{+0.04}_{-0.04}$	$0.59^{+0.01}_{-0.01}$	$51.4^{+0.4}_{-0.4}$	$24.08^{+0.05}_{-0.05}$	$26.75^{+0.07}_{-0.07}$	$22.75^{+0.05}_{-0.05}$
PS J0030-1525	$2.32^{+0.02}_{-0.02}$	$0.71^{+0.01}_{-0.01}$	$0.38^{+0.01}_{-0.01}$	$12.3^{+0.2}_{-0.2}$	$20.28^{+0.01}_{-0.01}$	$22.62^{+0.01}_{-0.01}$	$19.16^{+0.01}_{-0.01}$
DES J0053-2012	$5.98^{+0.02}_{-0.03}$	$0.66^{+0.01}_{-0.01}$	$0.76^{+0.01}_{-0.01}$	$-88.7^{+0.6}_{-0.5}$	$22.48^{+0.03}_{-0.03}$	$25.41^{+0.03}_{-0.04}$	$20.86^{+0.03}_{-0.04}$
PS J0147+4630	4.0	$1.57^{+0.01}_{-0.01}$	$0.90^{+0.01}_{-0.01}$	$34.9^{+1.2}_{-1.2}$	$21.36^{+0.01}_{-0.01}$	$23.58^{+0.02}_{-0.02}$	$19.89^{+0.01}_{-0.01}$
	1.0	$0.82^{+0.00}_{-0.00}$	$0.78^{+0.00}_{-0.01}$	$10.3^{+1.3}_{-1.1}$	–	–	–
WG0214-2105	$6.00^{+0.01}_{-0.01}$	$1.86^{+0.02}_{-0.02}$	$0.86^{+0.01}_{-0.01}$	$26.6^{+1.1}_{-1.1}$	$23.10^{+0.01}_{-0.01}$	–	$21.96^{+0.01}_{-0.01}$
SDSS J0248+1913 †	$2.94^{+0.21}_{-0.17}$	$0.27^{+0.01}_{-0.01}$	$0.44^{+0.01}_{-0.01}$	$79.7^{+0.6}_{-0.7}$	$21.38^{+0.08}_{-0.07}$	$25.40^{+0.10}_{-0.08}$	$19.87^{+0.08}_{-0.07}$
WISE J0259-1635	4.0	$0.26^{+0.03}_{-0.02}$	$0.27^{+0.01}_{-0.01}$	$73.5^{+0.8}_{-1.0}$	$21.73^{+0.14}_{-0.14}$	$24.95^{+0.13}_{-0.13}$	$20.36^{+0.16}_{-0.18}$
	1.0	$1.07^{+0.01}_{-0.01}$	$0.98^{+0.01}_{-0.01}$	$-63.6^{+18.2}_{-14.0}$	–	–	$20.79^{+0.03}_{-0.03}$
J0343-2828	4.0	$0.34^{+0.01}_{-0.01}$	$0.60^{+0.01}_{-0.01}$	$-39.7^{+0.3}_{-0.4}$	$19.90^{+0.02}_{-0.02}$	$22.10^{+0.02}_{-0.02}$	$19.06^{+0.02}_{-0.02}$
	1.0	$5.00^{+0.00}_{-0.01}$	$0.37^{+0.00}_{-0.00}$	$-41.6^{+0.3}_{-0.3}$	$24.92^{+0.01}_{-0.01}$	$26.60^{+0.01}_{-0.01}$	$23.61^{+0.01}_{-0.01}$
DES J0405-3308	$5.94^{+0.04}_{-0.08}$	$1.11^{+0.03}_{-0.03}$	$0.74^{+0.01}_{-0.01}$	$56.4^{+1.4}_{-1.5}$	$23.24^{+0.05}_{-0.05}$	$25.93^{+0.05}_{-0.05}$	$21.52^{+0.04}_{-0.05}$
DES J0420-4037	4.0	$0.46^{+0.01}_{-0.01}$	$0.73^{+0.01}_{-0.01}$	$61.0^{+0.5}_{-0.5}$	$19.75^{+0.01}_{-0.01}$	$21.97^{+0.01}_{-0.01}$	$18.12^{+0.05}_{-0.05}$
	1.0	$0.23^{+0.00}_{-0.00}$	$0.84^{+0.01}_{-0.01}$	$61.9^{+1.5}_{-1.6}$	$21.70^{+0.20}_{-0.16}$	$22.36^{+0.06}_{-0.07}$	–
DES J0530-3730	$5.53^{+0.34}_{-0.72}$	$0.11^{+0.02}_{-0.01}$	$0.52^{+0.15}_{-0.16}$	$60.1^{+16.5}_{-19.1}$	$20.98^{+0.29}_{-0.20}$	–	–
PS J0630-1201	4.0	$0.36^{+0.01}_{-0.01}$	$0.58^{+0.01}_{-0.01}$	$-56.0^{+0.5}_{-0.4}$	$21.42^{+0.05}_{-0.04}$	$23.68^{+0.05}_{-0.03}$	$19.61^{+0.06}_{-0.03}$
	1.0	$0.10^{+0.00}_{-0.00}$	$0.27^{+0.01}_{-0.00}$	$61.1^{+0.5}_{-0.9}$	–	–	–
J0659+1629	$5.75^{+0.05}_{-0.05}$	$1.48^{+0.03}_{-0.03}$	$0.95^{+0.01}_{-0.01}$	$-72.2^{+1.6}_{-1.6}$	$22.04^{+0.03}_{-0.03}$	$25.29^{+0.03}_{-0.03}$	$20.58^{+0.03}_{-0.03}$
J0818-2613	4.0	$2.43^{+0.01}_{-0.03}$	$0.70^{+0.01}_{-0.01}$	$49.2^{+0.4}_{-0.6}$	$22.57^{+0.01}_{-0.02}$	$25.34^{+0.01}_{-0.01}$	$20.83^{+0.01}_{-0.02}$
	1.0	$0.98^{+0.01}_{-0.01}$	$0.67^{+0.01}_{-0.01}$	$49.9^{+0.6}_{-0.5}$	–	–	–
W2M J1042+1641	$5.61^{+0.15}_{-0.15}$	$2.22^{+0.10}_{-0.10}$	$0.75^{+0.01}_{-0.01}$	$67.6^{+0.9}_{-0.8}$	$24.29^{+0.08}_{-0.08}$	$27.51^{+0.08}_{-0.08}$	$22.31^{+0.08}_{-0.08}$
J1131-4419	4.0	$0.29^{+0.01}_{-0.01}$	$0.61^{+0.01}_{-0.01}$	$83.4^{+0.7}_{-0.7}$	$19.17^{+0.03}_{-0.04}$	$21.65^{+0.03}_{-0.04}$	$18.31^{+0.03}_{-0.03}$
	1.0	$0.96^{+0.03}_{-0.03}$	$0.36^{+0.01}_{-0.01}$	$49.4^{+0.4}_{-0.5}$	$24.40^{+0.21}_{-0.20}$	–	$21.36^{+0.07}_{-0.08}$
2M1134-2103	$6.00^{+0.01}_{-0.01}$	$1.13^{+0.02}_{-0.04}$	$0.74^{+0.01}_{-0.01}$	$-58.1^{+0.9}_{-0.8}$	$22.23^{+0.03}_{-0.06}$	$24.88^{+0.03}_{-0.04}$	$20.94^{+0.03}_{-0.04}$
SDSS J1251+2935 †	4.0	$1.18^{+0.02}_{-0.02}$	$0.68^{+0.01}_{-0.01}$	$63.0^{+0.6}_{-0.6}$	$21.06^{+0.04}_{-0.03}$	$23.04^{+0.05}_{-0.05}$	$20.51^{+0.05}_{-0.06}$
	1.0	$0.83^{+0.01}_{-0.01}$	$0.66^{+0.01}_{-0.01}$	$55.4^{+1.2}_{-1.2}$	$21.31^{+0.06}_{-0.05}$	$22.70^{+0.05}_{-0.06}$	$19.66^{+0.04}_{-0.04}$
2M1310-1714	4.0	$0.84^{+0.01}_{-0.01}$	$0.63^{+0.01}_{-0.01}$	$-87.6^{+0.1}_{-0.1}$	$19.87^{+0.01}_{-0.01}$	$21.91^{+0.01}_{-0.01}$	$18.80^{+0.01}_{-0.01}$
	1.0	$5.00^{+0.00}_{-0.00}$	$0.63^{+0.00}_{-0.00}$	$-59.7^{+0.3}_{-0.3}$	$23.51^{+0.01}_{-0.01}$	$25.08^{+0.01}_{-0.01}$	$22.73^{+0.01}_{-0.01}$
SDSS J1330+1810	4.0	$1.47^{+0.02}_{-0.02}$	$0.36^{+0.01}_{-0.01}$	$65.4^{+0.1}_{-0.1}$	$21.39^{+0.02}_{-0.02}$	$23.39^{+0.03}_{-0.03}$	$20.53^{+0.03}_{-0.03}$
	1.0	$0.30^{+0.00}_{-0.00}$	$0.21^{+0.00}_{-0.00}$	$64.7^{+0.2}_{-0.2}$	$20.21^{+0.02}_{-0.02}$	$21.91^{+0.03}_{-0.03}$	$19.15^{+0.04}_{-0.04}$
SDSS J1433+6007	4.0	$0.58^{+0.01}_{-0.01}$	$0.59^{+0.01}_{-0.01}$	$-10.0^{+0.2}_{-0.2}$	$20.39^{+0.01}_{-0.01}$	$22.70^{+0.01}_{-0.01}$	$19.25^{+0.01}_{-0.01}$
	1.0	$3.63^{+0.05}_{-0.04}$	$0.51^{+0.01}_{-0.01}$	$-2.2^{+0.3}_{-0.3}$	$24.25^{+0.03}_{-0.02}$	$25.68^{+0.02}_{-0.02}$	$23.42^{+0.03}_{-0.03}$
J1537-3010 †	$7.16^{+0.08}_{-0.08}$	$2.55^{+0.05}_{-0.05}$	$0.76^{+0.01}_{-0.01}$	$57.5^{+0.3}_{-0.3}$	$23.22^{+0.04}_{-0.03}$	$25.91^{+0.04}_{-0.03}$	$21.90^{+0.04}_{-0.03}$
PS J1606-2333	$5.97^{+0.02}_{-0.04}$	$1.48^{+0.08}_{-0.08}$	$0.58^{+0.01}_{-0.01}$	$-73.1^{+0.9}_{-1.0}$	$23.69^{+0.07}_{-0.07}$	$26.98^{+0.07}_{-0.07}$	$22.04^{+0.07}_{-0.07}$
J1721+8842	$4.02^{+0.01}_{-0.01}$	$5.00^{+0.01}_{-0.01}$	$0.86^{+0.01}_{-0.01}$	$3.6^{+0.2}_{-0.2}$	$22.05^{+0.01}_{-0.01}$	$23.89^{+0.01}_{-0.01}$	$20.88^{+0.01}_{-0.01}$
J1817+2729	4.0	$2.00^{+0.05}_{-0.04}$	$0.27^{+0.01}_{-0.01}$	$30.2^{+0.1}_{-0.1}$	$22.57^{+0.02}_{-0.02}$	$25.06^{+0.02}_{-0.02}$	$21.48^{+0.03}_{-0.02}$
	1.0	$1.19^{+0.02}_{-0.03}$	$0.25^{+0.01}_{-0.01}$	$17.8^{+0.3}_{-0.3}$	–	–	–
DES J2038-4008	4.0	$2.85^{+0.01}_{-0.01}$	$0.63^{+0.01}_{-0.01}$	$53.0^{+0.1}_{-0.1}$	$21.24^{+0.01}_{-0.01}$	$23.05^{+0.01}_{-0.01}$	$20.16^{+0.01}_{-0.01}$
	1.0	$3.17^{+0.05}_{-0.04}$	$0.63^{+0.01}_{-0.01}$	$-26.2^{+0.4}_{-0.5}$	$22.90^{+0.04}_{-0.04}$	$24.26^{+0.04}_{-0.03}$	$22.14^{+0.05}_{-0.04}$
WG2100-4452	4.0	$0.96^{+0.01}_{-0.01}$	$0.61^{+0.01}_{-0.01}$	$86.0^{+0.1}_{-0.1}$	$20.05^{+0.01}_{-0.01}$	$21.78^{+0.01}_{-0.01}$	$18.95^{+0.01}_{-0.01}$
	1.0	$2.96^{+0.06}_{-0.05}$	$0.82^{+0.01}_{-0.01}$	$-30.2^{+1.3}_{-1.3}$	$22.70^{+0.04}_{-0.03}$	$24.01^{+0.04}_{-0.03}$	$22.14^{+0.05}_{-0.05}$
J2145+6345	$5.90^{+0.08}_{-0.15}$	$1.00^{+0.09}_{-0.09}$	$0.72^{+0.02}_{-0.02}$	$-54.8^{+2.1}_{-2.6}$	$22.71^{+0.13}_{-0.15}$	$25.15^{+0.12}_{-0.14}$	$21.00^{+0.12}_{-0.14}$
J2205-3727 †	$6.60^{+0.16}_{-0.13}$	$0.78^{+0.03}_{-0.03}$	$0.74^{+0.01}_{-0.01}$	$-76.7^{+0.6}_{-0.6}$	$21.78^{+0.07}_{-0.06}$	$24.58^{+0.07}_{-0.06}$	$20.84^{+0.07}_{-0.07}$
ATLAS J2344-3056 †	$3.60^{+0.21}_{-0.19}$	$1.45^{+0.10}_{-0.09}$	$0.84^{+0.01}_{-0.01}$	$-22.9^{+0.8}_{-1.0}$	$23.48^{+0.13}_{-0.12}$	–	$21.38^{+0.13}_{-0.12}$

†Lenses model reconstructed by pipeline before restricting Sérsic index of main deflector's light profile to 6.0.

Table 2.3: Astrometric positions of the main deflector's light profile centroid and lensed QSO images. The total uncertainty on relative astrometry is dominated by systematic errors associated with the reconstruction of the PSF on sub-pixel scale. We estimate it to be 6 mas by comparison with *Gaia* (§ 2.4.2.1). Formal random uncertainties are negligible in comparison and therefore not listed.

Name of	Location		Main Deflector		Image A		Image B		Image C		Image D	
Lens System	RA (degree)	DEC (degree)	ΔRA (arcsec)	ΔDEC (arcsec)	ΔRA (arcsec)	ΔDEC (arcsec)	ΔRA (arcsec)	ΔDEC (arcsec)	ΔRA (arcsec)	ΔDEC (arcsec)	ΔRA (arcsec)	ΔDEC (arcsec)
J0029-3814	7.419298	−38.240600	−0.134	−0.155	1.156	−0.513	−0.592	−0.490	−0.975	0.071	−0.321	0.384
PS J0030-1525	7.563492	−15.417800	−0.098	0.020	0.746	−0.908	−0.868	0.002	0.778	0.887	1.005	0.608
DES J0053-2012	13.435033	−20.209147	−0.422	0.429	−0.529	1.036	1.414	0.012	0.691	−0.731	−1.424	−1.111
PS J0147+4630	26.792372	46.511872	−0.145	−1.137	−0.317	−2.296	−1.218	0.836	0.029	0.936	1.191	0.526
WG0214-2105	33.568175	−21.093137	0.071	−0.015	0.556	−0.868	−0.706	−0.136	−0.260	0.790	0.633	0.517
SDSS J0248+1913	42.203067	19.225228	0.105	0.071	0.451	−0.748	−0.549	−0.135	−0.404	0.699	0.503	0.661
WISE J0259-1635	44.928533	−16.595370	0.058	−0.039	0.035	−0.730	−0.727	0.216	0.434	0.537	0.752	−0.342
J0343-2828 †	55.797650	−28.477948	−0.869	0.894	−1.251	1.352	1.959	1.349	1.364	−0.746	−1.329	−1.952
DES J0405-3308	61.498960	−33.147410	−0.014	−0.045	0.691	−0.279	−0.374	−0.605	−0.529	0.416	0.349	0.556
DES J0420-4037	65.194823	−40.624087	0.113	−0.001	0.821	−0.579	−0.586	−0.349	−0.339	0.675	0.287	0.796
DES J0530-3730	82.654075	−37.503113	0.325	−0.325	0.597	−0.517	−0.384	−0.237	−0.143	0.243	−0.018	0.311
PS J0630-1201	97.537708	−12.022081	−0.502	0.275	−1.370	1.157	1.151	0.416	0.822	−0.704	0.302	−1.268
J0659+1629	104.766545	16.485908	0.390	−0.066	2.192	−0.928	−2.481	−1.265	1.205	1.953	2.274	0.974
J0818-2613	124.617817	−26.223740	−0.882	1.184	−2.488	−2.982	−2.042	2.603	2.010	1.366	1.854	0.695
W2M J1042+1641	160.592005	16.687614	−0.052	0.034	−0.858	0.687	0.694	0.111	0.526	−0.468	−0.087	−0.803

†Astrometric position of 5th image for J0343-282: ΔRA = −0″.273, ΔDEC = 0″.473.

Table 2.4: Astrometric positions of the main deflector's light profile centroid and lensed QSO images. The total uncertainty on relative astrometry is dominated by systematic errors associated with the reconstruction of the PSF on sub-pixel scale. We estimate it to be 6 mas by comparison with *Gaia* (§ 2.4.2.1). Formal random uncertainties are negligible in comparison and therefore not listed.

Name of	Location		Main Deflector		Image A		Image B		Image C		Image D	
Lens System	RA (degree)	DEC (degree)	ΔRA (arcsec)	ΔDEC (arcsec)	ΔRA (arcsec)	ΔDEC (arcsec)	ΔRA (arcsec)	ΔDEC (arcsec)	ΔRA (arcsec)	ΔDEC (arcsec)	ΔRA (arcsec)	ΔDEC (arcsec)
J1131-4419	172.750079	−44.333469	−0.012	0.050	0.072	−0.742	−0.881	0.349	0.411	0.793	0.754	0.446
2M1134-2103	173.668952	−21.056299	−0.154	0.174	1.326	1.150	0.593	−0.609	−1.356	−1.384	−0.660	0.765
SDSS J1251+2935	192.781367	29.594673	0.185	−0.050	−0.885	0.278	0.829	0.286	0.895	−0.304	0.533	−0.678
2M1310-1714 †	197.583583	−17.249381	−0.191	0.522	−1.093	2.656	2.790	0.165	1.508	−2.447	−2.295	−2.222
SDSS J1330+1810	202.577718	18.175763	0.170	0.068	0.629	0.700	0.384	−0.902	−0.023	−0.910	−0.860	0.256
SDSS J1433+6007	218.345150	60.120839	0.451	−0.218	1.558	−0.338	−0.486	−1.913	−1.243	−0.288	−0.480	1.842
J1537-3010	234.355668	−30.171336	0.095	−0.030	1.491	−0.815	−0.471	−1.126	−1.352	0.822	0.772	0.970
PS J1606-2333	241.500980	−23.556122	0.035	0.025	0.852	0.414	0.065	−0.490	−0.765	−0.173	−0.272	0.567
J1721+8842	260.432958	88.705847	−0.287	0.261	−1.694	−0.094	0.312	2.378	1.589	0.965	1.242	−1.361
J1817+2729	274.378603	27.494383	0.096	0.105	0.655	−0.732	−0.692	−0.256	−0.607	0.553	0.671	0.709
DES J2038-4008	309.511333	−40.137050	0.117	0.074	0.819	0.938	0.945	−1.141	−0.572	−1.112	−1.367	0.569
WG2100-4452	315.062075	−44.868438	−0.078	0.072	−0.286	1.128	1.318	−0.401	−0.703	−1.083	−1.125	−0.749
J2145+6345	326.271094	63.761447	−0.174	0.394	−0.955	−0.650	−0.487	1.020	0.890	0.280	0.571	−0.298
J2205-3727	331.434422	−37.450361	−0.046	0.088	0.859	0.189	−0.342	−0.536	−0.780	0.066	−0.491	0.624
ATLAS J2344-3056	356.070733	−30.940611	0.055	−0.115	−0.431	0.073	0.150	0.425	0.442	−0.245	−0.191	−0.583

†Astrometric position of 5th image for 2M1310-1714: ΔRA = −0″.181, ΔDEC = 0″.070.

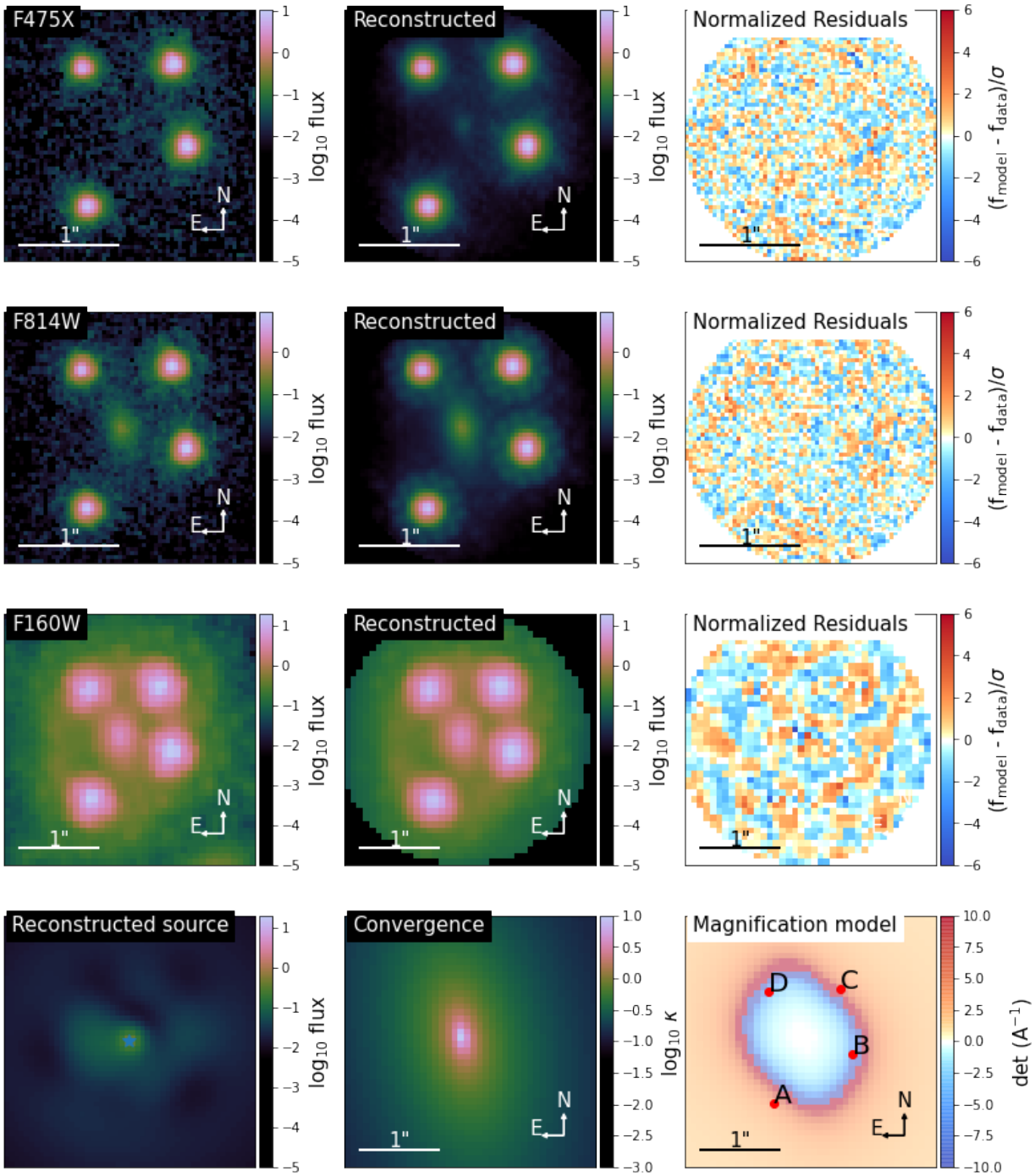

Figure 2.6: Comparison of observations with the reconstructed model for SDSS J0248+1913 in *HST* bands F475X (first row), F814W (second row), and F160W (third row). Also shown are the respective normalized residual for each band, after the subtraction of the data from the model. The last row shows the reconstructed source using information from the F160W band (column 1), a plot of the unitless convergence, $\kappa(\theta)$ (column 2), and a model plotting the magnification as well as the position of the lensed quasar images (column 3).

1) and the convergence, $\kappa(\theta)$, for the respective lens configuration (column 2). Lastly, the figures include a magnification model (column 3 in 4th row), indicating the position of the lensed quasar images. The corresponding convergence and external shear strength at the image positions can be found in Table 2.8, Table 2.9, and Table 2.10, along with the magnification for each QSO image. For our estimates of the stellar convergences, $\kappa_\star$, at the image positions we use the lens light flux in the F160W band and assume a constant mass-to-light ratio. The normalization factor has been chosen such that within an area of 1/2 of the effective radius, the integrated stellar convergence is 2/3, or less, of the integrated convergence (see Auger et al., 2010a).

2.4.2 Lens model parameters

The mean and associated uncertainties of the free model parameters for each lens are obtained from the MCMC chain. Therefore, the uncertainties listed do not account for systematic sources of error. In future analyses of this sample systematic errors will need to be estimated for each specific application. In some cases they can be dominant. We discuss some examples of systematic errors in the remainder of this paper and refer to the literature for additional examples.

A breakdown of the mass model components by attribute can be found in Table 2.1. These include the lens mass parameters of the main deflector, the attributes of the external shear profile associated with the combined impact of additional perturber along the line of sight, as well as the area enclosed by the inner caustics of the critical curve.

Table 2.2 details the lens light profile parameterization for each lensed system that is successfully processed by the pipeline. For lenses where the light profile of the main deflector is modeled by a double Sérsic, we first list the parameters of profile with the Sérsic index fixed at 4.0, the de Vaucouleurs profile (de Vaucouleurs, 1948), and immediately below show the parameters of the light profile with the Sérsic index fixed at 1.0, the exponential profile.

Tables 2.3 and 2.4 list the astrometry of the point sources and galaxy centroid as inferred

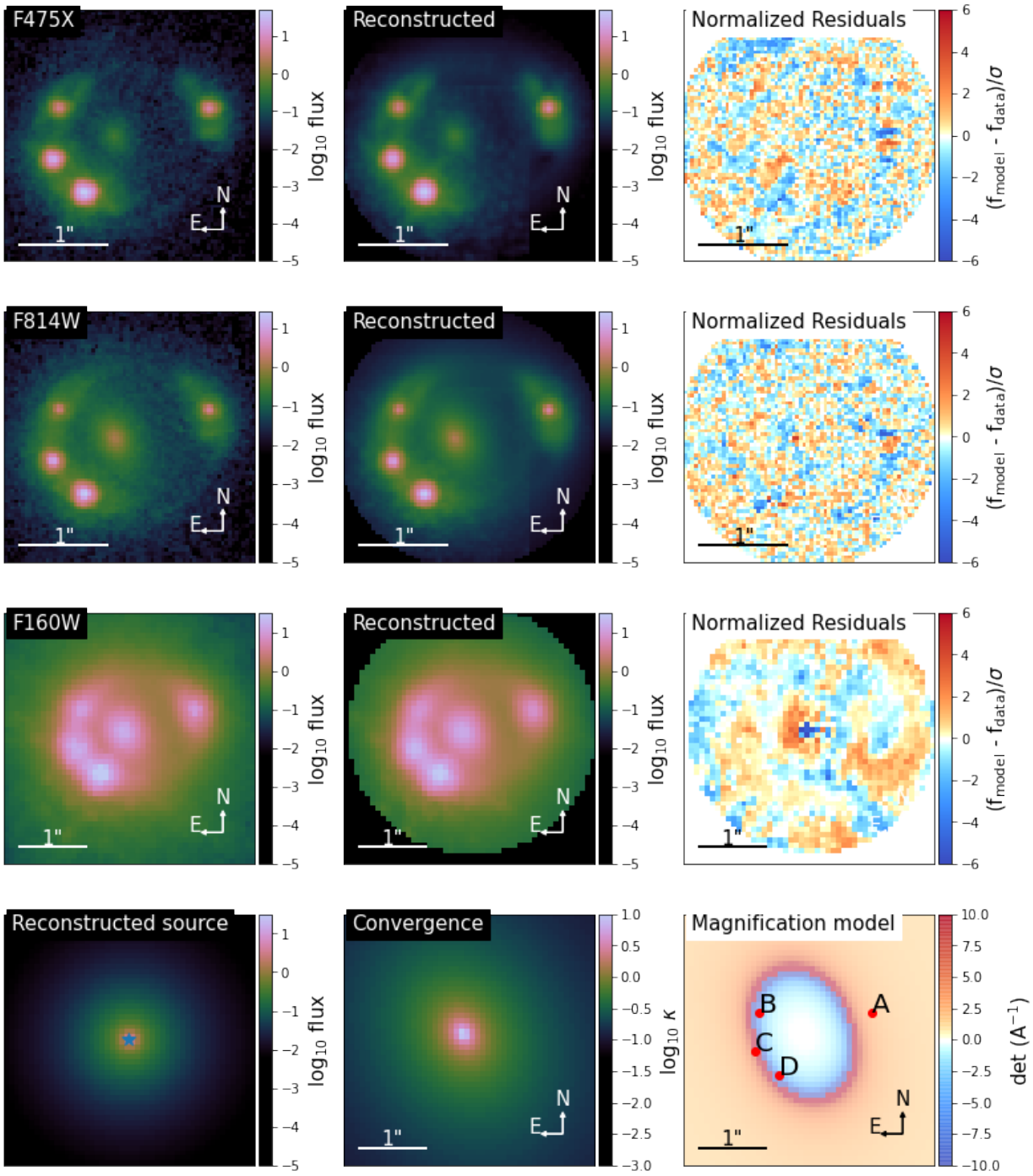

Figure 2.7: Comparison of observations with the reconstructed model for SDSSJ 1251+2935 in *HST* bands F475X (first row), F814W (second row), and F160W (third row). Also shown are the respective normalized residual for each band, after the subtraction of the data from the model. The last row shows the reconstructed source using information from the F160W band (column 1), a plot of the unitless convergence, $\kappa(\theta)$ (column 2), and a model plotting the magnification as well as the position of the lensed quasar images (column 3).

Table 2.5: Model parameters for source light distributions, which are median values. The associated uncertainties are statistical in nature and were computed using 84th and 16th percentiles.

Name of Lens System	$n_{\rm Sérsic}$	$\theta_{\rm e}$ (arcsec)	Centroid ΔRA (arcsec)	Centroid ΔDEC (arcsec)	F814W $n_{\rm max}$	F814W β (arcsec)	F475X $n_{\rm max}$	F475X β (arcsec)	F160W $n_{\rm max}$	F160W β (arcsec)
J0029-3814	$2.82^{+0.23}_{-0.21}$	$1.05^{+0.03}_{-0.06}$	$0.043^{+0.004}_{-0.005}$	$-0.243^{+0.004}_{-0.003}$	–	–	–	–	–	–
PS J0030-1525	$0.53^{+0.02}_{-0.01}$	$0.44^{+0.01}_{-0.01}$	$0.327^{+0.010}_{-0.012}$	$0.045^{+0.003}_{-0.003}$	–	–	–	–	–	–
DES J0053-2012	$0.50^{+0.01}_{-0.01}$	$0.77^{+0.03}_{-0.03}$	$-0.151^{+0.004}_{-0.005}$	$0.022^{+0.015}_{-0.013}$	–	–	–	–	–	–
PS J0147+4630	$1.30^{+0.23}_{-0.19}$	$0.01^{+0.01}_{-0.01}$	$-0.157^{+0.002}_{-0.002}$	$-0.720^{+0.014}_{-0.015}$	–	–	–	–	–	–
WG0214-2105	$0.92^{+0.26}_{-0.21}$	$0.06^{+0.01}_{-0.01}$	$0.096^{+0.001}_{-0.001}$	$-0.052^{+0.001}_{-0.001}$	–	–	–	–	–	–
SDSS J0248+1913	$3.62^{+0.12}_{-0.13}$	$1.91^{+0.06}_{-0.12}$	$0.112^{+0.001}_{-0.001}$	$0.031^{+0.002}_{-0.002}$	–	–	0	$0.100^{+0.015}_{-0.018}$	5	$0.187^{+0.010}_{-0.010}$
WISE J0259-1635	$3.96^{+0.03}_{-0.06}$	$1.09^{+0.01}_{-0.01}$	$0.016^{+0.001}_{-0.001}$	$-0.024^{+0.001}_{-0.001}$	3	$0.075^{+0.002}_{-0.002}$	4	$0.063^{+0.002}_{-0.001}$	1	$0.145^{+0.004}_{-0.004}$
J0343-2828	$3.99^{+0.01}_{-0.01}$	$0.06^{+0.01}_{-0.01}$	$-0.122^{+0.003}_{-0.003}$	$0.149^{+0.003}_{-0.003}$	8	$0.161^{+0.009}_{-0.007}$	3	$0.031^{+0.003}_{-0.005}$	–	–
DES J0405-3308	$3.96^{+0.03}_{-0.06}$	$0.17^{+0.01}_{-0.01}$	$0.017^{+0.001}_{-0.001}$	$-0.039^{+0.001}_{-0.001}$	–	–	–	–	–	–
DES J0420-4037	$0.59^{+0.39}_{-0.07}$	$0.91^{+0.11}_{-0.12}$	$0.166^{+0.001}_{-0.001}$	$-0.033^{+0.001}_{-0.001}$	15	$0.037^{+0.001}_{-0.001}$	15	$0.037^{+0.001}_{-0.001}$	15	$0.141^{+0.005}_{-0.005}$
DES J0530-3730	$1.27^{+1.02}_{-0.51}$	$1.09^{+0.01}_{-0.02}$	$0.172^{+0.019}_{-0.008}$	$-0.215^{+0.006}_{-0.005}$	5	$0.083^{+0.011}_{-0.012}$	5	$0.062^{+0.011}_{-0.016}$	–	–
PS J0630-1201	$1.70^{+0.08}_{-0.07}$	$1.10^{+0.01}_{-0.01}$	$-0.275^{+0.007}_{-0.007}$	$0.217^{+0.005}_{-0.005}$	–	–	–	–	–	–
J0659+1629	$2.18^{+0.14}_{-0.11}$	$1.10^{+0.01}_{-0.01}$	$0.028^{+0.011}_{-0.011}$	$-0.215^{+0.002}_{-0.002}$	–	–	–	–	–	–
J0818-2613	$0.50^{+0.01}_{-0.01}$	$0.01^{+0.01}_{-0.01}$	$-1.064^{+0.002}_{-0.001}$	$0.538^{+0.003}_{-0.002}$	–	–	–	–	6	$0.724^{+0.008}_{-0.001}$
W2M J1042+1641	$3.80^{+0.14}_{-0.30}$	$0.54^{+0.08}_{-0.09}$	$-0.194^{+0.002}_{-0.002}$	$0.105^{+0.002}_{-0.002}$	5	$0.010^{+0.001}_{-0.001}$	5	$0.011^{+0.001}_{-0.001}$	–	–

Table 2.6: Model parameters for source light distributions, which are median values. The associated uncertainties are statistical in nature and were computed using 84th and 16th percentiles.

Name of Lens System	$n_{\rm Sérsic}$	$\theta_{\rm e}$ (arcsec)	Centroid ΔRA (arcsec)	Centroid ΔDEC (arcsec)	F814W $n_{\rm max}$	F814W β (arcsec)	F475X $n_{\rm max}$	F475X β (arcsec)	F160W $n_{\rm max}$	F160W β (arcsec)
J1131-4419	$2.05^{+0.06}_{-0.05}$	$1.09^{+0.01}_{-0.02}$	$-0.052^{+0.002}_{-0.002}$	$0.078^{+0.003}_{-0.002}$	7	$0.075^{+0.002}_{-0.002}$	3	$0.123^{+0.004}_{-0.003}$	5	$0.471^{+0.007}_{-0.008}$
2M1134-2103	$3.99^{+0.01}_{-0.02}$	$1.10^{+0.01}_{-0.01}$	$-0.097^{+0.002}_{-0.002}$	$0.010^{+0.003}_{-0.002}$	–	–	–	–	–	–
SDSS J1251+2935	$3.27^{+0.17}_{-0.14}$	$0.24^{+0.01}_{-0.01}$	$-0.004^{+0.002}_{-0.002}$	$0.007^{+0.001}_{-0.001}$	5	$0.068^{+0.001}_{-0.001}$	5	$0.068^{+0.001}_{-0.001}$	–	–
2M1310-1714	$4.00^{+0.01}_{-0.01}$	$0.01^{+0.01}_{-0.01}$	$-0.153^{+0.001}_{-0.001}$	$-0.092^{+0.001}_{-0.001}$	20	$0.210^{+0.001}_{-0.002}$	8	$0.091^{+0.001}_{-0.001}$	1	$0.171^{+0.001}_{-0.001}$
SDSS J1330+1810	$1.90^{+0.09}_{-0.08}$	$1.10^{+0.01}_{-0.01}$	$0.045^{+0.006}_{-0.006}$	$0.016^{+0.002}_{-0.002}$	2	$0.325^{+0.011}_{-0.011}$	2	$0.311^{+0.015}_{-0.017}$	–	–
SDSS J1433+6007	$3.88^{+0.08}_{-0.15}$	$0.64^{+0.05}_{-0.04}$	$0.013^{+0.010}_{-0.010}$	$-0.078^{+0.003}_{-0.003}$	–	–	–	–	–	–
J1537-3010	$1.45^{+0.07}_{-0.07}$	$0.16^{+0.01}_{-0.01}$	$0.048^{+0.001}_{-0.001}$	$-0.017^{+0.001}_{-0.001}$	5	$0.068^{+0.001}_{-0.001}$	8	$0.056^{+0.001}_{-0.001}$	–	–
PS J1606-2333	$3.96^{+0.03}_{-0.07}$	$0.67^{+0.03}_{-0.03}$	$0.033^{+0.001}_{-0.001}$	$0.025^{+0.005}_{-0.005}$	9	$0.108^{+0.003}_{-0.003}$	9	$0.105^{+0.002}_{-0.002}$	–	–
J1721+8842	$1.73^{+0.22}_{-0.18}$	$1.10^{+0.01}_{-0.01}$	$-0.018^{+0.002}_{-0.002}$	$0.288^{+0.001}_{-0.001}$	6	$1.075^{+0.017}_{-0.030}$	6	$1.061^{+0.027}_{-0.039}$	10	$0.117^{+0.001}_{-0.001}$
J1817+2729	$0.83^{+0.19}_{-0.13}$	$0.46^{+0.06}_{-0.05}$	$0.143^{+0.001}_{-0.001}$	$0.027^{+0.001}_{-0.001}$	3	$0.012^{+0.002}_{-0.001}$	–	–	9	$0.643^{+0.019}_{-0.017}$
DES J2038-4008	$1.06^{+0.11}_{-0.10}$	$0.11^{+0.01}_{-0.01}$	$-0.027^{+0.001}_{-0.001}$	$-0.031^{+0.001}_{-0.001}$	8	$0.144^{+0.002}_{-0.002}$	10	$0.126^{+0.001}_{-0.001}$	3	$0.257^{+0.002}_{-0.002}$
WG2100-4452	$3.96^{+0.03}_{-0.07}$	$0.80^{+0.09}_{-0.08}$	$0.025^{+0.003}_{-0.004}$	$-0.075^{+0.006}_{-0.004}$	–	–	0	$0.179^{+0.009}_{-0.008}$	–	–
J2145+6345	$3.94^{+0.04}_{-0.07}$	$0.64^{+0.10}_{-0.08}$	$-0.197^{+0.001}_{-0.001}$	$0.214^{+0.005}_{-0.005}$	–	–	–	–	–	–
J2205-3727	$1.74^{+0.15}_{-0.12}$	$0.31^{+0.02}_{-0.02}$	$0.046^{+0.003}_{-0.003}$	$0.099^{+0.001}_{-0.001}$	–	–	–	–	–	–
ATLAS J2344-3056	$0.57^{+0.03}_{-0.03}$	$0.47^{+0.01}_{-0.01}$	$0.005^{+0.001}_{-0.001}$	$-0.085^{+0.001}_{-0.001}$	–	–	–	–	–	–

from our lens models.

Details on the reconstructed host galaxy of the lensed QSO can be found in Tables 2.5 and 2.6. We note that many of the free parameters are highly correlated; the pairwise Pearson correlation coefficients are listed in Table 2.7.

As further illustration, we briefly highlight some results for lens SDSS J0248+1913 and lens SDSS J1251+2935, which are shown in Figures 2.6 and 2.7, respectively. Analyzing the position angle (PA) of the lens mass distribution, we find that the convergence aligns well with orientation of the lens light profile for both systems, as can be seen in the corresponding UVIS filter F814W of the respective lens. For SDSS J0248+1913, the mass distribution's PA and the lens light distribution's PA are both 80 degrees North of East, while for SDSS J1251+2935 both PAs are 63 degrees North of East. To perform a similar analysis for all other systems, in Figure 2.9 we plot the difference between the PA of the main deflector's mass and primary lens light profile as a function of the light profile's axis ratio, with a resulting Pearson correlation coefficient of 0.9 as shown in Table 2.7. The shaded area in Figure 2.9 represents the prior on the PA difference as discussed in Section 2.3.3.

Even though our prior constraints allow for the convergence's axis ratio to be below the axis ratio of the light profile, we find that in both systems the lens mass distribution is more spherical compared to the respective lens light. In a similar analysis we plot in Figure 2.8 the axis ratio of the main deflector's mass profile as a function of the light profile's axis ratio for all systems in our sample and find no significant correlation as indicated by the low Pearson coefficient of 0.33, shown in Table 2.7. We also find that due to a nearby galaxy, approximately 90 degrees West of North, SDSS J0248+1913 experiences a stronger than average external shear, as reflected in the inferred value of $\gamma_{\rm ext} = 0.22$. Analogous evaluations can be performed for all remaining systems in our sample, using the results listed in the tables of this section.

Table 2.7: Cross-correlation strength between model parameters in our lens sample, as indicated by the pairwise Pearson correlation coefficient. Coefficients with an absolute value of 0.4 or greater are boldened to increase notability.

Parameter	$\theta_{\rm E}$	γ	$q_{\rm mass}$	$\Phi_{\rm mass}$	$\gamma_{\rm ext}$	$\phi_{\rm ext}$	$n_{\rm Sérsic}$ (lens)	$R_{\rm Sérsic}$ (lens)	$q_{\rm light}$	$\phi_{\rm light}$	$n_{\rm Sérsic}$ (source)	$R_{\rm Sérsic}$ (source)	$n_{\rm max}$ (F814W)	β (F814W)	$n_{\rm max}$ (F475X)	β (F475X)	$n_{\rm max}$ (F160W)	β (F160W)	z (lens)	z (source)	Caustic Area
$\theta_{\rm E}$	**1.0**	-0.09	0.14	-0.17	0.37	-0.02	-0.09	**0.44**	0.36	-0.16	-0.22	-0.17	-0.12	0.19	-0.14	0.21	0.15	0.33	-0.22	0.07	0.16
γ	-0.09	**1.0**	-0.16	0.34	-0.01	0.11	-0.01	0.07	-0.1	0.39	0.05	-0.16	-0.02	-0.14	0.12	-0.09	-0.06	0.08	0.01	-0.25	0.03
$q_{\rm mass}$	0.14	-0.16	**1.0**	-0.16	-0.26	**-0.45**	0.13	0.23	0.33	-0.06	-0.2	-0.25	-0.06	-0.06	-0.0	-0.06	0.12	-0.03	0.18	0.22	-0.17
$\phi_{\rm mass}$	-0.17	0.34	-0.16	**1.0**	-0.05	-0.07	-0.24	0.09	-0.37	**0.9**	-0.03	0.24	0.07	0.11	0.26	0.18	0.34	0.33	-0.05	-0.3	-0.3
$\gamma_{\rm ext}$	0.37	-0.01	-0.26	-0.05	**1.0**	-0.0	0.1	-0.04	0.02	-0.09	-0.02	0.21	-0.37	-0.1	-0.33	-0.15	-0.09	0.11	0.13	0.39	0.19
$\phi_{\rm ext}$	-0.02	0.11	**-0.45**	-0.07	-0.0	**1.0**	0.08	-0.29	0.01	-0.15	0.05	-0.04	0.27	-0.24	0.13	-0.24	-0.09	0.04	0.06	-0.13	0.1
$n_{\rm Sérsic}$ (lens)	-0.09	-0.01	0.13	-0.24	0.1	0.08	**1.0**	0.11	**0.43**	-0.29	0.12	-0.12	-0.13	-0.21	-0.03	-0.19	-0.36	-0.33	0.13	0.09	0.1
$R_{\rm Sérsic}$ (lens)	**0.44**	0.07	0.23	0.09	-0.04	-0.29	0.11	**1.0**	0.36	0.09	-0.26	-0.25	0.05	**0.62**	0.19	**0.65**	0.28	0.2	**-0.42**	-0.13	0.07
$q_{\rm light}$	0.36	-0.1	0.33	-0.37	0.02	0.01	**0.43**	0.36	**1.0**	-0.3	-0.15	-0.29	-0.08	0.05	-0.02	0.07	-0.09	-0.29	-0.17	-0.1	0.1
$\phi_{\rm light}$	-0.16	0.39	-0.06	**0.9**	-0.09	-0.15	-0.29	0.09	-0.3	**1.0**	-0.06	0.11	-0.02	0.02	0.18	0.11	0.29	0.28	0.06	-0.29	-0.3
$n_{\rm Sérsic}$ (source)	-0.22	0.05	-0.2	-0.03	-0.02	0.05	0.12	-0.26	-0.15	-0.06	**1.0**	0.17	0.12	0.0	0.01	-0.02	-0.33	-0.3	0.04	-0.25	0.18
$R_{\rm Sérsic}$ (source)	-0.17	-0.16	-0.25	0.24	0.21	-0.04	-0.12	-0.25	-0.29	0.11	0.17	**1.0**	-0.17	0.22	-0.07	0.26	0.19	-0.08	0.08	0.17	-0.14
$n_{\rm max}$ (F814W)	-0.12	-0.02	-0.06	0.07	-0.37	0.27	-0.13	0.05	-0.08	-0.02	0.12	-0.17	**1.0**	0.31	**0.87**	0.21	**0.42**	0.17	-0.23	-0.29	0.36
β (F814W)	0.19	-0.14	-0.06	0.11	-0.1	-0.24	-0.21	**0.62**	0.05	0.02	0.0	0.22	0.31	**1.0**	0.32	**0.97**	0.4	0.03	**-0.47**	-0.09	0.13
$n_{\rm max}$ (F475X)	-0.14	0.12	-0.0	0.26	-0.33	0.13	-0.03	0.19	-0.02	0.18	0.01	-0.07	**0.87**	0.32	**1.0**	0.28	**0.44**	0.04	-0.19	-0.37	0.14
β (F475X)	0.21	-0.09	-0.06	0.18	-0.15	-0.24	-0.19	**0.65**	0.07	0.11	-0.02	0.26	0.21	**0.97**	0.28	**1.0**	0.39	0.03	**-0.52**	-0.15	0.07
$n_{\rm max}$ (F160W)	0.15	-0.06	0.12	0.34	-0.09	-0.09	-0.36	0.28	-0.09	0.29	-0.33	0.19	**0.42**	0.4	**0.44**	0.39	**1.0**	**0.64**	-0.16	-0.03	-0.14
β (F160W)	0.33	0.08	-0.03	0.33	0.11	0.04	-0.33	0.2	-0.29	0.28	-0.3	-0.08	0.17	0.03	0.04	0.03	**0.64**	**1.0**	-0.01	-0.08	-0.1
z (lens)	-0.22	0.01	0.18	-0.05	0.13	0.06	0.13	**-0.42**	-0.17	0.06	0.04	0.08	-0.23	**-0.47**	-0.19	**-0.52**	-0.16	-0.01	**1.0**	0.29	-0.21
z (source)	0.07	-0.25	0.22	-0.3	0.39	-0.13	0.09	-0.13	-0.1	-0.29	-0.25	0.17	-0.29	-0.09	-0.37	-0.15	-0.03	-0.08	0.29	**1.0**	0.04
Caustic Area	0.16	0.03	-0.17	-0.3	0.19	0.1	0.1	0.07	0.1	-0.3	0.18	-0.14	0.36	0.13	0.14	0.07	-0.14	-0.1	-0.21	0.04	**1.0**

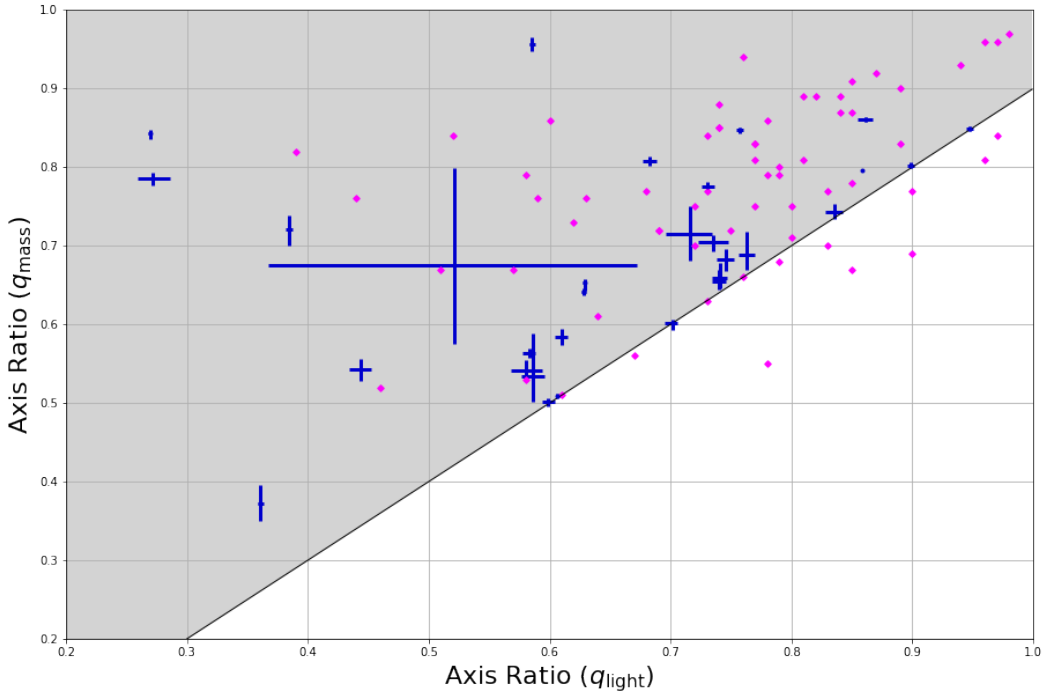

Figure 2.8: Axis ratio of main deflector's mass profile, q_{mass}, as function of the deflector's light profile axis ratio, q_{mass}, (blue markers). The shaded area represents the prior set for the lens masses axis ratio while the magenta diamond markers represent the strong lenses in the SLACS sample.

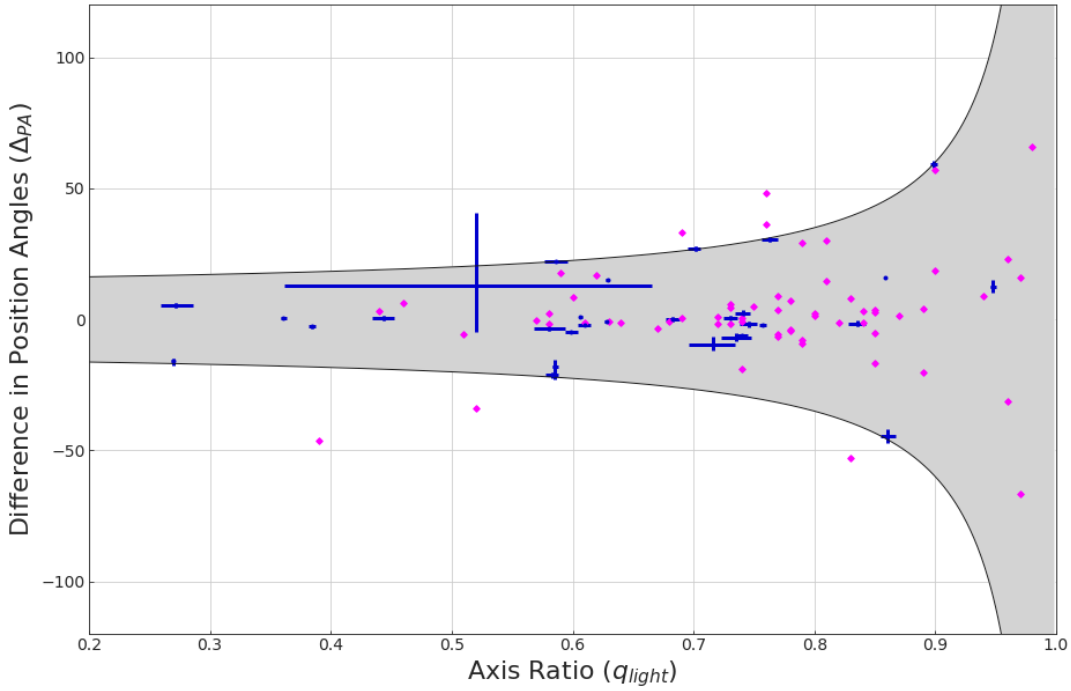

Figure 2.9: Difference in position angle between the main deflector's lens mass and lens light as function of the lens light's axis ratio for our lens sample (blue markers). The shaded area represents the prior set for the lens masses position angle while the magenta diamond markers represent the strong lenses in the SLACS sample.

2.4.2.1 Systematic uncertainties on astrometry

We can estimate the systematic uncertainties on our astrometry by comparing the relative positions of the multiply imaged quasars with independent measurements based on the *Gaia* satellite and with measurement based on the same *HST* images as analyzed in this paper, but with a different methodology (see Luhtaru et al., 2021). We do not expect the measurements to agree perfectly since our positions are inferred from a forward modeling procedure taking into account the surface brightness of the quasar host galaxies and of the perturbers, while the comparison positions are measured in the image plane, without a lens model. However, we expect that this comparison should give us a robust upper limit to the systematic uncertainty on astrometry, which we expect is dominated by the uncertainty on our reconstruction of the PSF at subpixel scales (Chen et al., 2021b).

Figure 2.10 shows the difference of the relative positions of the multiply image quasars measured in this work with respect to those measured from *Gaia* data release 3. Only systems for which *Gaia* measured at least three image positions are used for the comparison. The lens J1721+8842 is a clear outlier in terms of astrometric precision. This is not surprising considering that our pipeline is not intended to deal with the complexity of the system, composed of two sets of multiple images. Excluding J1721+8842, the r.m.s. scatter is 6 mas and 5 mas respectively in RA and DEC. A comparison with the astrometry of Luhtaru et al. (2021) yields very similar results, with r.m.s. scatter of 7 mas in both RA and DEC, excluding J1721+8842. Conservatively, assuming the *Gaia* error to be negligible, we assign a systematic error of 6 mas on our relative astrometry listed in Tables 2.3 and 2.4, with the exception of J1721+8842, for which a larger astrometry should be adopted until a more detailed model is developed.

The total astrometric uncertainty can be propagated into uncertainty in the estimated time delays and thus in the Hubble constant as described by Birrer and Treu (2019). For the lenses analyzed in this work 6 mas will yield uncertainties on the H_0 well below the 5% threshold and thus astrometric uncertainty is not a dominant contribution to the cos-

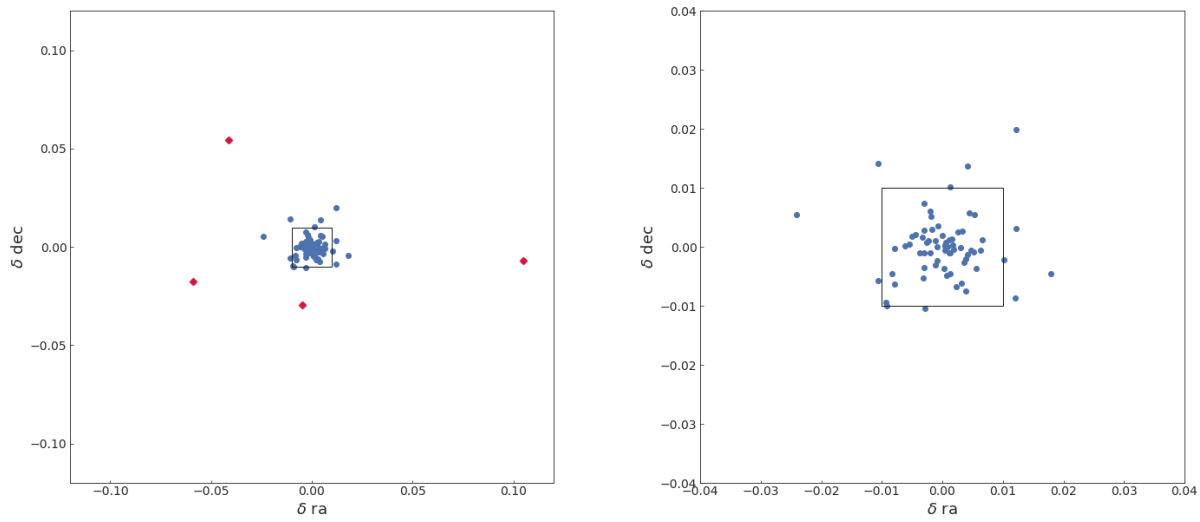

Figure 2.10: Comparison of the difference in quasar image positions that we inferred in this work by forward modeling *HST* images and the corresponding astrometry for systems with at least 3 detected images by the *Gaia* satellite. The left panel shows the comparison for all the systems with the crimson diamonds representing J1721+8842 differences. The right panel zooms in, excluding the outlier J1721+8842

mographic error budget. For time delay cosmography, systematic uncertainties arising from modeling choices can often be larger than the statistical errors estimated via the MCMC process. They are therefore a focal point of the remainder of this paper. The total error budget will of course need to include the statistical error, the error arising from modeling choices, and those arising from the residual uncertainty on the PSF reconstruction (Shajib et al., 2022), from the time delay measurements (Millon et al., 2020), and from the estimation of the effect of the mass along the line of sight (Greene et al., 2013).

2.4.2.2 Comparison to published mass models

For several systems, mass models based on ground-based imaging exist in the literature (e.g. Rusu and Lemon, 2018; Lemon et al., 2018, 2019, 2020, 2022). Given the difference in data resolution and depth, modeling approaches, treatment of perturbers, and parameterization it is difficult to perform a detailed quantitative comparison. Overall, quantities such as

Table 2.8: Median values for image magnification, unitless convergence, stellar convergence ($\kappa_\star$) estimated from the lens flux in the F160W band using a constant mass-to-light ratio (see Section 2.4.1), and shear at the position of the quasar images. The associated uncertainties are statistical in nature and were computed using 84th and 16th percentiles.

Name of Lens System	Image	κ	$\kappa_\star$	γ	Image Magnification
J0029-3814	A	$0.20^{+0.01}_{-0.01}$	$0.027^{+0.001}_{-0.001}$	$0.06^{+0.01}_{-0.01}$	$1.56^{+0.05}_{-0.04}$
	B	$0.84^{+0.02}_{-0.03}$	$0.335^{+0.010}_{-0.010}$	$0.99^{+0.03}_{-0.04}$	$-1.05^{+0.07}_{-0.09}$
	C	$0.38^{+0.02}_{-0.01}$	$0.067^{+0.003}_{-0.003}$	$0.12^{+0.01}_{-0.01}$	$2.70^{+0.14}_{-0.13}$
	D	$0.88^{+0.02}_{-0.03}$	$0.169^{+0.006}_{-0.007}$	$1.04^{+0.04}_{-0.04}$	$-0.93^{+0.06}_{-0.08}$
PS J0030-1525	A	$0.45^{+0.01}_{-0.01}$	$0.016^{+0.001}_{-0.001}$	$0.28^{+0.01}_{-0.01}$	$4.41^{+0.25}_{-0.20}$
	B	$0.70^{+0.02}_{-0.02}$	$0.411^{+0.016}_{-0.013}$	$0.60^{+0.02}_{-0.02}$	$-3.65^{+0.30}_{-0.35}$
	C	$0.55^{+0.01}_{-0.01}$	$0.051^{+0.002}_{-0.002}$	$0.42^{+0.01}_{-0.01}$	$35.73^{+3.68}_{-3.05}$
	D	$0.61^{+0.01}_{-0.01}$	$0.114^{+0.004}_{-0.003}$	$0.43^{+0.01}_{-0.01}$	$-29.01^{+2.29}_{-2.56}$
DES J0053-2012	A	$1.44^{+0.05}_{-0.05}$	$0.345^{+0.012}_{-0.013}$	$1.74^{+0.06}_{-0.08}$	$-0.36^{+0.02}_{-0.03}$
	B	$0.36^{+0.01}_{-0.01}$	$0.018^{+0.001}_{-0.001}$	$0.39^{+0.01}_{-0.01}$	$3.95^{+0.21}_{-0.17}$
	C	$0.50^{+0.01}_{-0.01}$	$0.034^{+0.001}_{-0.001}$	$0.71^{+0.01}_{-0.02}$	$-3.85^{+0.20}_{-0.26}$
	D	$0.29^{+0.01}_{-0.01}$	$0.028^{+0.001}_{-0.001}$	$0.30^{+0.01}_{-0.01}$	$2.43^{+0.11}_{-0.09}$
PS J0147+4630	A	$1.03^{+0.02}_{-0.02}$	$0.354^{+0.007}_{-0.009}$	$1.32^{+0.03}_{-0.04}$	$-0.57^{+0.03}_{-0.03}$
	B	$0.39^{+0.01}_{-0.01}$	$0.139^{+0.003}_{-0.003}$	$0.51^{+0.01}_{-0.01}$	$8.89^{+0.37}_{-0.34}$
	C	$0.42^{+0.01}_{-0.01}$	$0.175^{+0.003}_{-0.004}$	$0.63^{+0.01}_{-0.01}$	$-15.70^{+0.63}_{-0.67}$
	D	$0.37^{+0.01}_{-0.01}$	$0.174^{+0.003}_{-0.004}$	$0.54^{+0.01}_{-0.01}$	$9.38^{+0.39}_{-0.36}$
WG0214-2105	A	$0.40^{+0.01}_{-0.01}$	$0.137^{+0.001}_{-0.001}$	$0.37^{+0.01}_{-0.01}$	$4.46^{+0.26}_{-0.19}$
	B	$0.52^{+0.01}_{-0.01}$	$0.254^{+0.002}_{-0.002}$	$0.66^{+0.02}_{-0.02}$	$-4.66^{+0.23}_{-0.32}$
	C	$0.43^{+0.01}_{-0.01}$	$0.169^{+0.001}_{-0.001}$	$0.43^{+0.01}_{-0.01}$	$7.56^{+0.47}_{-0.34}$
	D	$0.48^{+0.01}_{-0.01}$	$0.261^{+0.002}_{-0.002}$	$0.67^{+0.02}_{-0.02}$	$-5.71^{+0.27}_{-0.37}$
SDSS J0248+1913	A	$0.43^{+0.03}_{-0.03}$	$0.016^{+0.004}_{-0.003}$	$0.31^{+0.01}_{-0.02}$	$4.42^{+0.65}_{-0.50}$
	B	$0.45^{+0.04}_{-0.03}$	$0.013^{+0.003}_{-0.003}$	$0.66^{+0.04}_{-0.04}$	$-7.17^{+0.82}_{-1.07}$
	C	$0.43^{+0.04}_{-0.03}$	$0.011^{+0.003}_{-0.002}$	$0.42^{+0.02}_{-0.02}$	$6.67^{+1.04}_{-0.79}$
	D	$0.60^{+0.03}_{-0.03}$	$0.050^{+0.010}_{-0.008}$	$0.60^{+0.04}_{-0.04}$	$-4.83^{+0.63}_{-0.74}$
WISE J0259-1635	A	$0.49^{+0.01}_{-0.01}$	$0.742^{+0.038}_{-0.041}$	$0.73^{+0.02}_{-0.01}$	$-3.52^{+0.15}_{-0.15}$
	B	$0.30^{+0.01}_{-0.01}$	$0.379^{+0.019}_{-0.020}$	$0.43^{+0.01}_{-0.01}$	$3.29^{+0.11}_{-0.12}$
	C	$0.49^{+0.01}_{-0.01}$	$0.749^{+0.043}_{-0.040}$	$0.76^{+0.02}_{-0.02}$	$-3.07^{+0.13}_{-0.13}$
	D	$0.35^{+0.01}_{-0.01}$	$0.839^{+0.045}_{-0.045}$	$0.49^{+0.01}_{-0.01}$	$5.25^{+0.20}_{-0.20}$
J0343-2828	A	$1.25^{+0.01}_{-0.01}$	$0.323^{+0.007}_{-0.008}$	$1.37^{+0.01}_{-0.01}$	$-0.55^{+0.01}_{-0.01}$
	B	$0.39^{+0.01}_{-0.01}$	$0.020^{+0.001}_{-0.001}$	$0.30^{+0.01}_{-0.01}$	$3.54^{+0.03}_{-0.03}$
	C	$0.57^{+0.01}_{-0.01}$	$0.065^{+0.002}_{-0.002}$	$0.71^{+0.01}_{-0.01}$	$-3.06^{+0.04}_{-0.04}$
	D	$0.36^{+0.01}_{-0.01}$	$0.017^{+0.001}_{-0.001}$	$0.24^{+0.01}_{-0.01}$	$2.80^{+0.02}_{-0.02}$
DES J0405-3308	A	$0.35^{+0.01}_{-0.01}$	$0.114^{+0.003}_{-0.003}$	$0.50^{+0.01}_{-0.01}$	$5.84^{+0.31}_{-0.26}$
	B	$0.55^{+0.01}_{-0.01}$	$0.238^{+0.006}_{-0.006}$	$0.68^{+0.02}_{-0.02}$	$-3.82^{+0.22}_{-0.24}$
	C	$0.34^{+0.01}_{-0.01}$	$0.127^{+0.004}_{-0.003}$	$0.53^{+0.01}_{-0.01}$	$6.74^{+0.34}_{-0.29}$
	D	$0.51^{+0.01}_{-0.01}$	$0.216^{+0.005}_{-0.005}$	$0.64^{+0.02}_{-0.02}$	$-5.78^{+0.34}_{-0.36}$
DES J0420-4037	A	$0.40^{+0.01}_{-0.02}$	$0.057^{+0.003}_{-0.003}$	$0.43^{+0.01}_{-0.01}$	$5.72^{+0.29}_{-0.27}$
	B	$0.54^{+0.01}_{-0.01}$	$0.122^{+0.006}_{-0.006}$	$0.59^{+0.02}_{-0.02}$	$-7.34^{+0.37}_{-0.39}$
	C	$0.46^{+0.01}_{-0.02}$	$0.083^{+0.004}_{-0.004}$	$0.47^{+0.01}_{-0.01}$	$15.13^{+0.80}_{-0.78}$
	D	$0.55^{+0.01}_{-0.01}$	$0.136^{+0.006}_{-0.006}$	$0.54^{+0.02}_{-0.01}$	$-10.90^{+0.61}_{-0.64}$

Table 2.9: Median values for image magnification, unitless convergence, stellar convergence ($\kappa_\star$) estimated from the lens flux in the F160W band using a constant mass-to-light ratio (see Section 2.4.1), and shear at the position of the quasar images. The associated uncertainties are statistical in nature and were computed using 84th and 16th percentiles.

Name of Lens System	Image	κ	$\kappa_\star$	γ	Image Magnification
DES J0530-3730	A	$0.40^{+0.03}_{-0.05}$	$2.362^{+0.869}_{-0.647}$	$0.55^{+0.04}_{-0.02}$	$12.50^{+19.34}_{-8.40}$
	B	$0.43^{+0.02}_{-0.03}$	$0.311^{+0.135}_{-0.099}$	$0.58^{+0.03}_{-0.03}$	$-51.51^{+75.11}_{-73.07}$
	C	$0.45^{+0.02}_{-0.04}$	$0.273^{+0.114}_{-0.089}$	$0.54^{+0.04}_{-0.02}$	$92.64^{+189.15}_{-184.91}$
	D	$0.49^{+0.03}_{-0.06}$	$0.342^{+0.171}_{-0.134}$	$0.53^{+0.04}_{-0.03}$	$-66.41^{+149.10}_{-147.22}$
PS J0630-1201	A	$0.62^{+0.02}_{-0.02}$	$0.295^{+0.067}_{-0.049}$	$0.88^{+0.03}_{-0.02}$	$-1.59^{+0.11}_{-0.10}$
	B	$0.33^{+0.01}_{-0.01}$	$0.038^{+0.009}_{-0.007}$	$0.64^{+0.01}_{-0.01}$	$21.69^{+0.59}_{-0.41}$
	C	$0.41^{+0.01}_{-0.01}$	$0.112^{+0.026}_{-0.019}$	$0.60^{+0.01}_{-0.01}$	$-63.78^{+2.04}_{-1.78}$
	D	$0.48^{+0.01}_{-0.01}$	$0.123^{+0.027}_{-0.019}$	$0.49^{+0.01}_{-0.01}$	$34.60^{+2.19}_{-1.99}$
J0659+1629	A	$0.67^{+0.01}_{-0.01}$	$0.080^{+0.003}_{-0.003}$	$0.53^{+0.02}_{-0.02}$	$-5.86^{+0.38}_{-0.44}$
	B	$0.40^{+0.01}_{-0.01}$	$0.029^{+0.001}_{-0.001}$	$0.25^{+0.01}_{-0.01}$	$3.40^{+0.18}_{-0.17}$
	C	$0.72^{+0.01}_{-0.01}$	$0.068^{+0.003}_{-0.003}$	$0.56^{+0.02}_{-0.02}$	$-4.31^{+0.29}_{-0.34}$
	D	$0.58^{+0.01}_{-0.01}$	$0.065^{+0.003}_{-0.002}$	$0.31^{+0.01}_{-0.01}$	$12.24^{+0.83}_{-0.73}$
J0818-2613	A	$0.40^{+0.01}_{-0.01}$	$0.142^{+0.001}_{-0.001}$	$0.18^{+0.01}_{-0.01}$	$3.02^{+0.05}_{-0.03}$
	B	$0.68^{+0.01}_{-0.02}$	$0.396^{+0.003}_{-0.003}$	$1.02^{+0.01}_{-0.01}$	$-1.07^{+0.02}_{-0.03}$
	C	$0.35^{+0.01}_{-0.01}$	$0.247^{+0.002}_{-0.004}$	$0.60^{+0.01}_{-0.01}$	$16.19^{+0.16}_{-0.11}$
	D	$0.36^{+0.01}_{-0.01}$	$0.234^{+0.002}_{-0.003}$	$0.69^{+0.01}_{-0.01}$	$-16.13^{+0.11}_{-0.17}$
W2M J1042+1641	A	$0.30^{+0.01}_{-0.01}$	$0.133^{+0.003}_{-0.003}$	$0.48^{+0.01}_{-0.01}$	$3.93^{+0.16}_{-0.18}$
	B	$0.40^{+0.01}_{-0.01}$	$0.246^{+0.005}_{-0.004}$	$0.65^{+0.01}_{-0.01}$	$-15.26^{+0.66}_{-0.60}$
	C	$0.38^{+0.01}_{-0.01}$	$0.226^{+0.005}_{-0.004}$	$0.59^{+0.01}_{-0.01}$	$22.60^{+1.01}_{-1.04}$
	D	$0.49^{+0.01}_{-0.01}$	$0.284^{+0.005}_{-0.005}$	$0.61^{+0.01}_{-0.01}$	$-9.13^{+0.56}_{-0.50}$
J1131-4419	A	$0.71^{+0.01}_{-0.01}$	$0.087^{+0.005}_{-0.005}$	$0.70^{+0.02}_{-0.02}$	$-2.49^{+0.13}_{-0.12}$
	B	$0.35^{+0.01}_{-0.01}$	$0.021^{+0.002}_{-0.002}$	$0.43^{+0.01}_{-0.01}$	$4.08^{+0.15}_{-0.17}$
	C	$0.58^{+0.01}_{-0.01}$	$0.149^{+0.007}_{-0.007}$	$0.55^{+0.01}_{-0.01}$	$-7.92^{+0.48}_{-0.42}$
	D	$0.44^{+0.01}_{-0.01}$	$0.091^{+0.005}_{-0.005}$	$0.46^{+0.01}_{-0.01}$	$9.82^{+0.42}_{-0.47}$
2M1134-2103	A	$0.22^{+0.01}_{-0.01}$	$0.036^{+0.001}_{-0.002}$	$0.14^{+0.01}_{-0.01}$	$1.72^{+0.03}_{-0.03}$
	B	$0.62^{+0.01}_{-0.02}$	$0.178^{+0.004}_{-0.005}$	$1.12^{+0.02}_{-0.02}$	$-0.90^{+0.03}_{-0.03}$
	C	$0.21^{+0.01}_{-0.01}$	$0.030^{+0.001}_{-0.001}$	$0.08^{+0.01}_{-0.01}$	$1.63^{+0.03}_{-0.03}$
	D	$0.96^{+0.02}_{-0.03}$	$0.335^{+0.008}_{-0.014}$	$1.54^{+0.03}_{-0.03}$	$-0.42^{+0.02}_{-0.01}$
SDSS J1251+2935	A	$0.30^{+0.01}_{-0.01}$	$0.077^{+0.003}_{-0.003}$	$0.28^{+0.01}_{-0.01}$	$2.44^{+0.04}_{-0.04}$
	B	$0.54^{+0.01}_{-0.01}$	$0.380^{+0.005}_{-0.004}$	$0.63^{+0.01}_{-0.01}$	$-5.49^{+0.11}_{-0.10}$
	C	$0.45^{+0.01}_{-0.01}$	$0.225^{+0.005}_{-0.005}$	$0.47^{+0.01}_{-0.01}$	$11.63^{+0.21}_{-0.21}$
	D	$0.50^{+0.01}_{-0.01}$	$0.278^{+0.008}_{-0.007}$	$0.63^{+0.01}_{-0.01}$	$-6.63^{+0.13}_{-0.13}$
2M1310-1714	A	$0.64^{+0.01}_{-0.01}$	$0.089^{+0.001}_{-0.001}$	$0.64^{+0.01}_{-0.01}$	$-3.64^{+0.13}_{-0.05}$
	B	$0.46^{+0.01}_{-0.01}$	$0.034^{+0.001}_{-0.001}$	$0.46^{+0.01}_{-0.01}$	$12.09^{+0.07}_{-0.19}$
	C	$0.54^{+0.01}_{-0.01}$	$0.048^{+0.001}_{-0.001}$	$0.54^{+0.01}_{-0.01}$	$-13.28^{+0.34}_{-0.13}$
	D	$0.46^{+0.01}_{-0.01}$	$0.028^{+0.001}_{-0.001}$	$0.44^{+0.01}_{-0.01}$	$9.60^{+0.07}_{-0.15}$
SDSS J1330+1810	A	$1.00^{+0.04}_{-0.04}$	$0.404^{+0.009}_{-0.005}$	$1.00^{+0.05}_{-0.05}$	$-1.01^{+0.10}_{-0.11}$
	B	$0.43^{+0.02}_{-0.02}$	$0.095^{+0.002}_{-0.002}$	$0.40^{+0.01}_{-0.01}$	$5.93^{+0.49}_{-0.50}$
	C	$0.66^{+0.01}_{-0.01}$	$0.230^{+0.005}_{-0.004}$	$0.58^{+0.02}_{-0.02}$	$-4.62^{+0.50}_{-0.53}$
	D	$0.27^{+0.02}_{-0.02}$	$0.038^{+0.001}_{-0.001}$	$0.45^{+0.01}_{-0.01}$	$2.99^{+0.19}_{-0.18}$

Table 2.10: Median values for image magnification, unitless convergence, stellar convergence ($\kappa_\star$) estimated from the lens flux in the F160W band using a constant mass-to-light ratio (see Section 2.4.1), and shear at the position of the quasar images. The associated uncertainties are statistical in nature and were computed using 84th and 16th percentiles.

Name of Lens System	Image	κ	$\kappa_\star$	γ	Image Magnification
SDSS J1433+6007	A	$0.74^{+0.01}_{-0.01}$	$0.191^{+0.009}_{-0.008}$	$0.75^{+0.02}_{-0.02}$	$-2.04^{+0.12}_{-0.13}$
	B	$0.49^{+0.01}_{-0.01}$	$0.031^{+0.002}_{-0.001}$	$0.32^{+0.01}_{-0.01}$	$6.45^{+0.35}_{-0.31}$
	C	$0.75^{+0.01}_{-0.01}$	$0.101^{+0.005}_{-0.005}$	$0.65^{+0.02}_{-0.02}$	$-2.81^{+0.14}_{-0.16}$
	D	$0.44^{+0.01}_{-0.01}$	$0.027^{+0.001}_{-0.001}$	$0.21^{+0.01}_{-0.01}$	$3.77^{+0.17}_{-0.16}$
J1537-3010	A	$0.39^{+0.01}_{-0.01}$	$0.094^{+0.001}_{-0.001}$	$0.29^{+0.01}_{-0.01}$	$3.51^{+0.11}_{-0.10}$
	B	$0.62^{+0.01}_{-0.01}$	$0.252^{+0.003}_{-0.003}$	$0.77^{+0.01}_{-0.01}$	$-2.24^{+0.08}_{-0.08}$
	C	$0.38^{+0.01}_{-0.01}$	$0.086^{+0.001}_{-0.001}$	$0.27^{+0.01}_{-0.01}$	$3.19^{+0.10}_{-0.09}$
	D	$0.61^{+0.01}_{-0.01}$	$0.262^{+0.003}_{-0.003}$	$0.75^{+0.01}_{-0.01}$	$-2.39^{+0.08}_{-0.09}$
PS J1606-2333	A	$0.33^{+0.01}_{-0.01}$	$0.073^{+0.005}_{-0.005}$	$0.19^{+0.01}_{-0.01}$	$2.43^{+0.06}_{-0.06}$
	B	$0.94^{+0.01}_{-0.01}$	$0.478^{+0.018}_{-0.021}$	$0.87^{+0.02}_{-0.02}$	$-1.34^{+0.05}_{-0.06}$
	C	$0.39^{+0.01}_{-0.01}$	$0.087^{+0.006}_{-0.006}$	$0.21^{+0.01}_{-0.01}$	$3.08^{+0.09}_{-0.08}$
	D	$0.81^{+0.01}_{-0.01}$	$0.352^{+0.014}_{-0.014}$	$0.81^{+0.01}_{-0.02}$	$-1.60^{+0.06}_{-0.07}$
J1721+8842	A	$0.78^{+0.01}_{-0.01}$	$0.475^{+0.001}_{-0.001}$	$0.81^{+0.01}_{-0.01}$	$-1.65^{+0.02}_{-0.02}$
	B	$0.44^{+0.01}_{-0.01}$	$0.207^{+0.001}_{-0.001}$	$0.37^{+0.01}_{-0.01}$	$5.54^{+0.07}_{-0.07}$
	C	$0.55^{+0.01}_{-0.01}$	$0.292^{+0.001}_{-0.001}$	$0.60^{+0.01}_{-0.01}$	$-6.34^{+0.09}_{-0.09}$
	D	$0.42^{+0.01}_{-0.01}$	$0.217^{+0.001}_{-0.001}$	$0.36^{+0.01}_{-0.01}$	$4.75^{+0.06}_{-0.05}$
J1817+2729	A	$0.43^{+0.01}_{-0.01}$	$0.057^{+0.002}_{-0.001}$	$0.46^{+0.01}_{-0.01}$	$9.02^{+0.53}_{-0.48}$
	B	$0.53^{+0.01}_{-0.01}$	$0.497^{+0.011}_{-0.012}$	$0.54^{+0.01}_{-0.01}$	$-14.09^{+0.88}_{-0.93}$
	C	$0.47^{+0.01}_{-0.01}$	$0.090^{+0.003}_{-0.003}$	$0.47^{+0.01}_{-0.01}$	$15.67^{+0.97}_{-0.88}$
	D	$0.52^{+0.01}_{-0.01}$	$0.504^{+0.009}_{-0.006}$	$0.58^{+0.01}_{-0.01}$	$-8.88^{+0.54}_{-0.58}$
DES J2038-4008	A	$0.58^{+0.01}_{-0.01}$	$0.458^{+0.001}_{-0.001}$	$1.06^{+0.01}_{-0.01}$	$-1.05^{+0.02}_{-0.02}$
	B	$0.24^{+0.01}_{-0.01}$	$0.178^{+0.001}_{-0.001}$	$0.48^{+0.01}_{-0.01}$	$2.88^{+0.04}_{-0.04}$
	C	$0.46^{+0.01}_{-0.01}$	$0.330^{+0.001}_{-0.001}$	$0.86^{+0.01}_{-0.01}$	$-2.28^{+0.04}_{-0.04}$
	D	$0.22^{+0.01}_{-0.01}$	$0.168^{+0.001}_{-0.001}$	$0.43^{+0.01}_{-0.01}$	$2.38^{+0.03}_{-0.03}$
WG2100-4452	A	$0.76^{+0.03}_{-0.02}$	$0.292^{+0.008}_{-0.006}$	$1.00^{+0.02}_{-0.03}$	$-1.07^{+0.04}_{-0.05}$
	B	$0.24^{+0.01}_{-0.01}$	$0.100^{+0.003}_{-0.002}$	$0.40^{+0.01}_{-0.01}$	$2.38^{+0.10}_{-0.06}$
	C	$0.49^{+0.02}_{-0.01}$	$0.181^{+0.005}_{-0.004}$	$0.66^{+0.01}_{-0.02}$	$-5.93^{+0.20}_{-0.28}$
	D	$0.35^{+0.02}_{-0.01}$	$0.132^{+0.004}_{-0.003}$	$0.53^{+0.01}_{-0.02}$	$7.25^{+0.31}_{-0.23}$
J2145+6345	A	$0.34^{+0.01}_{-0.01}$	$0.045^{+0.004}_{-0.004}$	$0.29^{+0.01}_{-0.01}$	$2.84^{+0.16}_{-0.13}$
	B	$0.87^{+0.04}_{-0.04}$	$0.280^{+0.022}_{-0.024}$	$1.00^{+0.04}_{-0.04}$	$-1.01^{+0.08}_{-0.09}$
	C	$0.40^{+0.01}_{-0.01}$	$0.082^{+0.007}_{-0.007}$	$0.43^{+0.01}_{-0.01}$	$5.80^{+0.36}_{-0.30}$
	D	$0.52^{+0.02}_{-0.02}$	$0.135^{+0.011}_{-0.011}$	$0.64^{+0.02}_{-0.02}$	$-5.43^{+0.35}_{-0.43}$
J2205-3727	A	$0.31^{+0.01}_{-0.01}$	$0.052^{+0.002}_{-0.002}$	$0.33^{+0.01}_{-0.01}$	$2.77^{+0.12}_{-0.10}$
	B	$0.59^{+0.01}_{-0.01}$	$0.125^{+0.004}_{-0.004}$	$0.65^{+0.02}_{-0.02}$	$-3.82^{+0.19}_{-0.23}$
	C	$0.42^{+0.01}_{-0.01}$	$0.082^{+0.003}_{-0.003}$	$0.46^{+0.01}_{-0.01}$	$8.13^{+0.41}_{-0.34}$
	D	$0.58^{+0.01}_{-0.01}$	$0.140^{+0.004}_{-0.004}$	$0.63^{+0.02}_{-0.02}$	$-4.53^{+0.21}_{-0.27}$
ATLAS J2344-3056	A	$0.61^{+0.01}_{-0.01}$	$0.328^{+0.006}_{-0.005}$	$0.65^{+0.02}_{-0.02}$	$-3.80^{+0.19}_{-0.22}$
	B	$0.40^{+0.01}_{-0.01}$	$0.235^{+0.003}_{-0.004}$	$0.39^{+0.01}_{-0.01}$	$4.80^{+0.22}_{-0.19}$
	C	$0.62^{+0.01}_{-0.01}$	$0.459^{+0.007}_{-0.007}$	$0.67^{+0.02}_{-0.02}$	$-3.31^{+0.17}_{-0.19}$
	D	$0.40^{+0.01}_{-0.01}$	$0.247^{+0.004}_{-0.003}$	$0.40^{+0.01}_{-0.01}$	$4.79^{+0.23}_{-0.20}$

Einstein radius, axis ratios, and position angle, are in agreement within the uncertainties. The external shear depends crucially on the choice of mass components and precision of the main galaxy position, which is often uncertain in ground based data. A more detailed comparison will have to be based on the same data, a common parameterization, and choice of mass model components.

Comparing our results for system DES J2038-4008 to those obtained via the cosmography-grade lens model of Shajib et al. (2022), we find excellent agreement for the power-law slope, Einstein radius, axis ratio and PA of the mass profile, shear strength and shear PA. We further find that our predicted time delays match very well the predictions by Shajib et al. (2022), with the largest difference of 0.6 days resulting from the greatest time delay prediction of 25.7 days, between images A and D, corresponding to a 2.3% difference.

For J1721+8842, we compare our results with those by Lemon et al. (2022) and find good agreement for the power-law slope (Lemon et al. (2022) used a singular isothermal ellipsoid or SIE, which is PEMD with a fixed slope of 2.0), the Einstein radius, axis ratio and PA of the mass profile, as well as for the shear strength. For the shear direction, we find a discrepancy of nearly 80 degrees, however, in our model we mask out the second image pair, which Lemon et al. (2022) use as additional constraint. A comparison of magnification values, shear, and convergence at the image positions with the best-fit model of Lemon et al. (2022) shows agreement within a few percent, which is remarkable given the complexity of the system and the assumption of an SIE in Lemon et al. (2022) versus the power law used in our model. We further compare our predicted time delays and find excellent agreement, with a largest difference of 0.6 days and the highest predicted time delay in Lemon et al. (2022) showing no difference to our result. Additionally, we compare our results for J1721+8842 with those by Mangat et al. (2021) and, again, find reasonable agreement for the power-law slope (Mangat et al. (2021) use an SIE), the Einstein radius, axis ratio and PA of the mass profile, and shear. After rescaling to the cosmology assumed by Mangat et al. (2021), we further find that our predicted time delays and image magnifications agree within a few

percent.

2.4.3 Predicted time delays

For each system, we predict the time delay, Δt, between images of the lensed quasar. These predictions can be used to determine for which system high-cadence observations are viable and to give guidance on the duration of long-term monitoring campaigns, as well as when to expect observed variations to appear in other images for the purpose of scheduling follow-up observations. To predict the time delays, we adopt a flat ΛCDM cosmology with standard values for present matter density, radiation, and the cosmological constant, at $\Omega_{\mathrm{m},0} = 0.3$, $\Omega_{\mathrm{r},0} = 0.0$, and $\Omega_{\Lambda,0} = 0.7$, respectively, and the Hubble constant at $H_0 = 70$ km s^{-1} Mpc^{-1}. For calculations where a component's redshift, due to lack of measurements, is currently unknown, we assume typical values of $z_{\mathrm{d}} = 0.5$, for the deflector, and of $z_{\mathrm{s}} = 2.0$, for the source. The predicted time delays for each successfully reconstructed lens model are summarized in Tables 2.11 and 2.12.

2.4.4 Efficiency of the uniform framework

To give an estimate on the time savings introduced by modeling strong lenses using our automated pipeline, we provide the total processing time for two systems, SDSS J0248+1913 and SDSS J1251+2935, broken down between the time needed for the PSO steps and the time required to probe the posterior distributions through an MCMC. In the case of SDSS J0248+1913, the PSO fitting time is 5 hours and 56 mins, while the run-time of the MCMC is 5 hours and 10 mins, giving a total reconstruction time of 11 hours and 6 mins. The PSO fitting time corresponds to using 19 threads on a machine with a hyper-threaded Intel(R) Core(TM) i9-9820X CPU clocked at 3.30 GHz, while the MCMC run-time corresponds to a computation using 20 threads on the same architecture. For SDSS J1251+2935, the PSO fitting time is 8 hours, 55 mins, and the associated MCMC time to find convergence is 8

Table 2.11: Median values for Fermat potential differences between quasar images and associated predicted time delays using listed measured or assumed redshifts. The associated uncertainties are statistical in nature and were computed using 84th and 16th percentiles. Our calculations assume a flat ΛCDM cosmology with $\Omega_{m,0} = 0.3$, $\Omega_{\Lambda,0} = 0.7$, and $H_0 = 70$ km s^{-1} Mpc^{-1}. For unmeasured deflector redshifts, we adopt a fiducial $z_d = 0.5$. It should be noted that a change in the redshifts for a system would rescale the corresponding predicted time delays.

Name of Lens System	z_d	z_s	$\Delta\Phi_{AB}$	$\Delta\Phi_{AC}$	$\Delta\Phi_{AD}$	Δt_{AB} (days)	Δt_{AC} (days)	Δt_{AD} (days)
J0029-3814	0.863	2.821	$-0.6295^{+0.0295}_{-0.0188}$	$-0.5754^{+0.0274}_{-0.0172}$	$-0.6436^{+0.0297}_{-0.0190}$	$-100.0^{+4.7}_{-3.0}$	$-91.4^{+4.4}_{-2.7}$	$-102.2^{+4.7}_{-3.0}$
PS J0030-1525 (†)	0.5	3.36	$-0.2685^{+0.0142}_{-0.0136}$	$-0.1151^{+0.0048}_{-0.0045}$	$-0.1158^{+0.0048}_{-0.0046}$	$-19.8^{+1.0}_{-1.0}$	$-8.5^{+0.4}_{-0.3}$	$-8.5^{+0.4}_{-0.3}$
DES J0053-2012 (†)	0.5	3.8	$1.3895^{+0.0263}_{-0.0391}$	$1.3460^{+0.0249}_{-0.0369}$	$1.6476^{+0.0323}_{-0.0501}$	$100.5^{+1.9}_{-2.8}$	$97.3^{+1.8}_{-2.7}$	$119.2^{+2.3}_{-3.6}$
PS J0147+4630	0.678	2.377	$2.5538^{+0.0434}_{-0.0479}$	$2.5329^{+0.0430}_{-0.0474}$	$2.5520^{+0.0434}_{-0.0478}$	$306.1^{+5.2}_{-5.7}$	$303.6^{+5.1}_{-5.7}$	$305.9^{+5.2}_{-5.7}$
WG0214-2105	0.22	3.229	$-0.1206^{+0.0040}_{-0.0039}$	$-0.0800^{+0.0027}_{-0.0026}$	$-0.1046^{+0.0035}_{-0.0034}$	$-3.5^{+0.1}_{-0.1}$	$-2.3^{+0.1}_{-0.1}$	$-3.0^{+0.1}_{-0.1}$
SDSS J0248+1913 (†)	0.5	2.44	$-0.0737^{+0.0051}_{-0.0051}$	$-0.0557^{+0.0039}_{-0.0040}$	$-0.1047^{+0.0078}_{-0.0080}$	$-5.8^{+0.4}_{-0.4}$	$-4.4^{+0.3}_{-0.3}$	$-8.2^{+0.6}_{-0.6}$
WISE J0259-1635	0.905	2.16	$0.1022^{+0.0023}_{-0.0023}$	$-0.0128^{+0.0003}_{-0.0003}$	$0.0279^{+0.0006}_{-0.0006}$	$20.3^{+0.5}_{-0.4}$	$-2.5^{+0.1}_{-0.1}$	$5.5^{+0.1}_{-0.1}$
J0343-2828	0.385	1.655	$1.8668^{+0.0071}_{-0.0081}$	$1.5985^{+0.0062}_{-0.0064}$	$2.2440^{+0.0092}_{-0.0106}$	$115.8^{+0.4}_{-0.5}$	$99.1^{+0.4}_{-0.4}$	$139.2^{+0.6}_{-0.7}$
DES J0405-3308 (†)	0.5	1.713	$-0.0587^{+0.0020}_{-0.0022}$	$-0.0074^{+0.0003}_{-0.0004}$	$-0.0308^{+0.0012}_{-0.0013}$	$-5.2^{+0.2}_{-0.2}$	$-0.7^{+0.1}_{-0.1}$	$-2.7^{+0.1}_{-0.1}$
DES J0420-4037	0.358	2.4	$-0.1101^{+0.0030}_{-0.0032}$	$-0.0870^{+0.0024}_{-0.0027}$	$-0.0930^{+0.0026}_{-0.0029}$	$-5.7^{+0.2}_{-0.2}$	$-4.5^{+0.1}_{-0.1}$	$-4.8^{+0.1}_{-0.1}$
DES J0530-3730 (†)	0.5	2.838	$-0.0159^{+0.0138}_{-0.0238}$	$-0.0152^{+0.0129}_{-0.0234}$	$-0.0153^{+0.0129}_{-0.0234}$	$-1.2^{+1.1}_{-1.8}$	$-1.2^{+1.0}_{-1.8}$	$-1.2^{+1.0}_{-1.8}$
PS J0630-1201 (†)	0.5	3.34	$0.9574^{+0.0334}_{-0.0324}$	$0.9520^{+0.0335}_{-0.0324}$	$0.9539^{+0.0335}_{-0.0325}$	$70.7^{+2.5}_{-2.4}$	$70.3^{+2.5}_{-2.4}$	$70.4^{+2.5}_{-2.4}$
J0659+1629	0.766	3.083	$2.3321^{+0.0751}_{-0.0674}$	$0.0404^{+0.0015}_{-0.0014}$	$0.1064^{+0.0047}_{-0.0043}$	$302.6^{+9.7}_{-8.7}$	$5.2^{+0.2}_{-0.2}$	$13.8^{+0.6}_{-0.6}$
J0818-2613 (†)	0.5	2.164	$-4.7682^{+0.0857}_{-0.0506}$	$-1.5446^{+0.0178}_{-0.0122}$	$-1.5484^{+0.0178}_{-0.0122}$	$-387.5^{+7.0}_{-4.1}$	$-125.5^{+1.4}_{-1.0}$	$-125.8^{+1.4}_{-1.0}$
W2M J1042+1641	0.599	2.5	$-0.1777^{+0.0066}_{-0.0078}$	$-0.1748^{+0.0065}_{-0.0077}$	$-0.1807^{+0.0066}_{-0.0079}$	$-17.6^{+0.7}_{-0.8}$	$-17.3^{+0.6}_{-0.8}$	$-17.9^{+0.7}_{-0.8}$

(†) System with a fiducial deflector redshift of $z_d = 0.5$.

Table 2.12: Median values for Fermat potential differences between quasar images and associated predicted time delays using listed measured or assumed redshifts. The associated uncertainties are statistical in nature and were computed using 84th and 16th percentiles. Our calculations assume a flat ΛCDM cosmology with $\Omega_{\mathrm{m},0} = 0.3$, $\Omega_{\Lambda,0} = 0.7$, and $H_0 = 70$ km s^{-1} Mpc^{-1}. For unmeasured deflector redshifts, we adopt a fiducial $z_{\mathrm{d}} = 0.5$. It should be noted that a change in the redshifts for a system would rescale the corresponding predicted time delays.

Name of Lens System	z_{d}	z_{s}	$\Delta\Phi_{\mathrm{AB}}$	$\Delta\Phi_{\mathrm{AC}}$	$\Delta\Phi_{\mathrm{AD}}$	Δt_{AB} (days)	Δt_{AC} (days)	Δt_{AD} (days)
J1131-4419 (†)	0.5	1.09	$0.2117^{+0.0060}_{-0.0053}$	$0.1023^{+0.0021}_{-0.0023}$	$0.1072^{+0.0023}_{-0.0024}$	$24.2^{+0.7}_{-0.6}$	$11.7^{+0.2}_{-0.3}$	$12.2^{+0.3}_{-0.3}$
2M1134-2103 (†)	0.5	2.77	$-0.4707^{+0.0077}_{-0.0085}$	$0.1825^{+0.0024}_{-0.0032}$	$-0.9526^{+0.0122}_{-0.0117}$	$-36.0^{+0.6}_{-0.7}$	$14.0^{+0.2}_{-0.2}$	$-72.8^{+0.9}_{-0.9}$
SDSS J1251+2935	0.41	0.802	$-0.3271^{+0.0031}_{-0.0031}$	$-0.3188^{+0.0030}_{-0.0030}$	$-0.3242^{+0.0031}_{-0.0030}$	$-33.6^{+0.3}_{-0.3}$	$-32.8^{+0.3}_{-0.3}$	$-33.3^{+0.3}_{-0.3}$
2M1310-1714	0.293	1.975	$1.0199^{+0.0214}_{-0.0085}$	$0.8912^{+0.0184}_{-0.0076}$	$1.2109^{+0.0259}_{-0.0103}$	$43.2^{+0.9}_{-0.4}$	$37.7^{+0.8}_{-0.3}$	$51.3^{+1.1}_{-0.4}$
SDSS J1330+1810	0.373	1.393	$0.2867^{+0.0126}_{-0.0127}$	$0.2808^{+0.0121}_{-0.0122}$	$0.4553^{+0.0251}_{-0.0242}$	$18.0^{+0.8}_{-0.8}$	$17.6^{+0.8}_{-0.8}$	$28.6^{+1.6}_{-1.5}$
SDSS J1433+6007	0.407	2.737	$0.6681^{+0.0202}_{-0.0184}$	$0.5380^{+0.0186}_{-0.0153}$	$1.0323^{+0.0257}_{-0.0265}$	$39.8^{+1.2}_{-1.1}$	$32.0^{+1.1}_{-0.9}$	$61.4^{+1.5}_{-1.6}$
J1537-3010	0.592	1.721	$-0.3265^{+0.0049}_{-0.0050}$	$0.0975^{+0.0016}_{-0.0017}$	$-0.2925^{+0.0046}_{-0.0042}$	$-36.9^{+0.6}_{-0.6}$	$11.0^{+0.2}_{-0.2}$	$-33.0^{+0.5}_{-0.5}$
PS J1606-2333 (†)	0.5	1.69	$-0.2161^{+0.0041}_{-0.0042}$	$-0.1102^{+0.0024}_{-0.0023}$	$-0.1868^{+0.0038}_{-0.0037}$	$-19.1^{+0.4}_{-0.4}$	$-9.7^{+0.2}_{-0.2}$	$-16.5^{+0.3}_{-0.3}$
J1721+8842	0.184	2.37	$1.1885^{+0.0068}_{-0.0071}$	$1.0683^{+0.0059}_{-0.0063}$	$1.2809^{+0.0074}_{-0.0079}$	$29.0^{+0.2}_{-0.2}$	$26.0^{+0.1}_{-0.2}$	$31.2^{+0.2}_{-0.2}$
J1817+2729 (†)	0.5	3.07	$-0.0474^{+0.0020}_{-0.0024}$	$-0.0385^{+0.0016}_{-0.0020}$	$-0.0724^{+0.0031}_{-0.0036}$	$-3.6^{+0.1}_{-0.2}$	$-2.9^{+0.1}_{-0.2}$	$-5.4^{+0.2}_{-0.3}$
DES J2038-4008	0.228	0.777	$0.5230^{+0.0043}_{-0.0038}$	$0.3863^{+0.0031}_{-0.0026}$	$0.6563^{+0.0059}_{-0.0050}$	$20.5^{+0.2}_{-0.1}$	$15.1^{+0.1}_{-0.1}$	$25.7^{+0.2}_{-0.2}$
WG2100-4452	0.203	0.92	$0.8140^{+0.0093}_{-0.0099}$	$0.4141^{+0.0040}_{-0.0051}$	$0.4206^{+0.0041}_{-0.0051}$	$25.8^{+0.3}_{-0.3}$	$13.1^{+0.1}_{-0.2}$	$13.3^{+0.1}_{-0.2}$
J2145+6345 (†)	0.5	1.56	$-0.5187^{+0.0242}_{-0.0221}$	$-0.1477^{+0.0086}_{-0.0084}$	$-0.1604^{+0.0092}_{-0.0090}$	$-47.5^{+2.2}_{-2.0}$	$-13.5^{+0.8}_{-0.8}$	$-14.7^{+0.8}_{-0.8}$
J2205-3727 (†)	0.5	1.848	$-0.2200^{+0.0075}_{-0.0058}$	$-0.2006^{+0.0069}_{-0.0054}$	$-0.2126^{+0.0072}_{-0.0056}$	$-18.8^{+0.6}_{-0.5}$	$-17.1^{+0.6}_{-0.5}$	$-18.2^{+0.6}_{-0.5}$
ATLAS J2344-3056 (†)	0.5	1.298	$0.0260^{+0.0007}_{-0.0008}$	$-0.0066^{+0.0002}_{-0.0002}$	$0.0264^{+0.0007}_{-0.0008}$	$2.6^{+0.1}_{-0.1}$	$-0.7^{+0.1}_{-0.1}$	$2.7^{+0.1}_{-0.1}$

(†) System with a fiducial deflector redshift of $z_{\mathrm{d}} = 0.5$.

hours, 12 mins, for a total computation time of 17 hours and 7 mins. The MCMC runtime corresponds to the same resource level as used for the modeling of SDSS J0248+1913, however, the PSO fitting is associated with 20 threads on a machine hosting an Intel(R) Core(TM) i9-10980XE CPU clocked at 3.00 GHz. By comparison, these processing times are much shorter than traditional lens modeling times, which can require up to 1 million CPU hours for extremely complex lens configurations. Furthermore, our pipeline's speed is comparable to the processing times of Shajib et al. (2019)'s framework, but it requires no human input and intervention along the reconstruction process.

The time required to set up the pipeline is conservatively estimated at 1 hour per lens. Additionally, we approximate another 6 hours of required investigator time per lens to reduce the data, prior to the pipeline processing, and 3 hours per system to review results and move data between machines, arriving at a conservative total of 10 hours of investigator overhead. This overhead represents a minimal level of investigator time and would be required for most types of analyses, considering the necessity of data preparation and quality control. This time is much smaller than the typical amount of investigator time adopted by previous non-automated studies, and comparable with the amount of time per system invested by Shajib et al. (2019).

2.4.5 Difference in Fermat potential of the quasar images as a metric for cosmography

To assess the stability in our models and their utility for cosmography, we introduce a new metric that tracks the changes in the Fermat potential at the position of the quasar images for each step or modeling choice in our pipeline. We then compute the absolute difference in the Fermat potential at the image positions and normalize it with the results of the final model.

We expect the stability of the Fermat potential difference to depend on three factors:

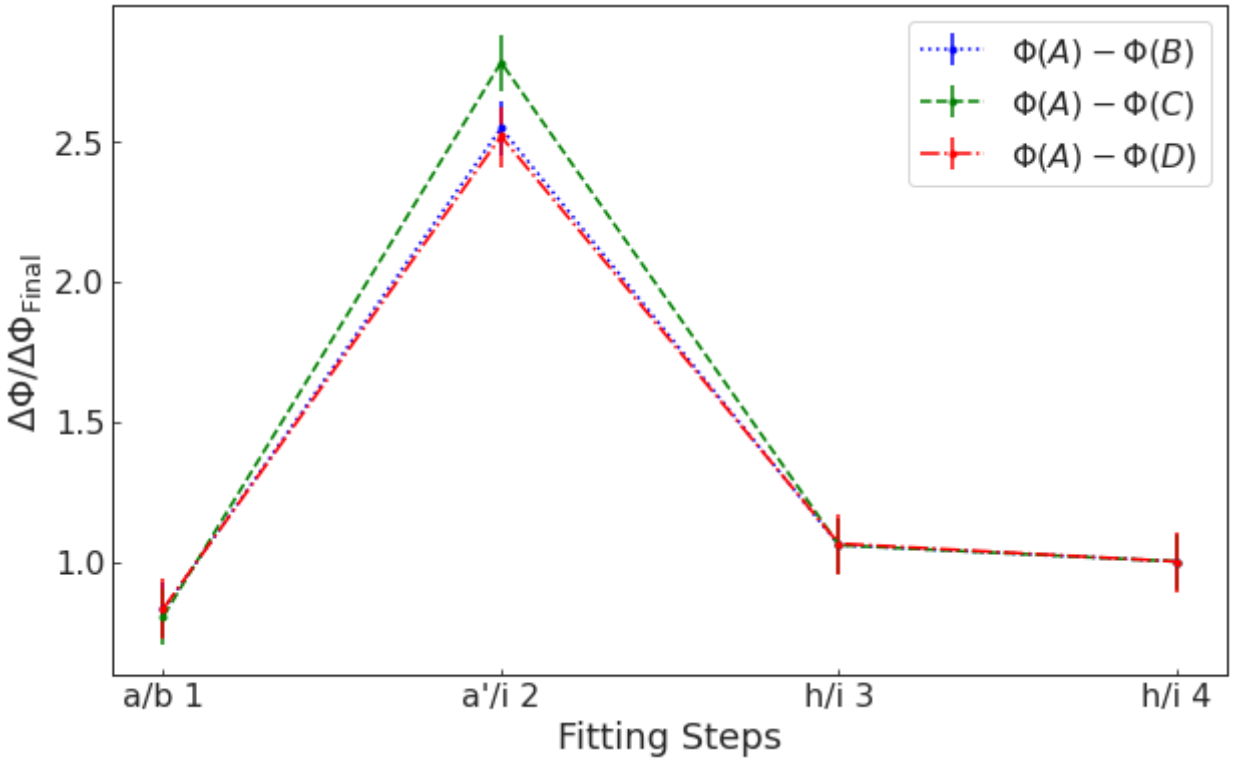

Figure 2.11: Difference in the Fermat potential between the image positions for SDSS J0248+1913, as a function of modeling steps, from the initial setup of the reconstruction through the final PSO fitting after adding additional source complexity to the model.

i) the information content of the multiple images of the extended source; ii) the overall symmetry and configuration of the multiple images of the quasars (highly symmetric crosses will have fairly similar potential at the location of the images); iii) complexity of the mass distribution of the deflector and presence of perturbers.

This metric allows us to visualize the impact of each model decision along the reconstruction. It also gives us a way to use the metric as a tool to evaluate systematic uncertainties resulting from modeling choices by applying it to a large sample as we will demonstrate for the case study SDSS J0248+1913 in Section 2.5.1. Ultimately, this new metric also gives us a way to assess how close our reconstructed models come to the quality required for cosmography.

In this section we first discuss in some detail a case study and then present some statistics about the performance of the pipeline with respect to this metric across the sample.

2.4.5.1 Case study

To demonstrate the described tracking mechanism for modeling choices, we show in Figure 2.11 the evolution of the difference in Fermat potential at the image positions for lens SDSS J0248+1913, starting with the first model setup up to the initialization of the MCMC run. Stepping through the decision framework, Figure 2.11 illustrates the resulting changes in Fermat potential differences from an initial configuration (step a.), used for fitting the most informative band (step b), through the first simultaneous fitting sequence of all bands (step a'/i), up to adding source complexity via increase in shapelet order in the final steps h/i 3 and h/i 4.

The conclusion of Figure 2.11 is that modeling choices can alter the difference in Fermat potential at a level that is significant w.r.t. our target precision of 3-5% and therefore need to be properly addressed. In contrast, the statistical uncertainties for a fixed model choice, as explored by the MCMC, are generally smaller. To further illustrate the distribution of lens mass and lens light parameters, we show a corner plot for system SDSSJ0248+1913 in

Appendix 2.D.

2.4.5.2 Assessment of Fermat potential stability on the sample

Table 2.13 summarizes the performance of our pipeline on the sample, in terms of Fermat potential stability. We focus on the absolute value of the Fermat potential difference between the images with the largest difference, since those will have the longest time delay. The longest time delay is the easiest one to measure precisely and therefore usually the dominant contributor to the cosmographic measurement. The first row describes the stability with respect to the last two steps for model changes within the PSO process, while the second row describes stability during the MCMC chain, which we derive from the comparison of the final MCMC result to the results for the final model of the PSO. As in the case study above, in most cases modeling choices, and not residual statistical errors once a model has been defined, are the dominant source of uncertainty in Fermat potential difference, so we will focus our discussion on the first row, which is the most novel aspect of our analysis. Of course, as discussed at the end of § 2.4.2.1, the full cosmographic error budget will have to account for random and systematic errors on modeling as well as for other sources of uncertainty.

For convenience, we bin the sample into four general categories: i) cosmography grade models, which we define as lenses with an uncertainty of less than 3%; ii) nearly cosmography grade, defined with errors of between $3-5\%$, which will require a likely modest amount of additional effort to achieve accurate Hubble constant measurements; iii) models with uncertainties in the range 5-10%, which may already be useful for other applications but require substantial work to reach cosmography grade; iv) models with uncertainties larger than 10%, which should be used only as a starting point for further investigation. We caution the reader that this assessment is indicative only and caveats apply. For example, we have used an informative prior on the mass density profile slope, which could bias the inference if not removed or properly accounted for. Furthermore, some systems may have good enough

lens models but may still yield low precision cosmology if the sources do not vary enough to measure the time delay or if the line of sight is overly complicated.

Remarkably, the pipeline yields cosmography-grade or nearly cosmography grade models (as defined above) for 10/30 systems (WG0214-2105, J0343-2828, DES J0420-4037, J0659+1629, 2M1310-1714, J1721+8842, J1817+2729, WG2100-4452 are cosmography grade; PS J0147+4630 and J1537-3010 are nearly cosmography grade); however, we urge caution with regards to the results of J1721+8842, as this system is highly complex and, as shown in Figure 2.10, we find small variances between our predicted image positions and the corresponding *Gaia* measurements. Six lenses are in the 5-10% range, but require substantial work (SDSS J0248+1913, WISE J0259-1635, J0818-2613, 2M1134-2103, DES J2038-4008, SDSS J1251+2935). The remaining fourteen systems we assess as currently far from cosmography grade given the stability in Fermat potential differences observed during the steps of model reconstruction.

The fact that half of the lenses are far from cosmography grade is not surprising, considering the quality of the data, the lensing configurations, and the simplifications inherent to our modeling procedure. Table 4.5 and Figures 2.14 to 2.17 shed some light on the causes of instability. In certain cases (e.g. J2145+6345) the quasars are so bright that little extended source light is visible. In others (e.g. ATLAS J233-3056) the image separation is so small and the system so symmetric (resulting in very short predicted time delays) that it is difficult to imagine getting a cosmography grade model with current technology. From the modeling point of view, some cases seem easily improvable, while others will require a more flexible modeling scheme than the one applied here. In the first category are all those systems for which there was a substantial jump in the Fermat potential difference between the one band and three band model. In many of those cases the three band model was considered acceptable but the metric still recorded the jump (e.g. J0029-3814). For some of those cases, further exploration may reveal that cosmography grade models are achievable within the present modeling assumptions. The latter category includes systems such as PS

Table 2.13: Stability in Fermat Potential. Listed are the number of systems for which a change in the Fermat potential difference is within the table's thresholds. The table includes both, model changes within the PSO and changes during the MCMC chain.

Stability	$< 3\%$	$3 - 5\%$	$5 - 10\%$	$\geq 10\%$
PSO	8	2	6	14
MCMC	24	3	2	1

J0630-1201, where there is clearly more than one deflector and therefore will require more complex models. Additional work, left for future studies, is needed to find out if those systems can be made cosmography grade with additional modeling efforts and/or better data, or whether it is more cost effective to focus on the low hanging fruits.

The fact that our automated pipeline yields "cosmography grade" models for a 1/3 of the sample is an important result, although some caveats must be kept in mind. The most important caveat is that our pipeline uses informative priors on the slope of the mass density profile, ellipticity, and alignment of mass and light profiles, to avoid non-physical solutions. However, such informative priors could have artificially reduced the uncertainty on the Fermat potential. For example, J1817+2729 and WG0214-2105 are labelled "cosmography grade", but the offset between the PA of mass and light is close to the boundary of the prior. It is thus possible that with a less informative prior the uncertainty would have been larger. Analyzing these types of issues is beyond the scope of our automated pipeline and is left for future work.

In conclusion, our finding that a third of the sample is "cosmography grade" – if confirmed by a more detailed analysis of a subset of the systems – would imply that investigator time can be cut significantly shorter than in previous state-of-the-art studies, paving the way for studies of much larger future samples.

2.5 Discussion

2.5.1 Systematics in source complexity

Even small increases in source complexity, represented by the maximum shapelet order, $n_{\max}$, have a substantial impact on the computational time in the reconstruction of the lens models. Additionally, unnecessary complexity would only result in "fitting the noise". Therefore, the models produced by our automated pipeline should have a sufficient complexity to accurately reflect the data, but not more.

To assess the impact of systematic uncertainties in a model's source light complexity, we use the metric established in Section 2.4.5 and introduce a small perturbation in the shapelet order, $n_{\max}$, of a successfully converged lens model. We first increase $n_{\max}$ by 2 and then probe the model's parameter space with a narrow search region using a PSO with 150 particles for 500 iterations. If the converged lens model does not include any shapelets for a particular band, we add the shapelet profile to the existing Sérsic light profile of the source. The particle number and iterations for the PSO routine are set high enough that any deviation in the stability of the Fermat potential will become apparent after the PSO's execution. We then re-evaluate the difference in the Fermat potential at the image positions, using the result of the perturbation, and compare it to the previously converged model result. This test in stability is repeated with a decrease in the model's source complexity. For this, we decrease $n_{\max}$ by 2, unless no shapelets were used to model additional source complexity. We repeat probing the parameter space with a PSO routine, using the same particle number, at the same same uncertainty level, and the same number of iterations as selected for investigating the impact of a higher source complexity. We then compare the Fermat potential difference of the quasar images between the perturbed and the baseline model.

For lens system SDSSJ0248+1913 we find no significant impact on the Fermat potential difference at the image positions for an increase in source complexity, as shown in Figure 2.12. Additionally, the PSO converged after 191 iterations, reflecting the model's stability. How-

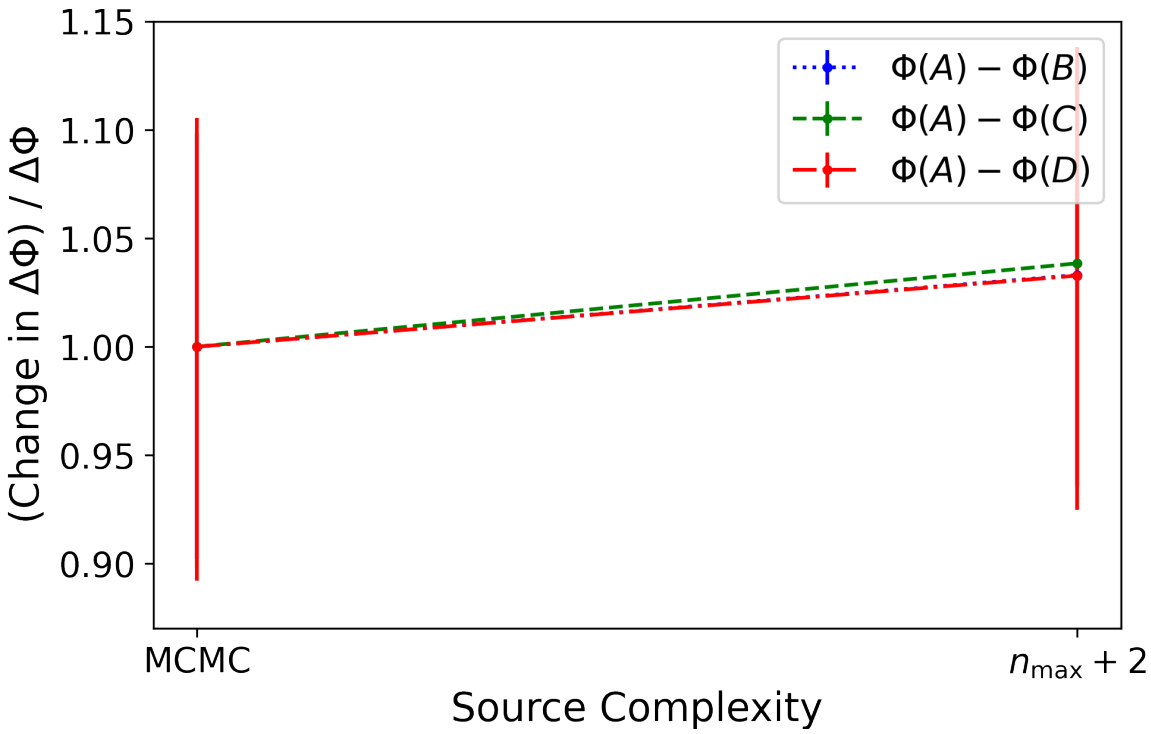

Figure 2.12: Stability of the difference in Fermat potential at the image positions, w.r.t. an increase in source complexity for SDSS J0248-1913. The increase of the highest shapelet order parameter, $n_{\max}$, by 2 results in a less than 4% change for all Fermat potential differences.

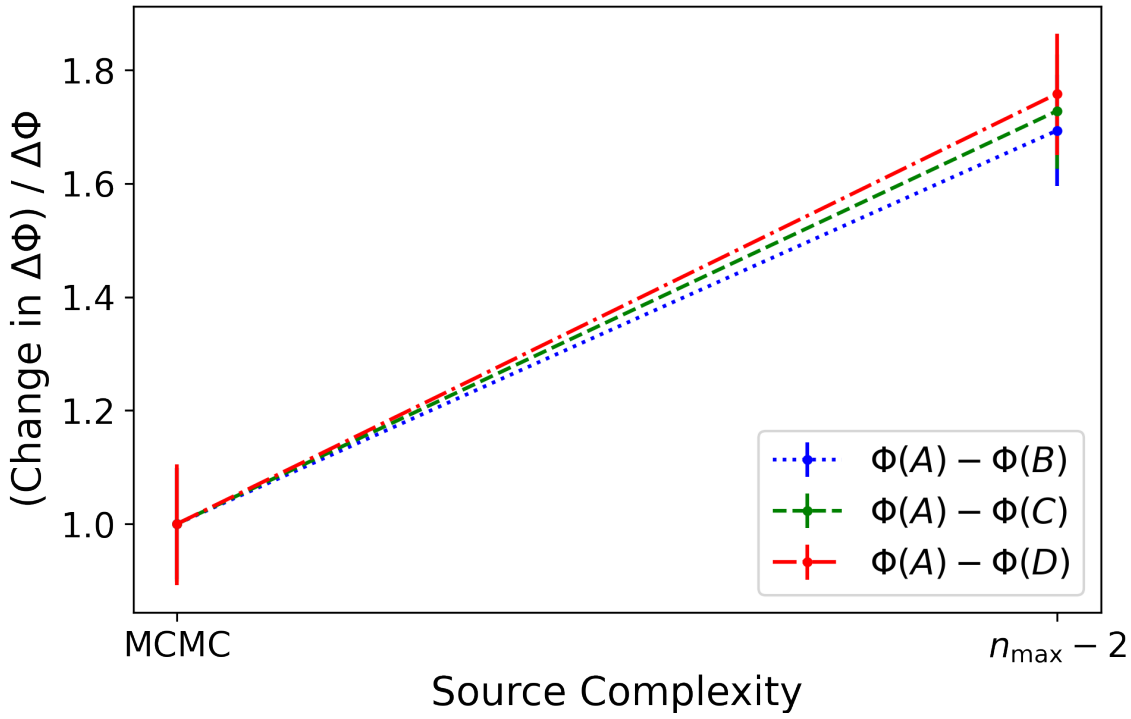

Figure 2.13: Stability of the difference in Fermat potential at the image positions, w.r.t. a decrease in source complexity for SDSS J0248-1913. The decrease in the maximum shapelet order, $n_{\max}$, by 2 drive the model towards changes that end in nearly doubling the images' Fermat potential difference.

ever, as illustrated in Figure 2.13, we find the opposite for a decrease in $n_{\max}$, where we observe a noteworthy change in the Fermat potential difference. These findings are reassuring, as they demonstrate the reconstructed model's stability, and further infer that adding unnecessary complexity does not change the derived model parameters. In contrast, lowering complexity enters a regime in which the model does not sufficiently describe the data and with it signals a change in the Fermat potential for the system. As Figures 2.12 and 2.13 demonstrate, the complexity increase results in a change of less than 4%, which is below our required uncertainty threshold, while a decrease in source complexity pushes the stable model towards a less precise description and with it results in a change far above our target of a 5% error budget.

2.5.2 Future improvements

The pipeline presented here is a major step forward. Future work should be able to further improve on our result by carrying out the following additional steps:

- Assess the impact of other modeling choices on the reconstruction of strongly lensed systems. Utilizing our pipeline on large samples will enable us to test how much models are affected by variations in parameters such as PSF symmetry, cut-out size, or sub-grid resolution.

- Expand and build up the capabilities of our pipeline to be able to reconstruct more complex lens model scenarios. For instance, our pipeline is limited to one main deflector. In cases where observations show two lensing galaxies (i.e. J0343-282 and 2M1310-1714) we currently designate one of the deflectors as primary, using a PEMD mass profile, and model the second lens galaxy as satellite with an SIS mass profile. This simplified approach, however, limits us when other significant perturbers, such as satellites to the main deflector, are present and their impact should not be ignored

in the reconstruction. Another aspect that could be generalized is the choice of a satellite's mass and light profile. Not every main deflector companion is sufficiently represented by our current modeling choice of an SIS with a circular Sérsic light profile, leaving room for the inclusion of other possible options, for instance a Singular Isothermal Ellipsoid.

- Develop the capability to model multi-lens-plane systems and massive perturbers. In most cases a single lens plane approximation proves sufficient for the model. However, if masssive perturbers are found outside the lens plane, these deflectors should be modeled at their correct respective distances to insure accurate computations of the Fermat potential difference between quasar images. Since we have observations in multiple bands available, we have the necessary information to incorporate photometric redshift estimates for all model components, and with it could potentially facilitate a multi-plane lens model reconstructions, if determined preferential.

- Given that our sample includes lenses for which a double Sérsic provides an improved but not yet complete description of the main deflector's light profile (i.e. DES J2038-4008), future versions of the pipeline would benefit from the inclusion of other lens light descriptors for highly complex systems, both, in addition or in lieu of the Sérsic functions used for this work.

2.6 Summary

We developed a lens modeling pipeline aimed at minimizing an investigator's time and providing a uniform modeling framework for large samples of lenses. We then applied it to a sample of 30 quadruply imaged quasars and one lensed compact galaxy. Out of these 31 lenses, 30 systems can be processed successfully by our pipeline, while the remaining system

is too complex for the current capabilities of the pipeline. Explicit details on specific model parameters for each lens system are shown in the tables of Section 2.4. Our main results can be summarized as follows:

- Our pipeline produces lens models using typically 10 hours of investigator time and 100 hours of CPU time. This is an improvement of many orders of magnitude with respect to studies of individual lenses and comparable to what was achieved by Shajib (2019), but for a larger sample and with less human intervention during the process.

- Based on the pipeline output, we provide for each lens an extensive set of lens model parameters and forecasted properties such as time delays, convergence, and magnification at the location of the images.

- We introduce a new metric to assess the quality of our models, i.e. the stability of the difference in the Fermat potential between multiple images. We demonstrate the usefulness of the metric in assessing the impact of modeling choices and recommend it as convergence/stability indicator in future studies. The factors contributing to the instability of the Fermat potential differences are i) overall information content in the multiple images of the extended sources, ii) symmetry and configuration of the multiple images of the quasars; iii) complexity of the lensing gravitational potential.

- We show that in terms of Fermat potential stability statistical errors are generally subdominant with respect to those induced by modeling choices.

- For a third of the sample (10/30), our pipeline produces models that are cosmography or nearly cosmography grade (i.e. stability in Fermat potential $< 3\%$ or 3-5%). For 6/30 quads, the models have Fermat potential differences stable within 5-10% and could therefore become cosmography grade with some additional effort. In the remaining 14/30 models, the Fermat potential differences are larger than 10%. Further investigations are needed to establish which of those systems could become cosmography grade with additional work based on the current pipeline, which ones will require

extensions of the pipeline, and which ones are instead intrinsically limited by the quality of the data and the lensing configuration.

- For a case study, we apply small perturbations, both upwards and downwards, to the source complexity of a converged model. We find that, as long as the level of source light is sufficiently well represented in our models, a perturbation does not significantly affect the Fermat potential difference between quasar image positions. Our pipeline enables future work to explore this source of potential systematic error automatically for large samples of systems.

Our modeling of an unprecedented large sample of quads is a major step forward in time-delay cosmography. Although further analysis and verification is needed before they can be used for cosmography, these results pave the way to the uniform modeling of large samples of quads (100 or more) that are expected to be discovered in the near future (e.g. Oguri and Marshall, 2010). Further improvements are possible by, both, running the existing pipeline more extensively, or carrying out the steps outlined in Section 2.5.2.

Going forward, the strategic question that needs to be answered for time-delay cosmography is whether to focus on the fraction of lenses that require less work to be modeled or whether it is necessary to tackle more complex systems at the cost of expanding and customizing the modeling pipeline. Up until today, painstaking work on individual lenses has been carried out, owing to a combination of small samples and the invaluable lessons learned from the study of the first few objects. As the samples of lenses increase by orders of magnitude, the strategy will have to adapt to harness the power of large samples (e.g., Sonnenfeld and Cautun, 2021; Sonnenfeld, 2021) and exploit the insights from detailed studies of smaller samples, while keeping the investigator time investment manageable and optimizing the observational resources needed for follow-up. For example, given large samples of lenses it may be preferable to prioritize those systems with expected long time delays (therefore more easily measurable at high precision) and with the main deflector galaxy not

completely overwhelmed by the lensed quasars light (and thus easier to measure spatially resolved kinematics).

Acknowledgements

This research is based on observations made with the NASA/ESA Hubble Space Telescope obtained from the Space Telescope Science Institute, which is operated by the Association of Universities for Research in Astronomy, Inc., under NASA contract NAS 5-26555. These observations are associated with programs HST-GO-15320 and HST-GO-15652. Support for the two programs was provided by NASA through a grant from the Space Telescope Science Institute, which is operated by the Association of Universities for Research in Astronomy, Inc., under NASA contract NAS 5-26555.

TS TT CDF acknowledge support by the the National Science Foundation through grant NSF-AST-1906976 and NSF-AST-1907396 "Collaborative Research: Toward a 1% measurement of the Hubble Constant with gravitational time delays". TT acknowledges support by the Packard Foundation through a Packard Research Fellowship. Support for this work was provided by NASA through the NASA Hubble Fellowship grant HST-HF2-51492 awarded to AJS by the Space Telescope Science Institute, which is operated by the Association of Universities for Research in Astronomy, Inc., for NASA, under contract NAS5-26555.

This programme is in part supported by the Swiss National Science Foundation (SNSF) and by the European Research Council (ERC) under the European Union's Horizon 2020 research and innovation programme (COSMICLENS: grant agreement No 787886). This project has received funding from the European Research Council (ERC) under the European Union's Horizon 2020 research and innovation programme (COSMICLENS : grant agreement No 787886).

The authors acknowledge data and feedback provided by E. Glikman and C.E.Rusu. AA's work is funded by Villum Experiment Grant *Cosmic Beacons* (project number 36225). TA

acknowledges support from FONDECYT Regular 1190335, the Millennium Science Initiative ICN12_009 and the ANID BASAL project FB210003. MWA-W acknowledges support from the Kavli Foundation. CS is supported by an 'Hintze Fellow' at the Oxford Centre for Astrophysical Surveys, which is funded through generous support from the Hintze Family Charitable Foundation. RGM would like to acknowledge the support of the UK Science and Technology Facilities Council (STFC). IK is supported by JSPS KAKENHI Grant Number JP20K04016. VM acknowledges support from project "Fortalecimiento del Sistema de Investigación e Innovación de la Universidad de Valparaíso (UVA20993)". SE, SS and SHS thank the Max Planck Society for support through the Max Planck Research Group for SHS. This research is supported in part by the Excellence Cluster ORIGINS which is funded by the Deutsche Forschungsgemeinschaft (DFG, German Research Foundation) under Germany's Excellence Strategy – EXC-2094 – 390783311.

Funding for the DES Projects has been provided by the U.S. Department of Energy, the U.S. National Science Foundation, the Ministry of Science and Education of Spain, the Science and Technology Facilities Council of the United Kingdom, the Higher Education Funding Council for England, the National Center for Supercomputing Applications at the University of Illinois at Urbana-Champaign, the Kavli Institute of Cosmological Physics at the University of Chicago, the Center for Cosmology and Astro-Particle Physics at the Ohio State University, the Mitchell Institute for Fundamental Physics and Astronomy at Texas A&M University, Financiadora de Estudos e Projetos, Fundação Carlos Chagas Filho de Amparo à Pesquisa do Estado do Rio de Janeiro, Conselho Nacional de Desenvolvimento Científico e Tecnológico and the Ministério da Ciência, Tecnologia e Inovação, the Deutsche Forschungsgemeinschaft and the Collaborating Institutions in the Dark Energy Survey.

The Collaborating Institutions are Argonne National Laboratory, the University of California at Santa Cruz, the University of Cambridge, Centro de Investigaciones Energéticas, Medioambientales y Tecnológicas-Madrid, the University of Chicago, University College London, the DES-Brazil Consortium, the University of Edinburgh, the Eidgenössische Tech-

nische Hochschule (ETH) Zürich, Fermi National Accelerator Laboratory, the University of Illinois at Urbana-Champaign, the Institut de Ciències de l'Espai (IEEC/CSIC), the Institut de Física d'Altes Energies, Lawrence Berkeley National Laboratory, the Ludwig-Maximilians Universität München and the associated Excellence Cluster Universe, the University of Michigan, NSF's NOIRLab, the University of Nottingham, The Ohio State University, the University of Pennsylvania, the University of Portsmouth, SLAC National Accelerator Laboratory, Stanford University, the University of Sussex, Texas A&M University, and the OzDES Membership Consortium.

Based in part on observations at Cerro Tololo Inter-American Observatory at NSF's NOIRLab (NOIRLab Prop. ID 2012B-0001; PI: J. Frieman), which is managed by the Association of Universities for Research in Astronomy (AURA) under a cooperative agreement with the National Science Foundation.

The DES data management system is supported by the National Science Foundation under Grant Numbers AST-1138766 and AST-1536171. The DES participants from Spanish institutions are partially supported by MICINN under grants ESP2017-89838, PGC2018-094773, PGC2018-102021, SEV-2016-0588, SEV-2016-0597, and MDM-2015-0509, some of which include ERDF funds from the European Union. IFAE is partially funded by the CERCA program of the Generalitat de Catalunya. Research leading to these results has received funding from the European Research Council under the European Union's Seventh Framework Program (FP7/2007-2013) including ERC grant agreements 240672, 291329, and 306478. We acknowledge support from the Brazilian Instituto Nacional de Ciência e Tecnologia (INCT) do e-Universo (CNPq grant 465376/2014-2).

This manuscript has been authored by Fermi Research Alliance, LLC under Contract No. DE-AC02-07CH11359 with the U.S. Department of Energy, Office of Science, Office of High Energy Physics.

This research made use of LENSTRONOMY (Birrer and Amara, 2018), EMCEE (Foreman-Mackey et al., 2013), FASTELL (Barkana, 1998), SEXTRACTOR (Bertin and Arnouts, 1996),

NumPy (Harris et al., 2020), SciPy (Virtanen et al., 2020), Astropy (Astropy Collaboration et al., 2018), Jupyter (Kluyver et al., 2016), Matplotlib (Hunter, 2007), seaborn (Waskom, 2021), corner (Foreman-Mackey, 2016), and draw.io at https://www.draw.io.

Data availability

All data underlying this article are publicly available through the *HST* archive.

2.A Photometry of Quasar Images

In Tables 2.14, 2.15, and 2.16, we report the QSO image magnitudes for each successfully modeled lens using the AB system.

2.B Fermat Potential Plots

In this section, we provide in Figures 2.14, 2.15, 2.16, and 2.17 the evolution of the difference in Fermat potential between image positions throughout the lens modeling process, along with the associated evolution of the predicted time delay differences.

2.C Lens Models

In addition to the models shown in Figure 2.6 and in Figure 2.7, this section provides the remaining model plots for the lenses in our sample in Figures 2.18, 2.19, 2.20, 2.21, 2.22, 2.23, and 2.24. The model plot for the failure mode is given in Appendix 2.E.

Table 2.14: Median values for quasar (and, in case of J0343-2828, compact galaxy) image magnitudes in the AB system. The associated uncertainties are statistical in nature and were computed using 84th and 16th percentiles.

Name of Lens	Filter	A	B	C	D
J0029-3814	F475X	$21.601^{+0.004}_{-0.004}$	$22.032^{+0.005}_{-0.005}$	$20.992^{+0.005}_{-0.006}$	$21.829^{+0.003}_{-0.004}$
	F814W	$21.397^{+0.004}_{-0.004}$	$21.816^{+0.002}_{-0.003}$	$20.628^{+0.003}_{-0.003}$	$21.533^{+0.003}_{-0.003}$
	F160W	$21.255^{+0.007}_{-0.005}$	$21.491^{+0.007}_{-0.007}$	$20.373^{+0.007}_{-0.005}$	$21.203^{+0.005}_{-0.005}$
PS J0030-1525	F475X	$22.066^{+0.010}_{-0.009}$	$22.699^{+0.024}_{-0.025}$	$21.836^{+0.009}_{-0.009}$	$22.872^{+0.019}_{-0.017}$
	F814W	$20.779^{+0.007}_{-0.008}$	$20.855^{+0.015}_{-0.016}$	$20.586^{+0.008}_{-0.009}$	$20.661^{+0.012}_{-0.013}$
	F160W	$19.299^{+0.008}_{-0.009}$	$20.142^{+0.031}_{-0.028}$	$19.344^{+0.014}_{-0.015}$	$18.799^{+0.017}_{-0.014}$
DES J0053-2012	F475X	$22.600^{+0.009}_{-0.009}$	$20.600^{+0.002}_{-0.002}$	$20.474^{+0.002}_{-0.002}$	$20.431^{+0.002}_{-0.002}$
	F814W	$21.473^{+0.013}_{-0.011}$	$19.767^{+0.004}_{-0.004}$	$19.651^{+0.004}_{-0.003}$	$19.589^{+0.004}_{-0.004}$
	F160W	$21.415^{+0.010}_{-0.010}$	$19.048^{+0.004}_{-0.003}$	$18.918^{+0.003}_{-0.003}$	$19.016^{+0.004}_{-0.004}$
PS J0147+4630	F475X	$18.681^{+0.001}_{-0.001}$	$17.256^{+0.001}_{-0.001}$	$16.477^{+0.001}_{-0.001}$	$16.712^{+0.001}_{-0.001}$
	F814W	$18.219^{+0.002}_{-0.001}$	$16.495^{+0.001}_{-0.001}$	$15.824^{+0.001}_{-0.001}$	$16.073^{+0.001}_{-0.001}$
	F160W	$18.068^{+0.007}_{-0.006}$	$16.102^{+0.002}_{-0.002}$	$15.376^{+0.001}_{-0.001}$	$15.756^{+0.002}_{-0.002}$
WG0214-2105	F475X	$20.664^{+0.003}_{-0.003}$	$20.603^{+0.004}_{-0.003}$	$20.617^{+0.004}_{-0.004}$	$21.405^{+0.006}_{-0.005}$
	F814W	$20.390^{+0.002}_{-0.002}$	$20.339^{+0.003}_{-0.003}$	$20.517^{+0.006}_{-0.005}$	$21.260^{+0.008}_{-0.006}$
	F160W	$19.874^{+0.004}_{-0.003}$	$19.837^{+0.003}_{-0.003}$	$19.920^{+0.006}_{-0.005}$	$20.601^{+0.006}_{-0.006}$
SDSS J0248+1913	F475X	$21.255^{+0.002}_{-0.002}$	$20.981^{+0.002}_{-0.002}$	$21.005^{+0.002}_{-0.002}$	$21.792^{+0.003}_{-0.004}$
	F814W	$20.405^{+0.002}_{-0.002}$	$20.174^{+0.002}_{-0.001}$	$20.172^{+0.002}_{-0.002}$	$20.715^{+0.006}_{-0.002}$
	F160W	$20.276^{+0.006}_{-0.005}$	$20.056^{+0.008}_{-0.008}$	$20.067^{+0.007}_{-0.007}$	$20.502^{+0.007}_{-0.007}$
WISE J0259-1635	F475X	$21.191^{+0.002}_{-0.002}$	$21.083^{+0.003}_{-0.003}$	$20.493^{+0.003}_{-0.002}$	$20.331^{+0.003}_{-0.003}$
	F814W	$19.731^{+0.004}_{-0.004}$	$19.424^{+0.003}_{-0.003}$	$19.024^{+0.003}_{-0.003}$	$18.747^{+0.003}_{-0.003}$
	F160W	$18.948^{+0.005}_{-0.005}$	$18.756^{+0.003}_{-0.003}$	$18.331^{+0.003}_{-0.003}$	$18.059^{+0.003}_{-0.003}$
J0343-2828	F475X	$24.532^{+0.078}_{-0.057}$	–	–	–
	F814W	$24.166^{+0.100}_{-0.069}$	$21.808^{+0.052}_{-0.045}$	$22.118^{+0.056}_{-0.046}$	$22.452^{+0.069}_{-0.053}$
	F160W	–	–	–	–
DES J0405-3308	F475X	$21.754^{+0.004}_{-0.004}$	$22.473^{+0.005}_{-0.005}$	$21.588^{+0.004}_{-0.004}$	$21.753^{+0.005}_{-0.005}$
	F814W	$19.975^{+0.002}_{-0.002}$	$20.482^{+0.003}_{-0.003}$	$19.863^{+0.003}_{-0.003}$	$20.083^{+0.002}_{-0.003}$
	F160W	$19.675^{+0.012}_{-0.010}$	$19.798^{+0.008}_{-0.009}$	$19.480^{+0.013}_{-0.012}$	$19.883^{+0.013}_{-0.014}$
DES J0420-4037	F475X	$21.779^{+0.006}_{-0.005}$	$19.921^{+0.004}_{-0.004}$	$20.537^{+0.005}_{-0.004}$	$21.562^{+0.005}_{-0.005}$
	F814W	$21.759^{+0.007}_{-0.008}$	$19.917^{+0.004}_{-0.004}$	$20.577^{+0.007}_{-0.008}$	$21.393^{+0.007}_{-0.007}$
	F160W	$21.781^{+0.022}_{-0.019}$	$20.352^{+0.017}_{-0.015}$	$20.738^{+0.025}_{-0.022}$	$22.493^{+0.092}_{-0.066}$

Table 2.15: Median values for quasar (and, in case of J0343-2828, compact galaxy) image magnitudes in the AB system. The associated uncertainties are statistical in nature and were computed using 84th and 16th percentiles.

Name of Lens	Filter	A	B	C	D
DES J0530-3730	F475X	$21.170^{+0.074}_{-0.030}$	$19.076^{+0.010}_{-0.008}$	$20.016^{+0.049}_{-0.056}$	$18.618^{+0.018}_{-0.013}$
	F814W	$21.220^{+0.132}_{-0.135}$	$18.814^{+0.032}_{-0.020}$	$19.030^{+0.041}_{-0.092}$	$18.147^{+0.038}_{-0.013}$
	F160W	–	$19.464^{+0.128}_{-0.093}$	$18.827^{+0.057}_{-0.058}$	$18.671^{+0.060}_{-0.067}$
PS J0630-1201	F475X	$23.477^{+0.023}_{-0.014}$	$21.053^{+0.003}_{-0.003}$	$21.162^{+0.004}_{-0.004}$	$21.218^{+0.005}_{-0.004}$
	F814W	$22.270^{+0.008}_{-0.008}$	$19.960^{+0.002}_{-0.002}$	$20.056^{+0.003}_{-0.003}$	$20.059^{+0.004}_{-0.003}$
	F160W	$21.020^{+0.009}_{-0.007}$	$18.778^{+0.002}_{-0.002}$	$18.692^{+0.002}_{-0.002}$	$18.825^{+0.002}_{-0.002}$
J0659+1629	F475X	$20.757^{+0.004}_{-0.004}$	$20.576^{+0.002}_{-0.002}$	$20.930^{+0.004}_{-0.004}$	$19.273^{+0.002}_{-0.002}$
	F814W	$20.280^{+0.003}_{-0.003}$	$19.985^{+0.002}_{-0.002}$	$20.383^{+0.004}_{-0.003}$	$18.735^{+0.002}_{-0.002}$
	F160W	$19.021^{+0.003}_{-0.003}$	$18.889^{+0.003}_{-0.002}$	$19.276^{+0.004}_{-0.004}$	$17.578^{+0.003}_{-0.002}$
J0818-2613	F475X	$20.876^{+0.003}_{-0.003}$	$21.021^{+0.003}_{-0.003}$	$19.075^{+0.002}_{-0.002}$	$19.254^{+0.002}_{-0.002}$
	F814W	$19.688^{+0.002}_{-0.003}$	$19.890^{+0.003}_{-0.002}$	$17.889^{+0.002}_{-0.003}$	$17.964^{+0.002}_{-0.002}$
	F160W	$18.688^{+0.002}_{-0.002}$	$18.811^{+0.005}_{-0.008}$	$16.887^{+0.002}_{-0.002}$	$16.985^{+0.003}_{-0.004}$
W2M J1042+1641	F475X	–	$22.526^{+0.036}_{-0.031}$	$23.709^{+0.045}_{-0.038}$	–
	F814W	$23.213^{+0.044}_{-0.039}$	$21.611^{+0.015}_{-0.016}$	$23.454^{+0.086}_{-0.074}$	$22.806^{+0.038}_{-0.036}$
	F160W	$21.291^{+0.016}_{-0.014}$	$17.706^{+0.006}_{-0.006}$	$20.344^{+0.017}_{-0.017}$	$20.549^{+0.011}_{-0.013}$
J1131-4419	F475X	$21.252^{+0.006}_{-0.006}$	$21.086^{+0.007}_{-0.007}$	$20.456^{+0.012}_{-0.012}$	$20.242^{+0.005}_{-0.007}$
	F814W	$20.629^{+0.010}_{-0.008}$	$20.782^{+0.023}_{-0.009}$	$20.035^{+0.007}_{-0.008}$	$19.890^{+0.008}_{-0.008}$
	F160W	$20.317^{+0.012}_{-0.014}$	$19.993^{+0.012}_{-0.009}$	$19.420^{+0.012}_{-0.011}$	$19.235^{+0.011}_{-0.012}$
2M1134-2103	F475X	$18.554^{+0.001}_{-0.002}$	$18.577^{+0.001}_{-0.001}$	$18.631^{+0.002}_{-0.002}$	$20.187^{+0.005}_{-0.003}$
	F814W	$17.784^{+0.001}_{-0.001}$	$17.943^{+0.003}_{-0.001}$	$17.826^{+0.001}_{-0.001}$	$19.679^{+0.006}_{-0.013}$
	F160W	$17.116^{+0.002}_{-0.003}$	$17.346^{+0.007}_{-0.003}$	$17.101^{+0.004}_{-0.003}$	$19.238^{+0.015}_{-0.014}$
SDSS J1251+2935	F475X	$21.466^{+0.007}_{-0.007}$	$21.864^{+0.009}_{-0.008}$	$20.169^{+0.007}_{-0.007}$	$19.183^{+0.002}_{-0.002}$
	F814W	$21.439^{+0.004}_{-0.004}$	$21.797^{+0.012}_{-0.012}$	$20.117^{+0.008}_{-0.009}$	$19.143^{+0.004}_{-0.004}$
	F160W	$21.796^{+0.079}_{-0.075}$	$22.027^{+0.165}_{-0.140}$	$20.147^{+0.043}_{-0.045}$	$19.305^{+0.018}_{-0.020}$
2M1310-1714	F475X	$21.719^{+0.026}_{-0.013}$	$20.982^{+0.014}_{-0.024}$	$20.612^{+0.004}_{-0.003}$	$20.670^{+0.012}_{-0.003}$
	F814W	$21.162^{+0.015}_{-0.013}$	$19.748^{+0.003}_{-0.003}$	$19.671^{+0.003}_{-0.003}$	$19.922^{+0.007}_{-0.005}$
	F160W	$21.211^{+0.029}_{-0.016}$	$19.952^{+0.019}_{-0.012}$	$19.422^{+0.008}_{-0.006}$	$20.053^{+0.025}_{-0.011}$
SDSS J1330+1810	F475X	$22.812^{+0.015}_{-0.015}$	$20.890^{+0.013}_{-0.012}$	$21.410^{+0.011}_{-0.010}$	$21.974^{+0.028}_{-0.026}$
	F814W	$21.497^{+0.015}_{-0.015}$	$19.880^{+0.010}_{-0.010}$	$20.169^{+0.009}_{-0.010}$	$20.933^{+0.014}_{-0.015}$
	F160W	$20.266^{+0.017}_{-0.017}$	$19.332^{+0.009}_{-0.009}$	$19.517^{+0.011}_{-0.011}$	$20.235^{+0.017}_{-0.015}$

Table 2.16: Median values for quasar (and, in case of J0343-2828, compact galaxy) image magnitudes in the AB system. The associated uncertainties are statistical in nature and were computed using 84th and 16th percentiles.

Name of Lens	Filter	A	B	C	D
SDSS J1433+6007	F475X	$21.972^{+0.004}_{-0.005}$	$20.095^{+0.001}_{-0.001}$	$20.468^{+0.002}_{-0.002}$	$20.265^{+0.001}_{-0.001}$
	F814W	$21.782^{+0.008}_{-0.011}$	$20.048^{+0.003}_{-0.003}$	$20.365^{+0.004}_{-0.004}$	$20.175^{+0.003}_{-0.003}$
	F160W	$21.793^{+0.012}_{-0.011}$	$20.369^{+0.004}_{-0.004}$	$20.455^{+0.007}_{-0.007}$	$20.518^{+0.004}_{-0.005}$
J1537-3010	F475X	$21.203^{+0.014}_{-0.014}$	$20.954^{+0.007}_{-0.006}$	$21.137^{+0.013}_{-0.014}$	$22.462^{+0.033}_{-0.033}$
	F814W	$21.049^{+0.016}_{-0.015}$	$20.359^{+0.008}_{-0.007}$	$20.743^{+0.014}_{-0.014}$	$21.835^{+0.026}_{-0.023}$
	F160W	$20.263^{+0.026}_{-0.027}$	$20.191^{+0.016}_{-0.014}$	$20.206^{+0.022}_{-0.021}$	$21.551^{+0.051}_{-0.049}$
PS J1606-2333	F475X	$19.524^{+0.004}_{-0.004}$	$19.938^{+0.002}_{-0.002}$	$19.712^{+0.005}_{-0.006}$	$20.249^{+0.004}_{-0.004}$
	F814W	$18.920^{+0.002}_{-0.003}$	$19.410^{+0.004}_{-0.004}$	$19.118^{+0.004}_{-0.004}$	$19.483^{+0.003}_{-0.003}$
	F160W	$19.450^{+0.011}_{-0.010}$	$20.364^{+0.024}_{-0.023}$	$19.830^{+0.014}_{-0.015}$	$19.537^{+0.013}_{-0.013}$
J1721+8842	F475X	$20.837^{+0.004}_{-0.004}$	$20.051^{+0.003}_{-0.003}$	$19.349^{+0.002}_{-0.002}$	$19.951^{+0.003}_{-0.003}$
	F814W	$20.476^{+0.007}_{-0.007}$	$19.196^{+0.003}_{-0.002}$	$18.621^{+0.002}_{-0.002}$	$19.303^{+0.003}_{-0.003}$
	F160W	$20.099^{+0.017}_{-0.017}$	$18.317^{+0.004}_{-0.004}$	$17.783^{+0.005}_{-0.005}$	$18.440^{+0.006}_{-0.007}$
J1817+2729	F475X	$20.796^{+0.005}_{-0.004}$	$22.176^{+0.015}_{-0.014}$	$19.836^{+0.002}_{-0.002}$	$21.492^{+0.007}_{-0.007}$
	F814W	$20.305^{+0.009}_{-0.011}$	$21.133^{+0.015}_{-0.014}$	$19.229^{+0.008}_{-0.008}$	$20.881^{+0.009}_{-0.009}$
	F160W	$18.936^{+0.010}_{-0.009}$	$19.792^{+0.008}_{-0.007}$	$18.111^{+0.008}_{-0.007}$	$19.238^{+0.004}_{-0.004}$
DES J2038-4008	F475X	$21.368^{+0.005}_{-0.005}$	$20.562^{+0.004}_{-0.004}$	$20.524^{+0.003}_{-0.003}$	$20.753^{+0.003}_{-0.003}$
	F814W	$20.567^{+0.010}_{-0.010}$	$19.571^{+0.008}_{-0.009}$	$19.632^{+0.008}_{-0.009}$	$19.770^{+0.007}_{-0.007}$
	F160W	$19.640^{+0.022}_{-0.022}$	$18.559^{+0.018}_{-0.017}$	$18.508^{+0.017}_{-0.016}$	$18.566^{+0.016}_{-0.014}$
WG2100-4452	F475X	$22.158^{+0.008}_{-0.008}$	$21.757^{+0.009}_{-0.009}$	$20.103^{+0.003}_{-0.003}$	$21.028^{+0.008}_{-0.008}$
	F814W	$21.581^{+0.002}_{-0.002}$	$21.240^{+0.003}_{-0.003}$	$19.211^{+0.002}_{-0.002}$	$20.292^{+0.003}_{-0.003}$
	F160W	$22.548^{+0.031}_{-0.028}$	$21.534^{+0.022}_{-0.019}$	$19.485^{+0.007}_{-0.006}$	$20.359^{+0.017}_{-0.018}$
J2145+6345	F475X	$19.384^{+0.002}_{-0.002}$	$19.717^{+0.002}_{-0.003}$	$18.336^{+0.003}_{-0.007}$	$17.872^{+0.001}_{-0.001}$
	F814W	$18.177^{+0.006}_{-0.005}$	$18.551^{+0.006}_{-0.006}$	$17.126^{+0.003}_{-0.003}$	$16.746^{+0.002}_{-0.002}$
	F160W	$17.478^{+0.023}_{-0.026}$	$17.768^{+0.014}_{-0.014}$	$16.314^{+0.010}_{-0.010}$	$15.914^{+0.004}_{-0.004}$
J2205-3727	F475X	$22.513^{+0.013}_{-0.010}$	$22.130^{+0.010}_{-0.010}$	$21.588^{+0.008}_{-0.007}$	$23.103^{+0.015}_{-0.015}$
	F814W	$21.902^{+0.007}_{-0.007}$	$21.554^{+0.007}_{-0.007}$	$21.035^{+0.005}_{-0.005}$	$22.285^{+0.009}_{-0.008}$
	F160W	$22.183^{+0.009}_{-0.008}$	$21.643^{+0.010}_{-0.010}$	$21.222^{+0.011}_{-0.010}$	$22.494^{+0.021}_{-0.018}$
ATLAS J2344-3056	F475X	$22.912^{+0.003}_{-0.004}$	$21.684^{+0.001}_{-0.001}$	$21.031^{+0.001}_{-0.001}$	$21.623^{+0.002}_{-0.002}$
	F814W	$21.835^{+0.007}_{-0.006}$	$21.214^{+0.005}_{-0.004}$	$20.785^{+0.003}_{-0.003}$	$21.281^{+0.004}_{-0.004}$
	F160W	$21.253^{+0.023}_{-0.021}$	$21.097^{+0.016}_{-0.015}$	$20.421^{+0.020}_{-0.018}$	$21.303^{+0.021}_{-0.019}$

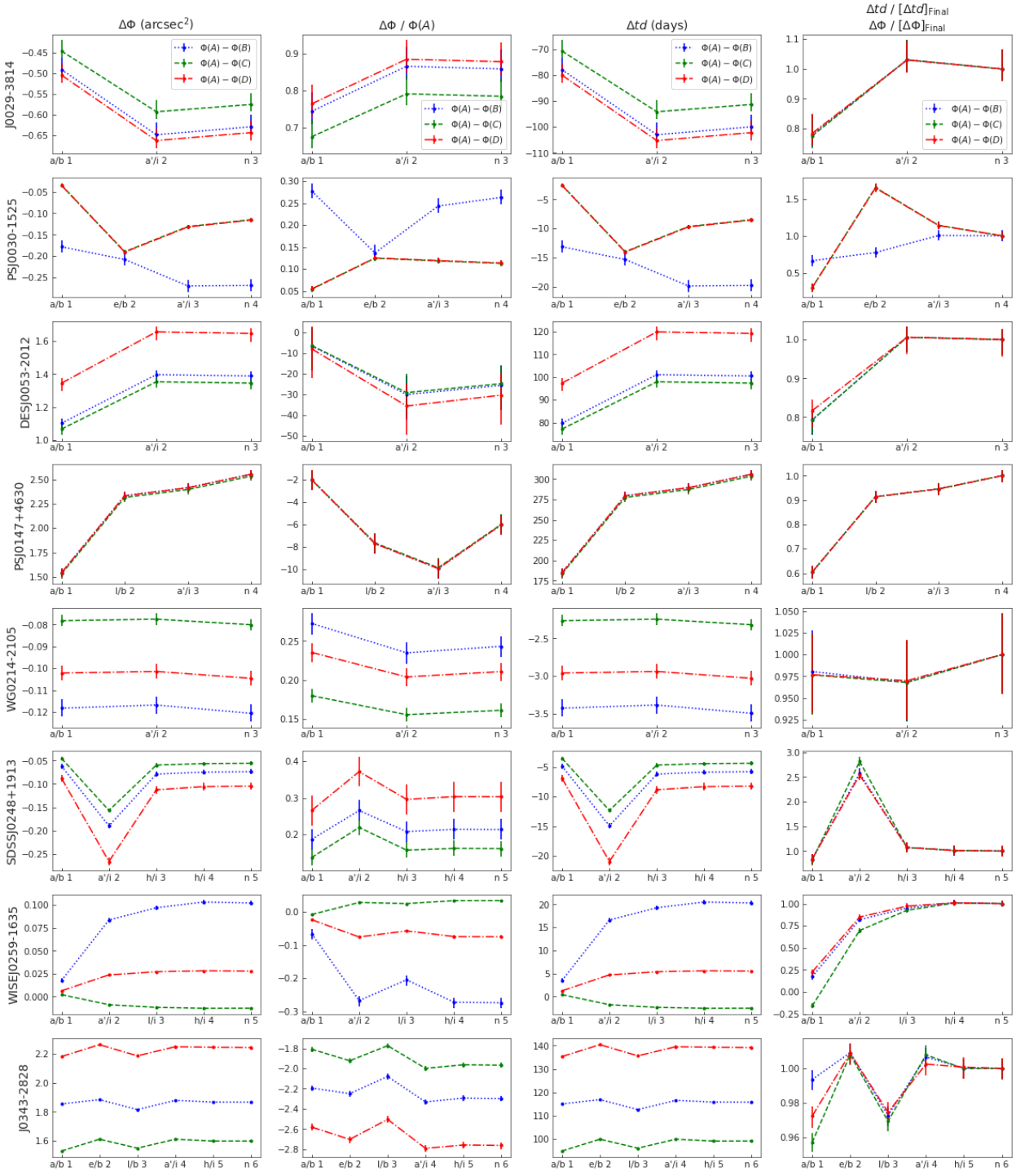

Figure 2.14: Difference in Fermat potential between image positions (column 1) and difference normalized by Fermat potential at image position A (column 2) for lens systems 1 - 8. Also shown are the differences in the predicted time delays between image positions associated with the Fermat potential differences (column 3). Column 4 shows the Fermat potential/time delay differences normalized by the final step in the reconstruction chain. In each plot, the dotted blue lines represent the difference between image A and B, the dashed green lines the difference between image A and C, and the dash-dotted red line the difference between image A and D.

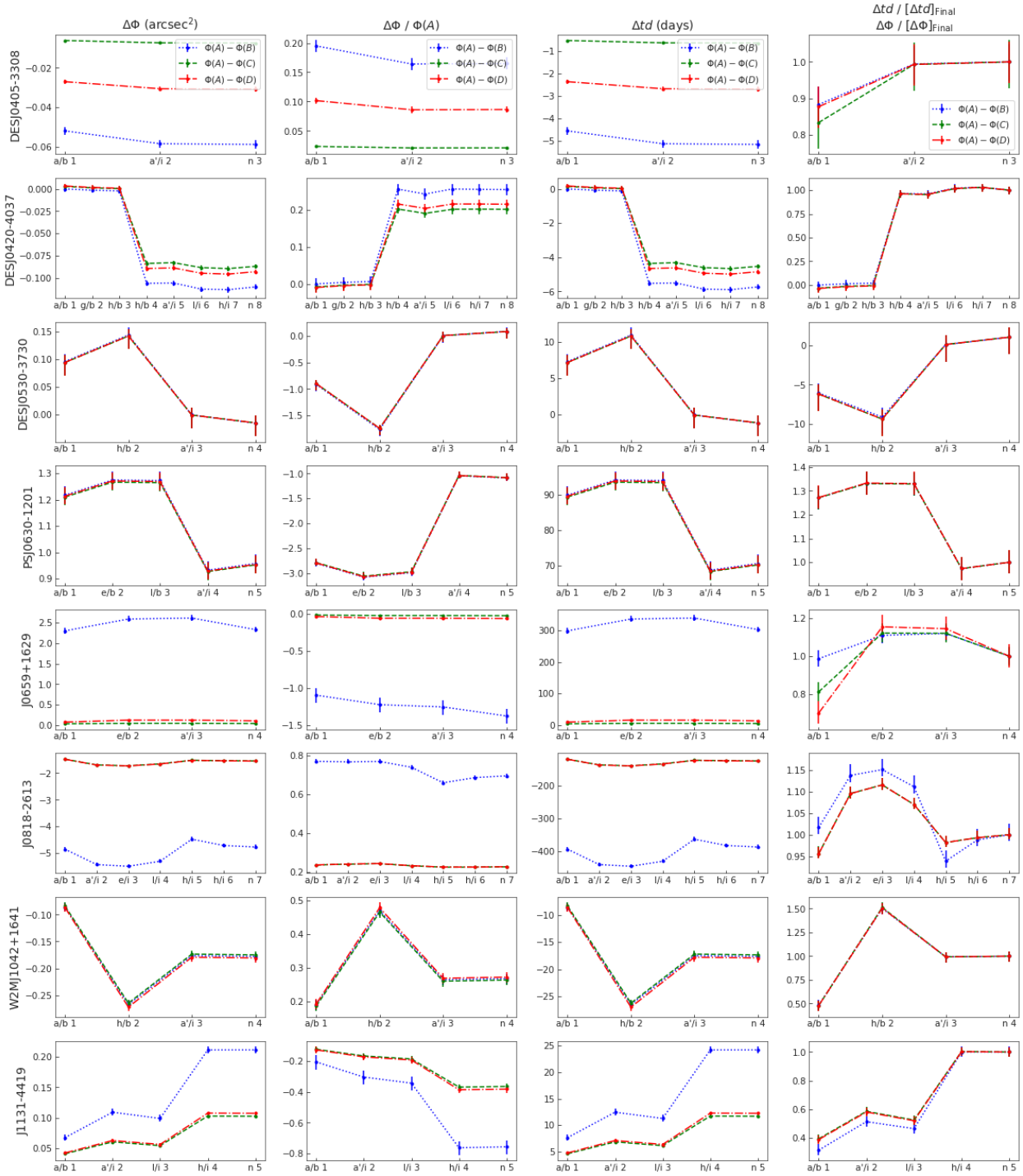

Figure 2.15: Difference in Fermat potential between image positions (column 1) and difference normalized by Fermat potential at image position A (column 2) for lens systems 9 - 16. Also shown are the differences in the predicted time delays between image positions associated with the Fermat potential differences (column 3). Column 4 shows the Fermat potential/time delay differences normalized by the final step in the reconstruction chain. In each plot, the dotted blue lines represent the difference between image A and B, the dashed green lines the difference between image A and C, and the dash-dotted red line the difference between image A and D.

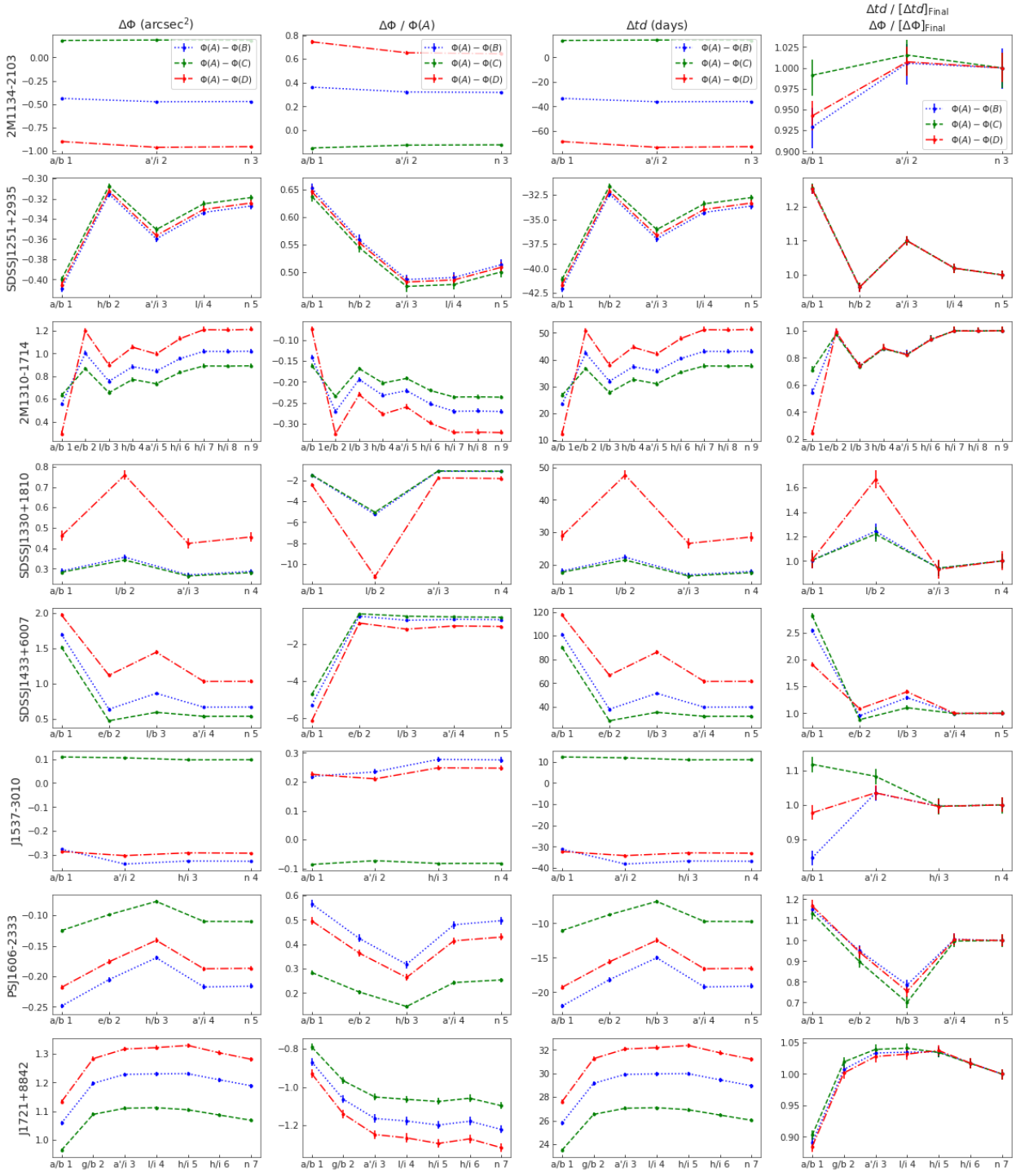

Figure 2.16: Difference in Fermat potential between image positions (column 1) and difference normalized by Fermat potential at image position A (column 2) for lens systems 17 - 24. Also shown are the differences in the predicted time delays between image positions associated with the Fermat potential differences (column 3). Column 4 shows the Fermat potential/time delay differences normalized by the final step in the reconstruction chain. In each plot, the dotted blue lines represent the difference between image A and B, the dashed green lines the difference between image A and C, and the dash-dotted red line the difference between image A and D.

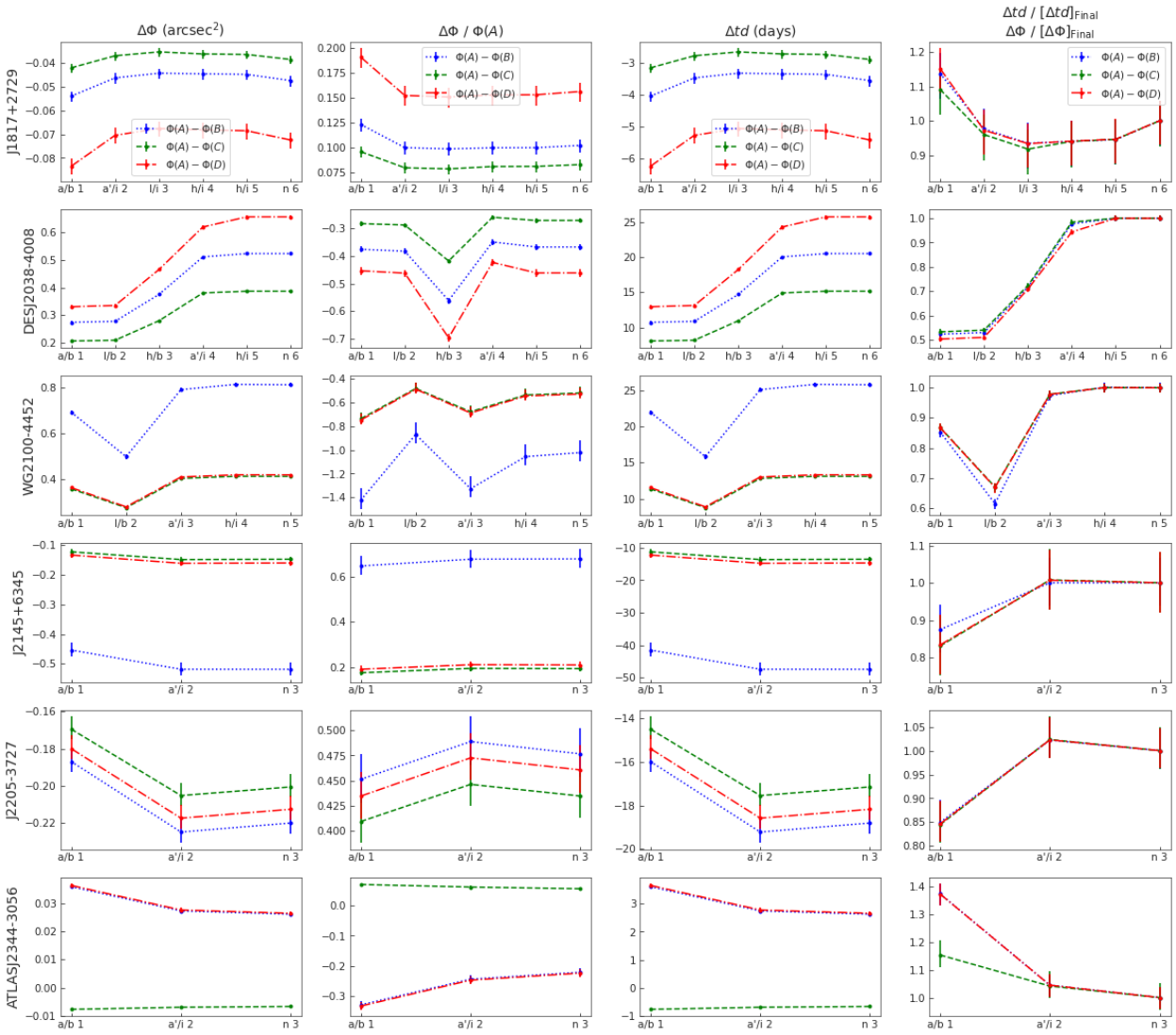

Figure 2.17: Difference in Fermat potential between image positions (column 1) and difference normalized by Fermat potential at image position A (column 2) for lens systems 25 - 30. Also shown are the differences in the predicted time delays between image positions associated with the Fermat potential differences (column 3). Column 4 shows the Fermat potential/time delay differences normalized by the final step in the reconstruction chain. In each plot, the dotted blue lines represent the difference between image A and B, the dashed green lines the difference between image A and C, and the dash-dotted red line the difference between image A and D.

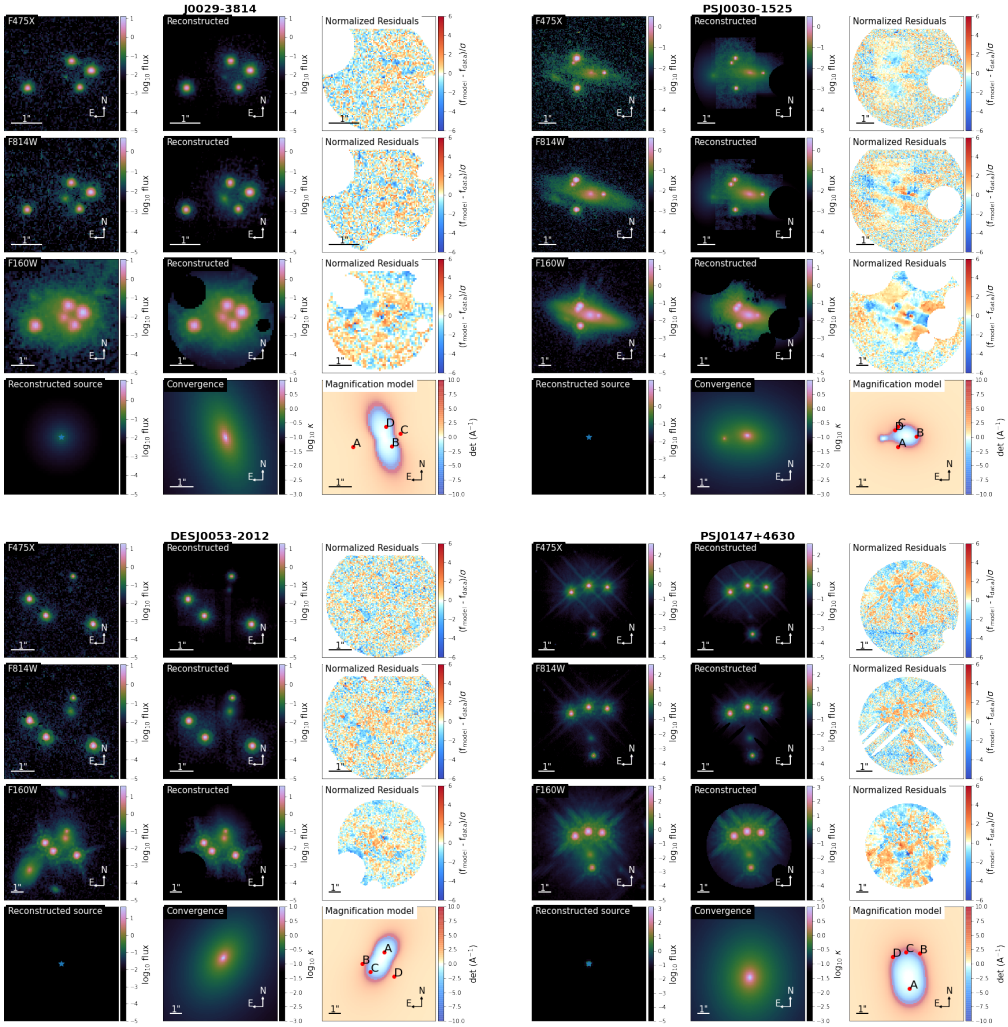

Figure 2.18: Comparison of observations with the reconstructed model for J0029-3814 (top left), PS J0030-1525 (top right), DES J0053-2012 (bottom left), and PS J0147+4630 (bottom right), in *HST* bands F475X (first row), F814W (second row), and F160W (third row). Also shown are the respective normalized residual for each band, after the subtraction of the data from the model. The last row shows the reconstructed source using information from the F160W band (column 1), a plot of the unitless convergence, $\kappa(\theta)$ (column 2), and a model plotting the magnification as well as the position of the lensed quasar images (column 3).

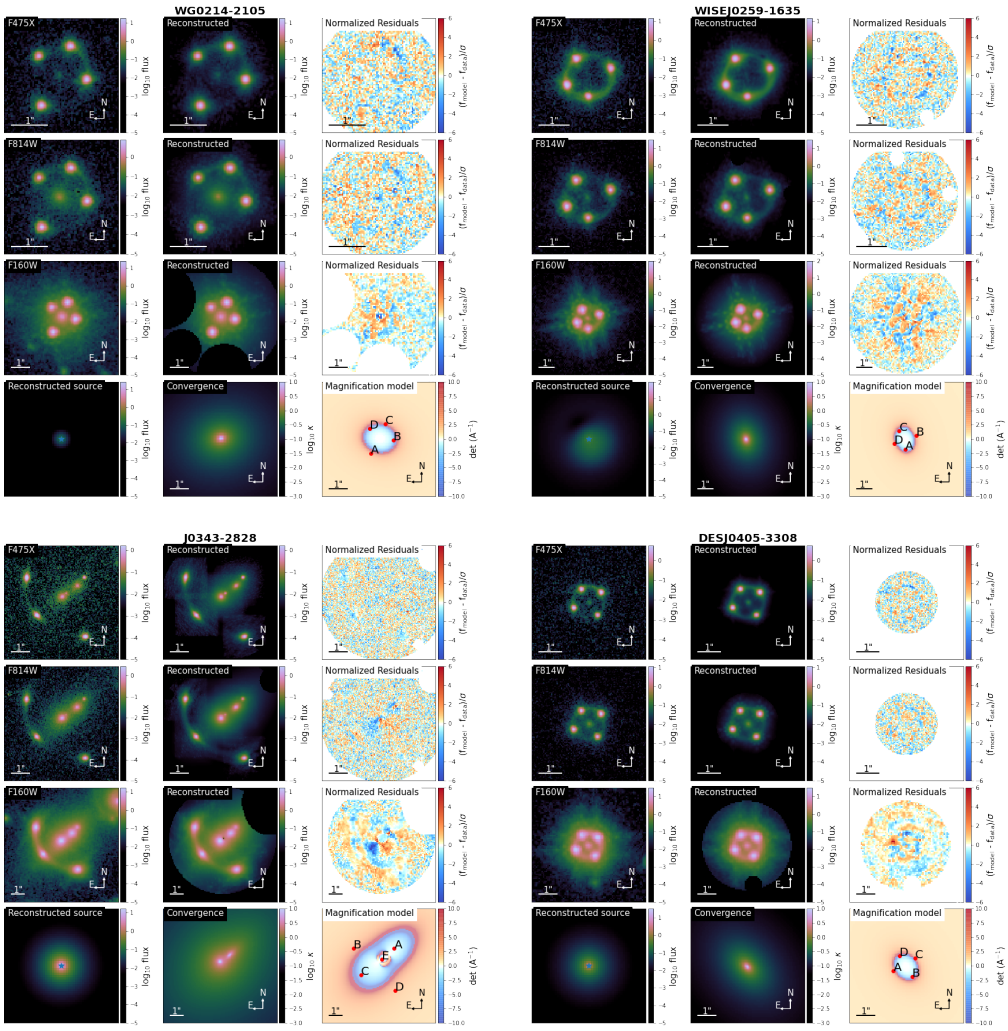

Figure 2.19: Comparison of observations with the reconstructed model for WG0214-2105 (top left), WISE J0259-1635 (top right), J0343-2828 (bottom left), and DES J0405-3308 (bottom right), in *HST* bands F475X (first row), F814W (second row), and F160W (third row). Also shown are the respective normalized residual for each band, after the subtraction of the data from the model. The last row shows the reconstructed source using information from the F160W band (column 1), a plot of the unitless convergence, $\kappa(\theta)$ (column 2), and a model plotting the magnification as well as the position of the lensed quasar images (column 3).

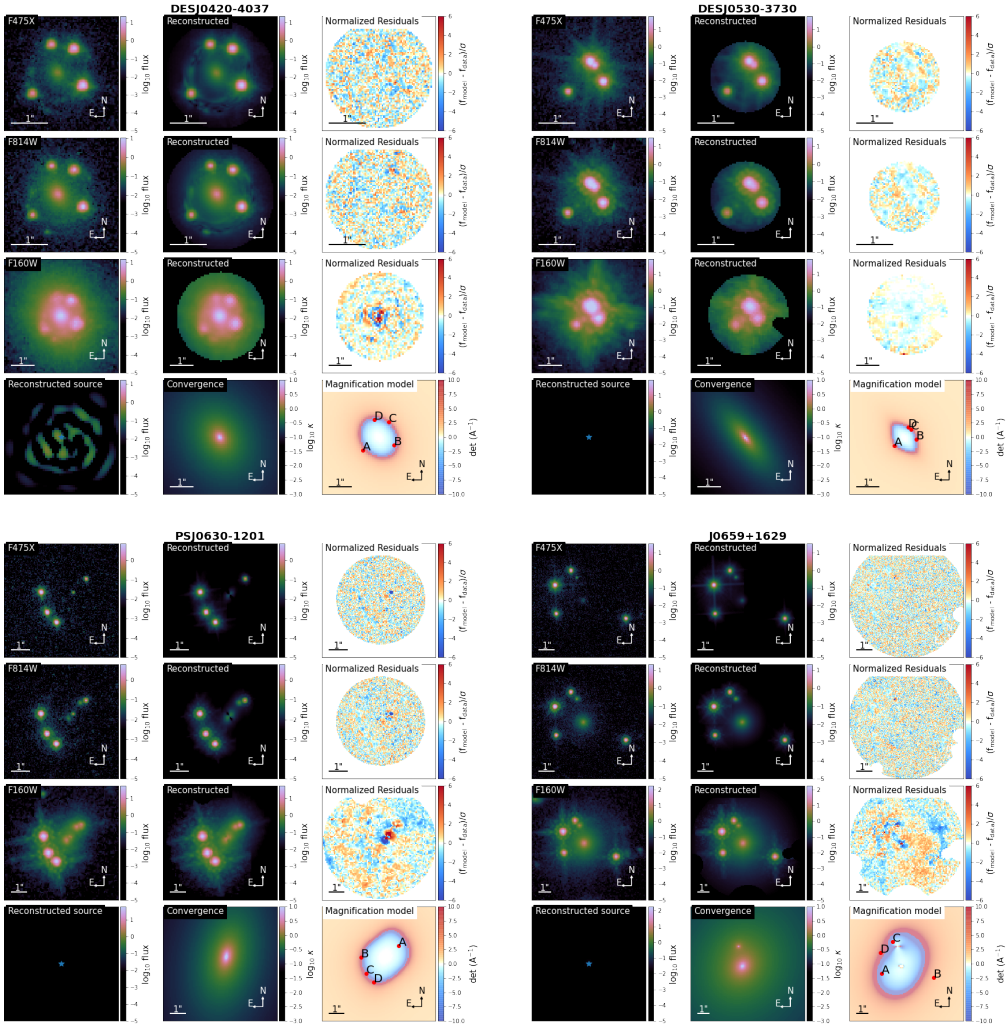

Figure 2.20: Comparison of observations with the reconstructed model for DES J0420-4037 (top left), DES J0530-3730 (top right), PS J0630-1201 (bottom left), and J0659+1629 (bottom right), in *HST* bands F475X (first row), F814W (second row), and F160W (third row). Also shown are the respective normalized residual for each band, after the subtraction of the data from the model. The last row shows the reconstructed source using information from the F160W band (column 1), a plot of the unitless convergence, $\kappa(\theta)$ (column 2), and a model plotting the magnification as well as the position of the lensed quasar images (column 3).

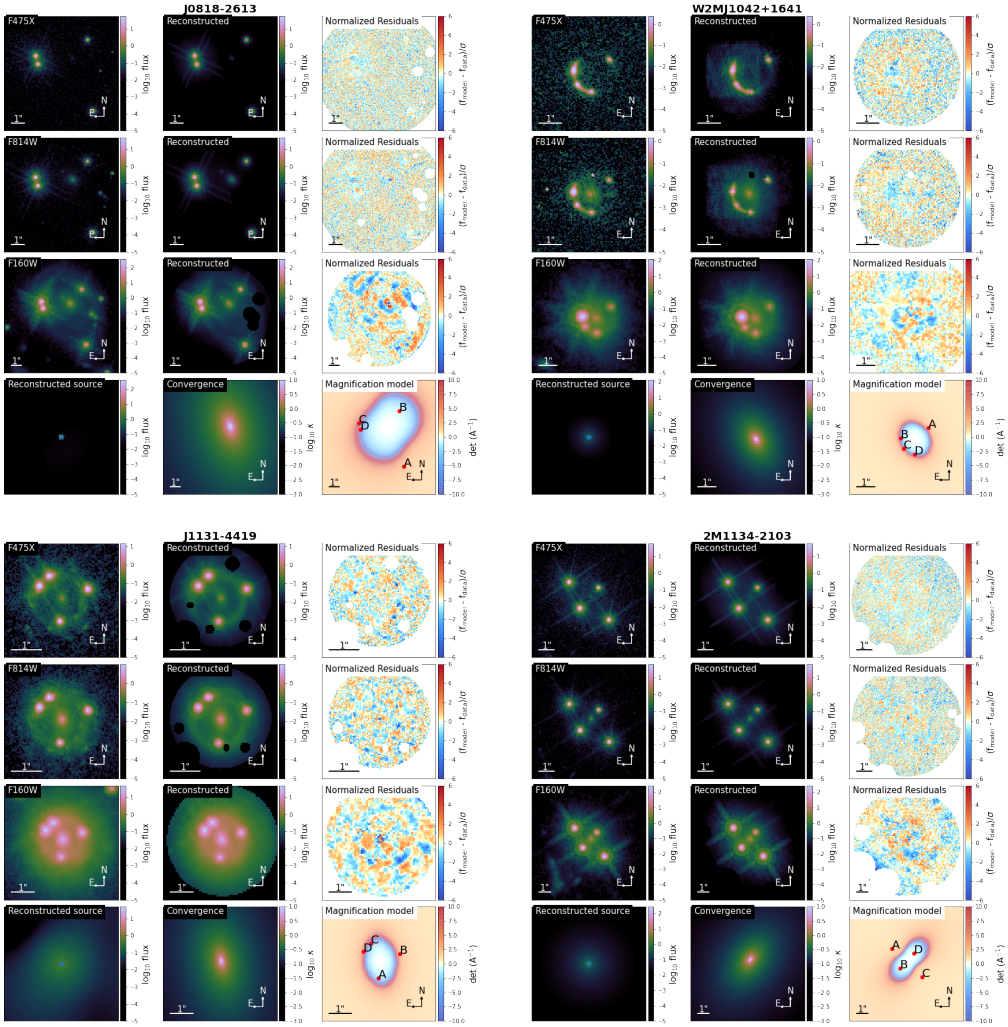

Figure 2.21: Comparison of observations with the reconstructed model for J0818-2613 (top left), W2M J1042+1641 (top right), J1131-4419 (bottom left), and 2M1134-2103 (bottom right), in *HST* bands F475X (first row), F814W (second row), and F160W (third row). Also shown are the respective normalized residual for each band, after the subtraction of the data from the model. The last row shows the reconstructed source using information from the F160W band (column 1), a plot of the unitless convergence, $\kappa(\theta)$ (column 2), and a model plotting the magnification as well as the position of the lensed quasar images (column 3).

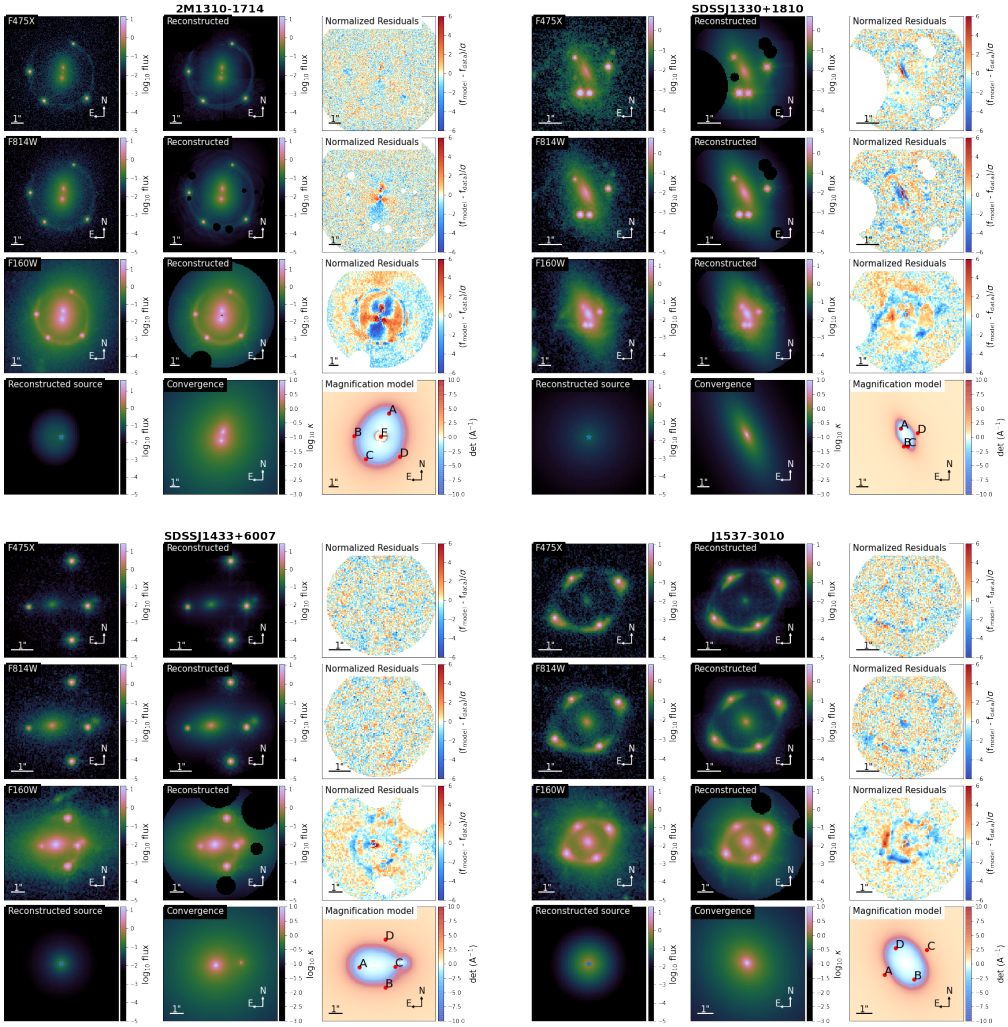

Figure 2.22: Comparison of observations with the reconstructed model for 2M1310-1714 (top left), SDSS J1330+1810 (top right), SDSS J1433+6007 (bottom left), and J1537-3010 (bottom right), in *HST* bands F475X (first row), F814W (second row), and F160W (third row). Also shown are the respective normalized residual for each band, after the subtraction of the data from the model. The last row shows the reconstructed source using information from the F160W band (column 1), a plot of the unitless convergence, $\kappa(\theta)$ (column 2), and a model plotting the magnification as well as the position of the lensed quasar images (column 3).

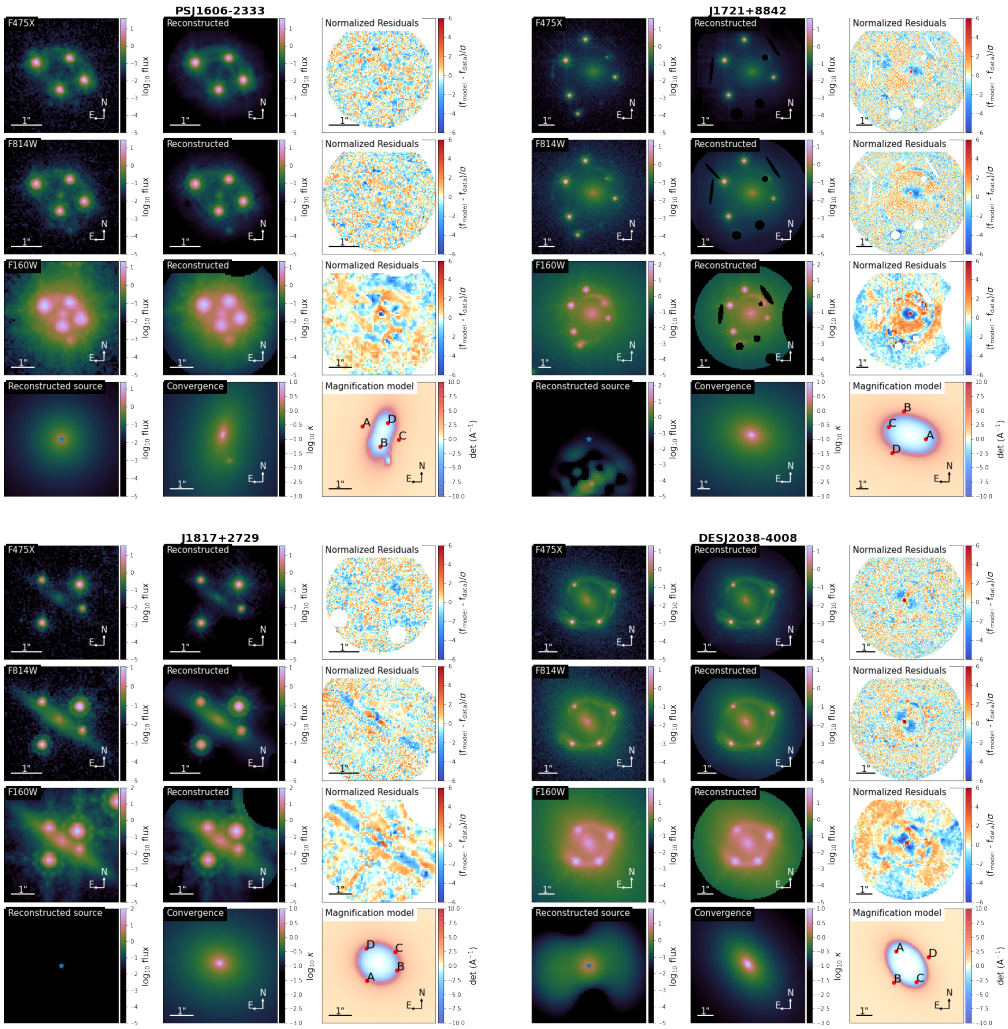

Figure 2.23: Comparison of observations with the reconstructed model for PS J1606-2333 (top left), J1721+8842 (top right), J1817+2729 (bottom left), and DES J2038-4008 (bottom right), in *HST* bands F475X (first row), F814W (second row), and F160W (third row). Also shown are the respective normalized residual for each band, after the subtraction of the data from the model. The last row shows the reconstructed source using information from the F160W band (column 1), a plot of the unitless convergence, $\kappa(\theta)$ (column 2), and a model plotting the magnification as well as the position of the lensed quasar images (column 3).

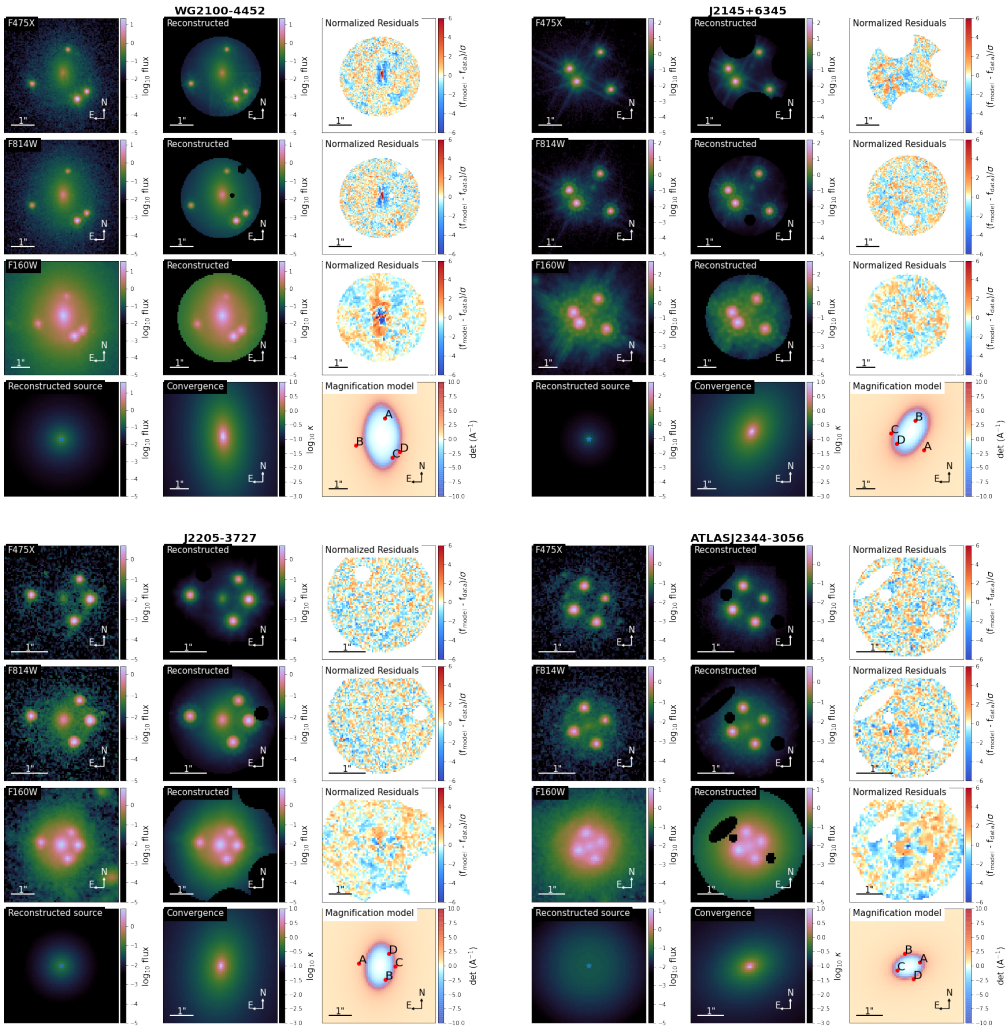

Figure 2.24: Comparison of observations with the reconstructed model for WG2100-4452 (top left), J2145+6345 (top right), J2205-3727 (bottom left), and ATLAS J2344-3056 (bottom right), in *HST* bands F475X (first row), F814W (second row), and F160W (third row). Also shown are the respective normalized residual for each band, after the subtraction of the data from the model. The last row shows the reconstructed source using information from the F160W band (column 1), a plot of the unitless convergence, $\kappa(\theta)$ (column 2), and a model plotting the magnification as well as the position of the lensed quasar images (column 3).

2.D Case study corner plot

In this section, we provide a corner plot to illustrate distribution of the lens mass and lens light parameters for system SDSS J0248+1913, used in the case study of Section 2.4.5.1 and Section 2.5.1. The blue dashed line in the 1-d posterior distribution of the power-law slope, γ, represents the informative prior placed on the main deflector's mass density profile, as described in Section 2.3.3.

2.E Failure modes

Our pipeline failed to produce a model for DES J0408-5354 with a sufficiently large p-vlaue or a χ^2-value below the threshold of 1.10. The main reason for the failure is the secondary lensed source, which has a different redshift than the primary primary lensed source that holds the QSO (see Shajib et al., 2020). As the pipeline in its current form is limited to a single source plane, the two lensed sources are modeled to be at the same redshift (or in the same plane), causing the secondary source to appear slightly offset in the lens plane. This can be seen in the NW residuals, particularly visible in the UVIS bands. A model plot of the lens reconstruction using the final PSO iteration is included in Figure 2.26.

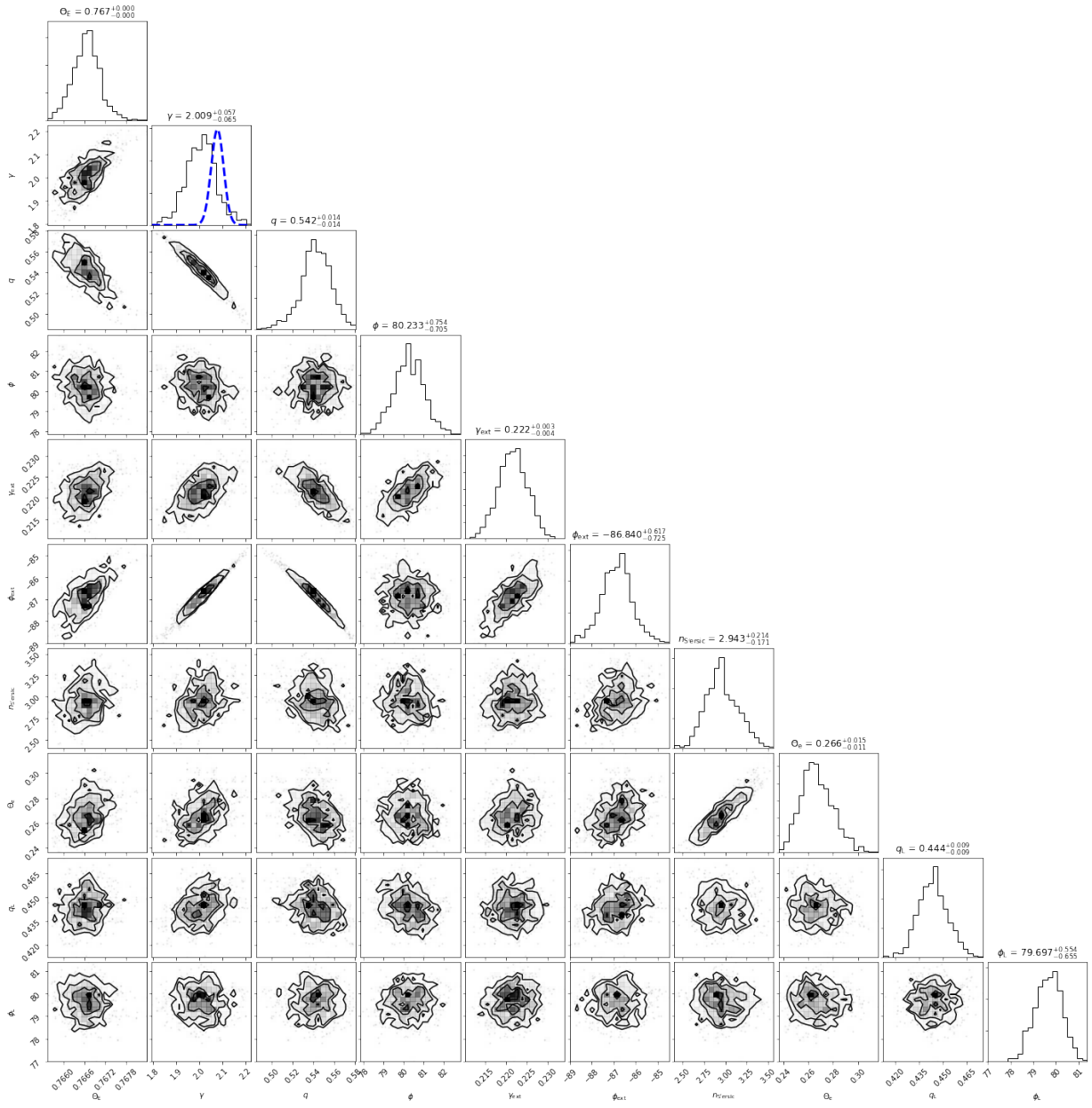

Figure 2.25: Corner plot, illustrating the distribution of lens mass and lens light parameters for system SDSS J0248+1913. The blue dashed line in the posterior distribution of the power-law slope, γ, represents the informative prior placed on the main deflector's mass density profile (see Section 2.3.3).

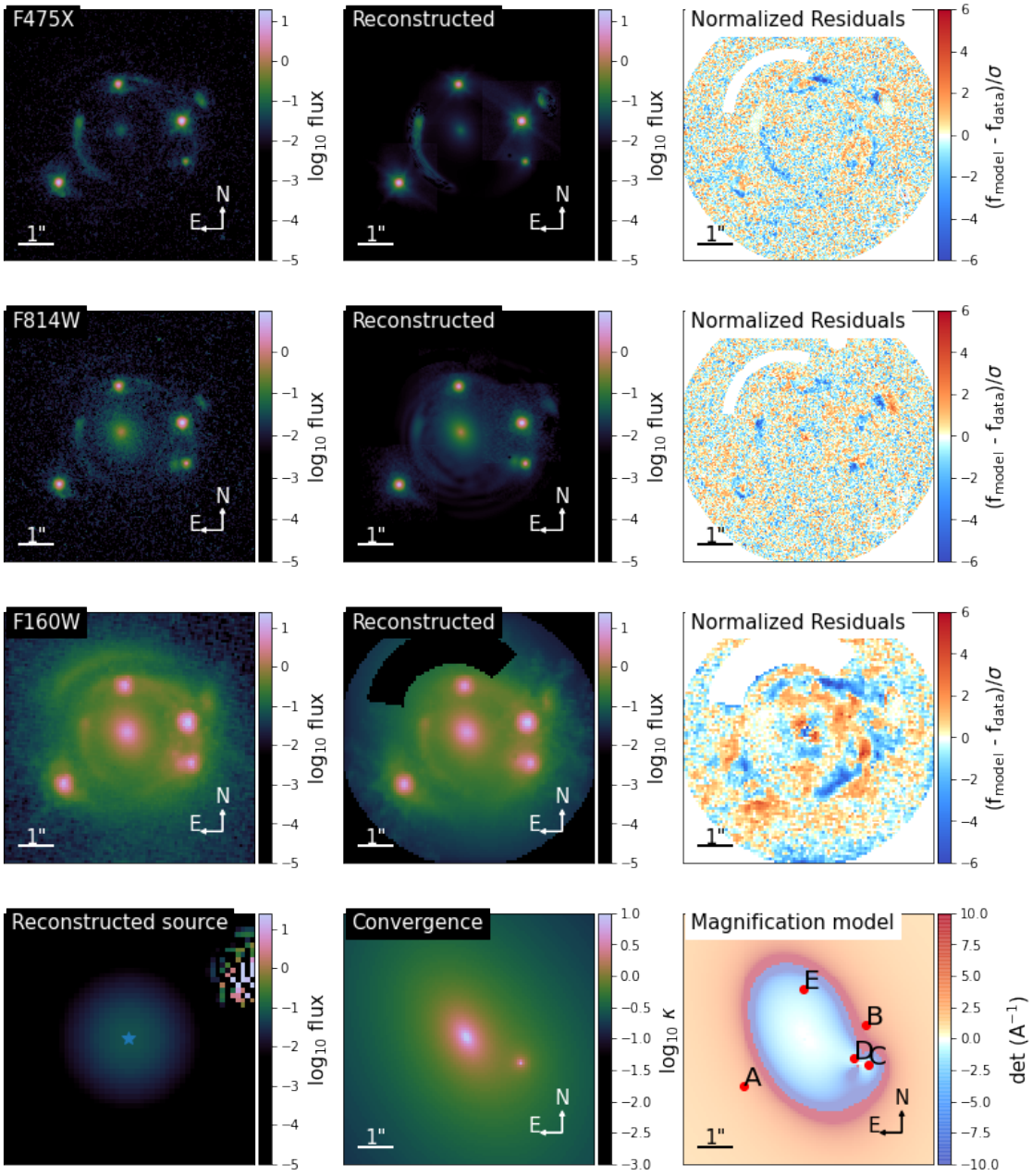

Figure 2.26: Comparison of observations with the reconstructed model for DES J0408-5354 in *HST* bands F475X (first row), F814W (second row), and F160W (third row). Also shown are the respective normalized residual for each band, after the subtraction of the data from the model. The last row shows the reconstructed source using information from the F160W band (column 1), a plot of the unitless convergence, $\kappa(\theta)$ (column 2), and a model plotting the magnification as well as the position of the lensed quasar images (column 3).

Chapter 3

Cosmography grade model and time-delay prediction for the extraordinary gravitational lens J1721+8842

3.1 Background

The Hubble constant H_0, the current expansion rate of the Universe, is a quantity of fundamental importance in the current cosmological debate. The standard cosmological model, based on Cold Dark Matter (CDM) and a cosmological constant Λ (hence ΛCDM), successfully matches a range of observations including the cosmic microwave background (CMB) radiation, the Big Bang nucleosynthesis, baryon acoustic oscillations (BAO), galaxy clustering and the formation of large scale structures, and measurements of Type Ia supernovae distances (e.g. Riess et al., 1998; Perlmutter et al., 1999; Eisenstein et al., 2005; Planck Collaboration et al., 2020). Yet, in flat ΛCDM there is an increasing tension between the Hubble constant inferred from early universe constraints and direct measurements using local uni-

verse probes. For example, the analysis of anisotropies in the CMB result in $H_0 = 67.4 \pm 0.5$ km s^{-1} Mpc^{-1} (Planck Collaboration et al., 2020) in flat ΛCDM, whereas local measurements based on Cepheid variables and Type Ia supernovae (SNIa) as rungs in the cosmic distance ladder result in $H_0 = 73.04 \pm 1.04$ km s^{-1} Mpc^{-1} (Riess et al., 2022). The difference results in a tension of high statistical significance (see, e.g., Abdalla et al., 2022, and references therein). If independent methods confirm the tension is not caused by unknown systematic uncertainties in the measurements, then new physics beyond flat ΛCDM model is required. Examples of proposed solution include changing the sound horizon at recombination through a currently unknown relativistic particle or a form of early dark energy (see e.g. Knox and Millea, 2020; Di Valentino et al., 2021; Schöneberg et al., 2022; Vagnozzi, 2023).

Strong gravitational lensing of a variable background source provides a powerful independent cosmological probe through which the Hubble constant can be measured in one step, bypassing the local distance ladder (Refsdal, 1964; Treu and Marshall, 2016; Treu et al., 2022; Treu and Shajib, 2024; Birrer et al., 2024). Instead of relying on standard candles, strong lensing measures distances (and therefore H_0) from the differences in the travel time of photons traversing the gravitational potential of the foreground deflector (see e.g. Treu and Koopmans, 2002; Suyu et al., 2010, 2014; Treu and Marshall, 2016; Birrer et al., 2016; Bonvin et al., 2017; Birrer et al., 2019; Shajib et al., 2020).

Several key components are required for a precise determination of the Hubble constant using galaxy-scale strong gravitational lensing time-delays: (a) high-resolution observations of the target and nearby environment with a high signal-to-noise ratio, preferably in multiple filters, to model the gravitational potential of the system and to determine the difference in the Fermat potential between the image positions of the lensed quasar; (b) light curves sufficient for high-precision time-delay measurements for the lensed images; (c) redshifts for the lensed sources, the primary deflector, and all perturbing galaxies that need to be included in the model of the system, (d) a spectroscopic stellar velocity dispersion measurement of the main deflector to break the mass sheet degeneracy, (e) multi-band photometric catalogs

to estimate the external convergence due to mass distribution along the line-of-sight.

We present models for the exceptionally complex gravitational lens system J1721+8842 (see Lemon et al., 2018, for discovery), which consists of two separately lensed quasars, resulting in a total of six quasar images, in addition to at least two other multiply imaged sources. This configuration of lensed background sources proves truly remarkable as it not only places tight constraints on the distribution of mass in the primary deflector, but compared to typical quadruply lensed quasars the system also provides a valuable additional image pair, and thus the potential to measure two independent sets of delays. The estimated percent level uncertainty of our time-delay predictions shows the tremendous potential of multi-source systems for cosmography (see Shajib et al., 2020, for a prior example that did not have two distinct lensed quasars and yet reached total 3.9% precision on H_0).

We concentrate on robust lens modeling and time-delay predictions for the images of the two lensed quasars as a necessary first step for a comprehensive cosmographic inference of the Hubble constant. Once ongoing monitoring campaigns provide observed delays, a stellar velocity dispersion measurement, and an estimate for the external convergence, the combination with our model will enable the measurement of H_0. We note that previous work has typically followed the reverse order with a lens model being the final step (notable exceptions are the work by Shajib et al., 2022; Chen et al., 2022). For the purpose of determining H_0 of course the order does not matter, and blindness can be imposed either way, in order to prevent unconscious experimenter bias.

This chapter is organized as follows. Section 3.2 summarizes the theoretical background of strong gravitational lensing, discuss strong lens observables, and reviews the formal notation for the Bayesian framework used in our inference of time-delay predictions. Section 3.3 describes the discovery of J1721+8842, the imaging of the target, and the data reduction. Section 3.4 discusses the individual components of our lens models and provides details on the parameterizations used in our analysis, including informative priors implemented to guide the results and the assessment of systematic uncertainties in the underlying choices

for lens model components. The results of our analysis are presented in Section 3.5 along with measurable time-delay predictions between images pairs of the two lensed quasars. Finally, Section 3.6 provides a brief summary. Whenever necessary, we use a cosmological concordance model with parameters $H_0 = 70$ km s^{-1} Mpc^{-1}, $\Omega_{\mathrm{m},0} = 0.3$, and $\Omega_{\Lambda,0} = 0.7$.

3.2 Modeling Analysis

Our analysis uses Hubble Space Telescope (*HST*) imaging data, $\boldsymbol{d}_{HST}$, in three bands, UVIS (F475X and F814W) as well as IR (F160W), to make an inference on the lensing potential, ψ, for J1721+8842 and on the position of the lensed sources, β. In addition to parameters for the mass model of the lens, ξ_{mass}, the *HST* observations further allow us to obtain constraints on the parameterization of the surface brightness distribution for the primary deflector, ξ_{light}, and for the lensed sources, ξ_{source}.

In terms of organization, this section first gives a description of the strong lensing formalism and describes how our models connect to observables, presented in Section 3.2.1. We then discuss lensing degeneracies and potential sources of systematic uncertainties in Section 3.2.2, while Section 3.2.3 outlines the formal notation of the Bayesian inference used in our analysis.

3.2.1 Lensing Theory and Strong-lensing Observables

Compared to a path without perturbation, the excess time-delay (see e.g. Schneider et al., 1992; Blandford and Narayan, 1992) for a lensed point source at position $\boldsymbol{\beta} = (\beta_1, \beta_2)$ in the source plane, observed at angular position $\boldsymbol{\theta} = (\theta_1, \theta_2)$ in the lens (or image) plane, is described by

$$t(\boldsymbol{\theta}; \boldsymbol{\beta}) = \frac{D_{\Delta t}}{c} \left[\frac{(\boldsymbol{\theta} - \boldsymbol{\beta})^2}{2} - \psi(\boldsymbol{\theta}) \right], \tag{3.1}$$

where c is the speed of light, $\psi(\boldsymbol{\theta})$ represents the deflection potential of the lens, and whereby

the timedelay distance, $D_{\Delta t}$, is defined as

$$D_{\Delta t} \equiv (1 + z_{\rm d}) \frac{D_{\rm d} D_{\rm s}}{D_{\rm ds}}, \tag{3.2}$$

with $D_{\rm d}$, $D_{\rm s}$, and $D_{\rm ds}$, as the angular diameter distance to the main deflector, to the lensed source, and between the source and the deflector, respectively. $z_{\rm d}$ represents the redshift of the lensing galaxy.

The delay in the arrival time of photons emitted by the same source, but observed at two different positions in the image plane, $\boldsymbol{\theta}_{\rm A}$ and $\boldsymbol{\theta}_{\rm B}$, can then be expressed as

$$\Delta t_{\rm AB} = \frac{D_{\Delta t}}{c} \Delta \phi_{\rm AB}, \tag{3.3}$$

where $\Delta \phi_{\rm AB}$ is the difference in the Fermat potential, $\phi(\boldsymbol{\theta_{\rm A}; \beta}) - \phi(\boldsymbol{\theta_{\rm B}; \beta})$, between the two image positions, with the Fermat potential defined as

$$\phi(\boldsymbol{\theta; \beta}) = \frac{1}{2}(\boldsymbol{\theta - \beta})^2 - \psi(\boldsymbol{\theta}). \tag{3.4}$$

With that definition

$$\Delta \phi_{\rm AB}(\boldsymbol{\theta_{\rm A}; \theta_{\rm B}; \beta}) = \frac{1}{2}\left[(\boldsymbol{\theta_{\rm A} - \beta})^2 - (\boldsymbol{\theta_{\rm B} - \beta})^2\right] - \left[\psi(\boldsymbol{\theta_{\rm A}}) - \psi(\boldsymbol{\theta_{\rm B}})\right], \tag{3.5}$$

where the first difference is the geometric term as the result of the light traversing paths of different lengths due to different deflection angles at the corresponding image positions, while the second term describes the difference in the gravitational delay photons experience while traveling through the potential of the lensing galaxy.

The deflection angle, $\boldsymbol{\alpha}(\boldsymbol{\theta})$, at an image position, $\boldsymbol{\theta}$, can be expressed as the gradient of the deflection potential, $\boldsymbol{\alpha}(\boldsymbol{\theta}) = \nabla \psi(\boldsymbol{\theta})$, and is dictated by the lens equation, $\boldsymbol{\beta} = \boldsymbol{\theta} - \boldsymbol{\alpha}(\boldsymbol{\theta})$, which describes the lensing of a source at position $\boldsymbol{\beta}$ by the deflection potential, $\psi(\boldsymbol{\theta})$. In the limit of the deflector mass being confined to a two-dimensional sheet (the lens plane) with a

physical projected surface mass density, $\Sigma(\boldsymbol{\theta})$, (the thin lens approximation), the deflection angle is related to the dimensionless projected surface mass density, or convergence, κ, by

$$\kappa(\boldsymbol{\theta}) = \frac{1}{2}\boldsymbol{\nabla} \cdot \boldsymbol{\alpha}(\boldsymbol{\theta}), \tag{3.6}$$

where $\kappa(\boldsymbol{\theta})$ is defined as the surface mass density scaled by the critical surface mass density, $\kappa(\boldsymbol{\theta}) \equiv \Sigma(\boldsymbol{\theta})/\Sigma_{\rm cr}$, with

$$\Sigma_{\rm cr} = \frac{c^2}{4\pi G}\frac{D_{\rm s}}{D_{\rm d}D_{\rm ds}}. \tag{3.7}$$

Therefore, the dimensionless convergence is related to the deflection potential of the lensing galaxy by

$$\kappa(\boldsymbol{\theta}) = \frac{1}{2}\nabla^2\psi(\boldsymbol{\theta}). \tag{3.8}$$

High-resolution observations, taken with the Hubble Space Telescope, allow us to constrain the deflections potential, ψ, along with the unknown position of the lensed source, $\boldsymbol{\beta}$, by constructing models that match the lensed positions of a multiply imaged background quasar. Furthermore, if the source galaxy hosting the lensed quasar is bright and spatially extended, the arc of the lensed background source provide additional constraint to distribution of the lensing potential. Together with measured time-delays, Δt, for the image positions, the Fermat potential difference between two images is used to infer the time-delay distance, $D_{\Delta t}$, which is inversely proportional to the Hubble constant, $D_{\Delta t} \propto H_0^{-1}$.

3.2.2 Lensing Degeneracies

Strong gravitational lens models suffer from a number of well known parameter degeneracies, whereby various combinations of distinct parameters produce different models that fit the observed data (see, e.g. Saha, 2000; Saha et al., 2006). One of the fundamental degeneracies in strong lens modeling is the mass sheet degeneracy (MSD) (see, e.g. Falco et al., 1985;

Schneider and Sluse, 2014), which refers to the fact that a model's convergence, κ, can be transformed by a constant factor, λ, such that observable quantities like image positions and flux ratios remain unchanged if the unknown source position, β, is re-scaled by the same factor, i.e.

$$\begin{aligned} \kappa_\lambda(\boldsymbol{\theta}) &= \lambda\kappa(\boldsymbol{\theta}) + (1-\lambda), \\ \boldsymbol{\beta}_\lambda &= \lambda\boldsymbol{\beta}. \end{aligned} \tag{3.9}$$

Mathematically, this mass sheet transformation (MST) corresponds to an addition of a uniform sheet of mass that changes the convergence term, but not the shear, while simultaneously re-scaling the angular distances.

It should be noted that the true physical convergence of the lens system, $\kappa_{\rm phys}(\boldsymbol{\theta})$, has two main components, namely the convergence associated with the primary deflector and neighboring galaxies, $\kappa_{\rm int}(\boldsymbol{\theta})$, thereby influencing the stellar kinematics of the lens galaxy, as well as an external convergence, $\kappa_{\rm ext}$, physically associated with the perturbation from line-of-sight structure, meaning

$$\kappa_{\rm phys}(\boldsymbol{\theta}) = \kappa_{\rm int}(\boldsymbol{\theta}) + \kappa_{\rm ext}. \tag{3.10}$$

However, the spatial extent of the lens galaxy, and with it the gravitational influence, is limited; therefore the convergence intrinsically associated with the main deflector is physically constrained to a certain radial span. In other words, the internal convergence vanishes at large radii, i.e. $\lim_{\boldsymbol{\theta}\to\infty}\kappa_{\rm int}(\boldsymbol{\theta}) = 0$, which implies that at a large distance away from the primary perturber the total physical convergence of the system is attributed entirely to the external convergence, i.e. $\lim_{\boldsymbol{\theta}\to\infty}\kappa_{\rm phys}(\boldsymbol{\theta}) = \kappa_{\rm ext}$.

Now, the convergence of any lens model, $\kappa_{\rm lens}(\boldsymbol{\theta})$, can itself be thought of as a transformation of the lens system's physical convergence, $\kappa_{\rm phys}(\boldsymbol{\theta})$, so

$$\kappa_{\rm lens}(\boldsymbol{\theta}) = \lambda\kappa_{\rm phys}(\boldsymbol{\theta}) + (1-\lambda). \tag{3.11}$$

During the modeling of the primary lens, however, the line-of-sight contribution to the convergence is commonly omitted, which means the convergence of the lens model, $\kappa_{\rm lens}(\boldsymbol{\theta})$, does not include the external convergence term, $\kappa_{\rm ext}$. Therefore, if we combine Expression 3.10 with Expression 3.11, then in the limit of $\boldsymbol{\theta} \to \infty$, we have $0 = \lambda(0 + \kappa_{\rm ext}) + (1-\lambda)$, which arranged for λ, simplifies to

$$\lambda = \frac{1}{1-\kappa_{\rm ext}}. \tag{3.12}$$

We can now use Expression 3.12 together with Expression 3.10 in Expression 3.11 to arrive at

$$\kappa_{\rm lens}(\boldsymbol{\theta}) = \frac{1}{1-\kappa_{\rm ext}}\left[\kappa_{\rm int}(\boldsymbol{\theta}) + \kappa_{\rm ext}\right] + \left(1 - \frac{1}{1-\kappa_{\rm ext}}\right), \tag{3.13}$$

which in terms of $\kappa_{\rm int}(\boldsymbol{\theta})$ simplifies to

$$\kappa_{\rm int}(\boldsymbol{\theta}) = (1-\kappa_{\rm ext})\kappa_{\rm lens}(\boldsymbol{\theta}). \tag{3.14}$$

All reconstructed models presented in this paper employ parameterized profiles, which mitigate the impact of the MSD on the convergence of such model. In other words, the convergence of a lens model, $\kappa_{\rm lens}(\boldsymbol{\theta})$, would be a transformation of such parameterized model, $\kappa_{\rm param}$. In the absence of the external convergence term, the MST (Expression 3.9) is

$$\kappa_{\rm lens}(\boldsymbol{\theta}) = \lambda_{\rm int}(\boldsymbol{\theta})\kappa_{\rm param}(\boldsymbol{\theta}) + \left[1 - \lambda_{\rm int}(\boldsymbol{\theta})\right]. \tag{3.15}$$

Lastly, combining Expression 3.15 with Expression 3.14 and using the result in Expression 3.10 gives the following expression for the real physical convergence of the lens system

in terms of a parameterized profile

$$\kappa_{\rm phys}(\boldsymbol{\theta}) = (1 - \kappa_{\rm ext}) \left[\lambda_{\rm int}(\boldsymbol{\theta})\kappa_{\rm param}(\boldsymbol{\theta}) + 1 - \lambda_{\rm int}(\boldsymbol{\theta})\right] + \kappa_{\rm ext}, \tag{3.16}$$

which simplifies to

$$\kappa_{\rm phys}(\boldsymbol{\theta}) = \lambda(\boldsymbol{\theta})\kappa_{\rm param}(\boldsymbol{\theta}) + \left[1 - \lambda(\boldsymbol{\theta})\right], \tag{3.17}$$

where

$$\lambda(\boldsymbol{\theta}) = \lambda_{\rm int}(\boldsymbol{\theta})(1 - \kappa_{\rm ext}). \tag{3.18}$$

Kinematic measurements, such as the stellar velocity dispersion in the primary deflector near the image positions, can be used in conjunction with corresponding mass estimates from strong lens models to break the degeneracy internal to the lens galaxy and thereby constrain the internal MST parameter, $\lambda_{\rm int}(\boldsymbol{\theta})$. An estimate for the external convergence, $\kappa_{\rm ext}$, can be obtained from environmental studies of the lens system, such as spectroscopic and photometric surveys which provide redshifts as well as a quantification for the perturber population along the line-of-sight.

As a consequence of the MSD, it should be noted that the expression for the Fermat potential (Expression 3.4) also re-scales under the MST, with

$$\phi_{\rm phys}(\boldsymbol{\theta};\boldsymbol{\beta}) = \lambda(\boldsymbol{\theta})\phi_{\rm param}(\boldsymbol{\theta};\boldsymbol{\beta}). \tag{3.19}$$

However, in the vicinity of the observed image positions, $\lambda_{\rm int}(\boldsymbol{\theta})$ is nearly invariable, so that $\lambda(\boldsymbol{\theta}) \rightarrow \lambda = \lambda_{\rm int}(1 - \kappa_{\rm ext})$. Therefore, the Fermat potential difference between two images A and B for the true physical convergence scales with the Fermat potential difference of the reconstructed parameterized model as

$$\Delta\phi_{\rm phys}(\boldsymbol{\theta_A};\boldsymbol{\theta_B};\boldsymbol{\beta}) = \lambda\Delta\phi_{\rm param}(\boldsymbol{\theta_A};\boldsymbol{\theta_B};\boldsymbol{\beta}). \tag{3.20}$$

In short, both, a measurement for the external convergence, $\kappa_{\rm ext}$, and the scale factor internal to the lens galaxy, $\lambda_{\rm int}$, near the image positions, are needed to make an inference of the Hubble constant using observations of strongly lensed quasars.

3.2.3 Bayesian analysis and likelihood

The aim of the analysis is to obtain posterior distributions for the parameters, ξ, of a model, M, given the data set from the *HST* observations, $\boldsymbol{d}_{HST}$. Using Bayes' theorem, we can express the probability of the model parameters as

$$\begin{aligned} P(\xi|\boldsymbol{d}_{HST}) &\propto P(\boldsymbol{d}_{HST}|\xi)P(\xi) \\ &= \int P(\boldsymbol{d}_{HST}|\xi, M)P(\xi|M)\mathrm{d}M \\ &= \int P(\boldsymbol{d}_{HST}|\xi_{\rm mass}, \xi_{\rm light}, \xi_{\rm source}, \mathscr{P}, M) \\ &\qquad \times P(\xi_{\rm mass}, \xi_{\rm light}, \xi_{\rm source}|M)P(\mathscr{P})\mathrm{d}M, \end{aligned} \tag{3.21}$$

where in the last step we have broken up the set of model parameters into the main components of a lens model; namely the parameters of the deflector mass, $\xi_{\rm mass}$, the parameters for the light profile of the deflector and the lensed source, $\xi_{\rm light}$ and $\xi_{\rm source}$, respectively, and the model for the point spread function, $\mathscr{P}$.

Then the posterior of a single attribute in the lens model, ξ_i, which is part of the set of all model parameters, can be determined by marginalizing over the remaining (nuisance) parameters, ξ_k

$$P(\xi_i|\boldsymbol{d}_{HST}, M) = \int P(\xi|\boldsymbol{d}_{HST}, M) \prod_{k=1}^{i-1} \mathrm{d}\xi_k. \tag{3.22}$$

It should be mentioned that not all models in this paper share the same parameters. Therefore, to substantiate a meaningful comparison between various models and to determine which model best matches our observations, we use the Bayesian information criterion, which is defined as

$$\mathrm{BIC} = k\ln(n) - 2\ln(\hat{L}), \tag{3.23}$$

where k is the number of all free and linear parameters in a model, n represents the number of data point (or pixels), and $\hat{L}$ stands for the maximum value of the likelihood function, $P(\boldsymbol{d}_{HST}|\xi, M)$, corresponding to the model.

3.3 Observations of Lens system J1721+8842

In this section we first discuss the discovery of J1721+8842 in Section 3.3.1 and then describe the target's observations as well as the imaging data reduction in Section 3.3.2.

3.3.1 Lens discovery

Originally discovered by Lemon et al. (2018) through a search for multiple *Gaia* detections around potential quasars, this system is confirmed to be a strongly lensed quasar with a redshift of $z \approx 2.37$, showing strong absorption features. A following in-depth analysis of the target by Lemon et al. (2022) reveals two distinct background quasars at similar redshifts ($z = 2.369 \pm 0.007$ and $z = 2.364 \pm 0.003$), with one quasar quadruply imaged and the other doubly imaged. Furthermore, the images A and C of the quadruply lensed quasar exhibit damped Lyman-α absorption signatures from neutral hydrogen at a redshift consistent with the measurements for the quasars.

The long-slit spectra of the lensing galaxy, obtained with the Intermediate-dispersion Spectrograph and Imaging System at the William Herschel Telescope, show multiple absorption features stemming from Ca H and K in the G-band, as well as Mg, Na, and Hβ. Fitting

these lines with a multi-component Gaussian, Lemon et al. (2022) estimate the redshift of the deflector to be $z = 0.1841 \pm 0.0005$. Lastly, the source is also detectable at radio wavelengths (see Mangat et al., 2021).

3.3.2 HST Imaging and Data Reduction

The high-resolution data for this lens comes from observations with the Hubble Space Telescope, taken under cycle 26 program HST-GO-15652 (PI: T. Treu; see Schmidt et al., 2023b), using the Wide Field Camera 3 (WFC3). Our dataset comprises imaging in filter F160W, to give near-IR modeling constraints, and UVIS exposures in band F475X and band F814W, for higher-resolution observations in the optical/UV spectrum. In the IR band a 4-point dither pattern is employed to improve the data sampling by eliminating hot pixels and other detector irregularities, while UVIS exposures implement 2-point dithering during observations. At each UVIS dither point exposures are split into one long and one short integration to ensure the full brightness span is captured between faint features of the lens and bright quasar images. The total integration time for the four IR exposures is $2,197$ s, whereas the exposure time in the UVIS totals $1,382$ s in filter F475X and $1,428$ s in filter F814W.

Cosmic ray hits are removed and the individual exposures in each filter are aligned and combined with the use of the Python package AstroDrizzle (Avila et al., 2015). The resulting reduced images have a pixel size of $0.04''$/pix in both UVIS bands and $0.08''$/pix for the IR imaging. A composite RGB image of the target, constructed from the reduced IR/UVIS exposures, is shown in Figure 3.1, identifying the lens and nearby perturbers, and in Figure 3.2, labeling the images for both lensed quasars and other lensed sources. The intensities for each channel in the color composites are entirely arbitrary and chosen to achieve the best visualization of all components in the lens system.

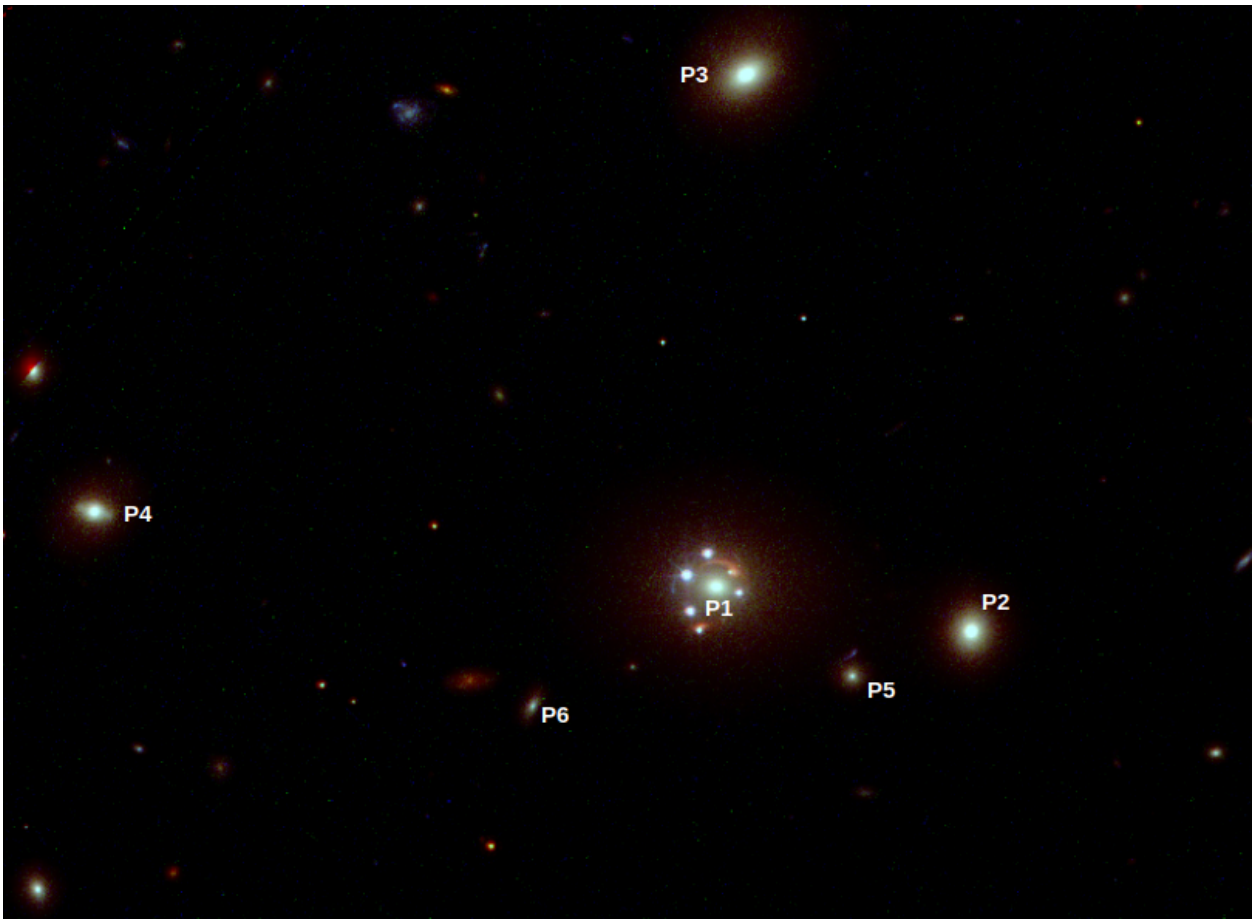

Figure 3.1: RGB composite image of J1721+8842 and nearby perturbers created by exposures in the HST band F160W (red), F814W (blue), and F475X (green).

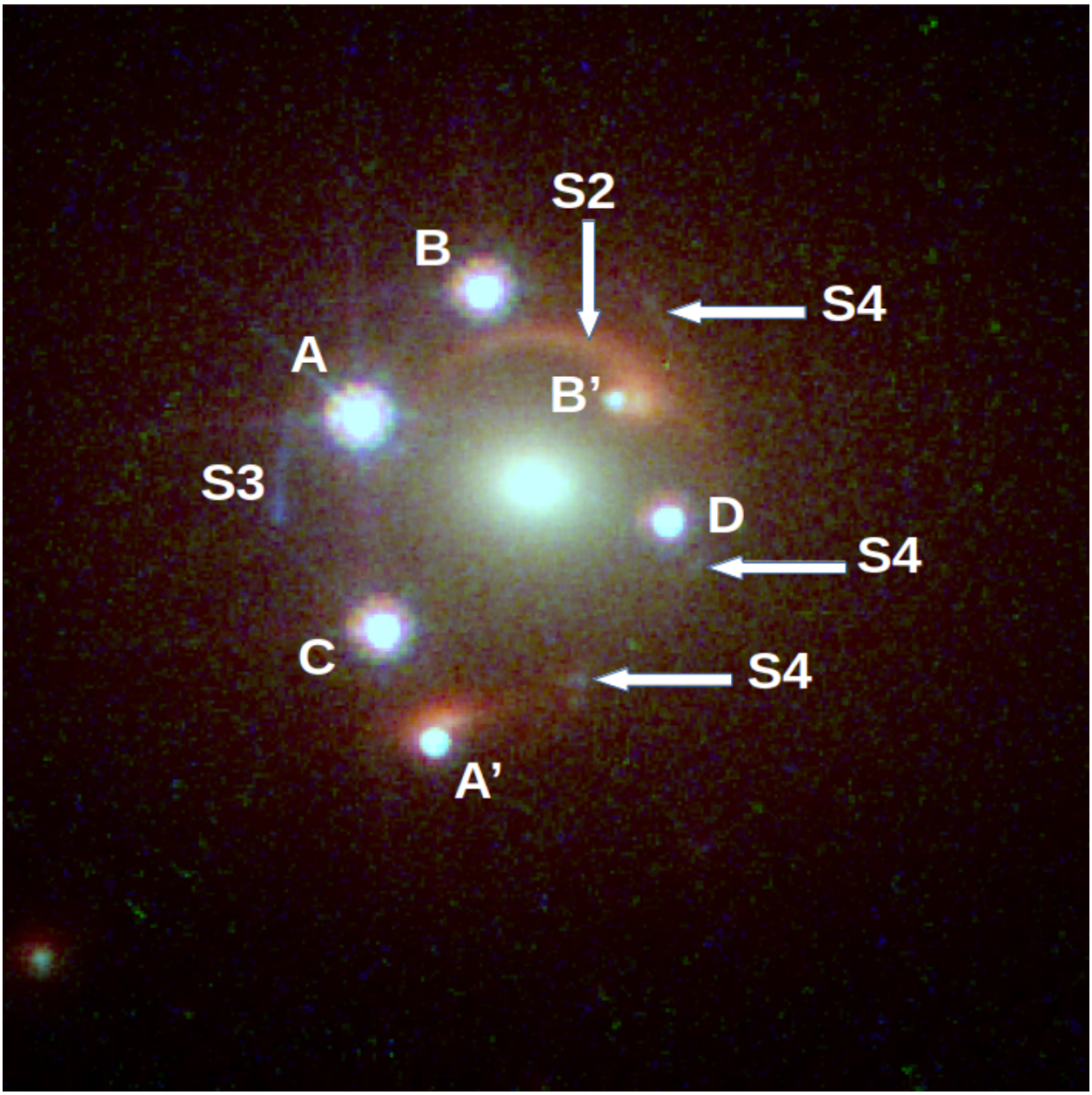

Figure 3.2: RGB composite image of J1721+8842 created by exposures in the HST band F160W (red), F814W (blue), and F475X (green).

3.4 Lens Models

In this section we describe the modeling choices for all components in the lens models of J1721+8842, broken down between main deflector description, lensed source light components, explicitly modeled line-of-sight perturbers, and structure resulting in additional distortions to the lens configuration. The parameterizations of the main deflector's mass profiles are discussed in Section 3.4.1.1, while the parameterization of the light profiles corresponding to the primary lensing galaxy are described in Section 3.4.1.2. The light profiles of the lensed sources and quasars are discussed in Section 3.4.2 and the modeling choices related to additional perturbing galaxies are outlined in Section 3.4.3. After that we describe the parameterization of LOS model components in Section 3.4.4, show assumed priors for specific parameters in Section 3.4.5, and conclude with a discussion on modeling choice related systematics in Section 3.4.6.

3.4.1 Main deflector

3.4.1.1 Main deflector mass profile parameterization

For the main deflector, we use two independent modeling choices (or "modeling families") to parameterize the mass profile. Option 1 relies on a singular power-law elliptical mass distribution to model the main deflector mass (Section 3.4.1.1.1) while for option 2 the mass of the deflector is modeled as a composite profile, where we separate the deflector's dark matter component from the luminous baryonic matter (see Section 3.4.1.1.2).

3.4.1.1.1 Power-law mass profile In this choice for parameterization, the mass profile of the main deflector is modeled with a power-law elliptical mass distribution (PEMD), which corresponds to a radial mass density profile of $\rho \propto r^{-\gamma}$, where γ is the power-law slope. The convergence, or dimensionless projected surface mass density, for the profile at position θ is parameterized as

$$\kappa(\theta_1, \theta_2) = \frac{3-\gamma}{2} \left(\frac{\theta_E}{\sqrt{q\theta_1^2 + \theta_2^2/q}} \right)^{\gamma-1} \tag{3.24}$$

where θ_1 and θ_2 are aligned along the semi-major and semi-minor axis through the rotational position angle $\phi = \arctan(\theta_2, q\theta_1)$, and where q represents the corresponding axis ratio.

3.4.1.1.2 Composite mass profile For the parameterization of this modeling option, we use two separate mass profiles: one to model the dark matter component of the main deflector mass and another profile to represent the baryonic matter. For the dark matter component, we adopt an elliptical Navarro–Frenk–White (NFW) profile, for which the three dimensional spherical mass density is given by:

$$\rho(r) = \frac{\rho_0}{(r/r_0)(1 + r/r_0)^2}, \tag{3.25}$$

where ρ_0 is the normalization constant and r_0 represents the scale radius (Navarro et al., 1997). Further details on the convergence and lensing potential of the NFW profile, as well as introduction of ellipticity in the potential, can be found in (Golse and Kneib, 2002).

The luminous baryonic matter of the main deflector mass is modeled by two elliptical Chameleon convergence profiles, which are superposed and joined via a common centroid. This mass profile is further tied to light profile model of the F160W IR band (see Section 3.4.1.2.2). The convergence of a Chameleon profile is given by the difference between two non-singular isothermal ellipsoids with different core sizes and is parameterized as

$$\kappa(\theta_1, \theta_2) = \frac{\kappa_0}{1+q} \left[\frac{1}{\sqrt{\theta_1^2 + \theta_2^2/q^2 + 4w_c^2/(1+q^2)}} - \frac{1}{\sqrt{\theta_1^2 + \theta_2^2/q^2 + 4w_t^2/(1+q^2)}} \right], \tag{3.26}$$

where w_c and w_t are the profile parameters for the two core sizes, where κ_0 represents the normalization constant, and where q is again the corresponding axis ratio (Dutton et al., 2011; Suyu et al., 2014). In contrast to a Sérsic profile, the Chameleon profile is based on closed-form expressions and thereby proves more convenient in the computation of lensing quantities (see Suyu et al., 2014). Furthermore, within a radius of between $0.5R_e$ and $3.0R_e$, where R_e is the effective radius of the Sérsic profile, the Chameleon profile approximates the Sérsic profile to within a few percent in mass residuals (Dutton et al., 2011).

As additional constraint to the composite mass profile parameterization, we force a common centroid between dark matter and baryonic matter components. This is achieved by allowing the centroid of the NFW profile to be offset from the Double Chameleon profile centroid by at most by 1 pixel, which corresponds to $0.04''$ in UVIS, and effectively joins the centroids of the two mass profiles.

3.4.1.2 Main deflector light profile parameterization

Analogous to Section 3.4.1.1, we use two modeling choices to parameterize the light profile of the main deflector, which depend on the deflector's mass profile parameterization. If the deflector's mass profile is described by a power-law, we model the main deflector light with Sérsic profiles, which is detailed in Section 3.4.1.2.1. In the composite mass profile case (Section 3.4.1.2.2), we use a Chameleon or Sérsic light profile parameterization, depending on the filter in which the target was observed.

3.4.1.2.1 Light profile parameterization to power-law mass profile In the case of the power-law mass profile modeling choice, we use a Double Sérsic profile (Sérsic, 1968) with a common centroid to model the light of the main deflector in all three bands. The parameterization of an elliptical Sérsic light profile is given by:

$$I(\theta) = I(\theta_e)\ \exp\left\{-C(n)\left[\left(\frac{(q_L\theta_1)^2+\theta_2^2}{q_L\theta_e^2}\right)^{\frac{1}{2n}}-1\right]\right\}, \tag{3.27}$$

where $C(n)$ is a normalization constant so that at the effective radius, θ_e, the profile includes half of the deflector's light. n represents the Sérsic index, θ_1 and θ_2 are the angular coordinates aligned along the semi-major and semi-minor axis through the rotational position angle $\phi_L = \arctan(\theta_2, q\theta_1)$ of the light profile, and q_L represents the corresponding axis ratio. In our models we hold the index of the first Sérsic light profile fixed at $n = 1.0$ across all filters, effectively making it an exponential Sérsic profile. The Sérsic index of the second light profile is allowed to vary within the restrictions of a flat prior as discussed in Section 3.4.5. Additionally, we allow the effective radii, the Sérsic index of the second light profile, the axis ratios, the position angles, and the centroids to vary across bands.

3.4.1.2.2 Light profile parameterization to composite mass profile For the composite mass profile option, we model the main deflector light with Double Sérsic profile (Expression 3.27) in the UVIS bands (filters F475X and F814W), as described above in Section 3.4.1.2.1. However, in the IR band (filter F160W), the parameterization of the deflector light is following the description of the profile representing the baryonic matter, where we model the main deflector with two joined elliptical Chameleon profiles, shown in Expression 3.26. For the light profile description, however, we replace the normalization constant, or convergence amplitude, κ_0, by the normalization contant for the flux amplitude, I_0. The remaining parameters of Expression 3.26 remain the identical and are all tied (or held in common) between the Double Chameleon mass and light profiles.

3.4.2 Lensed sources

3.4.2.1 Quasar host galaxies

The two galaxies that host the quadruply imaged and the doubly imaged quasar are both modeled with an elliptical Sérsic light profile (see Expression 3.27). Except for the centroids, which are held common across the three HST bands, all parameters for the Sérsic profiles are allowed to vary independently and are constrained by the flat priors described in Sec-

tion 3.4.5. To model additional complexity in the source light, which cannot be described by a the continuous or featureless flux distribution of a Sérsic profile, we add a set of two-dimensional Cartesian shapelets (Refregier, 2003; Birrer et al., 2015) to the light profile of the host galaxies. These shapelets share a common centroid with the Sérsic function of the respective host. The corresponding number of basis functions (or shapelet number) form an orthogonal basis and is given by

$$N_{\rm shapelet} = \frac{(n_{\rm max}+1)(n_{\rm max}+2)}{2}, \tag{3.28}$$

where the maximal source complexity, or $n_{\rm max}$, is related to the characteristic scale, β, by the maximum spatial scale, $l_{\rm max}$, defined as

$$l_{\rm max} = \beta\sqrt{n_{\rm max}+1}. \tag{3.29}$$

Increasing the shapelet order, $n_{\rm max}$, increases the complexity, or components of additional concentrated flux, in the source reconstruction of our models. To avoid the shapelet order to be driven to high values, resulting in degeneracies with other model parameters and further causing over-fitting by modeling noise in the data, we keep the parameter $n_{\rm max}$ for each band fixed during the fitting process for a given model and only allow the scale size, β, to vary within the confines of a flat prior.

The multiply imaged quasars within the lensed galaxies are modeled as point sources in the image plane and share the same centroid as their respective host in the source plane. To account for the lower resolution in the IR band (F160W), the point spread function (PSF) is supersampled in IR using a supersampling factor of 3. For the two UVIS bands, however, we do not use a supersampled PSF. As initial starting point we first estimate the PSF in each band using 5 to 10 suitable stars in the field of view near the target. To further optimize and improve the PSF, we run iterations of the PSF reconstruction between optimization routines that fit the free parameters for the respective lens model (see Birrer et al., 2019).

3.4.2.2 Lensed galaxies

Lensed sources not hosting a quasar are parameterized in our models by an elliptical Sérsic light profile as described by Expression 3.27. As the case with the quasar host galaxies, detailed in Section 3.4.2.1, only the centroids are joined across all bands for each source light profile, while all other parameters, such as ellipticity, Sérsic index, Sérsic radius, etc., are allowed to vary within the confines of the respective prior (see Section 3.4.5). If additional complexity is required to accurately describe the lensed source light, we use the two-dimensional Cartesian shapelet profile, outlined in Section 3.4.2.1 above, with the centroid joined to the respective Sérsic profile to further model concentrated flux features. Again, only the scale size, β, is allowed to vary while the shapelet order, $n_{\max}$, responsible for an increase in source complexity with larger values, is held fixed during the fitting process.

3.4.3 Additional perturbing galaxies

Galaxies near the main deflector can have a significant impact on the path of lensed quasar's light rays, depending on the strength of their deflection potential and the perturber's location with respect to the lens galaxy. Therefore, to ensure that higher order lensing effects beyond external convergence and external shear/flexion are properly addressed, we explicitly include certain line-of-sight perturbers in our models. In Section 3.4.3.1 we detail how we select nearby perturbers that are explicitly included in our models, followed by the description of the mass profile for modeled line-of-sight galaxies (Section 3.4.3.2).

3.4.3.1 Selection of nearby perturbers explicitly included in models

To determine which of the nearby perturbers should be explicitly included (or explicitly modeled), we use an estimate of the change in flexion produced by the perturbing galaxy. The magnitude of the flexion shift caused by a perturber of assumed point mass is given by

$$\Delta_3 x = f(\eta) \times \frac{(\theta_{\rm E}\theta_{\rm E,p})^2}{\theta^3}, \tag{3.30}$$

where $\theta_{\rm E}$ and $\theta_{\rm E,p}$ are the Einstein radius of the main deflector and the perturber, respectively (see Sluse et al., 2017; McCully et al., 2017). θ represents the angular separation between the perturber and the main deflector in the sky and the factor $f(\eta)$ is defined as follows

$$f(\eta) = (1-\eta)^2, \tag{3.31}$$

where

$$\eta = \frac{D_{\rm dp} D_{\rm s}}{D_{\rm p} D_{\rm ds}}. \tag{3.32}$$

$D_{\rm dp}$, $D_{\rm s}$, $D_{\rm p}$, and $D_{\rm ds}$ represent the angular diameter distances between the redshifts of the main deflector and the perturber, to the source, to the perturber, and between the deflector and the source, respectively.

At the time of our analysis redshift measurements for nearby perturbers are not available. Given that the additional galaxies in the field-of-view and the main deflector are similar in color, we make the simplifying assumption that all are part of the same galaxy overdensity and therefore at approximately the same redshift. With this assumption η goes to zero and the function $f(\eta)$ becomes unity, leaving the flexion shift magnitude at

$$\Delta_3 x = \frac{(\theta_{\rm E}\theta_{\rm E,p})^2}{\theta^3}. \tag{3.33}$$

Under the assumption of an isothermal profile, the Einstein radius of an additional perturber is given by

$$\theta_{\rm E,p} = 4\pi \frac{\sigma_v^2}{c^2} \frac{D_{\rm ps}}{D_{\rm s}}, \tag{3.34}$$

where $D_{\rm ps}$ and $D_{\rm s}$ are the angular diameter distance between redshifts of the perturber

and the lensed source and the angular diameter distance to the source, respectively. Using the Faber-Jackson (Faber and Jackson, 1976) relation, $L_* \propto \sigma^{\gamma}$, which relates the velocity dispersion, σ, to the stellar luminosity, L_*, with the power-law index, γ, equal to 4, we scale a perturbers's Einstein radius to the corresponding flux, F, as

$$\theta_{\mathrm{E,p}} \propto \sigma_v^2 \propto L^{1/2} \propto F^{1/2}. \tag{3.35}$$

Since we assume the perturbers to be in the same redshift plane as the main deflector, we have an expression for the Einstein radius based on the flux ratio

$$\theta_{\mathrm{E,p}} = \theta_{\mathrm{E}} \left(\frac{F_{\mathrm{p}}}{F_{\mathrm{d}}} \right)^{1/2}, \tag{3.36}$$

where F_p is the flux of the perturber and F_d the flux of the main delflector. Using Expression 3.36 in Expression 3.33, the estimated flexion shift magnitude produced by a perturber at the same redshift as the main deflector is then

$$\Delta_3 x = \frac{\theta_{\mathrm{E}}^4}{\theta^3} \left(\frac{F_{\mathrm{p}}}{F_{\mathrm{d}}} \right). \tag{3.37}$$

The flexion shift based on our flux ratio analysis for each perturber is listed in Table 3.1. As demonstrated in McCully et al. (2017) and Sluse et al. (2017), to prevent a significant bias in an H_0 measurement line-of-sight perturbers which produce a flexion shift magnitude of Δ_3x $> 10^{-4}$ arcsec should be explicitly included in the lens models. Adopting this conservative cutoff, we find that perturber P4 is located at a large enough angular separation for its impact to be negligible. In contrast, even though perturbers P5 and P6 have smaller angular scales compared to other nearby galaxies, their close proximity to the main deflector warrants their explicit inclusion in the lens models. Therefore, we include mass profiles to model perturbers P2, P3, P5, and P6, located in the same redshift plane as the main deflector, for our lens models.

Table 3.1: Flexion shift estimates for nearby perturbers based on a corresponding flux ratio analysis.

Perturber	$\Delta_3 x$ (arcsec)
P2	1.4×10^{-3}
P3	2.7×10^{-4}
P4	6.7×10^{-5}
P5	1.0×10^{-3}
P6	2.4×10^{-4}

3.4.3.2 Mass profile of nearby perturbers

Any additional perturbing galaxy near the main deflector, deemed to be explicitly included in our models based on the criteria described in Section 3.4.3.1, is modeled using a singular isothermal sphere (SIS) profile, which is a PEMD with a fixed power-law slope, γ, of 2.0 and a fixed axis ratio, q, of 1.0. In our models we fix the location of the mass centroid to coincide with the corresponding light centroid that is used to measure the angular separation from the main perturber.

We further employ a Gaussian prior on the Einstein radius for each additional perturber that is based on an assumed 0.1 dex scatter in the Faber-Jackson relation (see Equation 3.35). Furthermore, due to the complexity of the model and the underlying degeneracy for nearby line-of-sight perturbers, we hold Einstein radius for all the additional perturbers fixed at the estimates derived from the measured flux ratios (Equation 3.36) until we find a good fit for all other parameters. Once a fit for the remaining parameters in our model is found, we add the Einstein radii back to the free parameters fitted in the modeling process.

3.4.3.3 Light profile of nearby perturbers

Light profiles for additional perturbing galaxies are not included in our models as they do not contribute valuable information towards the assessment of the Fermat potential differences between the image positions of the lensed quasar.

3.4.4 Line of sight structure and higher-order distortions

Additional linear distortions can impact the lens model as a result of dark matter halos and large scale structures along the line of sight. We collectively account for such impact on the strong lens by including an external shear profile. The external shear strength of the combined tidal effect from the surrounding gravitational field is given by

$$\gamma_{\rm ext} = \sqrt{\gamma_{\rm ext,1}^2 + \gamma_{\rm ext,2}^2}, \tag{3.38}$$

where the components of the external shear matrix, $\gamma_{\rm ext,1}$ and $\gamma_{\rm ext,1}$, are related to the external shear angle, $\phi_{\rm ext}$, by

$$\phi_{\rm ext} = \frac{1}{2}\arctan\left(\gamma_{\rm ext,2}, \gamma_{\rm ext,1}\right). \tag{3.39}$$

In addition to the shear profile, we include flexion components in our power-law and composite models to collectively account for and model non-negligible higher-order distortions. The flexion effects emerge as arclike curvature and skewed anisotropic distortions in the images of the lensed quasar. Mathematically, the spin-1 flexion, $\vec{F}$, and spin-3 flexion, $\vec{G}$, can be expressed as the first derivative of the spin-0 convergence, κ, and first derivative of the spin-2 complex shear field, γ

$$\begin{aligned}
\vec{F} &= \vec{\nabla}\kappa = \vec{\nabla}^{*}\gamma, \\
\vec{F} &= |F|e^{i\phi}, \\
\vec{G} &= \vec{\nabla}\gamma, \\
\vec{G} &= |G|e^{3i\phi},
\end{aligned} \tag{3.40}$$

where ϕ represent the position angle of the corresponding flexion component (see e.g. Bacon et al., 2006; Retana-Montenegro et al., 2012; Viola et al., 2012). Using complex notation,

the spin-1 and spin-3 flexion can also be expressed in terms of the third order derivative of the lensing potential, ψ

$$
\begin{aligned}
F \equiv F_1 + iF_2 &= \frac{1}{2}[(\psi_{xxx} + \psi_{xyy}) + i(\psi_{xxy} + \psi_{yyy})], \\
G \equiv G_1 + iG_2 &= \frac{1}{2}[(\psi_{xxx} - 3\psi_{xyy}) + i(3\psi_{xxy} - \psi_{yyy})],
\end{aligned}
\tag{3.41}
$$

where ψ_{ijk} stands for $\partial_i \partial_j \partial_k \psi$.

3.4.5 Priors

This section provides details on the priors employed in the modeling process, which crucially quantify the intrinsic flexibility afforded to our lens models during parameter optimization. These informative constraints encapsulate observational and theoretical guidance towards realistic ranges in model parameters. The majority of parameters in our models rely on uniform priors that cover a broad physical range, with the exception of the NFW profile, in our composite model, and the Einstein radii of explicitly included nearby perturbers.

In addition to a flat prior, the centroid of the dark matter profile (NFW) is further constrained by the centroid of the Chameleon profile. To effectively link the centers of the two profiles, we allow for a deviation within the right ascension and declination of 1 pixel in UVIS, or $0.04''$. If for a model the NFW centroid exceeds the bound set by the Chameleon profile, a taxing punishment term is added to the model's likelihood. To constrain the scaling radius (r_0) of the NFW profile we employ a Gaussian prior, which was derived using the analysis in Gavazzi et al. (2007) of Sloan Lens ACS (SLACS) lenses (see Bolton et al., 2006). Our prior for the scaling radius is centered on $26.''82$ with a standard deviation of $3.''70$. When applying the prior on r_0, we only probe the space within 5σ of the mean, meaning from $8.''32$ to $45.''32$, and disregard all solutions outside that range. Lastly, due to a degeneracy with the external shear parameters, we also tightly constrain the ellipticity of the NFW profile with an additional prior that severely punishes the likelihood of a model

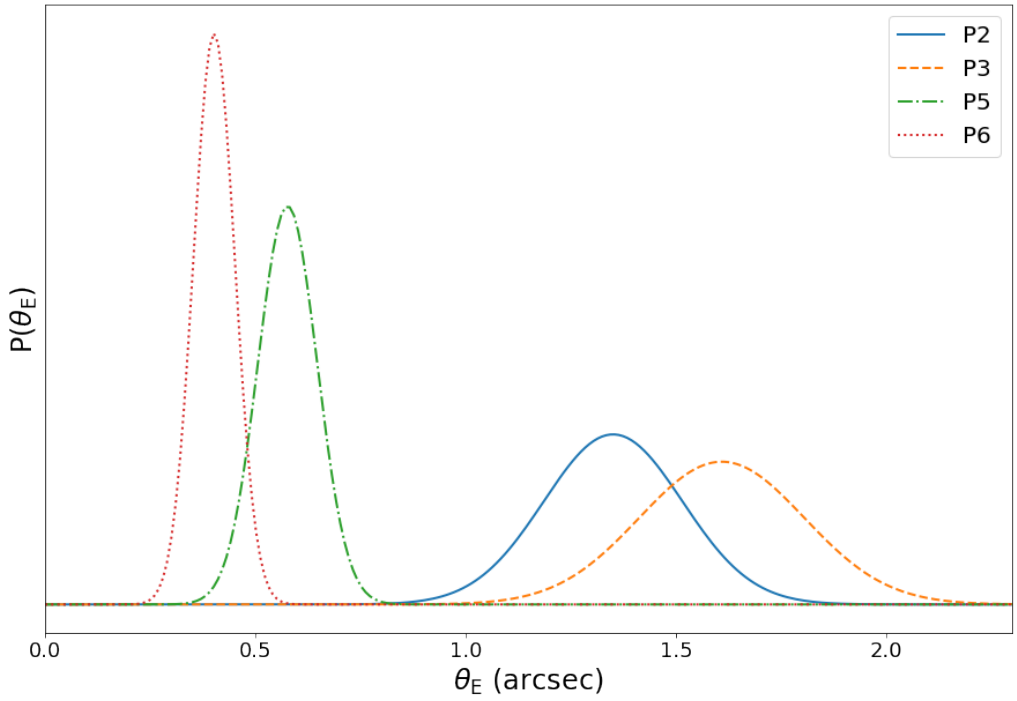

Figure 3.3: Priors on Einstein radii for nearby perturbing galaxies explicitly included in models.

for which the eccentricity parameters are greater than 0.1 or less than −0.1.

Explicitly modeling four of the nearby perturbers further increases the already high complexity of our models. Furthermore, two of these perturbers are located near each other and thereby introduce additional degeneracies. For this reason, we impose a Gaussian prior on the Einstein radii of each explicitly included perturbing galaxy and hold the mass centroid fixed at the corresponding center of light. The mean for the priors on the Einstein radii is derived using the flux ratio analysis in Expression 3.36 and the standard deviation is estimated based on a 0.1 dex scatter we assumed for the Faber-Jackson (Faber and Jackson, 1976) relation. We show the resulting probability density for each prior on the perturber's Einstein radius in Figure 3.3.

Finally, in Table 3.2 we summarize the priors employed in our models by component. In case of non-spherical profiles, instead of listing the priors for axis ratio, q, and position

angle, ϕ, we show the priors imposed on the corresponding eccentricity parameters, which are related to the axis ratio and position angle by:

$$\begin{aligned} e_1 &= \frac{1-q}{1+q} \times \cos(2\phi), \\ e_2 &= \frac{1-q}{1+q} \times \sin(2\phi). \end{aligned} \tag{3.42}$$

3.4.6 Assessment of systematic uncertainties from modeling choices

To assess the systematic impact of various parameter choices on the uncertainties in our models, we model the lens configuration under different assumptions for the mass profile of the primary deflector and with three separate sets for radius of the circular mask used for the likelihood computation. The size of the likelihood masking region in our fiducial models is chosen to encompass a region large enough to ensure all lensed features are included within and to capture the extend of the primary deflector's flux in each band. To test the impact of the likelihood masking size we increase and decrease the radius for each filter by $0.''5$ for our fiducial models and repeat the MCMC sampling procedures. We find no significant change in the time-delay difference between images as a result of these masking size changes and therefore opted to reduce the change in masking radii to $0.''1$ for our remaining systematic assessments.

We further evaluate the impact of various complexities in the lensed sources by changing the shapelet order, $n_{\max}$. Here, the lowest possible source complexity is represented by $n_{\max} = -$, which signifies no shapelets were added to the source light modeled by a Sérsic light profile.

To obtain posteriors for the changes in parameter choices, we initialize the changed model with the results of the corresponding fiducial model for main deflector profile choice (the seed) and run the MCMC sampling procedure with an iteration count similar to the seed model. To summarize our selections, the changes to the model configurations, itemized by modeling

Table 3.2: Priors on mass model parameters.

Model component	Parameter	Description	Prior
Main deflector (P1) mass profile (SPEMD)	γ	Power-law slope	Flat prior: [1.5, 2.5]
	$\theta_{\rm E,P1}$	Einstein radius	Flat prior: [0.01, 10.]
	$x_{\rm mass}(''$)	Centroid x-coordinate	Flat prior: [-10., 10.]
	$y_{\rm mass}(''$)	Centroid y-coordinate	Flat prior: [-10., 10.]
	e_1	Eccentricity in x-direction	Flat prior: [-0.5, 0.5]
	e_2	Eccentricity in y-direction	Flat prior: [-0.5, 0.5]
Main deflector (P1) mass profile (NFW)	$\alpha_{r_0}(''$)	Deflection angle	Flat prior: [0., 10.]
	$r_0(''$)	Scale radius	Gaussian prior: [26.82, 3.70] on top of flat prior: [8.32, 45.32]
	$x_{\rm mass}(''$)	Centroid x-coordinate	Flat prior: [-10., 10.]
	$y_{\rm mass}(''$)	Centroid y-coordinate	Flat prior: [-10., 10.]
	e_1	Eccentricity in x-direction	Flat prior: [-0.5, 0.5]
	e_2	Eccentricity in y-direction	Flat prior: [-0.5, 0.5]
Main deflector (P1) mass profile (Double Chameleon)	$\alpha_1(''$)	Deflection angle	Flat prior: [0., 10.]
	$I_{0,\rm Cham1}/I_{0,\rm Cham2}$	Ratio of deflection amplitudes	Flat prior: [0., 100.]
	$w_{c,\rm Cham1}$ ($''$)	Core size of component 1	Flat prior: [0.001, 10.]
	$w_{t,\rm Cham1}$ ($''$)	Core size of component 2	Flat prior: [0.001, 10.]
	$e_{1,\rm Cham1}$	Eccentricity in x-direction	Flat prior: [-0.5, 0.5]
	$e_{2,\rm Cham1}$	Eccentricity in y-direction	Flat prior: [-0.5, 0.5]
	$w_{c,\rm Cham2}$ ($''$)	Core size of component 1	Flat prior: [0.001, 10.]
	$w_{t,\rm Cham2}$ ($''$)	Core size of component 2	Flat prior: [0.001, 10.]
	$e_{1,\rm Cham2}$	Eccentricity in x-direction	Flat prior: [-0.5, 0.5]
	$e_{2,\rm Cham2}$	Eccentricity in y-direction	Flat prior: [-0.5, 0.5]
External shear	$\gamma_{\rm ext,1}, \gamma_{\rm ext,2}$	Shear components	Flat prior: [-0.5, 0.5]
Fexion	ψ_{xxx}, ψ_{xxy}, ψ_{xyy}, ψ_{yyy}	Flexion components	Flat prior: [-0.1, 0.1]
P2 mass (SIS)	$\theta_{\rm E,P2}$	Einstein radius	Gaussian prior: [1.35, 0.16]
P3 mass (SIS)	$\theta_{\rm E,P3}$	Einstein radius	Gaussian prior: [1.60, 0.20]
P5 mass (SIS)	$\theta_{\rm E,P5}$	Einstein radius	Gaussian prior: [0.58, 0.07]
P6 mass (SIS)	$\theta_{\rm E,P6}$	Einstein radius	Gaussian prior: [0.40, 0.05]

component, are as follows:

1. Two choices for the mass profile of the primary deflector:
   (a) Power-law profile
   (b) Composite profile
2. Three choices for the radius (in arcsec) of the likelihood computation masking region, sorted by band from shortest to longest wavelength, i.e. {F475X, F814W, F160W}:
   (a) {3.9, 4.0, 7.4}
   (b) {4.0, 5.0, 7.5}
   (c) {4.1, 5.1, 7.6}
3. Complexity in lensed source light ($n_{\max}$ values), sorted by source number, i.e. {S1, S2, S3, S4}:
   (a) $\{-, 5, -, 5\}$
   (b) $\{1, 7, 1, 7\}$
   (c) $\{-, 7, -, 7\}$
   (d) $\{-, 7, 1, 7\}$

Combining these choices in modeling components, we arrive at a total of 24 different configurations. To address stochasticity in the MCMC sampling, we perform the MCMC run for each model configuration two times, which increases the number of model results contributing in the assessment of systematic uncertainties to a toal of 48.

3.5 Results

We now present the reconstructed models for J1721+8842. In Section 3.5.1 we show the best fits for the profile parameters used in our modeling and discuss noteworthy findings.

Section 3.5.2 describes how results for model of different complexities and components are compared to one another and Section 3.5.3 presents predicted time-delays between lensed images based on the fits for our best models.

3.5.1 Lens model results

Figures 3.4 and 3.5 compare the reconstructed model with the data in each band. The first column in these figures shows the observations, ordered in terms of wavelength from short to long, i.e. filter F475X (top row), F814W (middle row), and F160W (bottom row). The second column presents the reconstructed model for a corresponding filter, while the third column shows the normalized residuals after subtracting the observations from the modeling results of each band.

In the corner plot of Figure 3.6 and Figure 3.7, we show the posterior distributions for mass model parameters of both assumptions for the primary deflector's profile, power-law (shown in red) and composite model (shown in blue), along with time-delays between image pairs of the quadruply and the doubly lensed quasar. To compare the results of the composite model with the results of the power-law assumption, we show the Einstein radius, $\theta_{\rm E}$, for the composite model as radius of the circularized profile at which the encompassed mean convergence equals unity. In the same fashion, the power-law slope, γ, for the composite assumption is then computed from the derivative of the corresponding convergence profile at the Einstein radius.

In our analysis we find the inclusion of higher order perturbations, i.e. flexion, is necessary as it significantly improves the residuals in our fits after subtracting the data from our modeling results. To be precise, with the addition of flexion components, we find an improvement in the BIC by 1,544 when comparing the best fit power-law model to a model only differing in terms of higher order perturbation. Furthermore, we find correlation between the spin 3 flexion, for both, strength ($|G|$) as well as direction ($\phi_{\rm G}$), and the time-delays predicted for the image pairs AB and AC of the quadruply lensed quasar. The time-delays

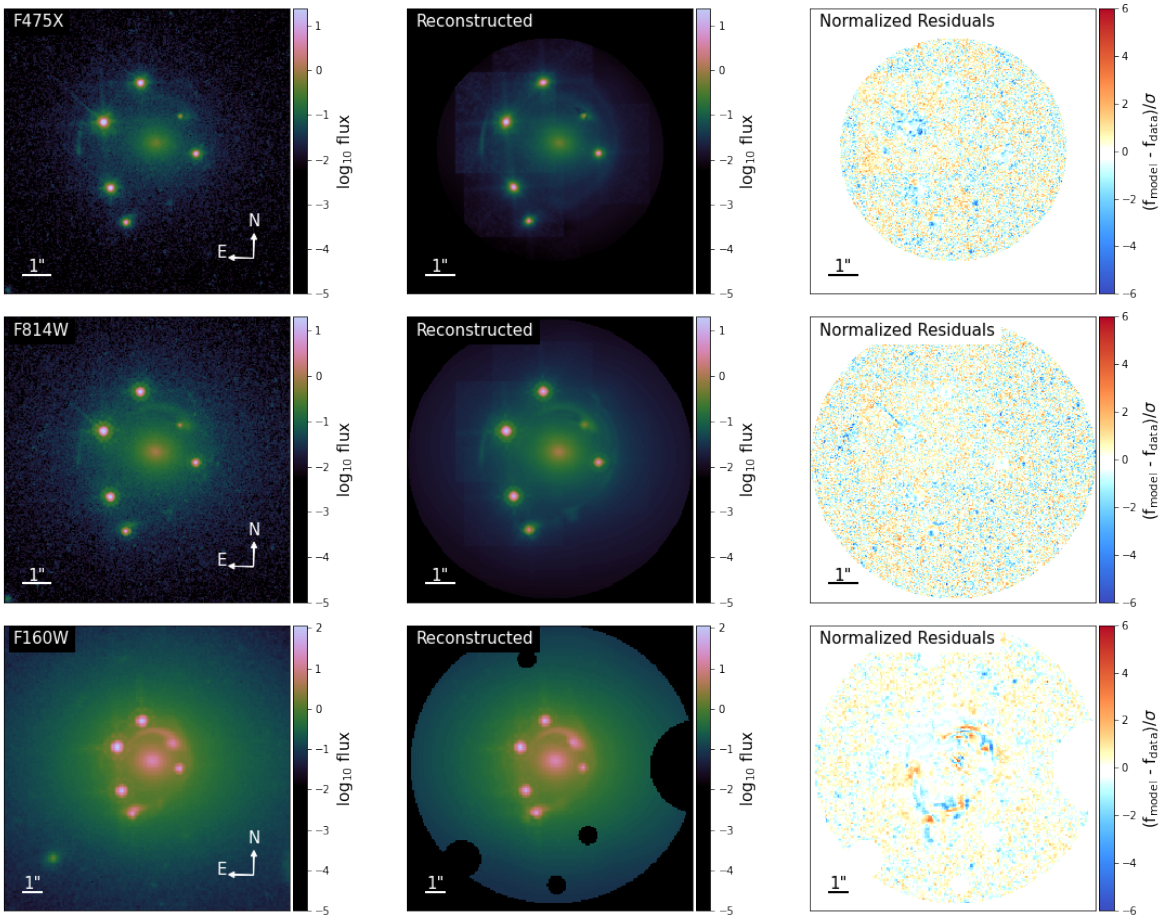

Figure 3.4: Reconstructed power-law model for J1721+8842. The first column (left) shows the observations in each band, sorted by wavelength from short to long. The second column (center) displays the reconstructed model for each filter and the third column (right) are the normalized residuals between our model and the observed data.

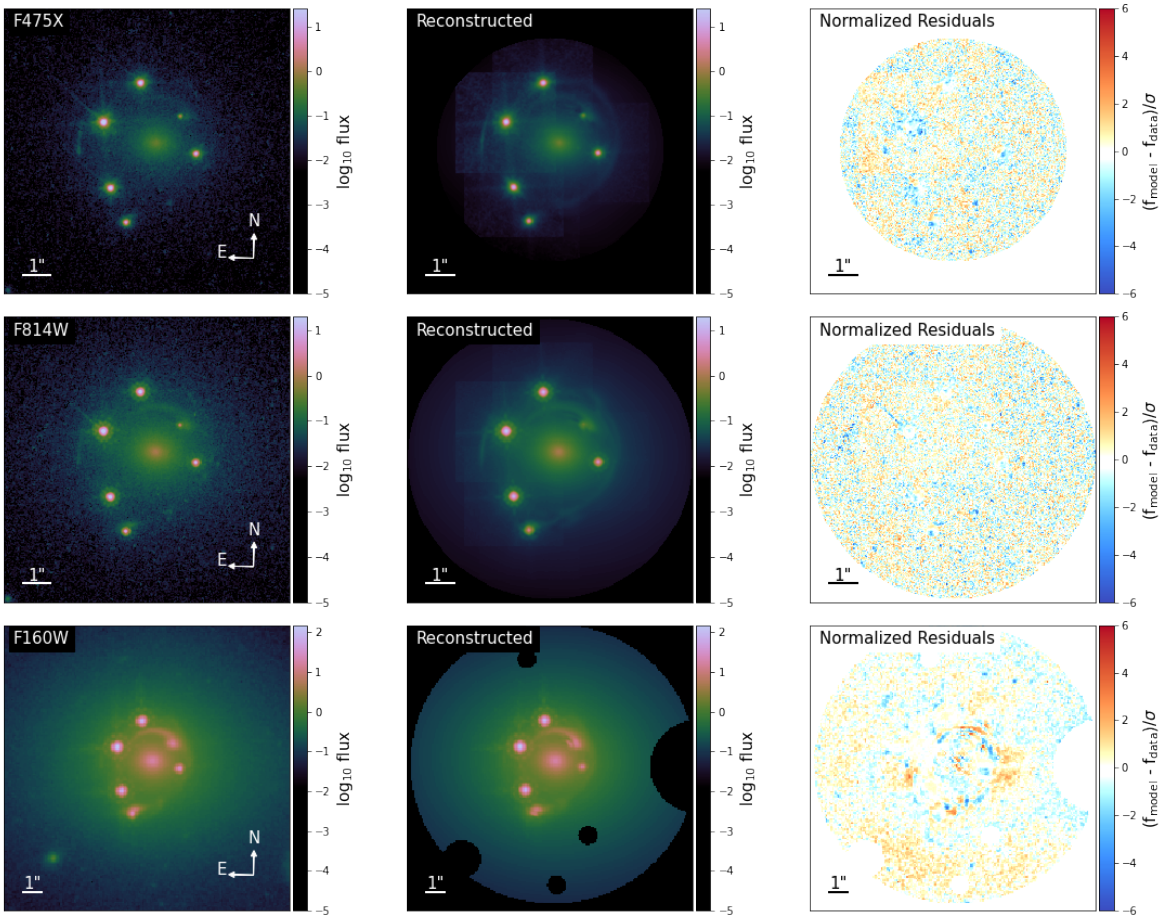

Figure 3.5: Reconstructed composite model for J1721+8842. The first column (left) shows the observations in each band, sorted by wavelength from short to long. The second column (center) displays the reconstructed model for each filter and the third column (right) are the normalized residuals between our model and the observed data.

for these two image pairs (AB and AC) appear also affected by the strength of the external shear, $\gamma_{\rm ext}$. On the other hand, we find that the comparatively larger predicted time-delay of the quad's image pair AD and the doubly imaged quasar's time-delay (pair A'B') are both primarily tied to the result of the primate deflector's power-law slope, γ. Lastly, our results show no observable relationship between the components of the spin 1 flexion and the time-delays between any of the image pairs.

Figure 3.8 shows the posterior distribution for the Einstein radii of all perturbers of our models. In the case of the composite model assumption for the primary deflector, we compute the Einstein radius using on the circular radius of the mean convergence. We find a degeneracy between the Einstein radius of perturber P2 and perturber P5, which is not unexpected since both perturbers are located in the approximately same direction. Additionally, we find a weak correlation in the Einstein radii of perturbers P3 and P6. If left unconstrained by priors, these correlations cause the Einstein radii of perturbers P5 and P6 to diverge to zero with associated offsets in the Einstein radii of perturbers P2 and P3.

Figure 3.9 illustrates the decomposition of the primary deflector convergence in the composite mass model case, with the convergence of the dark matter profile (NFW) shown in the left panel, the convergence of the stellar mass (Double Chameleon) in the center, and the resulting combined convergence (Composite) displayed in the right panel.

In Figure 3.10, we show the total convergence (left panels) from all mass model components, including explicitly modeled nearby perturbers, for both primary deflector mass model assumptions, power-law (top row) and composite (bottom row). For both cases of the underlying mass model, we also include a plot of the magnification model (right panels), which indicates the predicted location of the images for the quadruply and the doubly lensed quasar.

Figure 3.11 plots the mean convergence enclosed within a circle of radius r for the dark matter (NFW profile) and baryonic (Chameleon profile) components of the composite model and for the power-law model. We find that even with the assumption of a strong prior im-

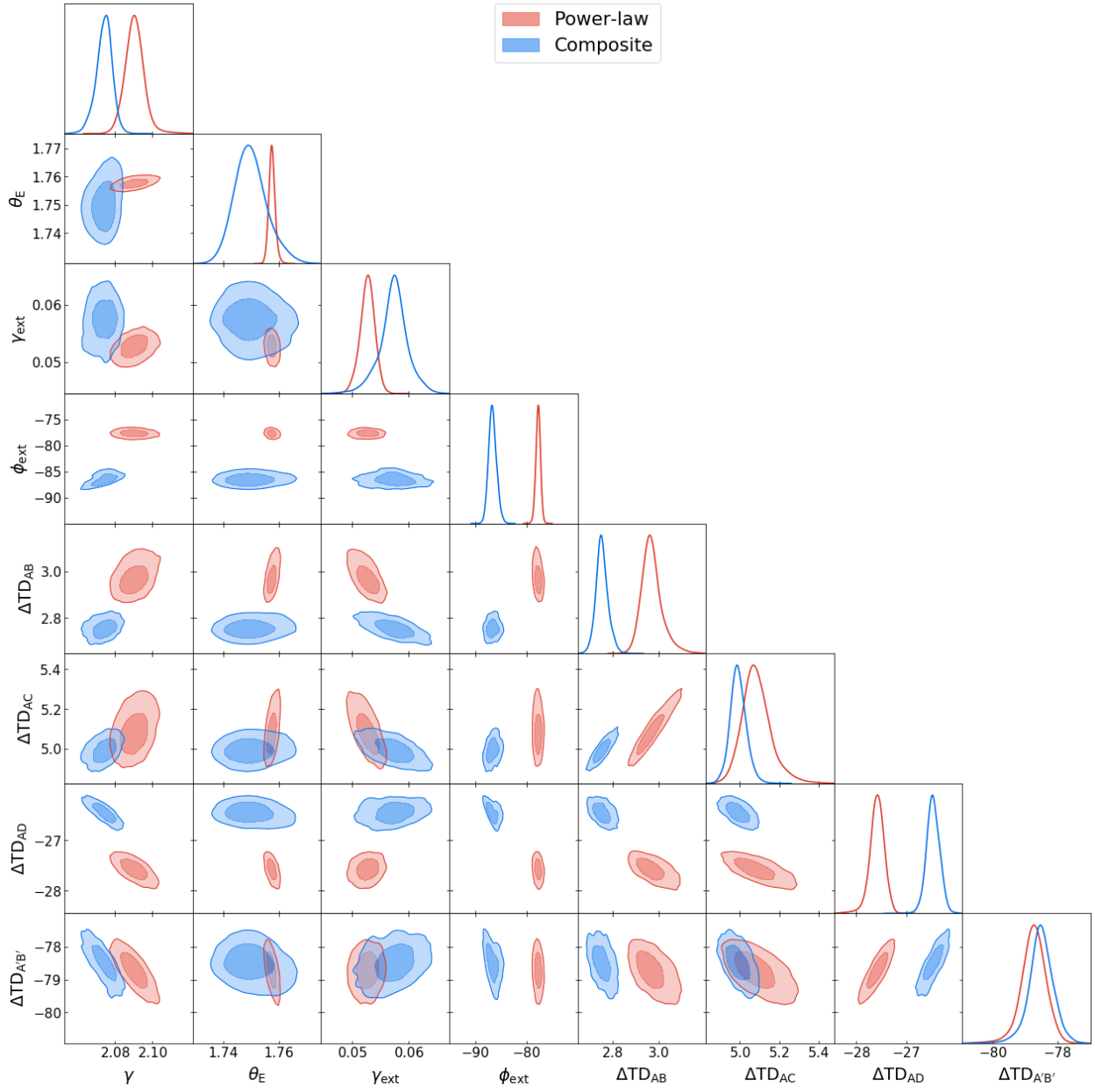

Figure 3.6: Mass model parameters and predicted time-delays for the two underlying assumptions of primary deflector's mass profile. The power-law model results are shown in red while the results for the composite model are colored in blue. In the composite model case, the Einstein radius of P1 is calculated via the circularized average of the convergence and the power-law slope represents the derivative of the convergence at the Einstein radius.

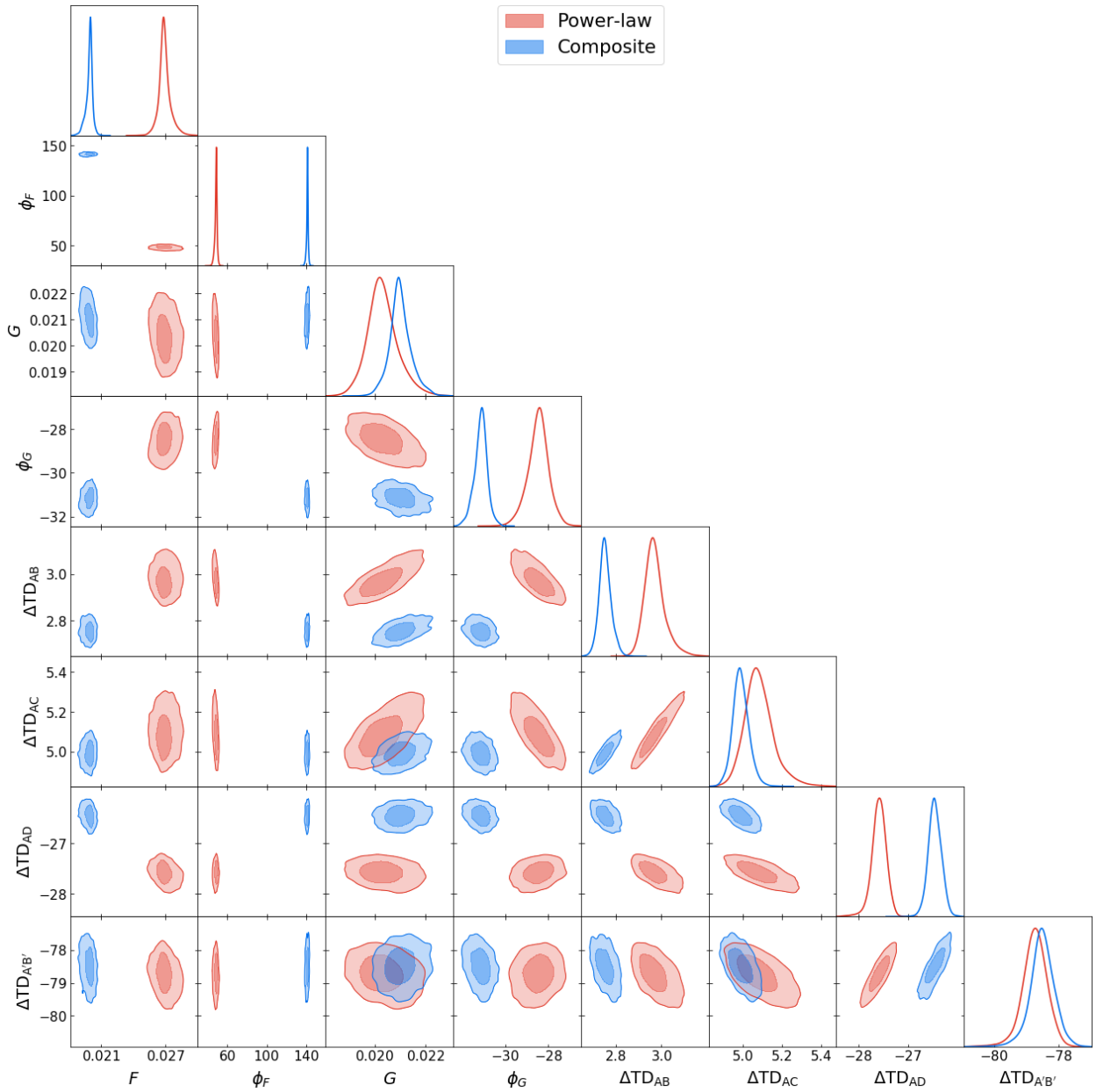

Figure 3.7: Flexion results and predicted time-delays for the two mass profile assumptions of the main deflector. The power-law and composite model results are shown in colors red and blue, respectively.

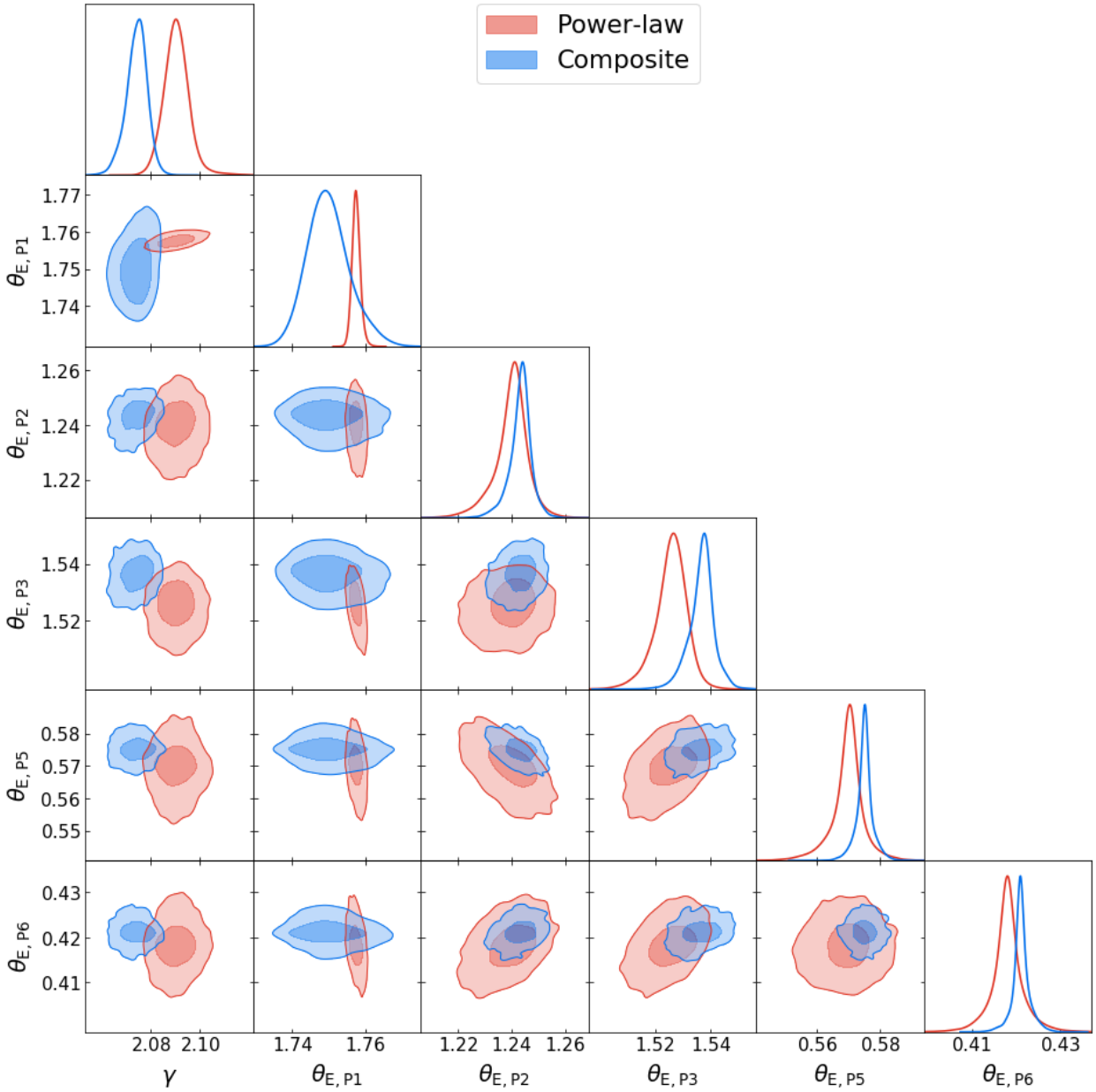

Figure 3.8: Comparison of main deflector and perturber Einstein raddii between power-law (red) and composite (blue) mass model assumption. In the composite model case, the Einstein radius of the primary deflector is calculated as circular radius of the mean convergence.

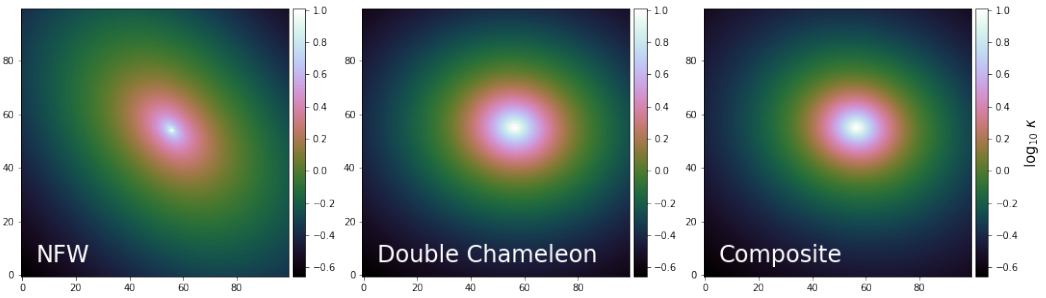

Figure 3.9: Convergence plots of the primary deflector mass in the composite profile case, showing the dark matter profile (left panel), the stellar mass (center panel), and the resulting combined projected mass distribution (right panel).

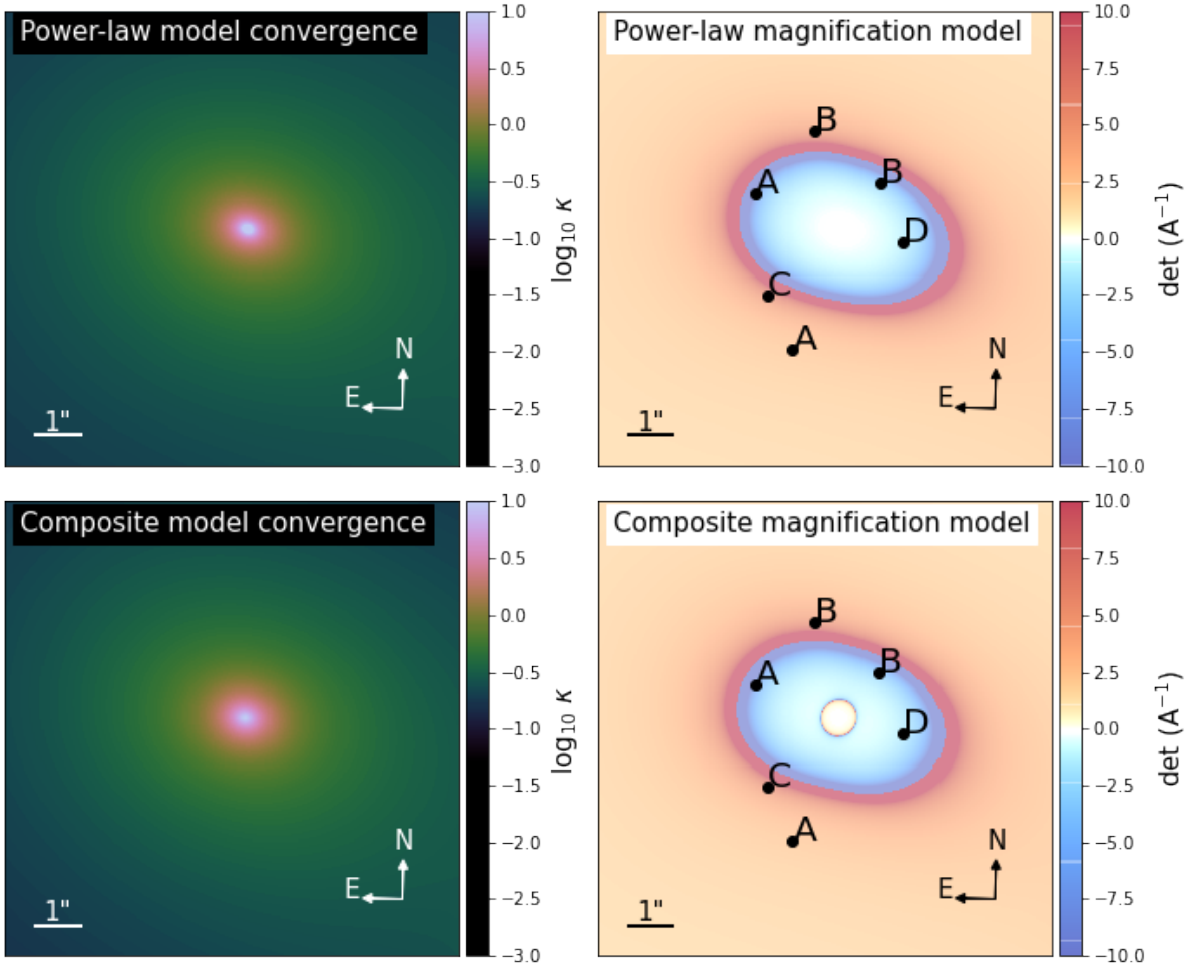

Figure 3.10: Convergence model (left) and magnification model (right) plots for both mass model assumptions of the the primary deflector, power-law (top) and composite (bottom) model. The magnification plots indicate the predicted position of the lensed quasar images.

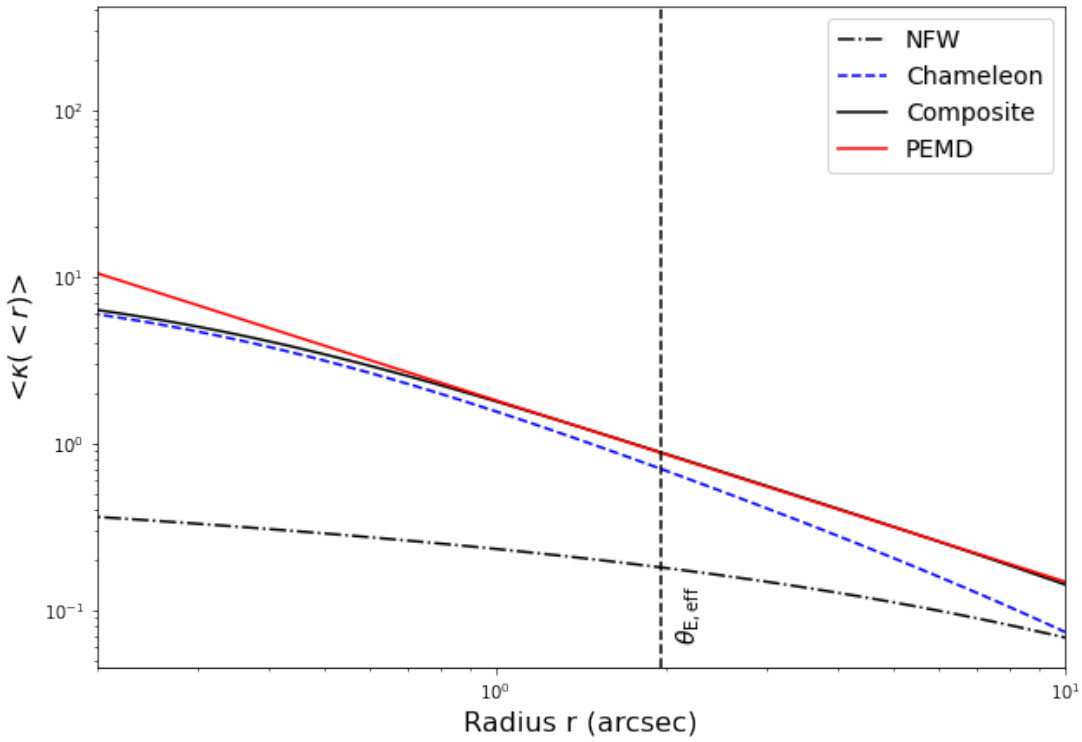

Figure 3.11: Mean convergence within a circle of radius r. Shown are components of the composite mass profile assumption for the primary deflector, NFW - black dashdotted line, Chameleon - blue dashed line, along with the combined convergence of the composite case, black solid line, and the power-law profile assumption, red solid line. Also plotted is the effective Einstein radius to provide a reference point.

posed on the axis ratio of the dark matter profile, the combined convergence of the composite model matches the convergence of the power-law mass profile case in the region where we observe the lensed quasar images. This is further demonstrated in Figure 3.12, where we show the ratio of the circularized mean convergence between the composite and power-law model main deflector assumption. As illustrated, the resulting convergence of the two model assumptions is nearly identical in the region from around $0.6\theta_{\rm E}$ up to approximately $5\theta_{\rm E}$. To differentiate between the two different model parameterizations, additional information is required, such as stellar velocity dispersion measurements of the primary deflector's central region.

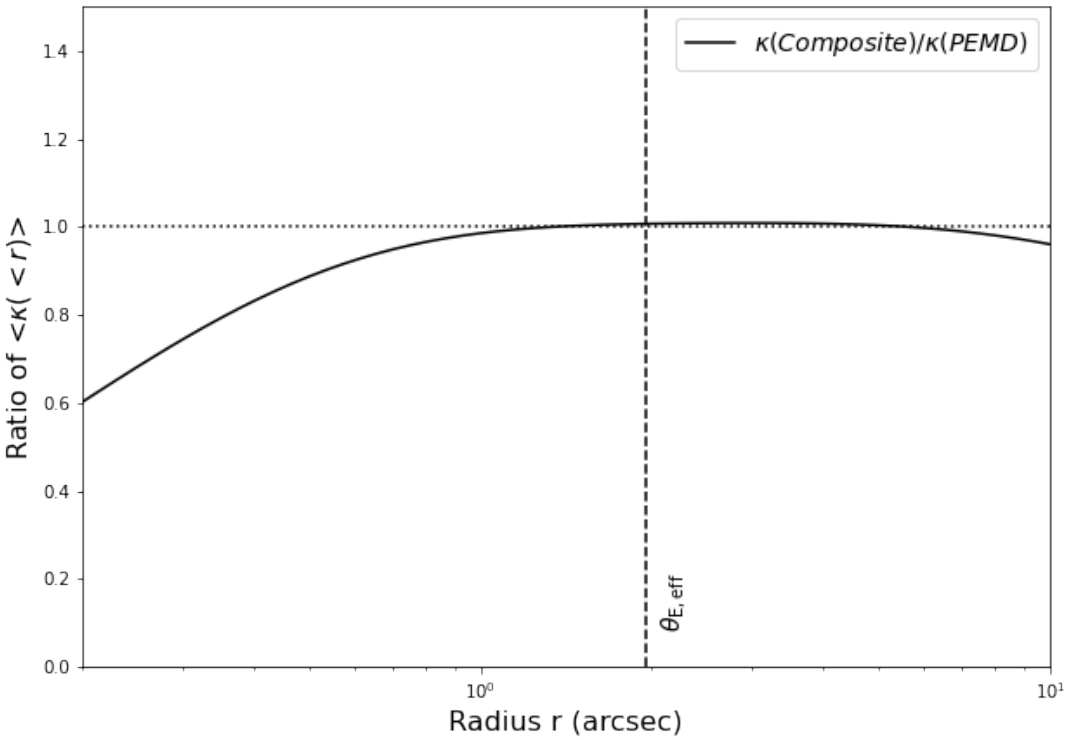

Figure 3.12: Ratio of the circularized averaged convergence, as a function of radius r, between composite and power-law mass model assumption of the primary deflector.

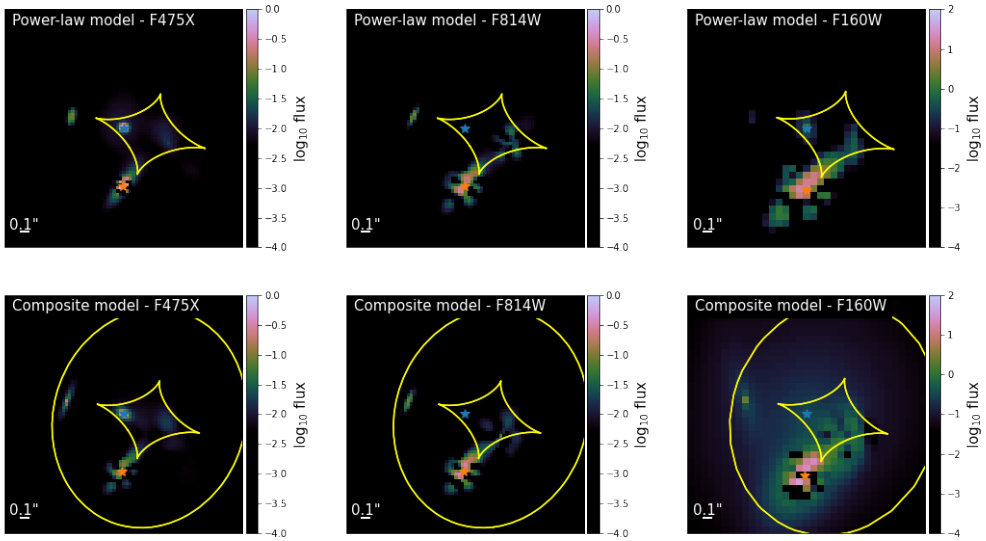

Figure 3.13: Reconstructed sources for both, power-law and composite models. The yellow lines represent the inner and outer caustics curves of the critical lines. The blue star and the orange start indicate the location of the quadruply and doubly imaged quasar, respectively, in the source plane.

Figure 3.13 shows models for the reconstructed lensed sources in the source plane for the power-law model profile assumption (top row) and the composite model (bottom row). For each model the reconstructed sources are sorted by band from shortest to longest wavelength, UVIS filters F475X and F814W in the left and center panels, respectively, and IR band F160W in the right panels. The yellow lines in the plots represent the inner and outer caustic lines, corresponding to the critical curves in the image plane. The location of the quadruply imaged quasar is marked by the blue star, while the position of the doubly lensed quasar is indicated by the orange star.

In Table 3.3 we list model parameters at the position of the quadruply and doubly imaged quasar for future microlensing time-delay studies. Specifically, we show total and the stellar convergence at the image positions along with the external shear strength, the strength of the spin 1 and spin 3 flexion, and the image magnification. The top part of the table tabulates the results of the power-law model assumptions while the lower portion list the

Table 3.3: Lensing results at image positions for quadruply and doubly imaged quasar, obtained from our fiducial power-law and composite model. We show the total convergence, κ, the stellar convergence, $\kappa_\star$, the shear, $\gamma_{\rm shear}$, the flexion strength, F and G, and the image magnification, μ. For the power-law model, the stellar convergence is estimated from the lens flux in the IR band, assuming a constant mass-to-light ratio, while the stellar convergence for the composite profile results directly from the the Chameleon mass profile fit(also linked to flux in IR band).

Model	Im	κ	$\kappa_\star$	$\gamma_{\rm shear}$	F	G	μ
Power-law	A	0.57	0.32	0.58	0.23	0.63	-6.73
	B	0.47	0.25	0.33	0.15	0.49	5.91
	C	0.42	0.26	0.36	0.14	0.56	4.85
	D	0.74	0.45	0.88	0.74	1.35	-1.43
	A'	0.29	0.18	0.23	0.10	0.26	2.24
	B'	0.67	0.44	0.62	0.36	1.68	-3.57
Composite	A	0.53	0.29	0.62	0.28	0.64	-6.51
	B	0.46	0.19	0.36	0.18	0.50	5.93
	C	0.40	0.21	0.38	0.17	0.56	4.63
	D	0.77	0.47	0.79	0.66	1.18	-1.72
	A'	0.29	0.12	0.23	0.12	0.26	2.25
	B'	0.72	0.43	0.59	0.46	1.45	-3.63

composite model results. The stellar convergence for the power-law profile is estimated from reconstructed flux in the F160W (IR) band under the assumption of a constant mass to light ratio. For the composite model assumption, we use the results of the Double Chameleon profile to estimate the stellar convergence at the image positions.

3.5.2 Model comparisons

The models presented in this paper vary significantly in terms of complexity and underlying assumptions for included model components. Furthermore, during the assessment of systematic uncertainties, we also change the size of the likelihood computation mask used to compute the a model's χ^2 value. To obtain a fair comparison between models, we need to account for the variations in model parameters and number of data points used during the likelihood computation. Therefore, we use the BIC, defined in Expression 3.23, as a proxy to scale the results of each model based on a corresponding statistical weight, w.

Now, the probability of a model M_i given the data, $\boldsymbol{d}_{HST}$, is formulated as

$$\begin{aligned} P(M_i|\boldsymbol{d}_{HST}) &\propto P(\boldsymbol{d}_{HST}|M_i)P(M_i) \\ &\approx \exp\left[-\frac{1}{2}\mathrm{BIC_i}\right] P(M_i). \end{aligned} \tag{3.43}$$

Hence, the relative probability between two models, M1 and M2, given the data, can be written in terms of the model's corresponding BIC values

$$\frac{P(M_1|\boldsymbol{d}_{HST})}{P(M_2|\boldsymbol{d}_{HST})} \propto \exp\left[-\frac{1}{2}(\mathrm{BIC}_1 - \mathrm{BIC}_2)\right]. \tag{3.44}$$

We use this formulation of relative probability and follow Birrer et al. (2019) and Shajib et al. (2022) to define the evidence ratio function, $f(x)$, based on the difference between a model's corresponding BIC value and the lowest BIC among all possible model configurations, $\mathrm{BIC}_{\mathrm{min}}$

$$f(x) \equiv \begin{cases} 1 & , x \leq \mathrm{BIC}_{\mathrm{min}} \\ \exp\left[-\frac{1}{2}(x - \mathrm{BIC}_{\mathrm{min}})\right] & , x > \mathrm{BIC}_{\mathrm{min}} \end{cases} \tag{3.45}$$

To find a model's associated statistical weight, w_i, we convolve the evidence ratio with a Gaussian, g, centered on the BIC value for the model with a variance of σ^2_{BIC}

$$w_i = f(x) * g(\mathrm{BIC}_i, \sigma_{\mathrm{BIC}}). \tag{3.46}$$

The standard deviation, σ^2_{BIC}, represents the total uncertainty in our models and is composed of statistical fluctuations, σ_{int}, and systematic uncertainties, σ_{sys}, added in quadrature

$$\sigma^2_{\mathrm{BIC}} = \sigma^2_{\mathrm{int}} + \sigma^2_{\mathrm{sys}}. \tag{3.47}$$

To determine intrinsic fluctuations, σ_{int}, that arise from the inherent stochasticity in the

MCMC, we run the chain for each model twice. The final statistical scatter added to the total uncertainty in Expression 3.47 is then computed by averaging the error between the twice executed chains across all models. We assess systematic uncertainties, $\sigma_{\rm sys}$, in similar fashion as described in Birrer et al. (2019) and Shajib et al. (2022), namely by finding the standard deviation in BIC values between models that differ in terms of configuration or complexity by only one component or only one fixed parameter setting. As with the intrinsic uncertainties, we take the mean of the systematic scatter across all models before adding it to our total error budget, $\sigma_{\rm BIC}$. Finally, we compute $\sigma_{\rm int}$ to be 20.32 and find $\sigma_{\rm sys} = 104.03$ for the power-law model and $\sigma_{\rm sys} = 240.61$ for the composite model, which combine to a total standard deviation for the BIC, used on the computation of the statistical weights (Expression 3.46), of $\sigma_{\rm BIC} = 106.00$ and $\sigma_{\rm BIC} = 240.61$ for the power-law and composite model, respectively.

Table 3.4 lists the BIC evaluation for our models sorted from lowest BIC number to highest. Each BIC is computed using the corresponding maximum value of the likelihood sampled in each MCMC chain. Since the radii of the likelihood computation mask differ for the assessment of systematic uncertainties, we separate the modeling results according to the masking radii. We further separate the models based on the mass profile assumption for the primary deflector, power-law vs. composite model, and show the difference in BIC for each result with respect to the best fit in each category. For each model we include the corresponding statistical weight used in the assessment of the total error budget.

In Figure 3.14 we plot the difference in RA and DEC between the image positions of the lensed quasars as inferred by our models and the astrometric positions of the quasar images as measured by the *Gaia* satellite. To provide reference points for the image position comparison we add a boxes at 10 mas, 40 mas, which corresponds to the pixel size in the UVIS bands. The outer box is drawn at 80 mas, reflecting the size of a pixel in the IR band.

As previously indicated, the two assumptions for the main deflector's mass profile result in a convergence that is nearly identical and differs only in the central region. To demonstrate that it would be possible to distinguish the two models through central stellar velocity

Table 3.4: BIC evaluations including corresponding statistical weights for various models, separated based on the mass profile assumption for the primary deflector. The models are sorted by the radii of the mask used in the computation of the likelihood and the Δ BIC is computed with respect to the best fit of each category.

Model	$n_{\max}$	MCMC Run	Size of likelihood computation mask 3.9/4.9/7.4 ($''$) BIC	Δ BIC	Weight	4.0/5.0/7.5 ($''$) BIC	Δ BIC	Weight	4.1/5.1/7.6 ($''$) BIC	Δ BIC	Weight
Power-law	$-, 5, -, 5$	1	88417.37	3.33	0.494	92448.85	4.40	0.490	96610.59	0.00	0.508
	$-, 5, -, 5$	2	88414.04	0.00	0.507	92444.45	0.00	0.507	96616.51	5.92	0.485
	$1, 7, 1, 7$	1	88682.86	268.83	0.006	92739.25	294.80	0.003	96895.26	284.67	0.004
	$1, 7, 1, 7$	2	88681.47	267.43	0.006	92738.42	293.96	0.003	96894.25	283.66	0.004
	$-, 7, -, 7$	1	88519.38	105.34	0.165	92575.57	131.12	0.112	96723.49	112.90	0.149
	$-, 7, -, 7$	2	88517.42	103.38	0.169	92576.79	132.34	0.109	96720.7	110.11	0.154
	$-, 7, 1, 7$	1	88596.13	182.09	0.045	92669.07	224.62	0.018	96811.69	201.10	0.030
	$-, 7, 1, 7$	2	88593.92	179.88	0.047	92665.98	221.53	0.019	96815.26	204.67	0.028
Composite	$-, 5, -, 5$	1	90944.51	0.00	0.504	95120.28	0.61	0.503	99351.19	7.40	0.492
	$-, 5, -, 5$	2	90948.09	3.58	0.497	95119.67	0.00	0.503	99343.79	0.00	0.503
	$1, 7, 1, 7$	1	91505.02	560.52	0.010	95704.91	585.24	0.007	99923.26	579.47	0.008
	$1, 7, 1, 7$	2	91510.14	565.63	0.010	95707.40	587.73	0.007	99928.32	584.53	0.008
	$-, 7, -, 7$	1	91442.27	497.76	0.020	95704.91	585.24	0.008	99856.77	512.98	0.017
	$-, 7, -, 7$	2	91431.59	487.08	0.022	95707.40	587.73	0.008	99858.16	514.37	0.017
	$-, 7, 1, 7$	1	91469.62	525.11	0.015	95704.91	585.24	0.008	99898.59	554.80	0.011
	$-, 7, 1, 7$	2	91458.47	513.96	0.017	95707.40	587.73	0.007	99892.46	548.67	0.012

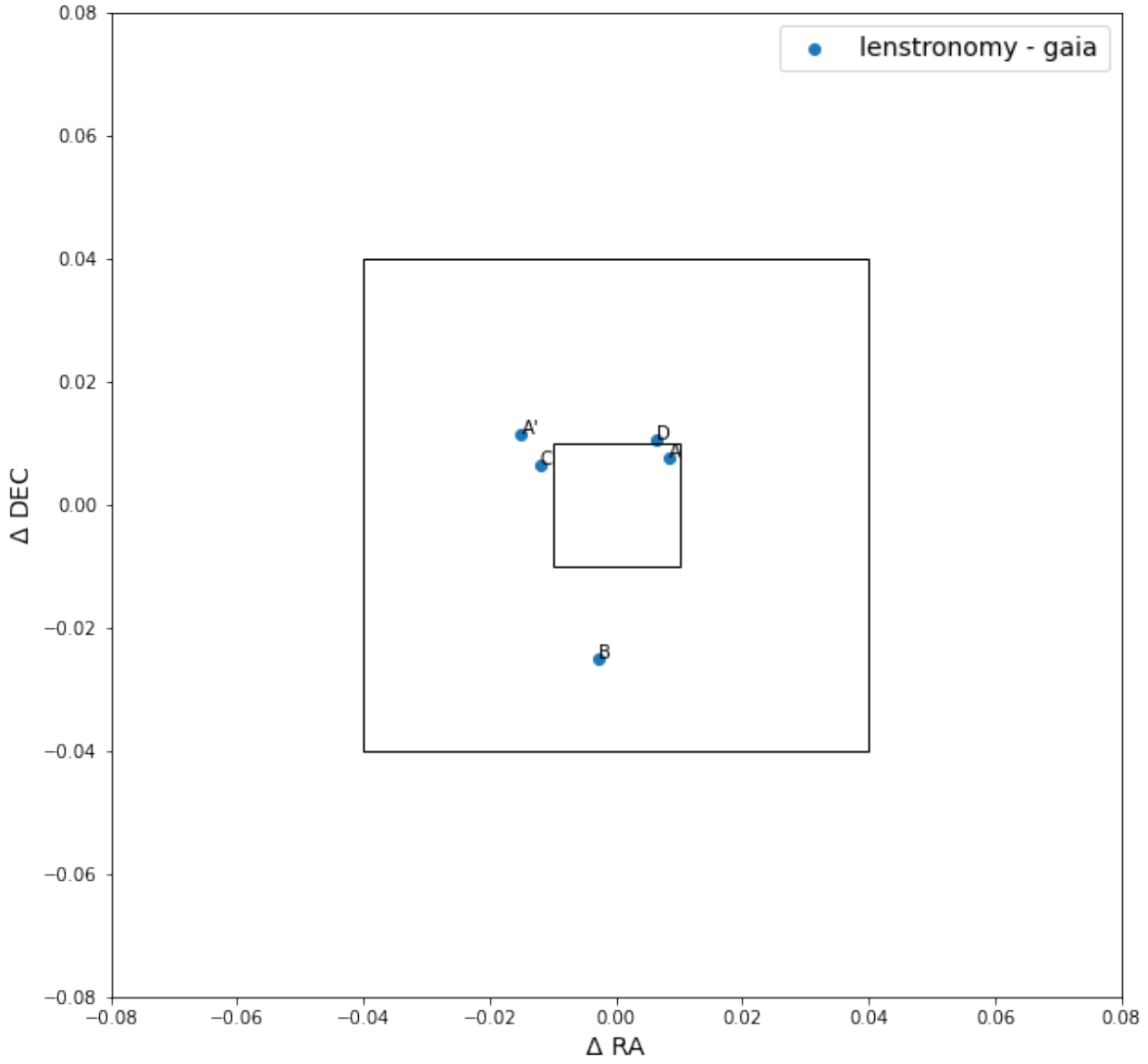

Figure 3.14: Comparison between image positions inferred by our models and astrometric image positions as measured by the *Gaia* satellite. For reference, boxes are drawn at 10 mas, 40 mas (pixel size in UVIS), and 80 mas (IR pixel size).

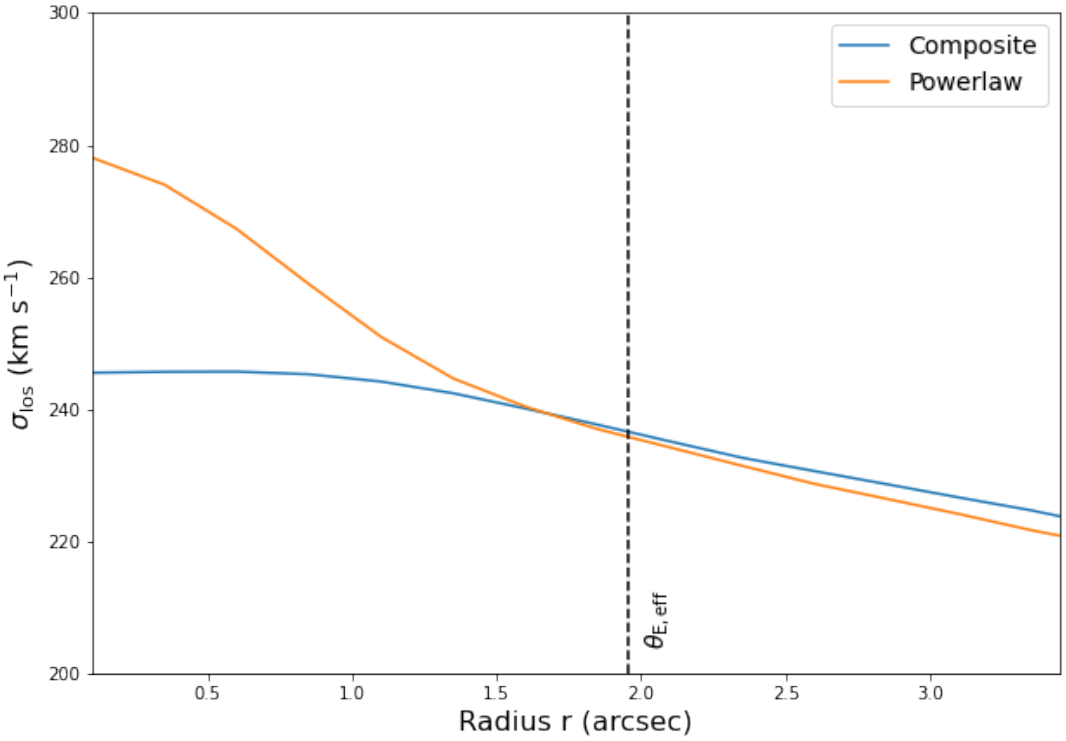

Figure 3.15: Line-of-sight stellar velocity dispersion profiles for the composite (blue line) and power-law (orange line) assumption of the main deflector mass. Both velocity dispersion profiles assume a 1.″ seeing with a 0.″25 binning.

dispersion measurements, we show in Figure 3.15 the line-of-sight velocity dispersion profiles computed for the power-law model (orange line) and for our composite model (blue line). In both cases the dispersion profiles assume a seeing of 1.″ and are binned at 0.25″. As demonstrated, we expect the stellar velocity dispersion of the composite model to stay approximately constant within the primary deflector's center, resulting from the flattened mass profile.

3.5.3 Predicted time-delays

Assuming a flat ΛCDM cosmology with $\Omega_m = 0.3$ we present predictions for measurable time-delays between image pairs for both lensed quasars. Table 3.5 lists the time-delays in

Table 3.5: Predicted time-delays between image positions of the quadruply and the doubly imaged quasar for power-law and composite model assumptions. The time-delay in the table assume a standard ΛCDM cosmology with $H_0 = 70$ km s^{-1} Mpc^{-1}.

Image Pair	Power-law	Composite	Combined
AB	2.97 ± 0.05	2.75 ± 0.03	2.88 ± 0.12
AC	5.09 ± 0.08	4.99 ± 0.04	5.04 ± 0.08
AD	-27.59 ± 0.15	-26.45 ± 0.14	-27.09 ± 0.58
A'B'	-78.74 ± 0.40	-78.51 ± 0.39	-78.64 ± 0.41

days, separated by underlying model assumption for the mass profile of the main deflector, power-law as well as composite profile. All delays in Table 3.5 include a factor of λh_{70}^{-1}, where λ represents the MSD factor introduced in Section 3.2.2, which includes the external convergence, $\kappa_{\rm ext}$, and the internal MST parameter, $\lambda_{\rm int}$. We define h_{70} as the dimensionless Hubble constant with value $h_{70} = H_0/70$ km s^{-1} Mpc^{-1}.

We find that the predicted time-delays of the composite model agree well with the predictions based on the power-law model assumption. This agreement can especially be observed in the time-delay prediction for the images of the doubly lensed quasar, were both model assumptions are within 0.3 percent. As demonstrated in the plots of Figures 3.6 and 3.7, the time-delay for the doubly imaged quasar is mainly driven by the power-law slope, while the shorter time-delays between image pairs AB and AC of the quad are mainly correlated with the spin 3 flexion components and the external shear strength.

Figure 3.16 shows probability densities of predicted time-delays for the image pair of the doubly lensed quasar based on the models explored during the assessment of systematic uncertainties. We further plot the probability densities for our fiducial power-law model (shown in solid red) and our fiducial model for the composite mass model assumption (shown in solid blue). Combining the probabilities based on the corresponding BIC weight, we also present the aggregate time-delay prediction of the doubly imaged quasar (solid black line).

Comparing our predictions to the time-delays presented in Lemon et al. (2022), we find generally good agreement, with the longest delay for the doubly imaged quasar shown by

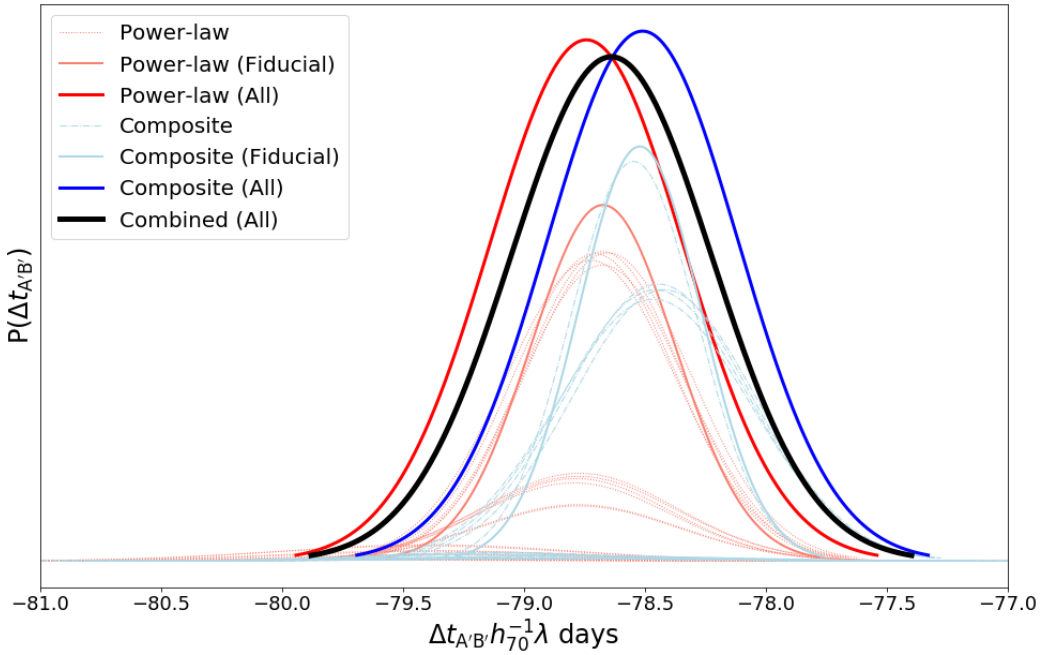

Figure 3.16: Probability density of predicted time-delay for image pair of the doubly lensed quasar. Shown are the delay predictions for the various power-law models (dotted salmon colored) and the various composite models (dot-dashed light blue), all according to their corresponding BIC weight. Also plotted are the delay predictions for the fiducial power-law model (solid red) and the fiducial composite model (solid blue). The thick black solid line represents the combined probability density of all BIC weighted models.

Lemon et al. (2022) at 79.2 days. The work in Lemon et al. (2022) also assumes a flat ΛCDM cosmology with $H_0 = 70$ km s^{-1} Mpc^{-1}. Compared to our prediction of 78.7 days from the power-law model, the difference between the results only represents only 0.6 percent. We further compare our predicted time-delays to the results presented in Mangat et al. (2021). The delay for the doubly lensed quasar is computed to be 88.1 days by Mangat et al. (2021), using a value for the Hubble constant of $H_0 = 67.8$ km s^{-1} Mpc^{-1}. Converting this result under the assumption of $H_0 = 70$ km s^{-1} Mpc^{-1} and comparing it to the time-delay prediction presented in this paper, we find a discrepancy of approximately 8 percent, which is not unexpected as the model in Mangat et al. (2021) relies on only one lensed source component decoupled from centroid of the quasar. In our models we find that the fits overwhelmingly improve for cases in which the centroids are joined between the host and the lensed quasar. Furthermore, our models incorporate secondary lensed sources, which provide additional constraints on the mass model of the lensing galaxy.

A comparison with the findings presented in Schmidt et al. (2023b) shows generally good agreement, with the time-delays for image pairs AB and AC matching the results of this works within the margin of error. The longest time-delay for the quadruply imaged quasar (image pair AD) is found to be 26.0 ± 0.2 days in the automated modeling pipeline results of Schmidt et al. (2023b), which is 0.5 days (or 1.7%) less than the prediction of our composite model.

3.6 Summary

We use HST observations of J1721+8842 to reconstruct the mass and light distribution of the system. We use the software package Lenstronomy (Birrer and Amara, 2018; Birrer et al., 2021) to model the lens system based on two distinct and standard assumptions for the parametrization of the main deflector, namely a power-law total mass density profile and a composite profile consisting of a dark matter halo and a stellar component that follows the

light. The main conclusions of our analysis are summarized by the following points:

- J1721+8842 is an extraordinary strong lens system with two lensed quasars, the first quadruply imaged and the second doubly imaged. In addition to the quasar hosts, we find two multiply imaged galaxies that we include in our models. With these four individual lensed sources, with images spanning a range of radii, we find that the mass distribution of the primary lensing galaxy is more constrained than in a typical quad consisting of a single multiply imaged source.

- Higher order perturbations beyond external convergence and shear are necessary to accurately model the mass distribution of J1721+8842. Quantitatively, we find that the exclusion of the spin 1 and spin 3 flexion model components results in a Bayes Information Criterion (BIC) increase of 1,544 compared to the best fit, a highly significant decrease in quality. Additionally, our analysis indicates a correlation between the spin 3 flexion and the time-delays for images pairs AB and AC of the quadruply imaged quasar. The time-delays for the same image pairs (AB and AC) also show a dependence on the external shear strength, $\gamma_{\rm ext}$. In constrast, the comparatively longer time-delays for image pair AD, of the quad, and image pair A'B', of the doubly imaged quasar, depend almost exclusively on the slope of the power-law profile, γ.

- In the radial range from approximately $0.6\theta_{\rm E}$ to around $5\theta_{\rm E}$ the mean convergence under the central deflector's best fit power-law mass profile is nearly identical to that of the composite profile model. In other words, the mass profiles for the two model assumptions (power-law vs. composite) become effectively indistinguishable in the region where the lensed quasar images are observed.

- Since our analysis demonstrates that data from HST observations alone proves insufficient to decisively favor one model assumption for the main deflector's mass profile over the other, we show that measurements of the central stellar velocity dispersion can be used to differentiate between the underlying model parameterizations. Under the

assumption of 1.″seeing with a circular profile binned at 0.″25, a measurement of the stellar velocity dispersion with precision 5-10% interior to 1.″ is sufficient to distinguish the two models.

- The time-delays for the doubly imaged quasar, which represents the longest delay in this configuration, agrees between both model assumption for the main deflector (power-law and composite model) at the percent level. In a flat ΛCDM cosmology, with $\Omega_{\rm m} = 0.3$ and $\Omega_\Lambda = 0.7$, the power-law model predicts the following time-delays between image pairs, in order from longest to shortest: $\Delta t_{\rm A'B'} = -78.7 \pm 0.4 h_{70}^{-1} \lambda$ days, $\Delta t_{\rm AD} = -27.6 \pm 0.2 h_{70}^{-1} \lambda$ days, $\Delta t_{\rm AC} = 5.1 \pm 0.1 h_{70}^{-1} \lambda$ days, and $\Delta t_{\rm AB} = 3.0 \pm 0.1 h_{70}^{-1} \lambda$ days, with $h_{70} = H_0/70$ km s^{-1} Mpc^{-1} as the dimensionless Hubble constant and λ as the MSD factor, which contains the internal MST parameter, $\lambda_{\rm int}$, and the external convergence, $\kappa_{\rm ext}$. Using the same cosmology, the time-delay predictions for the combined results of the power-law and composite models, again in order from longest to shortest, are: $\Delta t_{\rm A'B'} = -78.6 \pm 0.4 h_{70}^{-1} \lambda$ days, $\Delta t_{\rm AD} = -27.1 \pm 0.6 h_{70}^{-1} \lambda$ days, $\Delta t_{\rm AC} = 5.0 \pm 0.1 h_{70}^{-1} \lambda$ days, and $\Delta t_{\rm AB} = 2.9 \pm 0.1 h_{70}^{-1} \lambda$ days.

A future paper will build on our models and time-delay predictions for J1721+8842, and incorporate measurements of observed time-delay, a spectroscopic measurement of the stellar velocity dispersion, and an estimate for the external convergence based on a model for the line-of-sight mass distribution to present a complete H_0 inference.

Acknowledgements

This research is based on observations made with the NASA/ESA Hubble Space Telescope obtained from the Space Telescope Science Institute, which is operated by the Association of Universities for Research in Astronomy, Inc., under NASA contract NAS 5-26555. These observations are associated with programs HST-GO-15320 and HST-GO-15652. Support for the two programs was provided by NASA through a grant from the Space Telescope Science

Institute, which is operated by the Association of Universities for Research in Astronomy, Inc., under NASA contract NAS 5-26555.

TS TT acknowledge support by the the National Science Foundation through grant NSF-AST-1906976 and NSF-AST-1907396 "Collaborative Research: Toward a 1% measurement of the Hubble Constant with gravitational time-delays". TT acknowledges support by the Gordon and Betty Moore Foundation. MM acknowledges support by the Swiss National Science Foundation (SNSF) through mobility grant P500PT_203114. SB acknowledges support from the Department of Physics & Astronomy, Stony Brook University. DS acknowledges the support of the Fonds de la Recherche Scientifique-FNRS, Belgium, under grant No. 4.4503.1. This work is also supported by NASA through the NASA Hubble Fellowship grant HST-HF2-51492 awarded to AJS by the Space Telescope Science Institute, which is operated by the Association of Universities for Research in Astronomy, Inc., for NASA, under contract NAS5-26555. AG FC acknowledge funding and support by the SNSF.

This research made use of Lenstronomy (Birrer and Amara, 2018; Birrer et al., 2021), emcee (Foreman-Mackey et al., 2013), fastell (Barkana, 1998), sextractor (Bertin and Arnouts, 1996), NumPy (Oliphant, 2015), SciPy (Jones et al., 2001), Astropy (Astropy Collaboration et al., 2018), Jupyter (Kluyver et al., 2016), Matplotlib (Hunter, 2007), seaborn (Waskom, 2021), getdist (https://github.com/cmbant/getdist), and STARRED (Michalewicz et al., 2023; Millon et al., 2024) .

Chapter 4

Strong lens model and time-delay predictions for J1721+8842, the first Einstein zigzag lens

4.1 Background

The Hubble constant (H_0), the current expansion rate of the Universe, is a quantity of fundamental importance in the current cosmological debate. The standard cosmological model based on cold dark matter (CDM) and a cosmological constant, Λ (hence ΛCDM), successfully matches a range of observations including the cosmic microwave background (CMB) radiation, the Big Bang nucleosynthesis, baryon acoustic oscillations (BAOs), galaxy clustering and the formation of large-scale structures, and measurements of Type Ia supernovae (SNIa) distances (e.g., Riess et al., 1998; Perlmutter et al., 1999; Eisenstein et al., 2005; Planck Collaboration et al., 2020). Yet, in the flat ΛCDM, there is an increasing tension between the Hubble constant inferred from early Universe constraints and direct measurements using local Universe probes. For example, the analysis of anisotropies in the CMB result in $H_0 = 67.4 \pm 0.5$ km s^{-1} Mpc^{-1} (Planck Collaboration et al., 2020) in a flat ΛCDM,

whereas local measurements based on Cepheid variables and SNIa as rungs in the cosmic distance ladder give a Hubble constant of $H_0 = 73.04 \pm 1.04$ km s^{-1} Mpc^{-1} (Riess et al., 2022). The difference results in a tension of high statistical significance (see, e.g., Abdalla et al., 2022, and references therein). If independent methods confirm the tension is not caused by unknown systematic uncertainties in the measurements, then new physics beyond a flat ΛCDM model is required. Examples of proposed solutions include changing the sound horizon at recombination through a currently unknown relativistic particle or a form of early dark energy (see, e.g., Knox and Millea, 2020; Di Valentino et al., 2021; Schöneberg et al., 2022; Vagnozzi, 2023).

Strong gravitational lensing of a variable background source provides a powerful independent cosmological probe through which the Hubble constant can be measured in one step, thus bypassing the local distance ladder (Refsdal, 1964; Treu and Marshall, 2016; Treu et al., 2022; Treu and Shajib, 2024; Birrer et al., 2024). Instead of relying on standard candles, strong lensing measures distances (and therefore H_0) from the differences in the travel time of photons traversing the gravitational potential of the foreground deflector (see, e.g., Treu and Koopmans, 2002; Suyu et al., 2010, 2014; Treu and Marshall, 2016; Birrer et al., 2016; Bonvin et al., 2017; Birrer et al., 2019; Shajib et al., 2020).

One of the key ingredients of time-delay cosmography are accurate and precise gravitational lens models. In this paper, we present such models for the exceptionally complex gravitational lens system J1721+8842 (see Lemon et al., 2018, for discovery), the first-ever discovered galaxy-scale strong lens in an Einstein zigzag configuration (originally hypothesized by Collett and Bacon, 2016). Using recent JWST observations, Dux et al. (2025b) recently revealed that the system consists of a single active galactic nucleus at $z = 2.36$, producing six images as a result of compound lensing by two deflectors. The foreground lensing galaxy is located at redshift $z = 0.184$, and the deflector in between is at $z = 1.885$. This interpretation has been corroborated by the fact that all images measure the same redshift and that the light curves are identical within errors (Dux et al., 2025b). This discovery

renders the previous models by Mangat et al. (2021) and the automated models by Schmidt et al. (2023b) and Ertl et al. (2023) obsolete.

This zigzag configuration is truly remarkable, as it not only places tight constraints on the distribution of mass in the primary deflector, but – compared to typical quadruply lensed quasars – the system also provides additional images and thus increases the set of measurable delays from 6 to 15 (or from 3 to 5 for a single reference image). The specific configuration also strongly constrains the overall gravitational optics of the systems, as the creation of six images requires a very tight alignment.

Our aim is to show that this configuration results in percent-level uncertainty in the predicted time delays within the context of the herein presented models. The final precision and accuracy will of course depend on breaking the multiplane mass-sheet degeneracy (MSD; Falco et al., 1985; Schneider and Sluse, 2014; Schneider, 2019), which will be discussed in a forthcoming paper (Millon et al., in prep). However, the precision, number, and length (up to ∼200 days) of the predicted delays are crucial to breaking the MSD and demonstrating the tremendous potential of this Einstein zigzag for cosmography (for comparison, the most precise measurement to date reached a 3.9% precision on H_0; Shajib et al., 2020).

We note that the lens model has been constructed without knowledge of the measured time delays, which are currently being derived and kept blind from this modeling effort. Stellar velocity dispersion and external convergence are also currently being measured. Once all ingredients are available, we will combine them with the relative Fermat potentials, given by our model, to determine the Hubble constant (H_0) and other cosmological parameters. We note that the previous work by our collaboration has typically followed the reverse order, with a lens model being the final step (notable exceptions are the work by Shajib et al., 2022; Chen et al., 2022). For the purpose of determining H_0, the order does not matter, and blindness can be imposed either way in order to prevent unconscious experimenter bias.

This chapter is organized as follows. In Section 4.2 we summarize the theoretical background of strong gravitational lensing, discuss strong lens observables, and review the formal

notation for the Bayesian framework used in our inference of time-delay predictions. Section 4.3 presents a description of the discovery of J1721+8842, the imaging of the target, and the data reduction. In Section 4.4 we discuss the individual components of our lens models and provide details on the parameterizations used in our analysis, including informative priors implemented to guide the results and the assessment of systematic uncertainties in the underlying choices for lens model components. The results of our analysis are presented in Section 4.5 along with measurable time-delay predictions between images pairs of the lensed quasar. Finally, Section 4.6 provides a brief summary. Whenever necessary, we used a cosmological concordance model with parameters $H_0 = 70$ km s^{-1} Mpc^{-1}, $\Omega_{\mathrm{m},0} = 0.3$, and $\Omega_{\Lambda,0} = 0.7$.

4.2 Modeling analysis

Our analysis uses Hubble Space Telescope (*HST*) imaging data, $\boldsymbol{d}_{HST}$, in three bands, UVIS (F475X and F814W) as well as IR (F160W), to make an inference on the lensing potential, ψ, for J1721+8842 and on the position of the lensed source, β. In addition to parameters for the mass model of the lens, ξ_{mass}, the *HST* observations further allowed us to obtain constraints on the parameterization of the surface brightness distribution for the primary deflector, ξ_{light}, and for the lensed sources, ξ_{source}.

In terms of organization, this section first gives a description of the strong lensing formalism and describes how our models connect to observables, presented in Section 4.2.1. We then discuss lensing degeneracies and potential sources of systematic uncertainties in Section 4.2.2, while Section 4.2.3 outlines the formal notation of the Bayesian inference used in our analysis.

4.2.1 Lensing theory and strong-lensing observables

Compared to a path without perturbation, the excess time-delay (see, e.g., Schneider et al., 1992; Blandford and Narayan, 1992) for a lensed point source at position $\boldsymbol{\beta} = (\beta_1, \beta_2)$ in the source plane, observed at angular position $\boldsymbol{\theta} = (\theta_1, \theta_2)$ in the lens (or image) plane, is described by

$$t(\boldsymbol{\theta}; \boldsymbol{\beta}) = \frac{D_{\Delta t}}{c} \left[\frac{(\boldsymbol{\theta} - \boldsymbol{\beta})^2}{2} - \psi(\boldsymbol{\theta}) \right], \tag{4.1}$$

where c is the speed of light, $\psi(\boldsymbol{\theta})$ represents the deflection potential of the lens, and whereby the time-delay distance, $D_{\Delta t}$, is defined as

$$D_{\Delta t} \equiv (1 + z_{\rm d}) \frac{D_{\rm d} D_{\rm s}}{D_{\rm ds}}, \tag{4.2}$$

with $D_{\rm d}$, $D_{\rm s}$, and $D_{\rm ds}$, as the angular diameter distance to the main deflector, to the lensed source, and between the source and the deflector, respectively. $z_{\rm d}$ represents the redshift of the lensing galaxy.

The delay in the arrival time of photons emitted by the same source, but observed at two different positions in the image plane, $\boldsymbol{\theta}_{\rm A}$ and $\boldsymbol{\theta}_{\rm B}$, can then be expressed as

$$\Delta t_{\rm AB} = \frac{D_{\Delta t}}{c} \Delta\phi_{\rm AB}, \tag{4.3}$$

where $\Delta\phi_{\rm AB}$ is the difference in the Fermat potential, $\phi(\boldsymbol{\theta_{\rm A}}; \boldsymbol{\beta}) - \phi(\boldsymbol{\theta_{\rm B}}; \boldsymbol{\beta})$, between the two image positions, with the Fermat potential defined as

$$\phi(\boldsymbol{\theta}; \boldsymbol{\beta}) = \frac{1}{2}(\boldsymbol{\theta} - \boldsymbol{\beta})^2 - \psi(\boldsymbol{\theta}). \tag{4.4}$$

With that definition,

$$\Delta\phi_{\rm AB}(\boldsymbol{\theta_{\rm A}}; \boldsymbol{\theta_{\rm B}}; \boldsymbol{\beta}) = \frac{1}{2} \left[(\boldsymbol{\theta_{\rm A}} - \boldsymbol{\beta})^2 - (\boldsymbol{\theta_{\rm B}} - \boldsymbol{\beta})^2 \right] - \left[\psi(\boldsymbol{\theta_{\rm A}}) - \psi(\boldsymbol{\theta_{\rm B}}) \right], \tag{4.5}$$

where the first difference is the geometric term as the result of the light traversing paths of different lengths due to different deflection angles at the corresponding image positions, while the second term describes the difference in the gravitational delay photons experience while traveling through the potential of the lensing galaxy.

The deflection angle, $\boldsymbol{\alpha}(\boldsymbol{\theta})$, at an image position, $\boldsymbol{\theta}$, can be expressed as the gradient of the deflection potential, $\boldsymbol{\alpha}(\boldsymbol{\theta}) = \nabla\psi(\boldsymbol{\theta})$, and is dictated by the lens equation, $\boldsymbol{\beta} = \boldsymbol{\theta} - \boldsymbol{\alpha}(\boldsymbol{\theta})$, which describes the lensing of a source at position $\boldsymbol{\beta}$ by the deflection potential, $\psi(\boldsymbol{\theta})$. In the limit of the deflector mass being confined to a two-dimensional sheet (the lens plane) with a physical projected surface mass density, $\Sigma(\boldsymbol{\theta})$, (the thin lens approximation), the deflection angle is related to the dimensionless projected surface mass density, or convergence, κ, by

$$\kappa(\boldsymbol{\theta}) = \frac{1}{2}\boldsymbol{\nabla} \cdot \boldsymbol{\alpha}(\boldsymbol{\theta}), \tag{4.6}$$

where $\kappa(\boldsymbol{\theta})$ is defined as the surface mass density scaled by the critical surface mass density, $\kappa(\boldsymbol{\theta}) \equiv \Sigma(\boldsymbol{\theta})/\Sigma_{\rm cr}$, with

$$\Sigma_{\rm cr} = \frac{c^2}{4\pi G}\frac{D_{\rm s}}{D_{\rm d}D_{\rm ds}}. \tag{4.7}$$

Therefore, the dimensionless convergence is related to the deflection potential of the lensing galaxy by

$$\kappa(\boldsymbol{\theta}) = \frac{1}{2}\nabla^2\psi(\boldsymbol{\theta}). \tag{4.8}$$

High-resolution observations, taken with the Hubble Space Telescope, allow us to constrain the deflections potential, ψ, along with the unknown position of the lensed source, $\boldsymbol{\beta}$, by constructing models that match the lensed positions of a multiply imaged background quasar. Furthermore, if the source galaxy hosting the lensed quasar is bright and spatially extended, the arc of the lensed background source provide additional constraint to distribution of the lensing potential. Together with measured time delays, Δt, for the image

positions, the Fermat potential difference between two images is used to infer the time-delay distance, $D_{\Delta t}$, which is inversely proportional to the Hubble constant, $D_{\Delta t} \propto H_0^{-1}$.

4.2.2 Lensing degeneracies

Strong gravitational lens models suffer from a number of well-known parameter degeneracies, whereby various combinations of distinct parameters produce different models that fit the observed data (see, e.g., Saha, 2000; Saha et al., 2006). One of the fundamental degeneracies in strong lens modeling is the mass-sheet degeneracy, or MSD, (see, e.g., Falco et al., 1985; Schneider and Sluse, 2014), which refers to the fact that a model's convergence, κ, can be transformed by a constant factor, λ, such that observable quantities such as image positions and flux ratios remain unchanged if the unknown source position, β, is rescaled by the same factor, i.e.

$$\begin{aligned} \kappa_\lambda(\boldsymbol{\theta}) &= \lambda\kappa(\boldsymbol{\theta}) + (1-\lambda), \\ \boldsymbol{\beta}_\lambda &= \lambda\boldsymbol{\beta}. \end{aligned} \tag{4.9}$$

Mathematically, this mass sheet transformation (MST) corresponds to an addition of a uniform sheet of mass that changes the convergence term, but not the shear, while simultaneously re-scaling the angular distances.

It should be noted that the true physical convergence of the lens system, $\kappa_{\rm phys}(\boldsymbol{\theta})$, has two main components, namely the convergence associated with the primary deflector and neighboring galaxies, $\kappa_{\rm int}(\boldsymbol{\theta})$, thereby influencing the stellar kinematics of the lens galaxy, as well as an external convergence, $\kappa_{\rm ext}$, physically associated with the perturbation from line-of-sight structure, meaning

$$\kappa_{\rm phys}(\boldsymbol{\theta}) = \kappa_{\rm int}(\boldsymbol{\theta}) + \kappa_{\rm ext}. \tag{4.10}$$

However, the spatial extent of the lens galaxy, and with it the gravitational influence, is limited; therefore the convergence intrinsically associated with the main deflector is physically constrained to a certain radial span. In other words, the internal convergence vanishes at large radii, i.e. $\lim_{\boldsymbol{\theta}\to\infty}\kappa_{\rm int}(\boldsymbol{\theta}) = 0$, which implies that at a large distance away from the primary perturber the total physical convergence of the system is attributed entirely to the external convergence, i.e. $\lim_{\boldsymbol{\theta}\to\infty}\kappa_{\rm phys}(\boldsymbol{\theta}) = \kappa_{\rm ext}$.

At this point, the convergence of any lens model, $\kappa_{\rm lens}(\boldsymbol{\theta})$, can itself be thought of as a transformation of the lens system's physical convergence, $\kappa_{\rm phys}(\boldsymbol{\theta})$, so

$$\kappa_{\rm lens}(\boldsymbol{\theta}) = \lambda\kappa_{\rm phys}(\boldsymbol{\theta}) + (1-\lambda). \tag{4.11}$$

During the modeling of the primary lens, however, the line-of-sight contribution to the convergence is commonly omitted, which means the convergence of the lens model, $\kappa_{\rm lens}(\boldsymbol{\theta})$, does not include the external convergence term, $\kappa_{\rm ext}$. Therefore, if we combine Expression 4.10 with Expression 4.11, then in the limit of $\boldsymbol{\theta} \to \infty$, we have $0 = \lambda(0 + \kappa_{\rm ext}) + (1-\lambda)$, which arranged for λ, simplifies to

$$\lambda = \frac{1}{1-\kappa_{\rm ext}}. \tag{4.12}$$

We can now use Expression 4.12 together with Expression 4.10 in Expression 4.11 to arrive at

$$\kappa_{\rm lens}(\boldsymbol{\theta}) = \frac{1}{1-\kappa_{\rm ext}}\left[\kappa_{\rm int}(\boldsymbol{\theta}) + \kappa_{\rm ext}\right] + \left(1 - \frac{1}{1-\kappa_{\rm ext}}\right), \tag{4.13}$$

which in terms of $\kappa_{\rm int}(\boldsymbol{\theta})$ simplifies to

$$\kappa_{\rm int}(\boldsymbol{\theta}) = (1-\kappa_{\rm ext})\kappa_{\rm lens}(\boldsymbol{\theta}). \tag{4.14}$$

All reconstructed models presented in this paper employ parameterized profiles, which mitigate the impact of the MSD on the convergence of such a model. In other words, the convergence of a lens model, $\kappa_{\rm lens}(\boldsymbol{\theta})$, would be a transformation of such a parameterized model, $\kappa_{\rm param}$. In the absence of the external convergence term, the MST (Expression 4.9) is

$$\kappa_{\rm lens}(\boldsymbol{\theta}) = \lambda_{\rm int}(\boldsymbol{\theta})\kappa_{\rm param}(\boldsymbol{\theta}) + [1 - \lambda_{\rm int}(\boldsymbol{\theta})]\,. \tag{4.15}$$

Lastly, combining Expression 4.15 with Expression 4.14 and using the result in Expression 4.10 gives the following expression for the real physical convergence of the lens system in terms of a parameterized profile:

$$\kappa_{\rm phys}(\boldsymbol{\theta}) = (1 - \kappa_{\rm ext})\,[\lambda_{\rm int}(\boldsymbol{\theta})\kappa_{\rm param}(\boldsymbol{\theta}) + 1 - \lambda_{\rm int}(\boldsymbol{\theta})] + \kappa_{\rm ext}, \tag{4.16}$$

which simplifies to

$$\kappa_{\rm phys}(\boldsymbol{\theta}) = \lambda(\boldsymbol{\theta})\kappa_{\rm param}(\boldsymbol{\theta}) + [1 - \lambda(\boldsymbol{\theta})]\,, \tag{4.17}$$

where

$$\lambda(\boldsymbol{\theta}) = \lambda_{\rm int}(\boldsymbol{\theta})(1 - \kappa_{\rm ext}). \tag{4.18}$$

Kinematic measurements, such as the stellar velocity dispersion in the primary deflector near the image positions, can be used in conjunction with corresponding mass estimates from strong lens models to break the degeneracy internal to the lens galaxy and thereby constrain the internal MST parameter, $\lambda_{\rm int}(\boldsymbol{\theta})$. An estimate for the external convergence, $\kappa_{\rm ext}$, can be obtained from environmental studies of the lens system, such as spectroscopic and photometric surveys which provide redshifts as well as a quantification for the perturber population along the line of sight.

As a consequence of the MSD, it should be noted that the expression for the Fermat potential (Expression 4.4) also re-scales under the MST with

$$\phi_{\rm phys}(\boldsymbol{\theta};\boldsymbol{\beta}) = \lambda(\boldsymbol{\theta})\phi_{\rm param}(\boldsymbol{\theta};\boldsymbol{\beta}). \tag{4.19}$$

However, in the vicinity of the observed image positions, $\lambda_{\rm int}(\boldsymbol{\theta})$ is nearly invariable, so that $\lambda(\boldsymbol{\theta}) \rightarrow \lambda = \lambda_{\rm int}(1-\kappa_{\rm ext})$. Therefore, the Fermat potential difference between two images A and B for the true physical convergence scales with the Fermat potential difference of the reconstructed parameterized model as

$$\Delta\phi_{\rm phys}(\boldsymbol{\theta_A};\boldsymbol{\theta_B};\boldsymbol{\beta}) = \lambda\Delta\phi_{\rm param}(\boldsymbol{\theta_A};\boldsymbol{\theta_B};\boldsymbol{\beta}). \tag{4.20}$$

In short, both, a measurement for the external convergence, $\kappa_{\rm ext}$, and the scale factor internal to the lens galaxy, $\lambda_{\rm int}$, near the image positions, are needed to make an inference of the Hubble constant using observations of strongly lensed quasars.

One important caveat to note is that because of its multiplane nature, J1721 is less sensitive to the MST than standard lenses (e.g., Schneider and Sluse, 2014), and therefore one will have to consider the effects of the MSD in a multiplane framework when deriving cosmological constraints. The analysis presented in this paper does not account for the additional constraint imposed by the possible range of mass sheet transformations, but this work is left for a future investigation in Millon et al. (in prep).

4.2.3 Bayesian analysis and likelihood

The aim of this analysis is to obtain posterior distributions for the parameters, ξ, of a model, M, given the data set from the *HST* observations, $\boldsymbol{d}_{HST}$. Using Bayes' theorem, we can express the probability of the model parameters as

$$
\begin{aligned}
P(\xi|\boldsymbol{d}_{HST}) &\propto P(\boldsymbol{d}_{HST}|\xi)P(\xi) \\
&= \int P(\boldsymbol{d}_{HST}|\xi, M)P(\xi|M)\mathrm{d}M \\
&= \int P(\boldsymbol{d}_{HST}|\xi_{\mathrm{mass}}, \xi_{\mathrm{light}}, \xi_{\mathrm{source}}, \mathscr{P}, M) \\
&\qquad \times P(\xi_{\mathrm{mass}}, \xi_{\mathrm{light}}, \xi_{\mathrm{source}}|\mathscr{P}, M)\mathrm{d}\mathscr{P}\mathrm{d}M,
\end{aligned}
\tag{4.21}
$$

where in the last step we have broken up the set of model parameters into the main components of a lens model; namely the parameters of the deflector mass, ξ_{mass}, the parameters for the light profile of the deflector and the lensed source, ξ_{light} and ξ_{source}, respectively, and the model for the point spread function, $\mathscr{P}$.

The posterior of a single attribute in the lens model, ξ_i, which is part of the set of all model parameters, can then be determined by marginalizing over the remaining (nuisance) parameters, ξ_k:

$$
P(\xi_i|\boldsymbol{d}_{HST}, M) = \int P(\xi|\boldsymbol{d}_{HST}, M) \prod_{k=1}^{i-1} \mathrm{d}\xi_k. \tag{4.22}
$$

It should be mentioned that not all models in this paper share the same parameters. Therefore, to substantiate a meaningful comparison between various models and to determine which model best matches our observations, we use the Bayesian information criterion, which is defined as

$$
\mathrm{BIC} = k\ln(n) - 2\ln(\hat{L}), \tag{4.23}
$$

where k is the number of all free and linear parameters in a model, n represents the number of data points (or pixels), and $\hat{L}$ stands for the maximum value of the likelihood function, $P(\boldsymbol{d}_{HST}|\xi, M)$, corresponding to the model.

4.3 Observations of lens system J1721+8842

In this section we discuss the discovery of J1721+8842 in Section 4.3.1. We also describe the target's observations as well as the imaging data reduction in Section 4.3.2.

4.3.1 Lens discovery and redshift measurements

Originally discovered by Lemon et al. (2018) through a search for multiple *Gaia* detections around potential quasars, this system is confirmed to be a strongly lensed quasar with a redshift of $z \approx 2.37$, showing strong absorption features. Lemon et al. (2022) interpreted the system as the result of two distinct background quasars at similar redshifts ($z = 2.369 \pm 0.007$ and $z = 2.364 \pm 0.003$), with one quasar quadruply imaged and the other doubly imaged. This interpretation is now rendered obsolete by the information that became available later, identifying the Einstein zigzag configuration. Furthermore, the images A and C of the quadruply lensed quasar exhibit damped Lyman-α absorption signatures from neutral hydrogen at a redshift consistent with the measurements for the quasars.

The long-slit spectra of the lensing galaxy, obtained with the Intermediate-dispersion Spectrograph and Imaging System at the William Herschel Telescope, show multiple absorption features stemming from Ca H and K in the G-band, as well as Mg, Na, and Hβ. Fitting these lines with a multi-component Gaussian, Lemon et al. (2022) estimate the redshift of the deflector to be $z = 0.1841 \pm 0.0005$. Lastly, the source is also detectable at radio wavelengths (see Mangat et al., 2021).

Follow-up observations with the James Webb Space Telescope (*JWST*) Near InfraRed Spectrograph (NIRSpec; GO-2974; PI Treu; co-PI Shajib) have revealed the supposed host of the previously assumed doubly imaged quasar (see Mangat et al., 2021) to be another deflector at a redshift of $z = 1.885$, resulting in a six-image configuration of a single quasar lensed by two galaxies nearly perfectly aligned along the line of sight. Further evidence in support this Einstein zigzag configuration is demonstrated by the within-error identical light

curves for the images of the previously believed quadruply and doubly imaged quasars (see Dux et al., 2025b).

We also extracted the spectra for S3 and S4 from the NIRSpec data cube, which was centered on the lensing galaxy, placing S3 and S4 on the edge of the spectrograph. Still, these two sources extend over a few pixels within the NIRSpec field of view, allowing us to measure their redshift. From the detection of the $H\beta$, [OII]λ 3727Å, [OIII]λ 4959Å and [OIII]λ 5007Å, we confirm that theses sources are at the same redshift as the quasar, i.e. $z = 2.38$.

4.3.2 *HST* imaging and data reduction

The high-resolution data for this lens comes from observations with the Hubble Space Telescope, taken under cycle 26 program HST-GO-15652 (PI: T. Treu; see Schmidt et al., 2023b), using the Wide Field Camera 3 (WFC3). Our dataset comprises imaging in filter F160W, to give near-IR modeling constraints, and UVIS exposures in band F475X and band F814W, for higher-resolution observations in the optical/UV spectrum. In the IR band, a 4-point dither pattern is employed to improve the data sampling by eliminating hot pixels and other detector irregularities, while UVIS exposures implement 2-point dithering during observations. At each UVIS dither point exposures are split into one long and one short integration to ensure the full brightness span is captured between faint features of the lens and bright quasar images. The total integration time for the four IR exposures is $2,197$ s, whereas the exposure time in the UVIS totals $1,382$ s in filter F475X and $1,428$ s in filter F814W.

Cosmic ray hits are removed and the individual exposures in each filter are aligned and combined with the use of the Python package AstroDrizzle (Avila et al., 2015). The resulting reduced images have a pixel size of $0.04''$/pix in both UVIS bands and $0.08''$/pix for the IR imaging. A composite red-green-blue image of the target, constructed from the reduced IR/UVIS exposures, is shown in Figure 4.1, identifying the lens, nearby perturbing galaxies, and the deflector at redshift $z = 1.885$. Figure 4.2, labels the images of lensed

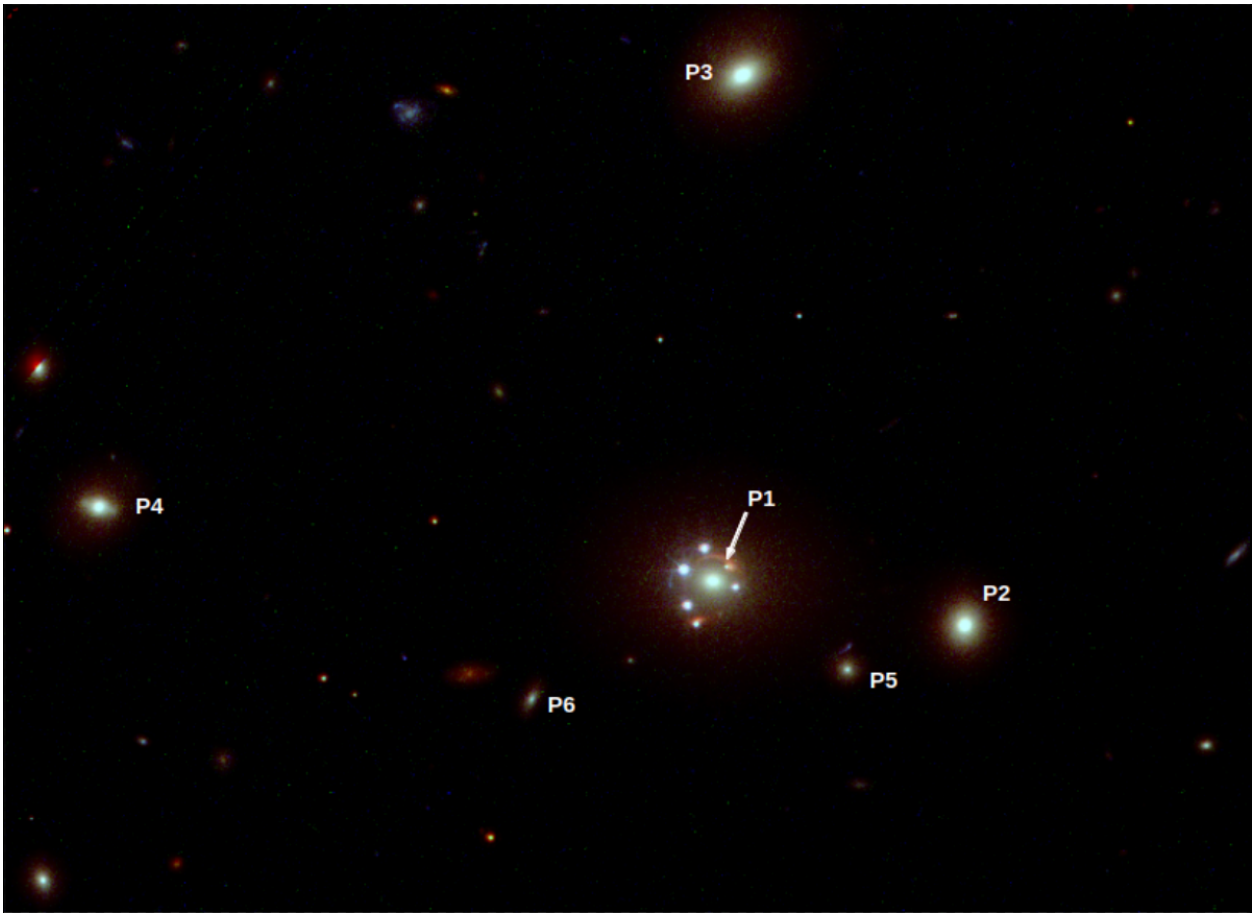

Figure 4.1: Red-green-blue composite image of J1721+8842 and nearby perturbers created by exposures in the *HST* band F160W (red), F814W (blue), and F475X (green).

quasar and other lensed sources. The intensities for each channel in the color composites are entirely arbitrary and chosen to achieve the best visualization of all components in the lens system.

4.4 Lens models

In this section we describe the modeling choices for all components in the lens models of J1721+8842, broken down between main deflector description, lensed source light components, explicitly modeled line-of-sight perturbers, and structure resulting in additional distortions to the lens configuration. The parameterizations of the main deflector's mass profiles

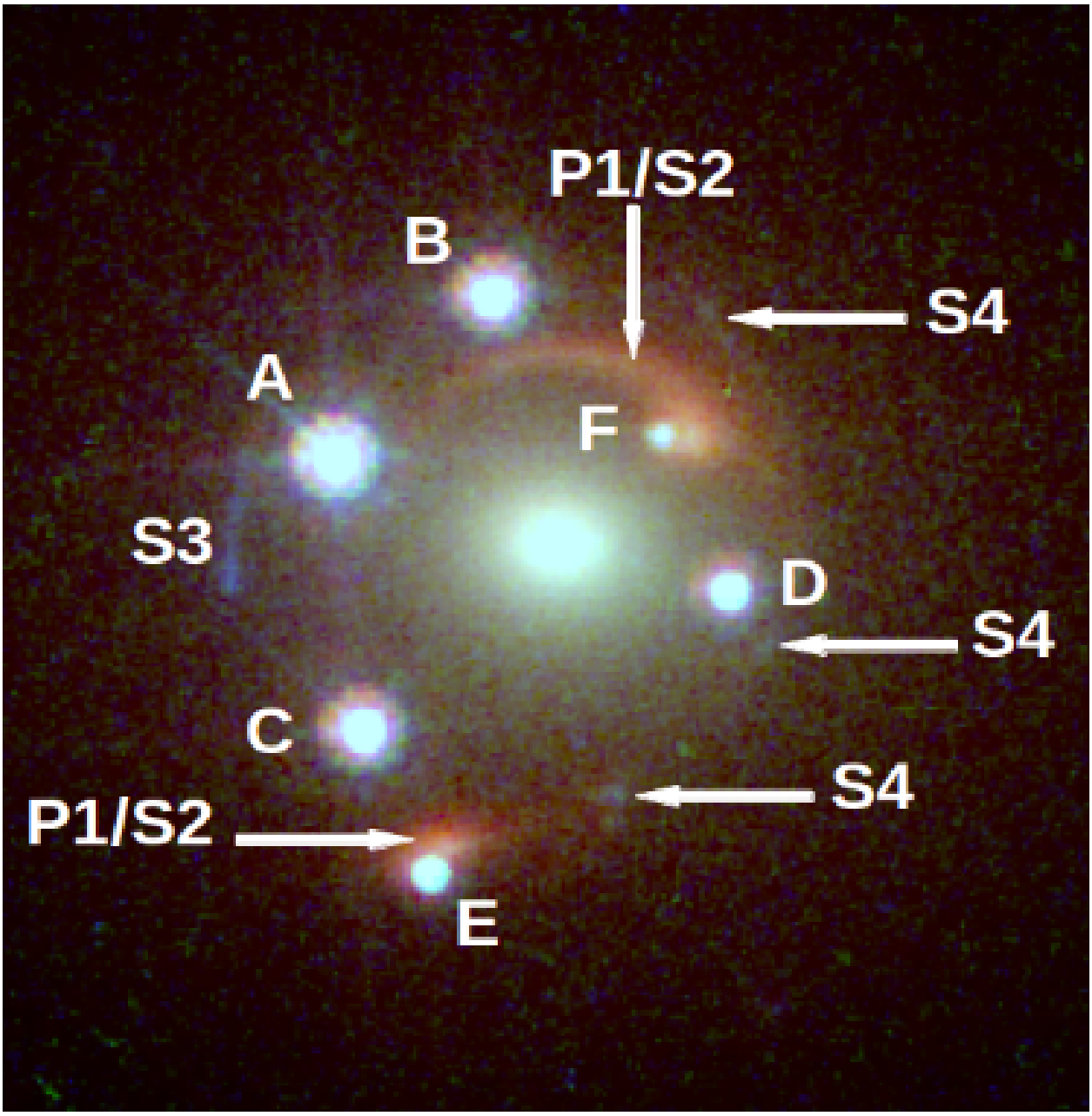

Figure 4.2: Red-green-blue composite image of J1721+8842 created by exposures in the *HST* band F160W (red), F814W (blue), and F475X (green).

are discussed in Section 4.4.1.1, while the parameterization of the light profiles corresponding to the primary lensing galaxy are described in Section 4.4.1.2. The light profiles of the lensed sources and quasar, including the light profile for the deflector at redshift $z = 1.885$, are discussed in Section 4.4.2 and the modeling choices related to all additional perturbing galaxies are outlined in Section 4.4.3. After that we describe the parameterization of LOS model components in Section 4.4.4, show assumed priors for specific parameters in Section 4.4.5, and conclude with a discussion on modeling choice related systematics in Section 4.4.6.

4.4.1 Main deflector

4.4.1.1 Main deflector mass profile parametrization

For the main deflector, we use two independent modeling choices (or "modeling families") to parameterize the mass profile. Option 1 relies on a singular power-law elliptical mass distribution to model the main deflector mass (see Power-law mass profile paragraph) while for option 2 the mass of the deflector is modeled as a composite profile, where we separate the deflector's dark matter component from the luminous baryonic matter (Composite mass profile paragraph).

4.4.1.1.1 Power-law mass profile In this choice for parametrization, the mass profile of the main deflector is modeled with a power-law elliptical mass distribution (PEMD), which corresponds to a radial mass density profile of $\rho \propto r^{-\gamma}$, where γ is the power-law slope. The convergence, or dimensionless projected surface mass density, for the profile at position θ is parameterized as

$$\kappa(\theta_1, \theta_2) = \frac{3-\gamma}{2} \left(\frac{\theta_E}{\sqrt{q\theta_1^2 + \theta_2^2/q}} \right)^{\gamma-1}, \tag{4.24}$$

where θ_1 and θ_2 are aligned along the semi-major and semi-minor axis through the rotational position angle $\phi = \arctan(\theta_2, q\theta_1)$, and where q represents the corresponding axis

ratio. The centroid of the main-deflector's mass model is linked to the corresponding light profile through a maximum allowed offset of 2 pixels as well as a Gaussian prior with a variance of 1 pixel, which corresponds to 0.″04 in UVIS.

4.4.1.1.2 Composite mass profile For the parametrization of this modeling option, we use two separate mass profiles: one to model the dark matter component of the main deflector mass and another profile to represent the baryonic matter. For the dark matter component, we adopt an spherical Navarro–Frenk–White (NFW) profile, for which the three dimensional mass density is given by

$$\rho(r) = \frac{\rho_0}{(r/r_0)(1 + r/r_0)^2}, \tag{4.25}$$

where ρ_0 is the normalization constant and r_0 represents the scale radius (Navarro et al., 1997). Further details on the convergence and lensing potential of the NFW profile can be found in (Golse and Kneib, 2002).

The luminous baryonic matter of the main deflector mass is modeled by two elliptical chameleon convergence profiles, which are superposed and joined via a common centroid. This mass profile is further tied to light profile model of the F160W IR band (see Section 4.4.1.2.2). The convergence of a chameleon profile is given by the difference between two non-singular isothermal ellipsoids with different core sizes and is parameterized as

$$\kappa(\theta_1, \theta_2) = \frac{\kappa_0}{1+q}\left[\frac{1}{\sqrt{\theta_1^2 + \theta_2^2/q^2 + 4w_\mathrm{c}^2/(1+q^2)}} - \frac{1}{\sqrt{\theta_1^2 + \theta_2^2/q^2 + 4w_\mathrm{t}^2/(1+q^2)}}\right], \tag{4.26}$$

where w_c and w_t are the profile parameters for the two core sizes, where κ_0 represents the normalization constant, and where q is again the corresponding axis ratio (Dutton et al., 2011; Suyu et al., 2014). In contrast to a Sérsic profile, the chameleon profile is based on

closed-form expressions and thereby proves more convenient in the computation of lensing quantities (see Suyu et al., 2014). Furthermore, within a radius of between $0.5R_e$ and $3.0R_e$, where R_e is the effective radius of the Sérsic profile, the chameleon profile approximates the Sérsic profile to within a few percent in mass residuals (Dutton et al., 2011).

As additional constraint to the composite mass profile parameterization, we force a common centroid between dark matter and baryonic matter components. This is achieved by allowing the centroid of the NFW profile to be offset from the double chameleon profile centroid by at most by 1 pixel, which corresponds to 0.″04 in UVIS, and effectively joins the centroids of the two mass profiles.

4.4.1.2 Main deflector light profile parameterization

Analogous to Section 4.4.1.1, we use two modeling choices to parameterize the light profile of the main deflector, which depend on the deflector's mass profile parameterization. If the deflector's mass profile is described by a power-law, we model the main deflector light with Sérsic profiles, which is detailed in Section 4.4.1.2.1. In the composite mass profile case (Section 4.4.1.2.2), we used a chameleon or Sérsic light profile parameterization, depending on the filter in which the target was observed.

4.4.1.2.1 Light profile parameterization to power-law mass profile In the case of the power-law mass profile modeling choice, we use a Double Sérsic profile (Sérsic, 1968) with a common centroid to model the light of the main deflector in all three bands. The parameterization of an elliptical Sérsic light profile is given by

$$I(\theta) = I(\theta_{\rm e})\ \exp\left\{-C(n)\left[\left(\frac{(q_{\rm L}\theta_1)^2+\theta_2^2}{q_{\rm L}\theta_{\rm e}^2}\right)^{\frac{1}{2n}}-1\right]\right\}, \tag{4.27}$$

where $C(n)$ is a normalization constant so that at the effective radius, $\theta_{\rm e}$, the profile includes half of the deflector's light. n represents the Sérsic index, θ_1 and θ_2 are the angular coordinates aligned along the semi-major and semi-minor axis through the rotational position

angle $\phi_{\rm L} = \arctan(\theta_2, q\theta_1)$ of the light profile, and $q_{\rm L}$ represents the corresponding axis ratio. In our models we hold the index of the first Sérsic light profile fixed at $n = 1.0$ across all filters, effectively making it an exponential Sérsic profile. The Sérsic index of the second light profile is allowed to vary within the restrictions of a flat prior as discussed in Section 4.4.5. Additionally, we allow the effective radii, the Sérsic index of the second light profile, the axis ratios, the position angles, and the centroids to vary across bands.

4.4.1.2.2 Light profile parameterization to composite mass profile For the composite mass profile option, we model the main deflector light with Double Sérsic profile (Expression 4.27) in the UVIS bands (filters F475X and F814W), as described above in Section 4.4.1.2.1. However, in the IR band (filter F160W), the parameterization of the deflector light is following the description of the profile representing the baryonic matter, where we model the main deflector with two joined elliptical chameleon profiles, shown in Expression 4.26. For the light profile description, however, we replaced the normalization constant, or convergence amplitude, κ_0, by the normalization constant for the flux amplitude, I_0. The remaining parameters of Expression 4.26 remain the identical and are all tied (or held in common) between the double chameleon mass and light profiles.

4.4.2 Lensed sources

4.4.2.1 Quasar host galaxy

The galaxy hosting the sextuply imaged quasar is modeled with an elliptical Sérsic light profile (see Expression 4.27). Except for the centroids, which are held common across the three *HST* bands, all parameters for the Sérsic profiles are allowed to vary independently and are constrained by the flat priors described in Section 4.4.5. To model additional complexity in the source light, which cannot be described by a continuous or featureless flux distribution of a Sérsic profile, we add a set of two-dimensional Cartesian shapelets (Refregier, 2003; Birrer et al., 2015) to the light profile of the host galaxy. These shapelets share a common centroid

with the Sérsic function of the associated host. The corresponding number of basis functions (or shapelet number) form an orthogonal basis and is given by

$$N_{\rm shapelet} = \frac{(n_{\rm max}+1)(n_{\rm max}+2)}{2}, \tag{4.28}$$

where the maximal source complexity, or $n_{\rm max}$, is related to the characteristic scale, β, by the maximum spatial scale, $l_{\rm max}$, defined as

$$l_{\rm max} = \beta\sqrt{n_{\rm max}+1}. \tag{4.29}$$

Increasing the shapelet order, $n_{\rm max}$, increases the complexity, or components of additional concentrated flux, in the source reconstruction of our models. To prevent the shapelet order from being driven to high values, which would result in degeneracies with other model parameters and further cause overfitting by modeling noise in the data, we kept the parameter $n_{\rm max}$ for each band fixed during the fitting process for a given model and only allowed the scale size, β, to vary within the confines of a flat prior.

The multiply imaged quasar hosted by the lensed galaxy is modeled as point source in the image plane and shares the same centroid as the associated host in the source plane. To account for the lower resolution in the IR band (F160W), the point spread function (PSF) is supersampled in IR using a supersampling factor of 3. For the two UVIS bands, however, we do not use a supersampled PSF. As initial starting point we first estimate the PSF in each band using 5 to 10 suitable stars in the field of view near the target. Then, to further refine and improve the PSF, we run iterations of the PSF reconstruction between optimization routines that fit the free parameters for the respective lens model (see Birrer et al., 2019).

4.4.2.2 Lensed galaxies

Analogous to the quasar host, additional lensed sources, including the light of the deflector at redshift $z = 1.885$, are parameterized in our models by an elliptical Sérsic light profile

as described by Expression 4.27. As the case with the quasar host galaxy, detailed in Section 4.4.2.1, only the centroids are joined across all bands for each source light profile, while all other parameters, such as ellipticity, Sérsic index, and Sérsic radius, are allowed to vary within the confines of the respective prior (see Section 4.4.5). If additional complexity is required to accurately describe the lensed source light, we use the two-dimensional Cartesian shapelet profile, outlined in Section 4.4.2.1 above, with the centroid joined to the respective Sérsic profile to further model concentrated flux features. Again, only the scale size, β, is allowed to vary while the shapelet order, $n_{\max}$, responsible for an increase in source complexity with larger values, is held fixed during the fitting process.

4.4.3 Additional perturbing galaxies

Galaxies near the main deflector and, in general, galaxies along the line of sight, can have a significant impact on the path of lensed quasar's light rays, depending on the strength of their deflection potential and the perturber's location with respect to the lens galaxy. Therefore, to ensure that higher order lensing effects beyond external convergence and external shear or flexion are properly addressed, we explicitly include certain line-of-sight perturbers in our models. In Section 4.4.3.1 we detail how we select nearby perturbers that are explicitly included in our models, followed by the description of the mass profile for modeled line-of-sight galaxies (Section 4.4.3.2).

4.4.3.1 Selection of nearby perturbers explicitly included in models

To determine which of the nearby perturbers should be explictly included (or explicitly modeled) in the plane of the main deflector, we use an estimate of the change in flexion produced by the perturbing galaxy. It should be noted that the perturber at redshift $z = 1.885$ is already deemed to be explicitly included in our models in a separate redshift plane and is therefore omitted from the flexion shift assessment.

The magnitude of the flexion shift caused by a perturber of assumed point mass is given

by

$$\Delta_3 x = f(\eta) \times \frac{(\theta_{\rm E}\theta_{\rm E,p})^2}{\theta^3}, \tag{4.30}$$

where $\theta_{\rm E}$ and $\theta_{\rm E,p}$ are the Einstein radius of the main deflector and the perturber, respectively (see Sluse et al., 2017; McCully et al., 2017). θ represents the angular separation between the perturber and the main deflector in the sky and the factor $f(\eta)$ is defined as follows:

$$f(\eta) = (1-\eta)^2, \tag{4.31}$$

where

$$\eta = \frac{D_{\rm dp} D_{\rm s}}{D_{\rm p} D_{\rm ds}}. \tag{4.32}$$

$D_{\rm dp}$, $D_{\rm s}$, $D_{\rm p}$, and $D_{\rm ds}$ represent the angular diameter distances between the redshifts of the main deflector and the perturber, to the source, to the perturber, and between the deflector and the source, respectively.

At the time of our analysis redshift measurements for nearby perturbers are not available. Given that the additional galaxies in the field-of-view and the main deflector are similar in color, we make the simplifying assumption that all are part of the same galaxy overdensity and therefore at approximately the same redshift. With this assumption η goes to zero and the function $f(\eta)$ becomes unity, leaving the flexion shift magnitude at

$$\Delta_3 x = \frac{(\theta_{\rm E}\theta_{\rm E,p})^2}{\theta^3}. \tag{4.33}$$

Under the assumption of an isothermal profile, the Einstein radius of an additional perturber is given by

$$\theta_{\rm E,p} = 4\pi \frac{\sigma_v^2}{c^2} \frac{D_{\rm ps}}{D_{\rm s}}, \tag{4.34}$$

where $D_{\rm ps}$ and $D_{\rm s}$ are the angular diameter distance between redshifts of the perturber and the lensed source and the angular diameter distance to the source, respectively. Using the Faber-Jackson (Faber and Jackson, 1976) relation, $L_* \propto \sigma^{\gamma}$, which relates the velocity dispersion, σ, to the stellar luminosity, L_*, with the power-law index, γ, equal to 4, we scale a perturbers's Einstein radius to the corresponding flux, F, as

$$\theta_{\rm E,p} \propto \sigma_v^2 \propto L^{1/2} \propto F^{1/2}. \tag{4.35}$$

Since we assume the perturbers to be in the same redshift plane as the main deflector, we have an expression for the Einstein radius based on the flux ratio:

$$\theta_{\rm E,p} = \theta_{\rm E} \left(\frac{F_{\rm p}}{F_{\rm d}} \right)^{1/2}, \tag{4.36}$$

where F_p is the flux of the perturber and F_d the flux of the main deflector. Using Expression 4.36 in Expression 4.33, the estimated flexion shift magnitude produced by a perturber at the same redshift as the main deflector is then

$$\Delta_3 x = \frac{\theta_{\rm E}^4}{\theta^3} \left(\frac{F_{\rm p}}{F_{\rm d}} \right). \tag{4.37}$$

The flexion shift based on our flux ratio analysis for each perturber is listed in Table 4.1. As demonstrated in McCully et al. (2017), to prevent a significant bias in an H_0 measurement line-of-sight perturbers which produce a flexion shift magnitude of $\Delta_3 \mathrm{x} > 10^{-4}$ arcsec should be explicitly included in the lens models. Adopting this conservative cutoff, we find that perturber P4 is located at a large enough angular separation for its impact to be negligible. In contrast, even though perturbers P5 and P6 have smaller angular scales compared to other nearby galaxies, their close proximity to the main deflector warrants their explicit inclusion in the lens models. Therefore, we include mass profiles to model perturbers P2, P3, P5, and P6, located in the same redshift plane as the main deflector, for our lens models.

Table 4.1: Flexion shift estimates for nearby perturbers based on a corresponding flux ratio analysis.

Perturber	$\Delta_3 x$ (arcsec)
P2	1.4×10^{-3}
P3	2.7×10^{-4}
P4	6.7×10^{-5}
P5	1.0×10^{-3}
P6	2.4×10^{-4}

4.4.3.2 Mass profile of nearby perturbers

Any additional perturbing galaxy, namely the deflector at redshift $z = 1.885$ as well as galaxies near the main deflector, deemed to be explicitly included in our models based on the criteria described in Section 4.4.3.1, is modeled using a singular isothermal sphere (SIS) profile, which represents a PEMD with a fixed power-law slope, γ, of 2.0 and a fixed axis ratio, q, of 1.0. For the perturbers located in the plane of the main deflector we fix the location of the mass centroid in our models to coincide with the corresponding light centroid that is used to measure the angular separation from the main perturber. As for the deflector at redshift $z = 1.885$, we link the mass centroid with the centroid of the corresponding Sérsic profile modeling the perturber's light distribution as described in Section 4.4.2.2.

In the case of the perturbers in the main deflector plane, namely perturbers P2 through P6, we further employ a Gaussian prior on the Einstein radius that is based on an assumed 0.1 dex scatter in the Faber-Jackson relation (see Equation 4.35). Furthermore, due to the complexity of the model and the underlying degeneracy for nearby line-of-sight perturbers, we hold Einstein radius for all the additional perturbers fixed at the estimates derived from the measured flux ratios (Equation 4.36) until we find a good fit for all other parameters. Once a fit for the remaining parameters in our model is found, we add the Einstein radii back to the list of free parameters fit in the modeling process.

4.4.3.3 Light profile of nearby perturbers

With the exception of the deflector at redshift $z = 1.885$, for which the modeled light profile is described in Section 4.4.2.2 above, which covers the treatment of additional lensed galaxies, the light profiles for additional perturbing galaxies are not included in our models as they do not contribute valuable information toward the assessment of the Fermat potential differences between the image positions of the lensed quasar.

4.4.4 Line of sight structure and higher-order distortions

Additional linear distortions can impact the lens model as a result of dark matter halos and large scale structures along the line of sight. We collectively account for such an impact on the strong lens by including an external shear profile. The external shear strength of the combined tidal effect from the surrounding gravitational field is given by

$$\gamma_{\rm ext} = \sqrt{\gamma_{\rm ext,1}^2 + \gamma_{\rm ext,2}^2}, \tag{4.38}$$

where the components of the external shear matrix, $\gamma_{\rm ext,1}$ and $\gamma_{\rm ext,1}$, are related to the external shear angle, $\phi_{\rm ext}$, by

$$\phi_{\rm ext} = \frac{1}{2} \arctan\left(\gamma_{\rm ext,2}, \gamma_{\rm ext,1}\right). \tag{4.39}$$

4.4.5 Priors

This section provides details on the priors employed in the modeling process, which crucially quantify the intrinsic flexibility afforded to our lens models during parameter optimization. These informative constraints encapsulate observational and theoretical guidance toward realistic ranges in model parameters. The majority of parameters in our models rely on uniform priors that cover a broad physical range, with the exception of the NFW profile, in our composite model, and the Einstein radii of explicitly included nearby perturbers.

In addition to a flat prior, the centroid of the dark matter profile (NFW) is further constrained by the centroid of the chameleon profile. To effectively link the centers of the two profiles, we allowed for a deviation within the right ascension and declination of 1 pixel in UVIS, or 0.″04. If for a model the NFW centroid exceeds the bound set by the chameleon profile, a taxing punishment term is added to the model's likelihood. To constrain the scaling radius (r_0) of the NFW profile we employ a Gaussian prior, which was derived using the analysis in Gavazzi et al. (2007) of Sloan Lens ACS (SLACS) lenses (see Bolton et al., 2006). Our prior for the scaling radius is centered on 26.″82 with a standard deviation of 3.″70. When applying the prior on r_0, we only probe the space within 5σ of the mean, meaning from 8.″32 to 45.″32, and disregard all solutions outside that range. Lastly, due to a degeneracy with the external shear parameters and associated convergence issues, we opted to employ a spherical NFW profile rather than punishing the likelihood of models with excessive results for eccentricity parameters.

Explicitly modeling four of the nearby perturbers, P2 through P6, further increases the already high complexity of our models. Furthermore, two of these perturbers are located near each other and thereby introduce additional degeneracies. For this reason, we impose a Gaussian prior on the Einstein radii of each explicitly included perturbing galaxy, with the exception of the deflector at redshift $z = 1.885$, and hold the mass centroid fixed at the corresponding center of light. The mean for the priors on the Einstein radii is derived using the flux ratio analysis in Expression 4.36 and the standard deviation is estimated based on a 0.1 dex scatter we assumed for the Faber-Jackson (Faber and Jackson, 1976) relation. We show the resulting probability density for each prior on the perturber's Einstein radius in Figure 4.3.

Finally, in Table 4.2 we summarize the priors employed in our models by component. In case of non-spherical profiles, instead of listing the priors for axis ratio, q, and position angle, ϕ, we show the priors imposed on the corresponding eccentricity parameters, which are related to the axis ratio and position angle by

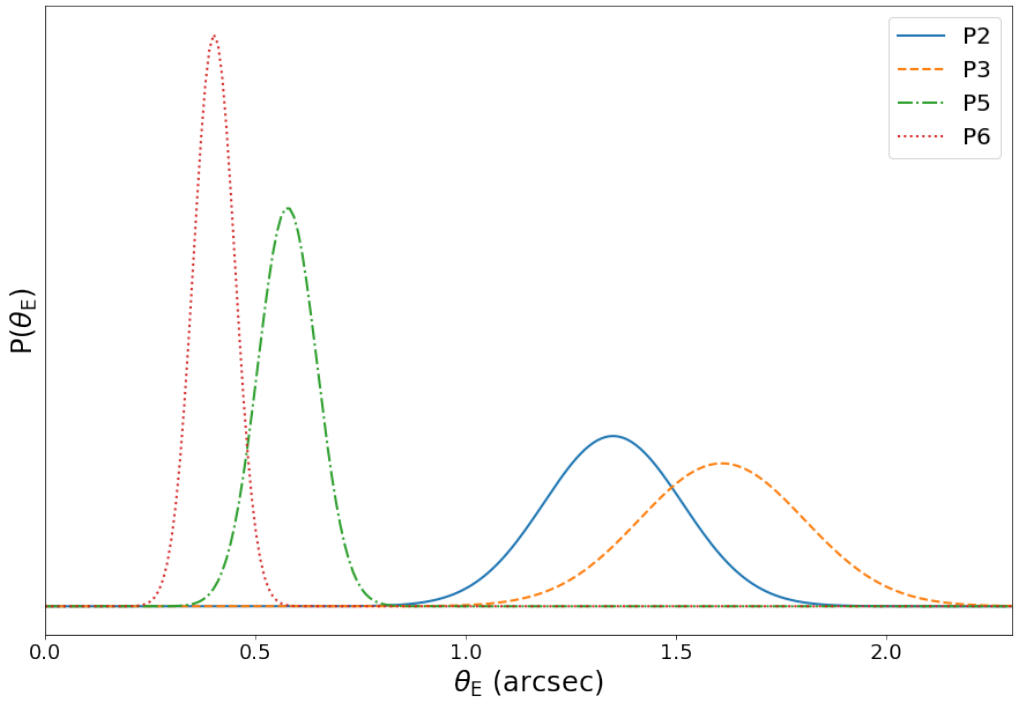

Figure 4.3: Priors on Einstein radii for nearby perturbing galaxies explicitly included in the models.

$$e_1 = \frac{1-q}{1+q} \times \cos(2\phi),$$
$$e_2 = \frac{1-q}{1+q} \times \sin(2\phi). \tag{4.40}$$

4.4.6 Assessment of systematic uncertainties from modeling choices

To assess the systematic impact of various parameter choices on the uncertainties in our models, we model the lens configuration under different assumptions for the mass profile of the primary deflector and with three separate sets for radius of the circular mask used for the likelihood computation. The size of the likelihood masking region in our fiducial models is chosen to encompass a region large enough to ensure all lensed features are included within and to capture the extend of the primary deflector's flux in each band. To test the impact of the likelihood masking size we increase and decrease the radius for each filter by $0.''5$ for our fiducial models and repeat the MCMC sampling procedures. We find no significant change in the time-delay difference between images as a result of these masking size changes and therefore opted to reduce the change in masking radii to $0.''1$ for our remaining systematic assessments.

We further evaluate the impact of various complexities in the lensed sources by changing the shapelet order, $n_{\max}$. Here, the lowest possible source complexity is represented by $n_{\max} = -$, which signifies no shapelets were added to the source light modeled by a Sérsic light profile.

To obtain posteriors for the changes in parameter choices, we initialize the changed model with the results of the corresponding fiducial model for main deflector profile choice (the seed) and run the MCMC sampling procedure with an iteration count similar to the seed model. To summarize our selections, the changes to the model configurations, itemized by modeling component, are as follows:

Table 4.2: Priors on mass model parameters.

Model component	Parameter	Description	Prior
Main deflector (P0) mass profile (SPEMD)	γ	Power-law slope	Flat prior: [1.5, 2.5]
	$\theta_{\rm E,P1}$	Einstein radius	Flat prior: [0.01, 10.]
	$x_{\rm mass}(''$)	Centroid x-coordinate	Flat prior: [-10., 10.]
	$y_{\rm mass}(''$)	Centroid y-coordinate	Flat prior: [-10., 10.]
	e_1	Eccentricity in x-direction	Flat prior: [-0.5, 0.5]
	e_2	Eccentricity in y-direction	Flat prior: [-0.5, 0.5]
Main deflector (P0) mass profile (NFW)	$\alpha_{r_0}(''$)	Deflection angle	Flat prior: [0., 10.]
	$r_0(''$)	Scale radius	Gaussian prior: [26.82, 3.70] on top of flat prior: [8.32, 45.32]
	$x_{\rm mass}(''$)	Centroid x-coordinate	Flat prior: [-10., 10.]
	$y_{\rm mass}(''$)	Centroid y-coordinate	Flat prior: [-10., 10.]
Main deflector (P0) mass profile (Double chameleon)	$\alpha_1(''$)	Deflection angle	Flat prior: [0., 10.]
	$I_{0,\rm Cham1}/I_{0,\rm Cham2}$	Ratio of deflection amplitudes	Flat prior: [0., 100.]
	$w_{c,\rm Cham1}$ ($''$)	Core size of component 1	Flat prior: [0.001, 10.]
	$w_{t,\rm Cham1}$ ($''$)	Core size of component 2	Flat prior: [0.001, 10.]
	$e_{1,\rm Cham1}$	Eccentricity in x-direction	Flat prior: [-0.5, 0.5]
	$e_{2,\rm Cham1}$	Eccentricity in y-direction	Flat prior: [-0.5, 0.5]
	$w_{c,\rm Cham2}$ ($''$)	Core size of component 1	Flat prior: [0.001, 10.]
	$w_{t,\rm Cham2}$ ($''$)	Core size of component 2	Flat prior: [0.001, 10.]
	$e_{1,\rm Cham2}$	Eccentricity in x-direction	Flat prior: [-0.5, 0.5]
	$e_{2,\rm Cham2}$	Eccentricity in y-direction	Flat prior: [-0.5, 0.5]
External shear	$\gamma_{\rm ext,1}, \gamma_{\rm ext,2}$	Shear components	Flat prior: [-0.5, 0.5]
P1 mass (SIS)	$\theta_{\rm E,P1}$	Einstein radius	Flat prior: [0.01, 10.]
P2 mass (SIS)	$\theta_{\rm E,P2}$	Einstein radius	Gaussian prior: [1.35, 0.16]
P3 mass (SIS)	$\theta_{\rm E,P3}$	Einstein radius	Gaussian prior: [1.60, 0.20]
P5 mass (SIS)	$\theta_{\rm E,P5}$	Einstein radius	Gaussian prior: [0.58, 0.07]
P6 mass (SIS)	$\theta_{\rm E,P6}$	Einstein radius	Gaussian prior: [0.40, 0.05]

For Gaussian priors, the numbers in the bracket showns the mean, followed by the standard deviation, while for flat priors the bracket reflects the respective lower and upper bounds.

1. Two choices for the mass profile of the primary deflector:

   (a) Power-law profile

   (b) Composite profile

2. Three choices for the radius (in arcsec) of the likelihood computation masking region, sorted by band from shortest to longest wavelength, i.e. {F475X, F814W, F160W}:

   (a) {3.9, 4.0, 7.4}

   (b) {4.0, 5.0, 7.5}

   (c) {4.1, 5.1, 7.6}

3. Complexity in lensed source light ($n_{\max}$ values), sorted by source number, i.e. {S1, S2, S3, S4}:

   (a) $\{-, 2, -, 5\}$

   (b) $\{-, 4, -, 7\}$

   (c) $\{-, 4, 1, 7\}$

   (d) $\{1, 4, 1, 7\}$

Combining these choices in modeling components, we arrive at a total of 24 different configurations. To address stochasticity in the MCMC sampling, we performed the MCMC run for each model configuration two times, which increases the number of model results contributing in the assessment of systematic uncertainties to a total of 48.

4.5 Results

We now present the reconstructed models for J1721+8842. In Section 4.5.1 we show the best fits for the profile parameters used in our modeling and discuss noteworthy findings. Section 4.5.2 describes how results for model of different complexities and components are

compared to one another and Section 4.5.3 presents predicted time delays between lensed images based on the fits for our best models.

4.5.1 Lens model results

Figures 4.4 and 4.5 compare the reconstructed model with the data in each band. The first column in these figures shows the observations, ordered in terms of wavelength from short to long, i.e. filter F475X (top row), F814W (middle row), and F160W (bottom row). The second column presents the reconstructed model for a corresponding filter, while the third column shows the normalized residuals after subtracting the observations from the modeling results of each band.

In the corner plot of Figure 4.6 and Figure 4.7, we show the posterior distributions for mass model parameters of both assumptions for the primary deflector's profile, power-law (shown in red), and composite models (shown in blue) along with time delays between image pairs AD, AE, and AF of the sextuply lensed quasar. To compare the results of the composite model with the results of the power-law assumption, we show the Einstein radius, $\theta_{\rm E}$, for the composite model as radius of the circularized profile at which the encompassed mean convergence equals unity. In the same fashion, the power-law slope, γ, for the composite assumption is then computed from the derivative of the corresponding convergence profile at the Einstein radius.

The time delays for image pairs with longer delays (AD, AE, and AF) show a correlation with the external shear strength, $\gamma_{\rm ext}$, as well as the external shear angle, $\phi_{\rm ext}$. Furthermore, we find a strong correlation between the external shear and the power-law slope, γ, which then translates into the strong correlation observed between the power-law slope and the plotted time delays. Owing to the computational challenges of sampling the parameter space in the composite model, we hold the external shear parameters fixed at the findings for the power-law model. Therefore no composite model posteriors are shown for the external shear in Figure 4.6.

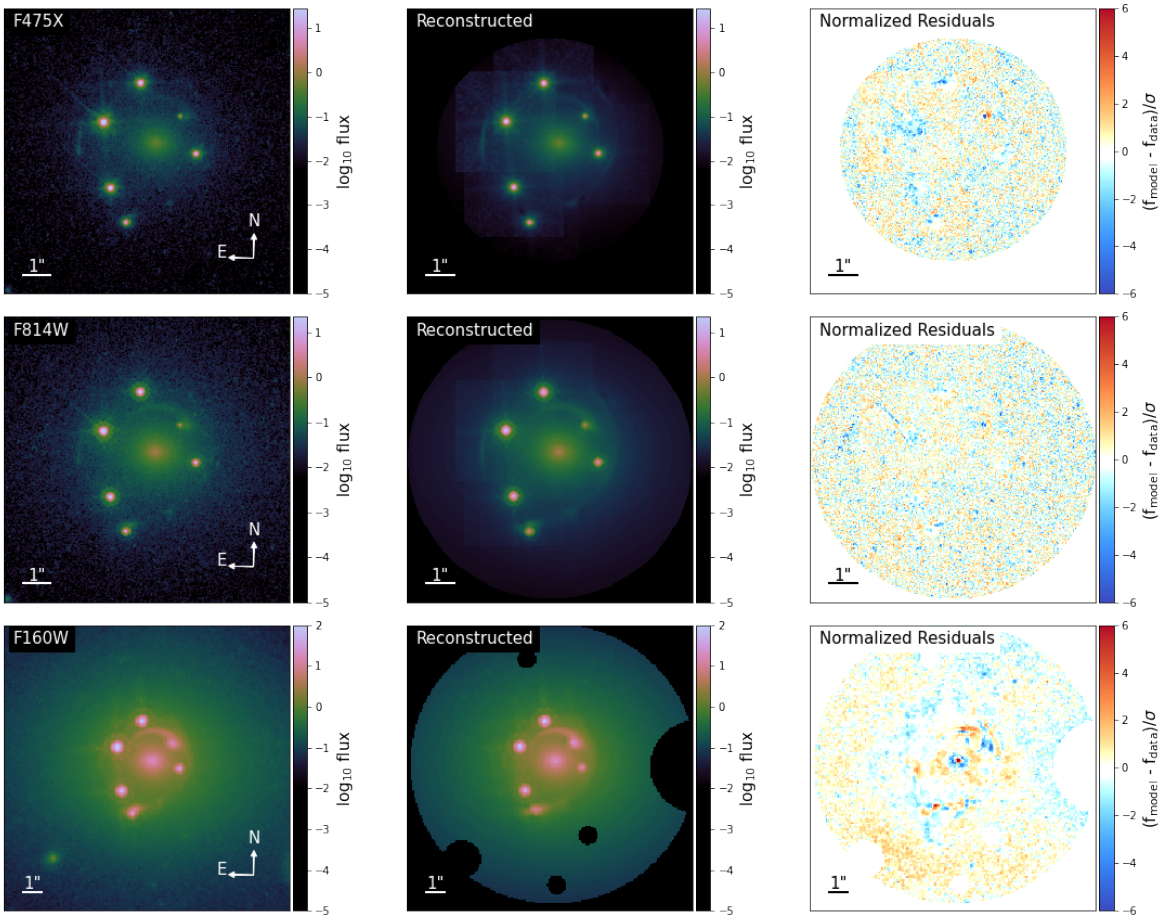

Figure 4.4: Reconstructed power-law model for J1721+8842. The first column (left) shows the observations in each band, sorted by wavelength from short to long. The second column (center) displays the reconstructed model for each filter, and in the third column (right) are the normalized residuals between our model and the observed data.

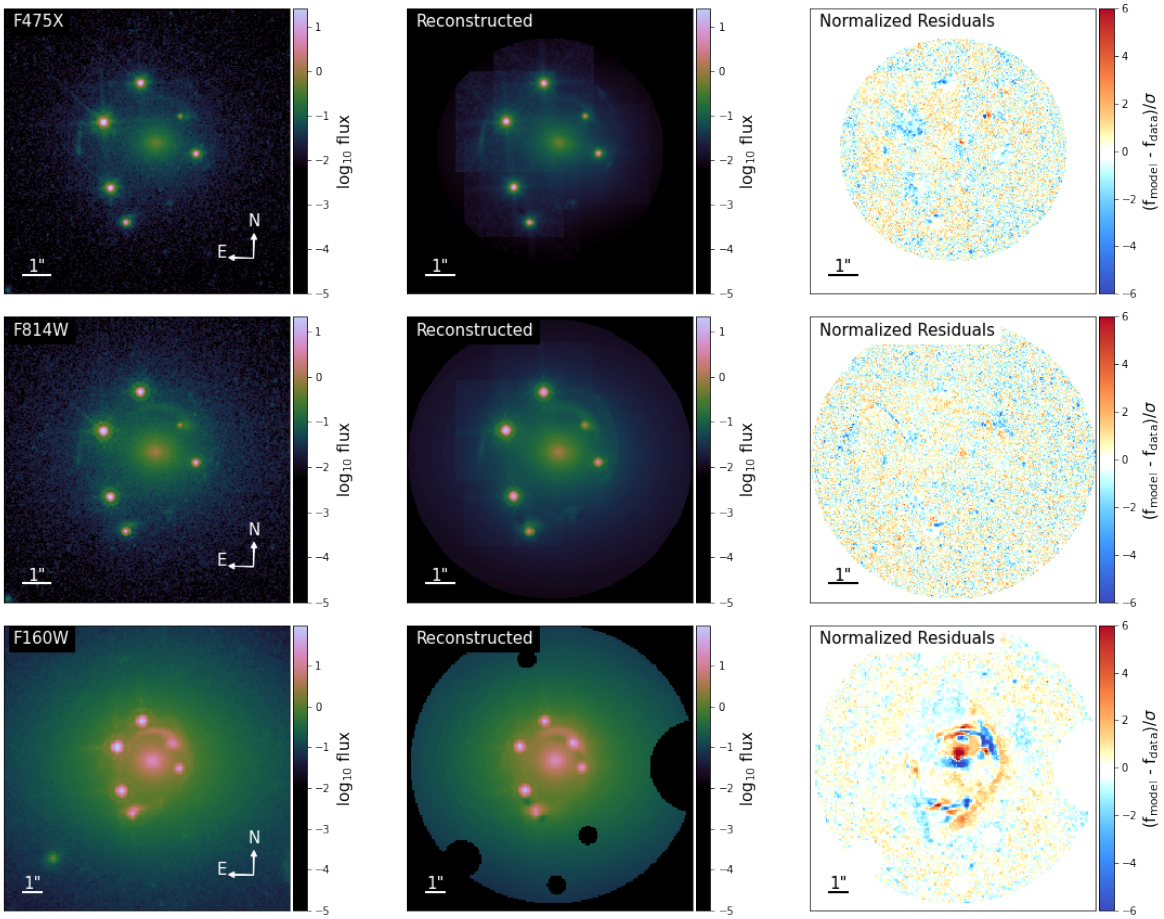

Figure 4.5: Reconstructed composite model for J1721+8842. The first column (left) shows the observations in each band, sorted by wavelength from short to long. The second column (center) displays the reconstructed model for each filter, and in the third column (right) are the normalized residuals between our model and the observed data.

In Figure 4.7 we demonstrate the impact of the deflector's mass at redshift $z = 1.885$ on the time delays as well as the strong correlation with the power-law slope of main deflector. As in the case of the external shear, the Einstein radius of the deflector at redshift $z = 1.885$ was held fixed at $0.''33$ to remedy convergence issues, and therefore no posteriors are shown in Figure 4.7 for the composite model assumption.

Figure 4.8 shows the posterior distribution for the Einstein radii of all perturbers in our models. Due to convergence issues in the case of the composite model assumption, some parameters were held fixed, and therefore only the power-law results are shown. We find a degeneracy between the Einstein radius of the deflector, P1, at redshift $z = 1.885$ and the Einstein radius of the nearby perturber P2. We further note that both, P1 and P2, exhibit a degeneracy with the power-law slope, γ. Additionally, we find correlations in the Einstein radii of perturbers P2 and P5, as well as perturbers P2 and P6. If left unconstrained by priors, these correlations cause the Einstein radii of perturbers P5 and P6 to diverge to zero with associated offsets in the Einstein radii of nearby perturbers P2 and P3 and the deflector P1 at redshift $z = 1.885$.

Figure 4.9 illustrates the decomposition of the primary deflector convergence in the composite mass model case, with the convergence of the dark matter profile (NFW) shown in the left panel, the convergence of the stellar mass (double chameleon) in the center, and the resulting combined convergence (Composite) displayed in the right panel.

In Figure 4.10, we show the total convergence (left panels) from all mass model components, including explicitly modeled nearby perturbers, for both primary deflector mass model assumptions, power law (top row), and composite (bottom row). For both cases of the underlying mass model, we also include a plot of the magnification model (right panels), which indicates the predicted location of the images for the quadruply and the doubly lensed quasar.

Figure 4.11 plots the mean convergence enclosed within a circle of radius r for the dark matter (NFW profile) and baryonic (chameleon profile) components of the composite model

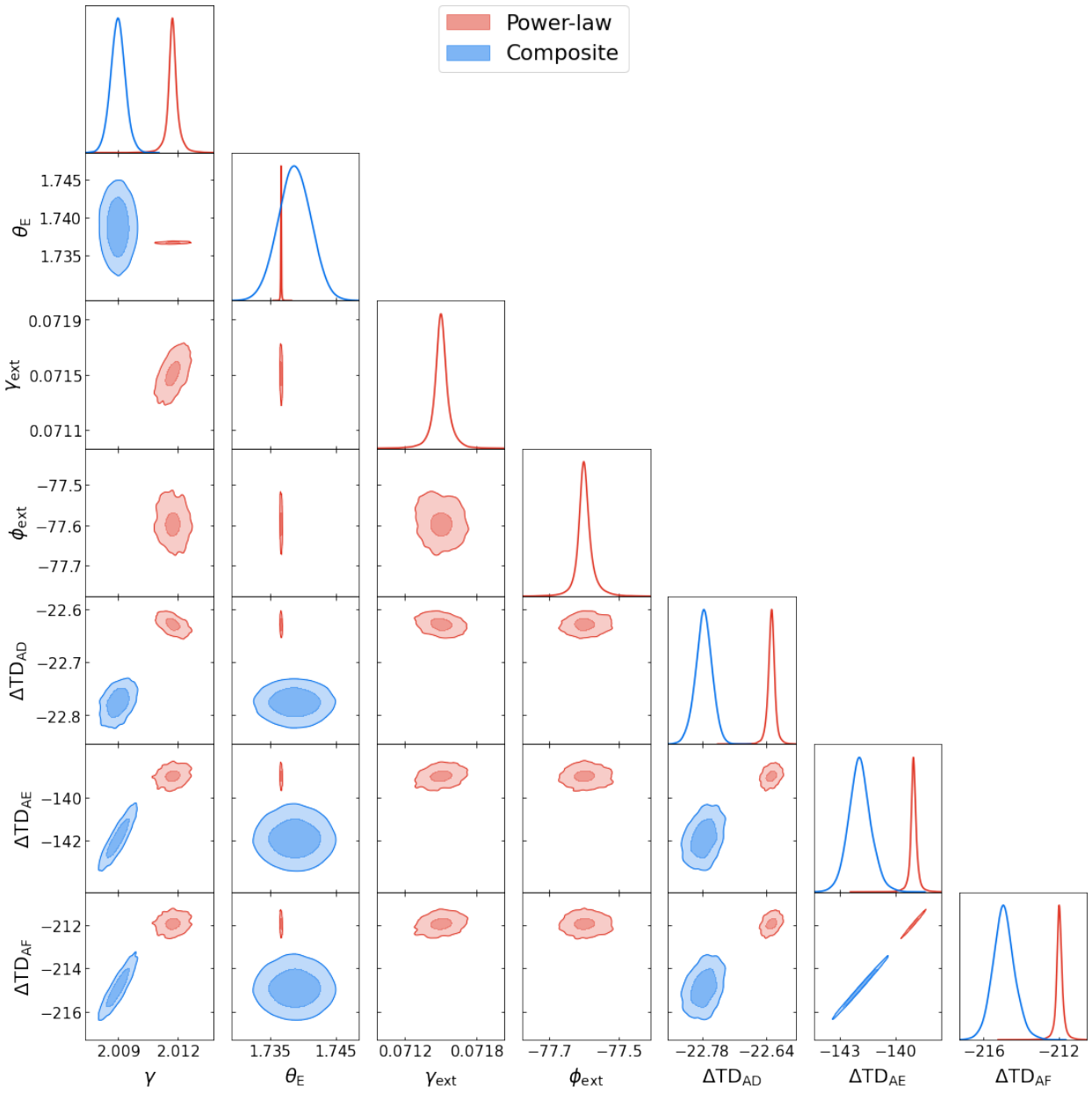

Figure 4.6: Mass model parameters and predicted time delays for the two underlying assumptions of the primary deflector's mass profile. The power-law model results are shown in red while the results for the composite model are colored in blue. In the composite model case, the Einstein radius of the main deflector, P0, is calculated via the circularized average of the convergence and the power-law slope represents the derivative of the convergence at the Einstein radius. To address computational challenges in sampling the composite model parameter space, the external shear is held fixed at the power-law model results, and therefore no composite model posteriors are shown.

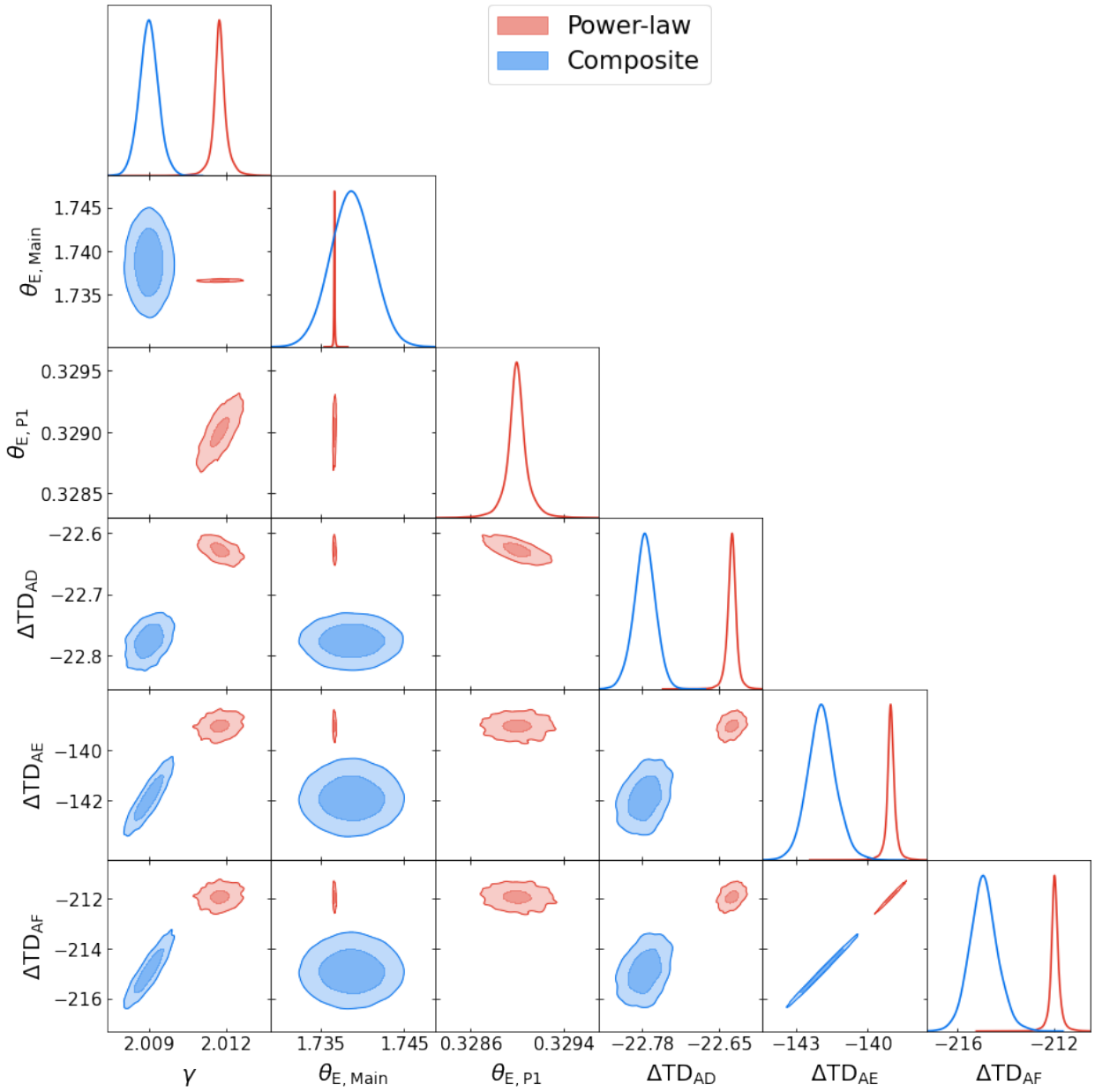

Figure 4.7: Power-law slope, Einstein radii for both deflectors, P0 (main deflector) and P1, and predicted time delays for the two mass profile assumptions of the main deflector. The power-law and composite model results are shown in colors red and blue, respectively. In the composite model case, the Einstein radius of the main deflector, P0, is calculated via the circularized average of the convergence and the power-law slope represents the derivative of the convergence at the Einstein radius. To address computational challenges in sampling the composite model parameter space, the mass of deflector P1 is held fixed at the power-law model results, and therefore no composite model posteriors are shown.

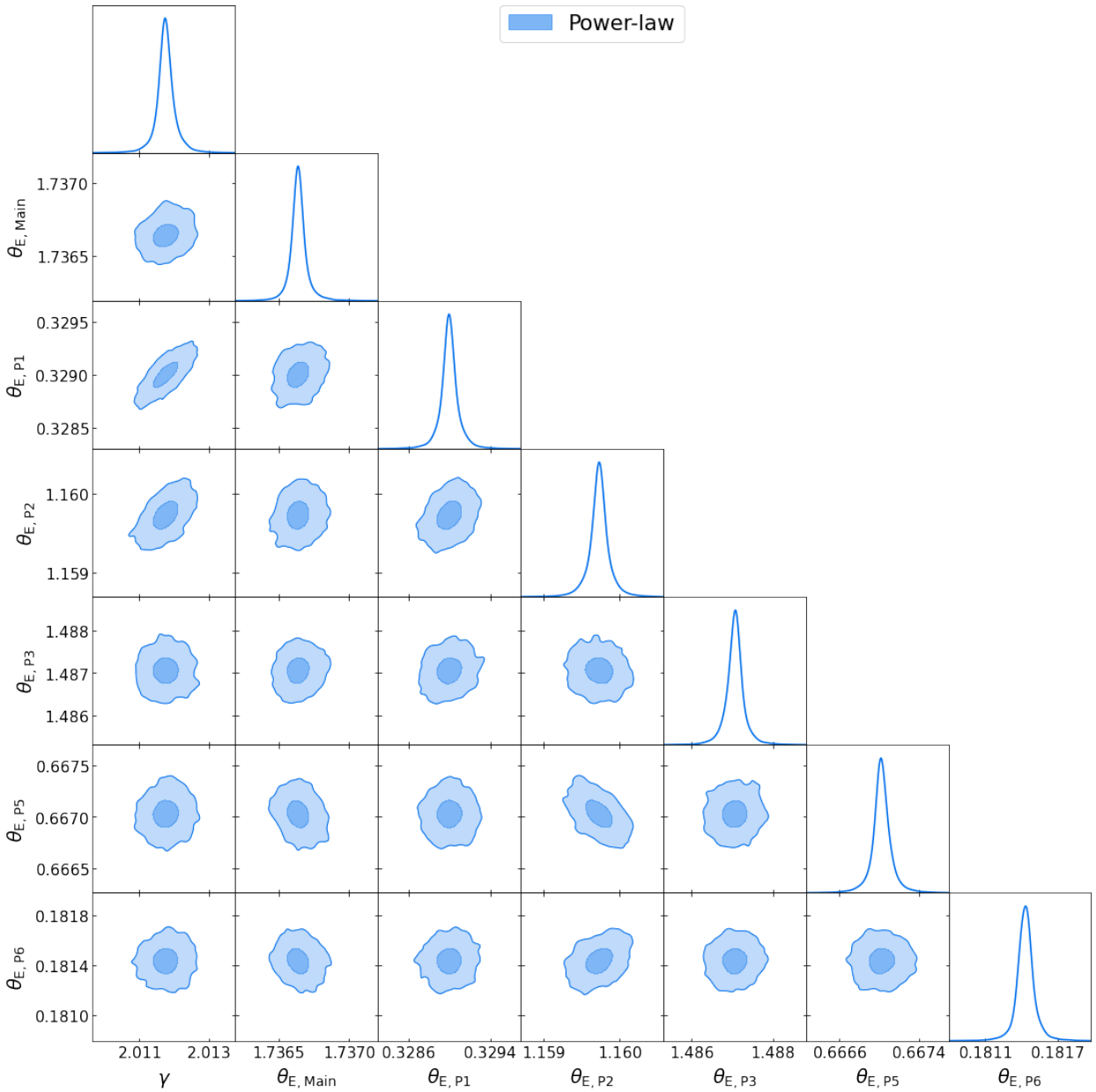

Figure 4.8: Comparison of the main deflector and the perturber Einstein raddii for the power-law mass model assumption.

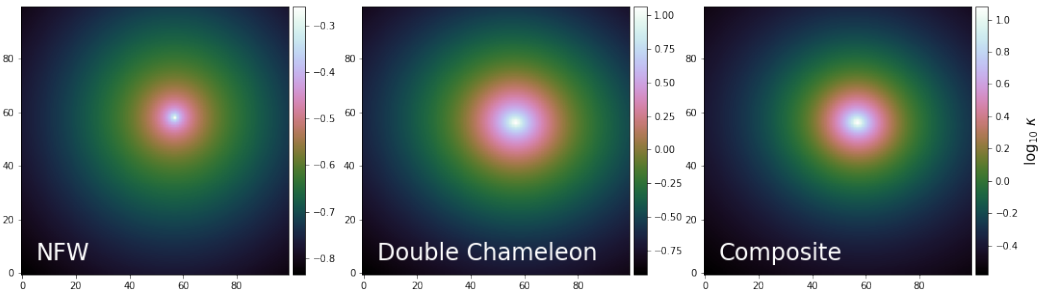

Figure 4.9: Convergence plots of the primary deflector mass in the composite profile case showing the dark matter profile (left panel), the stellar mass (center panel), and the resulting combined projected mass distribution (right panel).

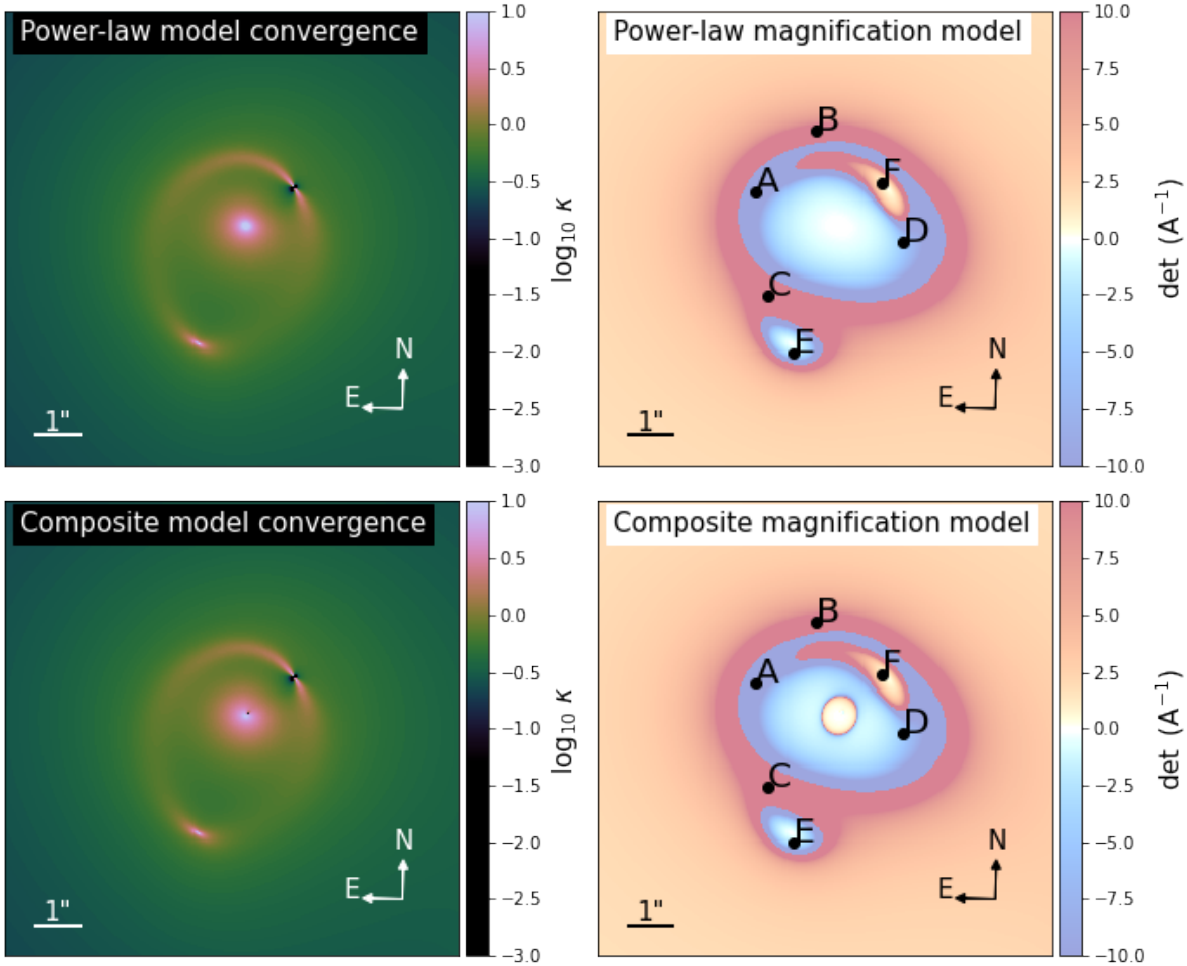

Figure 4.10: Convergence model (left) and magnification model (right) plots for both mass model assumptions of the primary deflector, the power-law (top), and the composite (bottom) model. The magnification plots indicate the predicted position of the lensed quasar images.

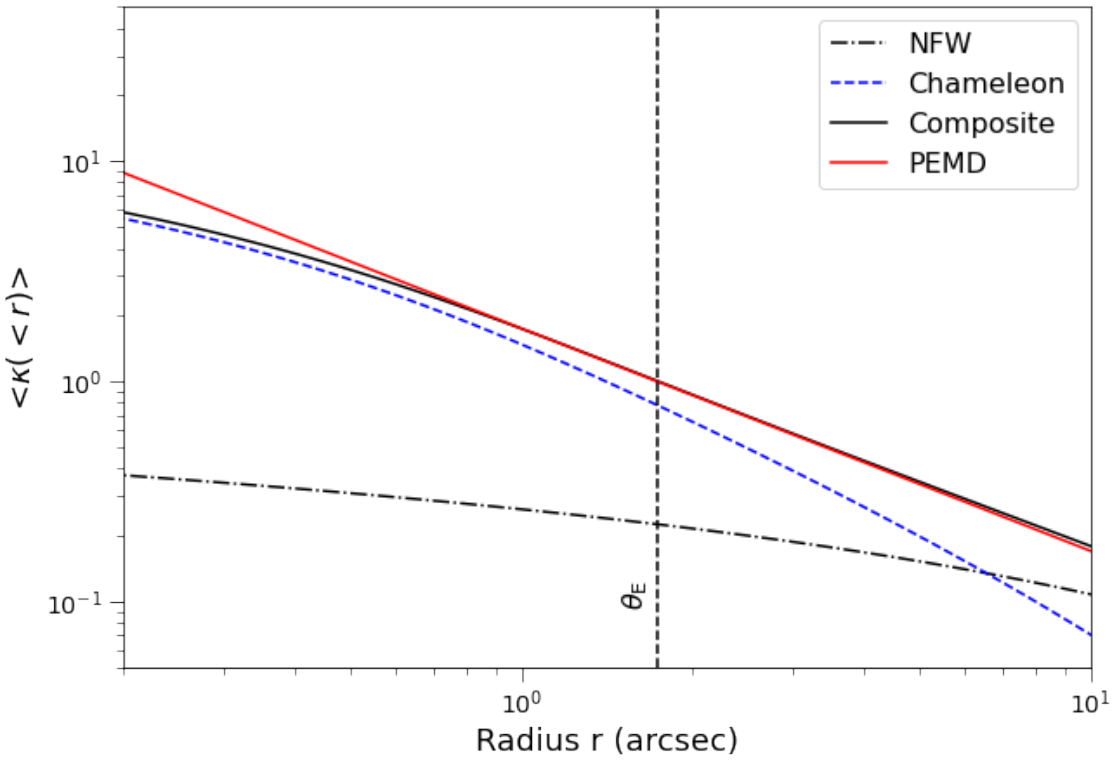

Figure 4.11: Mean convergence within a circle of radius r. Shown are the components of the composite mass profile assumption for the primary deflector, NFW (black dashdotted line), and chameleon (blue dashed line), along with the combined convergence of the composite case (black solid line) and the power-law profile assumption (red solid line). Also plotted is the effective Einstein radius to provide a reference point.

and for the power-law model. We find that even under the assumption of a spherical dark matter profile (i.e., omission of ellipticity), the combined convergence of the composite model matches the convergence of the power-law mass profile case in the region where we observe the lensed quasar images. This is further demonstrated in Figure 4.12, where we show the ratio of the circularized mean convergence between the composite and power-law model main deflector assumption. As illustrated, the resulting convergence of the two model assumptions is nearly identical in the region from around $0.5\theta_{\rm E}$ up to approximately $6\theta_{\rm E}$. To differentiate between the two different model parameterizations, additional information is required, such as stellar velocity dispersion measurements of the primary deflector's central region.

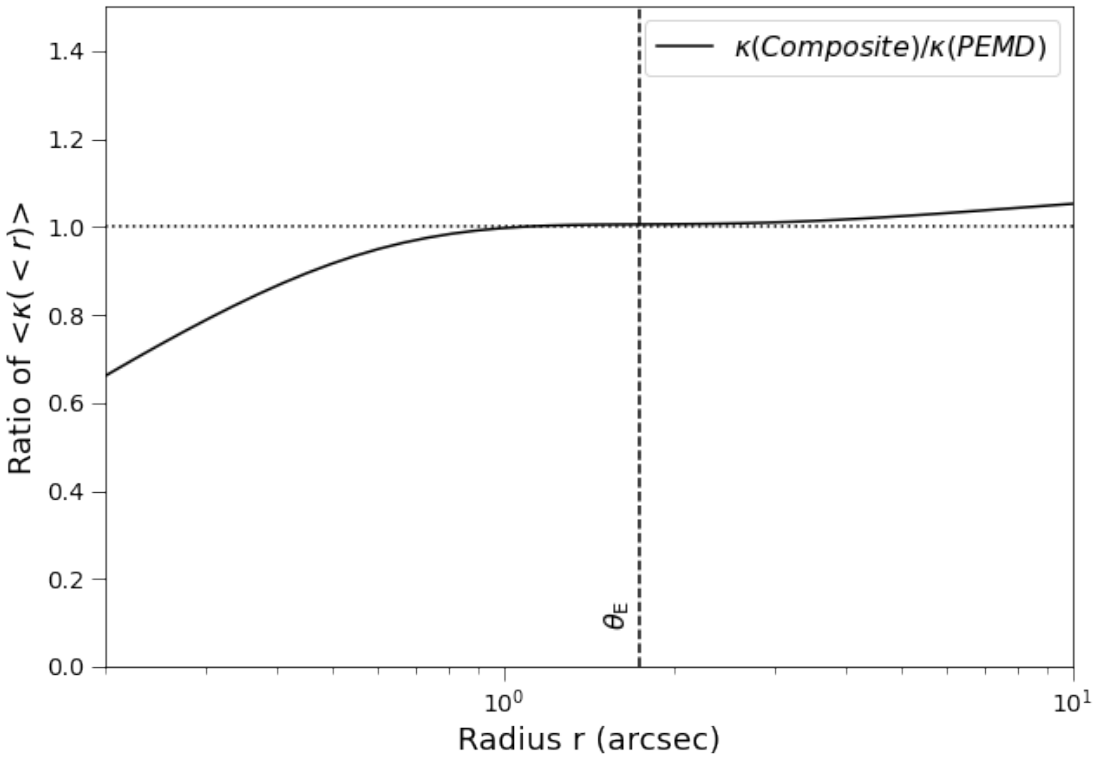

Figure 4.12: Ratio of the circularized averaged convergence as a function of radius, r, between composite and power-law mass model assumptions of the primary deflector.

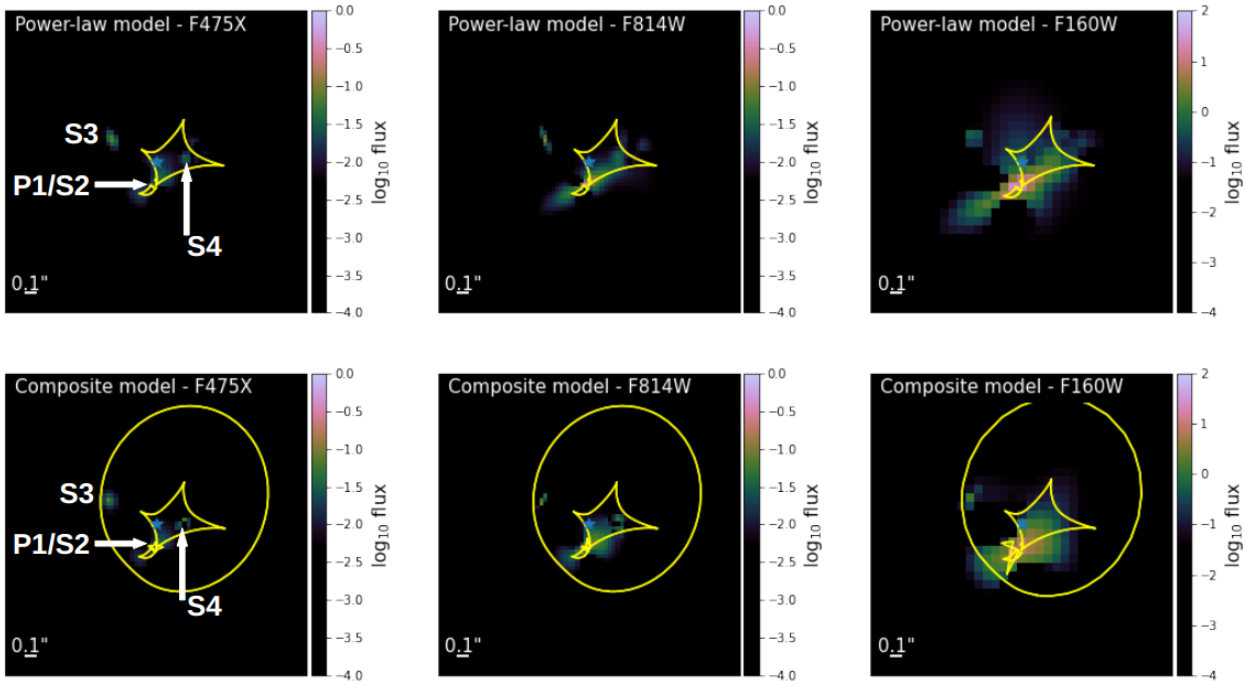

Figure 4.13: Reconstructed sources for both the power-law and composite models. The yellow lines represent the inner and outer caustics curves of the critical lines. The blue star indicates the location of the sextuply imaged quasar in the source plane. For band F475X, we also mark the positions of the additionally lensed sources, S3 and S4, in the source plane as well as the location of the in-between perturber, S2.

Figure 4.13 shows models for the reconstructed lensed sources in the source plane for the power-law model profile assumption (top row) and the composite model (bottom row). For each model the reconstructed sources are sorted by band from shortest to longest wavelength, UVIS filters F475X and F814W in the left and center panels, respectively, and IR band F160W in the right panels. The yellow lines in the plots represent the inner and outer caustic lines, corresponding to the critical curves in the image plane, while the position of the sextuply imaged quasar in the source plane is indicated by the blue star.

In Table 4.3 we list model parameters at the image positions of the sextuply lensed quasar for future microlensing time-delay studies. Specifically, we show total and the stellar convergence at the image positions along with the external shear strength, and the image magnification. The top part of the table tabulates the results of the power-law model assumptions while the lower portion list the composite model results. The stellar convergence

Table 4.3: Lensing results at image positions of the sextuply lensed quasar, obtained from our fiducial power-law and composite model. We show the total convergence, κ, the stellar convergence, $\kappa_\star$, the shear, $\gamma_{\rm shear}$, and the image magnification, μ. For the power-law model, the stellar convergence is estimated from the lens flux in the IR band, assuming a constant mass-to-light ratio, while the stellar convergence for the composite profile results directly from the chameleon mass profile fit(also linked to flux in IR band).

Model	Im	κ	$\kappa_\star$	$\gamma_{\rm shear}$	μ
Power law	A	0.59	0.38	0.61	-5.00
	B	0.53	0.26	0.42	23.15
	C	0.51	0.28	0.39	11.93
	D	0.96	0.64	0.63	-2.51
	E	0.40	0.16	0.20	3.20
	F	0.96	0.60	0.40	-6.29
Composite	A	0.60	0.27	0.60	-4.92
	B	0.54	0.20	0.42	23.31
	C	0.51	0.20	0.39	11.38
	D	0.97	0.43	0.63	-2.51
	E	0.41	0.12	0.20	3.23
	F	0.96	0.43	0.39	-6.75

for the power-law profile is estimated from reconstructed flux in the F160W (IR) band under the assumption of a constant mass to light ratio. For the composite model assumption, we use the results of the double chameleon profile to estimate the stellar convergence at the image positions.

4.5.2 Model comparisons

The models presented in this paper vary significantly in terms of complexity and underlying assumptions for included model components. Furthermore, during the assessment of systematic uncertainties, we also change the size of the likelihood computation mask used to compute the a model's χ^2 value. To obtain a fair comparison between models, we need to account for the variations in model parameters and number of data points used during the likelihood computation. Therefore, we used BIC, defined in Expression 4.23, as a proxy to scale the results of each model based on a corresponding statistical weight, w.

Now, the probability of a model M_i given the data, $\boldsymbol{d}_{HST}$, is formulated as

$$
\begin{aligned}
P(M_i|\boldsymbol{d}_{HST}) &\propto P(\boldsymbol{d}_{HST}|M_i)P(M_i) \\
&\approx \exp\left[-\frac{1}{2}\mathrm{BIC_i}\right] P(M_i).
\end{aligned}
\tag{4.41}
$$

Hence, the relative probability between two models, M1 and M2, given the data, can be written in terms of the model's corresponding BIC values:

$$
\frac{P(M_1|\boldsymbol{d}_{HST})}{P(M_2|\boldsymbol{d}_{HST})} = \exp\left[-\frac{1}{2}(\mathrm{BIC}_1 - \mathrm{BIC}_2)\right]. \tag{4.42}
$$

We used this formulation of relative probability and followed Birrer et al. (2019) and Shajib et al. (2022) to define the evidence ratio function, $f(x)$, based on the difference between a model's corresponding BIC value and the lowest BIC among all possible model configurations, $\mathrm{BIC_{min}}$:

$$
f(x) \equiv \begin{cases} 1 & , x \leq \mathrm{BIC_{min}} \\ \exp\left[-\frac{1}{2}(x - \mathrm{BIC_{min}})\right] & , x > \mathrm{BIC_{min}} \end{cases} \tag{4.43}
$$

To find a model's associated statistical weight, w_i, we convolved the evidence ratio with a Gaussian, g, centered on the BIC value for the model with a variance of σ^2_{BIC}:

$$
w_i = f(x) * g(\mathrm{BIC}_i, \sigma_{\mathrm{BIC}}). \tag{4.44}
$$

The standard deviation, σ^2_{BIC}, represents the total uncertainty in our models and is composed of statistical fluctuations, σ_{int}, and systematic uncertainties, σ_{sys}, added in quadrature:

$$
\sigma^2_{\mathrm{BIC}} = \sigma^2_{\mathrm{int}} + \sigma^2_{\mathrm{sys}}. \tag{4.45}
$$

To determine intrinsic fluctuations, σ_{int}, that arise from the inherent stochasticity in the MCMC, we run the chain for each model twice. The final statistical scatter added to the total

uncertainty in Expression 4.45 is then computed by averaging the error between the twice executed chains across all models. We assess systematic uncertainties, $\sigma_{\rm sys}$, in similar fashion as described in Birrer et al. (2019) and Shajib et al. (2022), namely by finding the standard deviation in BIC values between models that differ in terms of configuration or complexity by only one component or only one fixed parameter setting. As with the intrinsic uncertainties, we take the mean of the systematic scatter across all models before adding it to our total error budget, $\sigma_{\rm BIC}$. Finally, we compute $\sigma_{\rm int}$ to be 20.32 and find $\sigma_{\rm sys} = 104.03$ for the power-law model and $\sigma_{\rm sys} = 240.61$ for the composite model, which combine to a total standard deviation for the BIC, used on the computation of the statistical weights (Expression 4.44), of $\sigma_{\rm BIC} = 106.00$ and $\sigma_{\rm BIC} = 240.61$ for the power-law and composite model, respectively.

Table 4.4 lists the BIC evaluation for our models sorted from lowest BIC number to highest. Each BIC is computed using the corresponding maximum value of the likelihood sampled in each MCMC chain. Since the radii of the likelihood computation mask differ for the assessment of systematic uncertainties, we separate the modeling results according to the masking radii. We further separate the models based on the mass profile assumption for the primary deflector, power-law versus composite model, and show the difference in BIC for each result with respect to the best fit in each category. For each model we include the corresponding statistical weight used in the assessment of the total error budget.

Figure 4.14 shows the measured image positions in the *HST* exposures used for our models as well as the astrometric positions of the quasar images as measured by the *Gaia* satellite. It should be noted that for quasar image F, a *Gaia* measurement is not available. In Figure 4.15 we plot the difference in RA and DEC between the measured astrometric image positions of the lensed quasar in our *HST* exposures and the *Gaia* astrometric position measurements. To provide reference points for the image position comparison we add a boxes at 10 mas, 40 mas, which corresponds to the pixel size in the UVIS bands. The outer box is drawn at 80 mas, reflecting the size of a pixel in the IR band.

As previously indicated, the two assumptions for the main deflector's mass profile result

Table 4.4: BIC evaluations and corresponding statistical weights.

Model	$n_{\max}$	MCMC	Size of likelihood computation mask								
			3.9/4.9/7.4 (″)			4.0/5.0/7.5 (″)			4.1/5.1/7.6 (″)		
		Run	BIC	Δ BIC	Weight	BIC	Δ BIC	Weight	BIC	Δ BIC	Weight
Power law	$-, 2, -, 5$	1	94804.28	30.43	0.368	99051.82	26.67	0.385	103344.45	18.82	0.421
	$-, 2, -, 5$	2	94806.74	32.88	0.357	99047.86	22.71	0.403	103346.83	21.2	0.409
	$-, 4, -, 7$	1	94773.86	0.00	0.509	99026.90	1.75	0.501	103325.63	0.00	0.510
	$-, 4, -, 7$	2	94774.80	0.95	0.504	99025.15	0.00	0.509	103326.76	1.13	0.505
Composite	$-, 2, -, 5$	1				107713.33	43.01	0.313			
	$-, 2, -, 5$	2				107670.32	0.00	0.509			

BIC evaluations including corresponding statistical weights for various models, separated based on the mass profile assumption for the primary deflector. The models are sorted by the radii of the mask used in the computation of the likelihood and the Δ BIC is computed with respect to the best fit of each category.

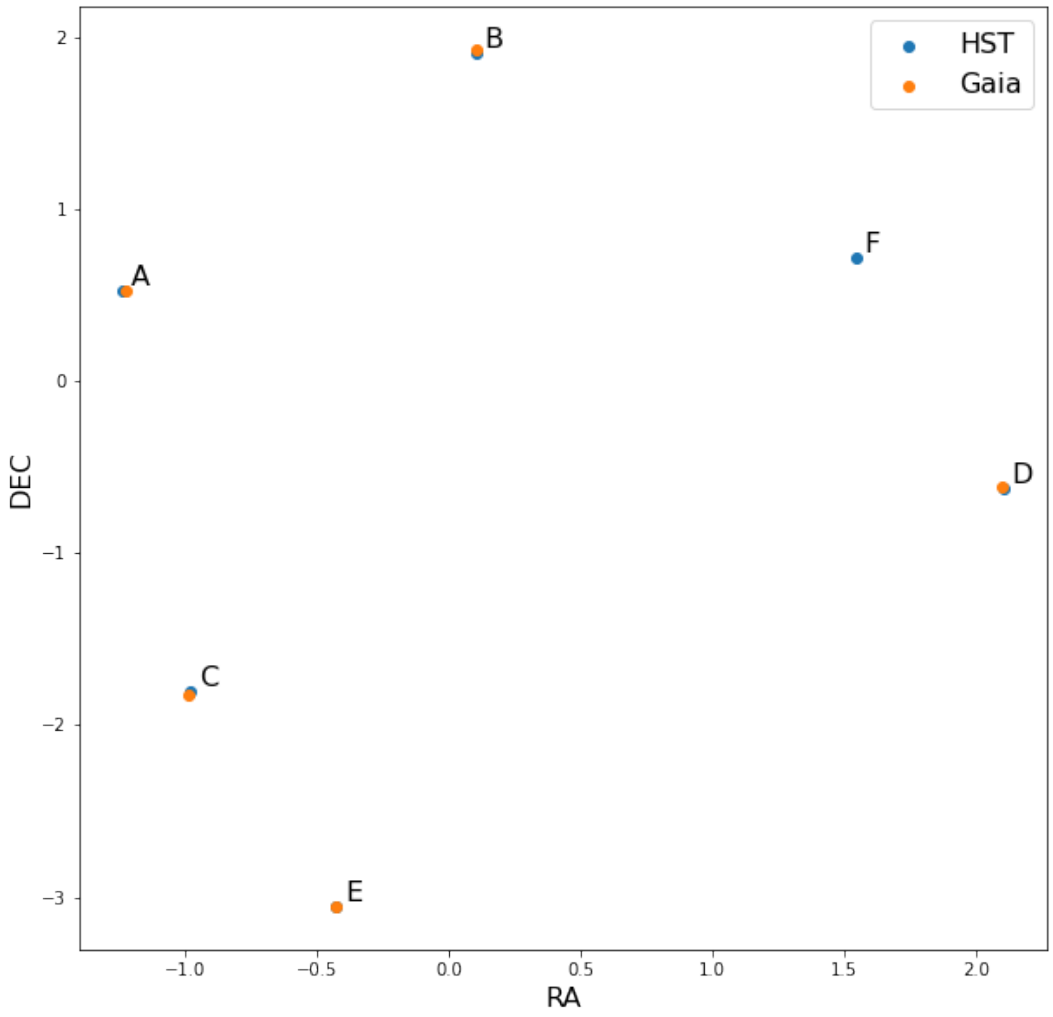

Figure 4.14: Comparison between *HST* astrometry image positions and astrometric image positions as measured by the *Gaia* satellite.

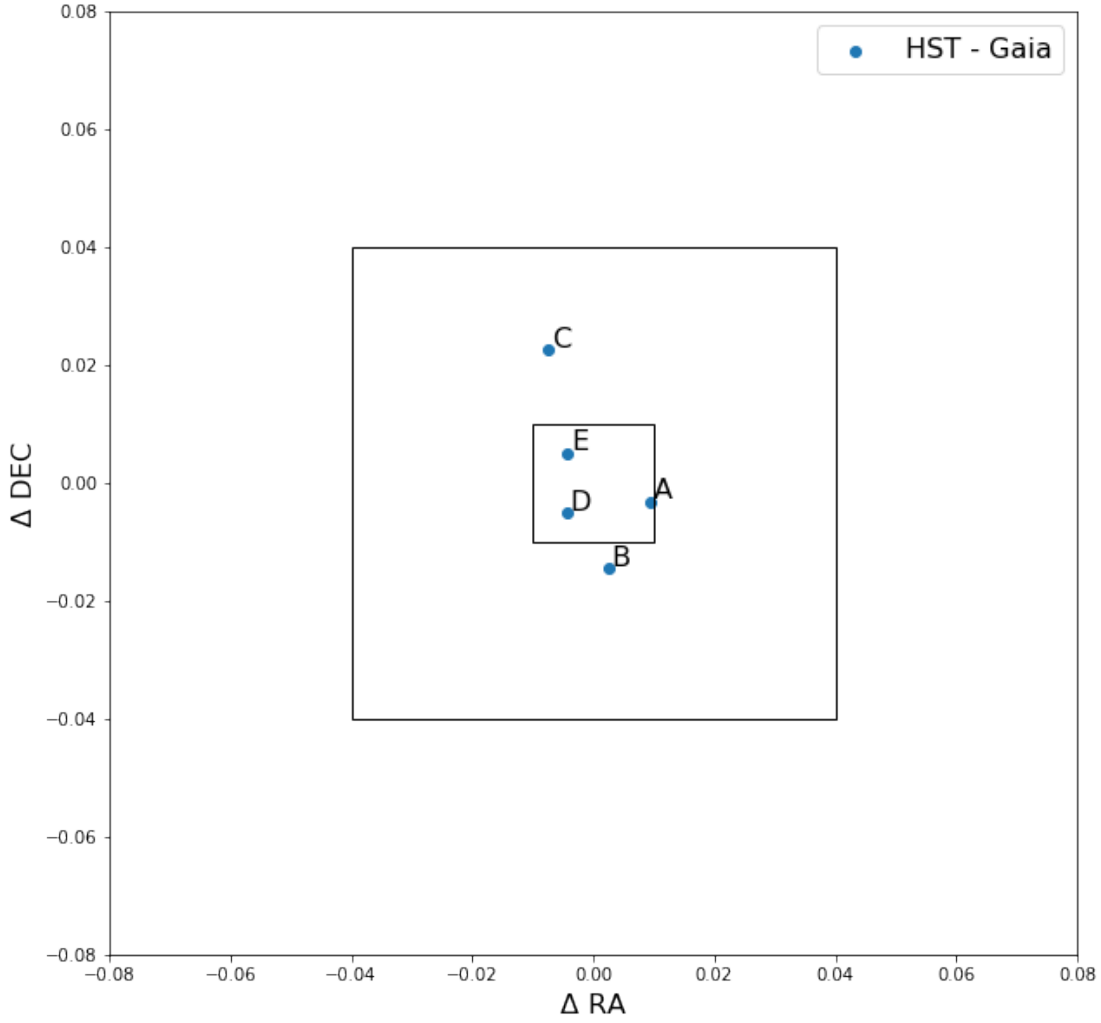

Figure 4.15: Difference between *HST* astrometry image positions and astrometric image positions as measured by the *Gaia* satellite. For reference, boxes are drawn at 10 mas, 40 mas (pixel size in WFC3-UVIS), and 80 mas (drizzled WFC3-IR pixel size).

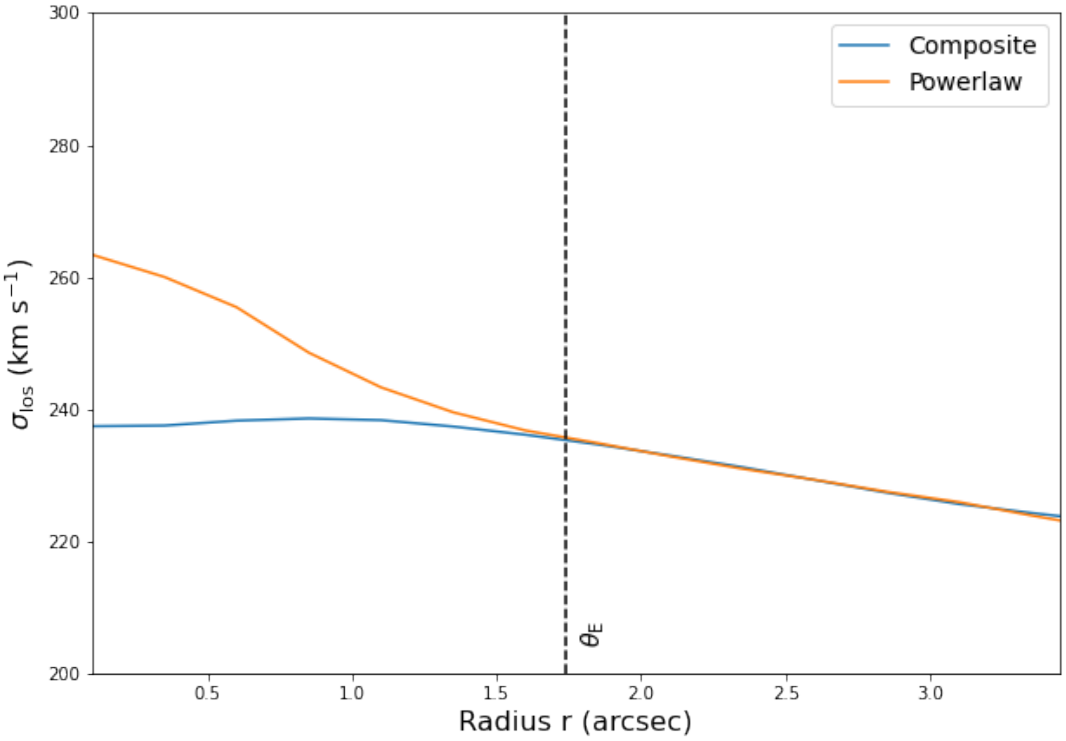

Figure 4.16: Line-of-sight stellar velocity dispersion profiles for the composite (blue line) and power-law (orange line) assumption of the main deflector mass. Both velocity dispersion profiles assume a 1.″ seeing with a 0.″25 binning.

in a convergence that is nearly identical and differs only in the central region. To demonstrate that it would be possible to distinguish the two models through central stellar velocity dispersion measurements, we show in Figure 4.16 the line-of-sight velocity dispersion profiles computed for the power-law model (orange line) and for our composite model (blue line). In both cases the dispersion profiles assume a seeing of 1.″ and are binned at 0.″25. As demonstrated, we expect the stellar velocity dispersion of the composite model to stay approximately constant within the primary deflector's center, resulting from the flattened mass profile.

Table 4.5: Predicted time delays between image positions of the sextuply lensed quasar for power-law and composite model assumptions. The time-delays in the table assume a standard ΛCDM cosmology with $H_0 = 70$ km s^{-1} Mpc^{-1}.

Im. Pair	Power law	Composite	Combined
AB	1.99 ± 0.01	2.08 ± 0.03	2.02 ± 0.04
AC	3.86 ± 0.01	4.06 ± 0.02	3.93 ± 0.09
AD	-22.63 ± 0.01	-22.78 ± 0.02	-22.68 ± 0.07
AE	-139.03 ± 0.23	-141.91 ± 0.61	-139.99 ± 1.41
AF	-211.95 ± 0.23	-214.91 ± 0.60	-212.93 ± 1.45

4.5.3 Predicted time delays

Assuming a flat ΛCDM cosmology with $\Omega_m = 0.3$ we present predictions for measurable time delays between image pairs of the sextuply lensed quasar. Table 4.5 lists the time delays in days, separated by underlying model assumption for the mass profile of the main deflector, power-law, and composite profile. All delays in Table 4.5 include a factor of λh_{70}^{-1}, where λ represents the MSD factor introduced in Section 4.2.2, which includes the external convergence, $\kappa_{\rm ext}$, and the internal MST parameter, $\lambda_{\rm int}$. We define h_{70} as the dimensionless Hubble constant with value $h_{70} = H_0/70$ km s^{-1} Mpc^{-1}.

We find that the predicted time delays of the composite model agree well with the predictions based on the power-law model assumption. As demonstrated in the plots of Figures 4.6 and 4.7, the larger time delays of the imaged quasar are mainly driven by the power-law slope but also show a correlation with the external shear components as well as the Einstein radius of the deflector at redshift $z = 1.885$.

In Figure 4.17, 4.18, 4.19 we show probability densities of predicted time delays for the image pairs of the sextuply lensed quasar AD, AE, and AF, respectively, based on the models explored during the assessment of systematic uncertainties. We further plot the probability densities for our fiducial power-law model (shown in solid red) and our fiducial model for the composite mass model assumption (shown in solid blue). Combining the probabilities based on the corresponding BIC weight, we also present the aggregate time-delay prediction of the sextuply imaged quasar (solid black line).

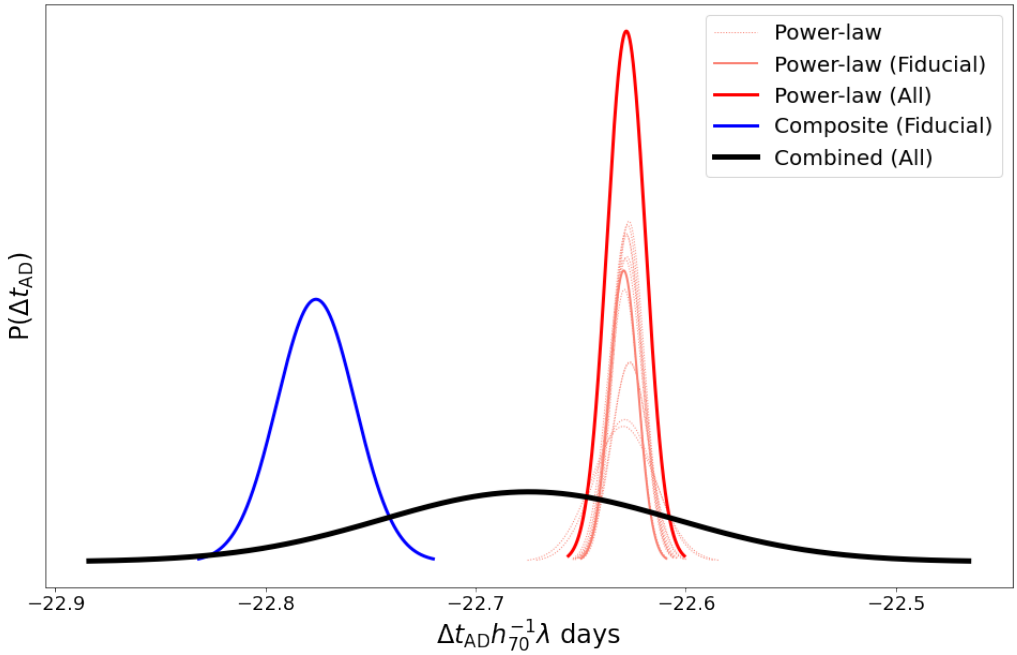

Figure 4.17: Probability density of predicted time-delay for image pair AD of the sextuply lensed quasar. Shown are the delay predictions for the various power-law models (dotted salmon colored) according to their corresponding BIC weight. Also plotted are the delay predictions for the fiducial power-law model (solid red) and the fiducial composite model (solid blue). The thick black solid line represents the combined probability density of all BIC weighted models. The factor λ represents the presently unknown external convergence and the MST factor, to be determined with ancillary data.

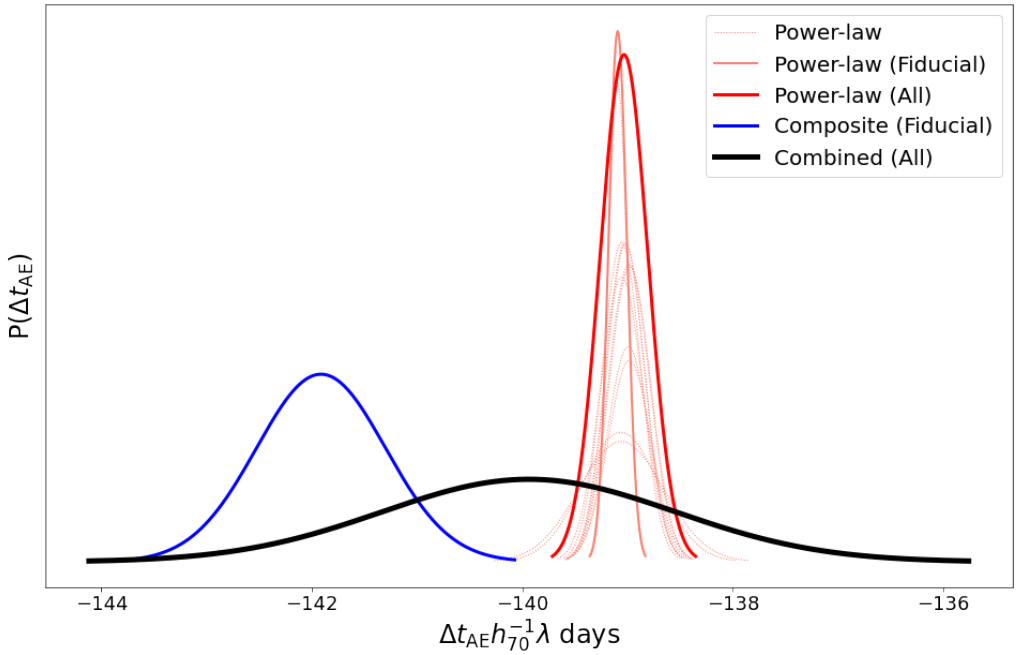

Figure 4.18: Probability density of predicted time-delay for image pair AE of the sextuply lensed quasar. Shown are the delay predictions for the various power-law models (dotted salmon colored) according to their corresponding BIC weight. Also plotted are the delay predictions for the fiducial power-law model (solid red) and the fiducial composite model (solid blue). The thick black solid line represents the combined probability density of all BIC weighted models. The factor λ represents the presently unknown external convergence and the MST factor, to be determined with ancillary data.

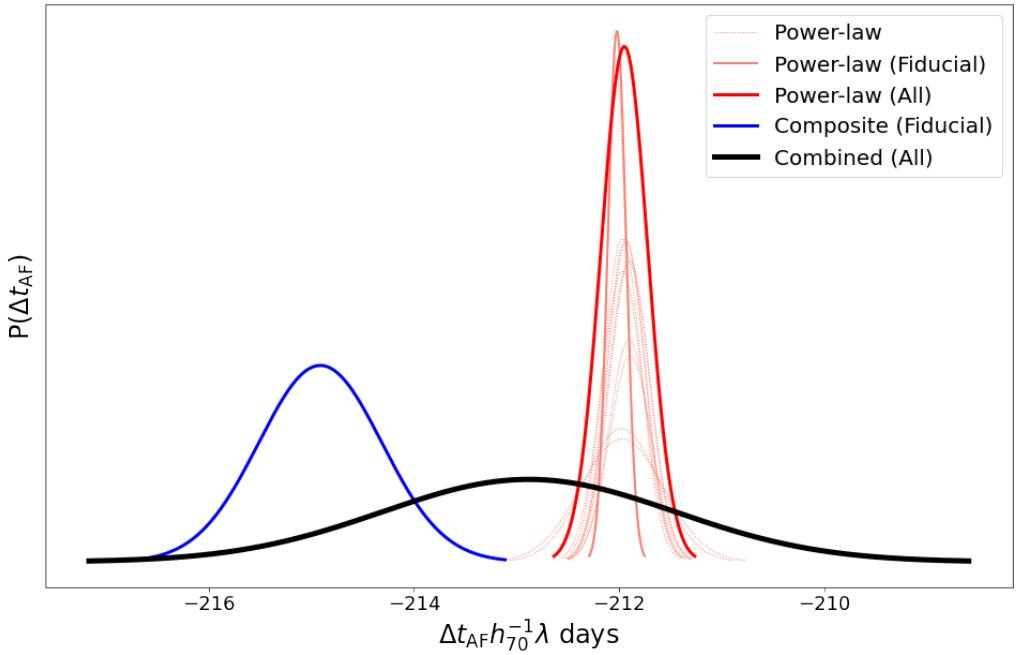

Figure 4.19: Probability density of predicted time-delay for image pair AF of the sextuply lensed quasar. Shown are the delay predictions for the various power-law models (dotted salmon colored) according to their corresponding BIC weight. Also plotted are the delay predictions for the fiducial power-law model (solid red) and the fiducial composite model (solid blue). The thick black solid line represents the combined probability density of all BIC weighted models. The factor λ represents the presently unknown external convergence and the MST factor, to be determined with ancillary data.

We do not expect our predicted time delays to agree with those from previous works published before the identification of the Einstein zigzag configuration. However, we performed a comparison in the interest of understanding the history of the modeling of this system. Compared to the time delays presented by Lemon et al. (2022), we find a difference of more than 3 days for the image pair AD and a difference of over 6 days for the quasar pair EF assumed to be doubly imaged byLemon et al. (2022). The findings presented by Schmidt et al. (2023b), showing results of an automated modeling pipeline, have the same difference of slightly over 3 days for the image pair AD. The work in Lemon et al. (2022) and the results in Schmidt et al. (2023b) both assume a flat ΛCDM cosmology with $H_0 = 70$ km s^{-1} Mpc^{-1}.

We can further compare our predicted time delays to the results presented in Mangat et al. (2021). The delay for the doubly lensed quasar in Mangat et al. (2021) is computed to be 88.1 days, using a value for the Hubble constant of $H_0 = 67.8$ km s^{-1} Mpc^{-1}. Converting this result under the assumption of $H_0 = 70$ km s^{-1} Mpc^{-1} and comparing it to the time-delay prediction presented in this paper, we find a difference of more than 12 days. Clearly, these older models should be not be used for any quantitative study.

4.6 Summary

We have used *HST* observations of J1721+8842 to reconstruct the mass and light distribution of the system. Utilizing the software package Lenstronomy (Birrer and Amara, 2018; Birrer et al., 2021), we modeled the multiplane lens system based on two distinct standard assumptions for the parametrization of the main deflector, namely a power-law mass density profile and a composite profile consisting of a dark matter halo and a stellar component that follows the distribution of light. Both underlying parameterization assumptions explicitly describe an Einstein zigzag and reproduce the observed six-image configuration. The main conclusions of our analysis are summarized by the following points:

- J1721+8842 represents an extraordinary strong lens system comprised of the first-ever discovered sextuply imaged quasar in an Einstein zigzag configuration as the result of strong lensing by two deflectors at different redshifts, which are nearly perfectly aligned with the lensed quasar source along the line of sight. In addition to the multiply imaged quasar and the lensed perturber located in a higher redshift plane, we found two more lensed galaxies in the source plane, which we included in our models. With these three individually lensed sources and the lensed deflector at redshift $z = 1.885$, and with resulting images spanning a range of radii, we find that the mass distribution of the primary lensing galaxy is more constrained compared to a typical quad consisting of a single multiply imaged source.

- Our analysis indicates a correlation between the external shear components and the time delays for image pairs with larger delays (AD, AE, and AF). These longer time delays also correlate with the power-law slope, γ, of the main deflector. Further, we find a dependency for the time delays on the deflector's mass at redshift $z = 1.885$. Additionally, the Einstein radius for this "in-between" deflector also exhibits a degeneracy with the nearby perturber P2, in the main deflector plane, as well as with the power-law slope, γ. As our findings indicate, constraining the mass of the nearby perturber P2 could place limits on the mass of the "in-between" perturber P1 and by extension constrain the predicted time delays even further than the percent level achieved here.

- In the radial range from approximately $0.5\theta_{\rm E}$ to around $6\theta_{\rm E}$, the mean convergence under the central deflector's best-fit power-law mass profile is nearly identical to that of the composite profile model. In other words, the mass profiles for the two model assumptions (power law versus composite) become effectively indistinguishable in the

region where the lensed quasar images are observed.

- We show that measurements of the central stellar velocity dispersion can be used to differentiate between the underlying model parameterizations. Under the assumption of 1.″ seeing with a circular profile binned at 0.″25, a measurement of the stellar velocity dispersion with a precision of 5-10% interior to 1.″ is sufficient to distinguish the two models.

- The time delays for the sextuply imaged quasar, resulting from the first-ever discovered Einstein zigzag configuration, agree at the percent level between both model assumptions for the main deflector (power-law and composite model). In a flat ΛCDM cosmology, with $\Omega_{\rm m} = 0.3$ and $\Omega_\Lambda = 0.7$, the power-law model predicts the following time delays between image pairs, in order from longest to shortest: $\Delta t_{\rm AF} = (-212.0 \pm 0.2) h_{70}^{-1} \lambda$ days, $\Delta t_{\rm AE} = (-139.0 \pm 0.2) h_{70}^{-1} \lambda$ days, $\Delta t_{\rm AD} = (-22.6 \pm 0.01) h_{70}^{-1} \lambda$ days, $\Delta t_{\rm AC} = (3.9 \pm 0.01) h_{70}^{-1} \lambda$ days, and $\Delta t_{\rm AB} = (2.0 \pm 0.01) h_{70}^{-1} \lambda$ days, with $h_{70} = H_0/70$ km s^{-1} Mpc^{-1} as the dimensionless Hubble constant and λ as the MSD factor, which contains the internal MST parameter, $\lambda_{\rm int}$, and the external convergence, $\kappa_{\rm ext}$. Using the same cosmology, the time-delay predictions for the combined results of the power-law and composite models, again in order from longest to shortest, are $\Delta t_{\rm AF} = (-212.9 \pm 1.5) h_{70}^{-1} \lambda$ days, $\Delta t_{\rm AE} = (-140.0 \pm 1.4) h_{70}^{-1} \lambda$ days, $\Delta t_{\rm AD} = (-22.7 \pm 0.07) h_{70}^{-1} \lambda$ days, $\Delta t_{\rm AC} = (3.9 \pm 0.09) h_{70}^{-1} \lambda$ days, and $\Delta t_{\rm AB} = (2.0 \pm 0.04) h_{70}^{-1} \lambda$ days. Even though the analysis for this target was blinded with regard to measured time delays between image pairs, we point out that Dux et al. (2025b) find a preliminary delay between images D and E of $\Delta t_{\rm DE} \sim -35$ days, while the combined result from our power-law and composite models show a delay of $\Delta t_{\rm DE} \sim -117 h_{70}^{-1} \lambda$ days for this image pair. Further work is required to combine these measurements to account for the multiplane

MSD, as discussed below.

A future paper will build on our models and time-delay predictions for J1721+8842 and incorporate measurements of observed time delay, a spectroscopic measurement of the stellar velocity dispersion, and an estimate for the external convergence based on a model for the line-of-sight mass distribution to present a complete H_0 inference. Furthermore, the unusual configuration means that we have to consider the possibility of a mass sheet and external shear within both the main-deflector plane and the redshift $z = 1.885$ plane. Considering the degeneracy between the mass of the in-between deflector P1 and the observed time delays, constraining the mass sheet and shear in the $z = 1.885$ plane will be crucial for cosmological analysis. At the same time, the unique configuration gives us some leverage in addressing this degeneracy with lensing data alone. These topics will be addressed in a future paper (Millon et al., in prep).

Acknowledgements

This research is based on observations made with the NASA/ESA Hubble Space Telescope obtained from the Space Telescope Science Institute, which is operated by the Association of Universities for Research in Astronomy, Inc., under NASA contract NAS 5-26555. These observations are associated with programs HST-GO-15320 and HST-GO-15652. Support for the two programs was provided by NASA through a grant from the Space Telescope Science Institute, which is operated by the Association of Universities for Research in Astronomy, Inc., under NASA contract NAS 5-26555.

We thank the referee for constructive reports.

TS TT acknowledge support by the National Science Foundation through grant NSF-AST-1906976 and NSF-AST-1907396 "Collaborative Research: Toward a 1% measurement

of the Hubble Constant with gravitational time delays". TT acknowledges support by the Gordon and Betty Moore Foundation. MM acknowledges support by the Swiss National Science Foundation (SNSF) through mobility grant P500PT_203114. SB acknowledges support from the Department of Physics & Astronomy, Stony Brook University. DS acknowledges the support of the Fonds de la Recherche Scientifique-FNRS, Belgium, under grant No. 4.4503.1. This work is also supported by NASA through the NASA Hubble Fellowship grant HST-HF2-51492 awarded to AJS by the Space Telescope Science Institute, which is operated by the Association of Universities for Research in Astronomy, Inc., for NASA, under contract NAS5-26555. AJS also received support from NASA through the Space Telescope Science Institute grants HST-GO-16773 and JWST-GO-2974. AG FC acknowledge funding and support by the SNSF. This project has received funding from the European Union's Horizon Europe research and innovation programme under the Marie Sklodovska-Curie grant agreement No 101105725. This work has received support by the Swiss National Science Foundation (SNSF) and by the European Research Council (ERC) under the European Unions Horizon 2020 research and innovation programme (COSMICLENS: grant agreement No 787886).

This research made use of LENSTRONOMY (Birrer and Amara, 2018; Birrer et al., 2021), EMCEE (Foreman-Mackey et al., 2013), FASTELL (Barkana, 1998), SEXTRACTOR (Bertin and Arnouts, 1996), NUMPY (Oliphant, 2015), SCIPY (Jones et al., 2001), ASTROPY (Astropy Collaboration et al., 2018), JUPYTER (Kluyver et al., 2016), MATPLOTLIB (Hunter, 2007), SEABORN (Waskom, 2021), GETDIST (https://github.com/cmbant/getdist), and STARRED (Michalewicz et al., 2023; Millon et al., 2024) .

Chapter 5

Conclusion

5.1 Summaries

In this thesis, I present significant advances in strong gravitational lensing methodologies for cosmological parameter measurements, with particular focus on the Hubble constant, H_0. My work described herein spans from developing an efficient automated strong lens modeling pipeline for large strong lens samples to detailed analyses of an extraordinary individual system that promise unprecedented precision in time-delay cosmography.

This research demonstrates that uniform, cosmography-grade modeling of strong lens systems can be achieved at large scale through automated pipelines, reducing both computational overhead and human time investment by orders of magnitude (see Chapter 2). Applied to 31 strong lens systems observed with *HST* during cycles 25 and 26, this approach successfully produces cosmography-ready models for approximately 1/3 of the sample, with remaining systems just below or near this standard. This represents a crucial step toward exploiting the wealth of strong lens discoveries expected over the coming decades.

In two detailed case studies of the remarkable system J1721+8842, I showcase the extraordinary potential of complex lensing configurations for high-precision cosmology (Chapters 3 and 4). Modeled as both an unprecedented dual AGN system and the first-ever confirmed

Einstein zigzag lens, J1721+8842 provides exceptional constraints on lens mass profiles and enables long-desired percent-level precision in time-delay predictions along with measurements of other cosmological parameters. The system's unique geometry offers a pathway to high-precision cosmography and with it an independent H_0 measurements that could aid in the resolution or further increase the current Hubble tensions.

5.1.1 Chapter 2: Automated uniform models for 30 quadruply imaged quasars

Gravitational time delays provide a powerful one step measurement of H_0, independent of all other probes. One key ingredient in time delay cosmography are high accuracy lens models. Those are currently expensive to obtain, both, in terms of computing and investigator time (10^{5-6} CPU hours and $\sim$0.5-1 year, respectively). Major improvements in modeling speed are therefore necessary to exploit the large number of lenses that are forecast to be discovered over the current decade. In order to bypass this roadblock, we develop an automated modeling pipeline and apply it to a sample of 31 lens systems, observed by the Hubble Space Telescope in multiple bands. Our automated pipeline can derive models for 30/31 lenses with few hours of human time and $<$100 CPU hours of computing time for a typical system. For each lens, we provide measurements of key parameters and predictions of magnification as well as time delays for the multiple images. We characterize the cosmography-readiness of our models using the stability of differences in Fermat potential (proportional to time delay) w.r.t. modeling choices. We find that for 10/30 lenses our models are cosmography or nearly cosmography grade ($<$3% and 3-5% variations). For 6/30 lenses the models are close to cosmography grade (5-10%). These results utilize informative priors and will need to be confirmed by further analysis. However, they are also likely to improve by extending the pipeline modeling sequence and options. In conclusion, we show that uniform cosmography grade modeling of large strong lens samples is within reach.

5.1.2 Chapter 3: Cosmography grade model and time-delay prediction for the extraordinary gravitational lens J1721+8842

We present lens models for J1721+8842, an unprecedented galaxy-scale strong lens consisting of four separate lensed galaxies, under the assumption of two of the sources hosting a quasar each, one quadruply imaged and the second doubly imaged. The dual AGN interpretation presented in this analysis is superseded by models presented in Chapter 4 due to the following discoveries: Time-delay and JWST spectroscopic measurements reveal that the previously believed dual AGN images belong to the same background quasar, lensed by two separate deflectors at different redshifts. Specifically, the JWST observations show that one of the lensed galaxies, previously thought to host the doubly imaged quasar, is in fact a lensed galaxy at a redshift between the primary lens and the consequently sextuply-imaged quasar. This discovery was made after the original dual-AGN analysis was completed and submitted for publication.

Nevertheless, the configuration of four lensed sources tightly constrains the lensing galaxy's mass profile. Using two standard descriptions for the main perturber's mass distribution - total power-law profile and composite dark and stellar mass - the inferred convergence around the location of the lensed images is in excellent agreement. Additionally, our results show that even with accounting for nearby perturbers, external distortion of higher order than shear and convergence (i.e., flexion) must be allowed in order to match the exquisite data.

While the strong lensing data alone does not significantly favor either of our profile assumption for the main deflector's mass distribution, we show that a central stellar velocity dispersion measurement can distinguish or validate them. Using a standard ΛCDM cosmology with $H_0 = 70$ km s^{-1} Mpc^{-1}, we present time-delay predictions between the lensed quasar images for both models.

A combination our model with the deflector's stellar velocity dispersion, the line of sight convergence, and with observed time-delays will constrain the angular diameter distance for J1721+8842, resulting in a one-step determination of H_0, independent of other methods.

Owing to the extraordinary configuration, the precision and accuracy of the long delay prediction results in modeling errors at the percent level, making this an extremely promising system for the determination of H_0.

5.1.3 Chapter 4: Strong lens model and time-delay predictions for J1721+8842, the first Einstein zigzag lens

We present lens models for J1721+8842, the first-ever discovered galaxy-scale strong lens in an Einstein zigzag configuration. The model consists of four separate lensed galaxies, with the primary source hosting a quasar, lensed into six images by two deflectors at redshifts $z_1 = 0.184$ and $z_2 = 1.885$. The configuration of three lensed sources and the lensed light of the deflector at redshift $z_2 = 1.885$ tightly constrain the mass profile of the primary lensing galaxy. Using two standard descriptions for the main perturber's mass distribution - a total power-law profile and a composite dark and stellar mass - the inferred convergence around the location of the lensed images is in excellent agreement.

While the strong lensing data alone does not significantly favor either of our profile assumptions for the main deflector's mass distribution, we show that a central stellar velocity dispersion measurement can distinguish or validate them. Using a standard ΛCDM cosmology with $H_0 = 70$ km s^{-1} Mpc^{-1}, we present time-delay predictions between the lensed quasar images for both models at the percent level modulo a multiplane mass sheet transform.

Our models are the first step toward constraining the time-delay distance ratios for J1721+8842, and thus also H_0, independent of other methods. In order to achieve an H_0 measurement, our models need to be combined in a multiplane lensing analysis with the stellar velocity dispersion for the deflectors, the line-of-sight convergence, and the observed time delays. Owing to its extraordinary configuration, this is an extremely promising system for a high-precision determination of H_0.

5.2 Final remarks

The work presented in this thesis addresses critical bottlenecks in time-delay cosmography while demonstrating the remarkable diversity and scientific potential of strong gravitational lens systems. By developing automated modeling capabilities in addition to detailed analyses of the exceptional strong lens configuration known as J1721+8842, this research continues to expand and build on strong lensing concepts to add to an already expansive catalog of strong lens H_0 measurements, and further contributes to future high-precision cosmological measurements for the next generation of strong lens surveys.

The combination of efficient modeling techniques with extraordinary natural laboratories such as Einstein zigzag strong lens configurations position strong lensing as an increasingly powerful tool for addressing fundamental questions in cosmology. Furthermore, as lens discovery rates accelerate with upcoming surveys, the automated modeling approach and the detailed case studies presented in this thesis pave the way to transform strong lensing from a specialized technique into a cornerstone method for high-precision measurements of H_0 and other cosmological parameters.

Bibliography

Abdalla, E., Abellán, G. F., Aboubrahim, A., Agnello, A., Akarsu, Ö., Akrami, Y., Alestas, G., Aloni, D., Amendola, L., Anchordoqui, L. A., Anderson, R. I., Arendse, N., Asgari, M., Ballardini, M., Barger, V., Basilakos, S., Batista, R. C., Battistelli, E. S., Battye, R., Benetti, M., Benisty, D., Berlin, A., de Bernardis, P., Berti, E., Bidenko, B., Birrer, S., Blakeslee, J. P., Boddy, K. K., Bom, C. R., Bonilla, A., Borghi, N., Bouchet, F. R., Braglia, M., Buchert, T., Buckley-Geer, E., Calabrese, E., Caldwell, R. R., Camarena, D., Capozziello, S., Casertano, S., Chen, G. C. F., Chluba, J., Chen, A., Chen, H.-Y., Chudaykin, A., Cicoli, M., Copi, C. J., Courbin, F., Cyr-Racine, F.-Y., Czerny, B., Dainotti, M., D'Amico, G., Davis, A.-C., de Cruz Pérez, J., de Haro, J., Delabrouille, J., Denton, P. B., Dhawan, S., Dienes, K. R., Di Valentino, E., Du, P., Eckert, D., Escamilla-Rivera, C., Ferté, A., Finelli, F., Fosalba, P., Freedman, W. L., Frusciante, N., Gaztañaga, E., Giarè, W., Giusarma, E., Gómez-Valent, A., Handley, W., Harrison, I., Hart, L., Hazra, D. K., Heavens, A., Heinesen, A., Hildebrandt, H., Hill, J. C., Hogg, N. B., Holz, D. E., Hooper, D. C., Hosseininejad, N., Huterer, D., Ishak, M., Ivanov, M. M., Jaffe, A. H., Jang, I. S., Jedamzik, K., Jimenez, R., Joseph, M., Joudaki, S., Kamionkowski, M., Karwal, T., Kazantzidis, L., Keeley, R. E., Klasen, M., Komatsu, E., Koopmans, L. V. E., Kumar, S., Lamagna, L., Lazkoz, R., Lee, C.-C., Lesgourgues, J., Levi Said, J., Lewis, T. R., L'Huillier, B., Lucca, M., Maartens, R., Macri, L. M., Marfatia, D., Marra, V., Martins, C. J. A. P., Masi, S., Matarrese, S., Mazumdar, A., Melchiorri, A., Mena, O., Mersini-Houghton, L., Mertens, J., Milaković, D., Minami, Y., Miranda, V., Moreno-Pulido, C.,

Moresco, M., Mota, D. F., Mottola, E., Mozzon, S., Muir, J., Mukherjee, A., Mukherjee, S., Naselsky, P., Nath, P., Nesseris, S., Niedermann, F., Notari, A., Nunes, R. C., Ó Colgáin, E., Owens, K. A., Özülker, E., Pace, F., Paliathanasis, A., Palmese, A., Pan, S., Paoletti, D., Perez Bergliaffa, S. E., Perivolaropoulos, L., Pesce, D. W., Pettorino, V., Philcox, O. H. E., Pogosian, L., Poulin, V., Poulot, G., Raveri, M., Reid, M. J., Renzi, F., Riess, A. G., Sabla, V. I., Salucci, P., Salzano, V., Saridakis, E. N., Sathyaprakash, B. S., Schmaltz, M., Schöneberg, N., Scolnic, D., Sen, A. A., Sehgal, N., Shafieloo, A., Sheikh-Jabbari, M. M., Silk, J., Silvestri, A., Skara, F., Sloth, M. S., Soares-Santos, M., Solà Peracaula, J., Songsheng, Y.-Y., Soriano, J. F., Staicova, D., Starkman, G. D., Szapudi, I., Teixeira, E. M., Thomas, B., Treu, T., Trott, E., van de Bruck, C., Vazquez, J. A., Verde, L., Visinelli, L., Wang, D., Wang, J.-M., Wang, S.-J., Watkins, R., Watson, S., Webb, J. K., Weiner, N., Weltman, A., Witte, S. J., Wojtak, R., Yadav, A. K., Yang, W., Zhao, G.-B., and Zumalacárregui, M. (2022). Cosmology intertwined: A review of the particle physics, astrophysics, and cosmology associated with the cosmological tensions and anomalies. *Journal of High Energy Astrophysics*, 34:49–211.

Agnello, A. (2018). WG021416.37-210535.3, A Quadruply Lensed Quasar in Three Public Surveys. *Research Notes of the American Astronomical Society*, 2(2):42.

Agnello, A., Kelly, B. C., Treu, T., and Marshall, P. J. (2015). Data mining for gravitationally lensed quasars. *MNRAS*, 448(2):1446–1462.

Agnello, A. and Spiniello, C. (2019). Quasar lenses in the south: searches over the DES public footprint. *MNRAS*, 489(2):2525–2535.

Anguita, T., Schechter, P. L., Kuropatkin, N., Morgan, N. D., Ostrovski, F., Abramson, L. E., Agnello, A., Apostolovski, Y., Fassnacht, C. D., Hsueh, J. W., Motta, V., Rojas, K., Rusu, C. E., Treu, T., Williams, P., Auger, M., Buckley-Geer, E., Lin, H., McMahon, R., Abbott, T. M. C., Allam, S., Annis, J., Bernstein, R. A., Bertin, E., Brooks, D., Burke, D. L., Carnero Rosell, A., Carrasco-Kind, M., Carretero, J., Cunha, C. E., D'Andrea,

C. B., De Vicente, J., DePoy, D. L., Desai, S., Diehl, H. T., Doel, P., Flaugher, B., García-Bellido, J., Gerdes, D. W., Gruen, D., Gruendl, R. A., Gschwend, J., Hartley, W. G., Hollowood, D. L., Honscheid, K., James, D. J., Kuehn, K., Lima, M., Maia, M. A. G., Miquel, R., Plazas, A. A., Sanchez, E., Scarpine, V., Smith, M., Soares-Santos, M., Sobreira, F., Suchyta, E., Tarle, G., and Walker, A. R. (2018). The STRong lensing Insights into the Dark Energy Survey (STRIDES) 2016 follow-up campaign - II. New quasar lenses from double component fitting. *MNRAS*, 480(4):5017–5028.

Astropy Collaboration, Price-Whelan, A. M., Sipőcz, B. M., Günther, H. M., Lim, P. L., Crawford, S. M., Conseil, S., Shupe, D. L., Craig, M. W., Dencheva, N., Ginsburg, A., VanderPlas, J. T., Bradley, L. D., Pérez-Suárez, D., de Val-Borro, M., Aldcroft, T. L., Cruz, K. L., Robitaille, T. P., Tollerud, E. J., Ardelean, C., Babej, T., Bach, Y. P., Bachetti, M., Bakanov, A. V., Bamford, S. P., Barentsen, G., Barmby, P., Baumbach, A., Berry, K. L., Biscani, F., Boquien, M., Bostroem, K. A., Bouma, L. G., Brammer, G. B., Bray, E. M., Breytenbach, H., Buddelmeijer, H., Burke, D. J., Calderone, G., Cano Rodríguez, J. L., Cara, M., Cardoso, J. V. M., Cheedella, S., Copin, Y., Corrales, L., Crichton, D., D'Avella, D., Deil, C., Depagne, É., Dietrich, J. P., Donath, A., Droettboom, M., Earl, N., Erben, T., Fabbro, S., Ferreira, L. A., Finethy, T., Fox, R. T., Garrison, L. H., Gibbons, S. L. J., Goldstein, D. A., Gommers, R., Greco, J. P., Greenfield, P., Groener, A. M., Grollier, F., Hagen, A., Hirst, P., Homeier, D., Horton, A. J., Hosseinzadeh, G., Hu, L., Hunkeler, J. S., Ivezić, Ž., Jain, A., Jenness, T., Kanarek, G., Kendrew, S., Kern, N. S., Kerzendorf, W. E., Khvalko, A., King, J., Kirkby, D., Kulkarni, A. M., Kumar, A., Lee, A., Lenz, D., Littlefair, S. P., Ma, Z., Macleod, D. M., Mastropietro, M., McCully, C., Montagnac, S., Morris, B. M., Mueller, M., Mumford, S. J., Muna, D., Murphy, N. A., Nelson, S., Nguyen, G. H., Ninan, J. P., Nöthe, M., Ogaz, S., Oh, S., Parejko, J. K., Parley, N., Pascual, S., Patil, R., Patil, A. A., Plunkett, A. L., Prochaska, J. X., Rastogi, T., Reddy Janga, V., Sabater, J., Sakurikar, P., Seifert, M., Sherbert, L. E., Sherwood-Taylor, H., Shih, A. Y., Sick, J., Silbiger, M. T., Singanamalla, S., Singer, L. P., Sladen,

P. H., Sooley, K. A., Sornarajah, S., Streicher, O., Teuben, P., Thomas, S. W., Tremblay, G. R., Turner, J. E. H., Terrón, V., van Kerkwijk, M. H., de la Vega, A., Watkins, L. L., Weaver, B. A., Whitmore, J. B., Woillez, J., Zabalza, V., and Astropy Contributors (2018). The Astropy Project: Building an Open-science Project and Status of the v2.0 Core Package. *AJ*, 156(3):123.

Astropy Collaboration, Robitaille, T. P., Tollerud, E. J., Greenfield, P., Droettboom, M., Bray, E., Aldcroft, T., Davis, M., Ginsburg, A., Price-Whelan, A. M., Kerzendorf, W. E., Conley, A., Crighton, N., Barbary, K., Muna, D., Ferguson, H., Grollier, F., Parikh, M. M., Nair, P. H., Unther, H. M., Deil, C., Woillez, J., Conseil, S., Kramer, R., Turner, J. E. H., Singer, L., Fox, R., Weaver, B. A., Zabalza, V., Edwards, Z. I., Azalee Bostroem, K., Burke, D. J., Casey, A. R., Crawford, S. M., Dencheva, N., Ely, J., Jenness, T., Labrie, K., Lim, P. L., Pierfederici, F., Pontzen, A., Ptak, A., Refsdal, B., Servillat, M., and Streicher, O. (2013). Astropy: A community Python package for astronomy. *A&A*, 558:A33.

Auger, M. W., Treu, T., Bolton, A. S., Gavazzi, R., Koopmans, L. V. E., Marshall, P. J., Moustakas, L. A., and Burles, S. (2010a). The Sloan Lens ACS Survey. X. Stellar, Dynamical, and Total Mass Correlations of Massive Early-type Galaxies. *ApJ*, 724(1):511–525.

Auger, M. W., Treu, T., Gavazzi, R., Bolton, A. S., Koopmans, L. V. E., and Marshall, P. J. (2010b). Dark Matter Contraction and the Stellar Content of Massive Early-type Galaxies: Disfavoring "Light" Initial Mass Functions. *ApJ*, 721(2):L163–L167.

Avila, R. J., Hack, W., Cara, M., Borncamp, D., Mack, J., Smith, L., and Ubeda, L. (2015). DrizzlePac 2.0 - Introducing New Features. In Taylor, A. R. and Rosolowsky, E., editors, *Astronomical Data Analysis Software an Systems XXIV (ADASS XXIV)*, volume 495 of *Astronomical Society of the Pacific Conference Series*, page 281.

Bacon, D. J., Goldberg, D. M., Rowe, B. T. P., and Taylor, A. N. (2006). Weak gravitational flexion. *MNRAS*, 365(2):414–428.

Barkana, R. (1998). Fast Calculation of a Family of Elliptical Mass Gravitational Lens Models. *ApJ*, 502(2):531–537.

Bertin, E. and Arnouts, S. (1996). SExtractor: Software for source extraction. *A&AS*, 117:393–404.

Birrer, S. and 20 colleagues, including Schmidt, T. (2021). lenstronomy II: A gravitational lensing software ecosystem. *The Journal of Open Source Software*, 6(62):3283.

Birrer, S. and Amara, A. (2018). lenstronomy: Multi-purpose gravitational lens modelling software package. *Physics of the Dark Universe*, 22:189–201.

Birrer, S., Amara, A., and Refregier, A. (2015). Gravitational Lens Modeling with Basis Sets. *ApJ*, 813(2):102.

Birrer, S., Amara, A., and Refregier, A. (2016). The mass-sheet degeneracy and time-delay cosmography: analysis of the strong lens RXJ1131-1231. *J. Cosmology Astropart. Phys.*, 2016(8):020.

Birrer, S., Millon, M., Sluse, D., Shajib, A. J., Courbin, F., Erickson, S., Koopmans, L. V. E., Suyu, S. H., and Treu, T. (2024). Time-Delay Cosmography: Measuring the Hubble Constant and Other Cosmological Parameters with Strong Gravitational Lensing. *Space Sci. Rev.*, 220(5):48.

Birrer, S., Shajib, A., Gilman, D., Galan, A., Aalbers, J., Millon, M., Morgan, R., Pagano, G., Park, J., Teodori, L., Tessore, N., Ueland, M., Van de Vyvere, L., Wagner-Carena, S., Wempe, E., Yang, L., Ding, X., Schmidt, T., Sluse, D., Zhang, M., and Amara, A. (2021). lenstronomy II: A gravitational lensing software ecosystem. *The Journal of Open Source Software*, 6(62):3283.

Birrer, S., Shajib, A. J., Galan, A., Millon, M., Treu, T., Agnello, A., Auger, M., Chen, G. C. F., Christensen, L., Collett, T., Courbin, F., Fassnacht, C. D., Koopmans, L. V. E., Marshall, P. J., Park, J. W., Rusu, C. E., Sluse, D., Spiniello, C., Suyu, S. H., Wagner-Carena, S., Wong, K. C., Barnabè, M., Bolton, A. S., Czoske, O., Ding, X., Frieman, J. A., and Van de Vyvere, L. (2020). Tdcosmo iv: Hierarchical time-delay cosmography – joint inference of the hubble constant and galaxy density profiles. *arXiv e-prints*, page 2007.02941.

Birrer, S. and Treu, T. (2019). Astrometric requirements for strong lensing time-delay cosmography. *MNRAS*, 489(2):2097–2103.

Birrer, S. and Treu, T. (2021). TDCOSMO. V. Strategies for precise and accurate measurements of the Hubble constant with strong lensing. *A&A*, 649:A61.

Birrer, S., Treu, T., Rusu, C. E., Bonvin, V., Fassnacht, C. D., Chan, J. H. H., Agnello, A., Shajib, A. J., Chen, G. C. F., Auger, M., Courbin, F., Hilbert, S., Sluse, D., Suyu, S. H., Wong, K. C., Marshall, P., Lemaux, B. C., and Meylan, G. (2019). H0LiCOW - IX. Cosmographic analysis of the doubly imaged quasar SDSS 1206+4332 and a new measurement of the Hubble constant. *MNRAS*, 484(4):4726–4753.

Blandford, R. and Narayan, R. (1986). Fermat's principle, caustics, and the classification of gravitational lens images. *ApJ*, 310:568.

Blandford, R. D. and Narayan, R. (1992). Cosmological applications of gravitational lensing. *ARA&A*, 30:311–358.

Bolton, A. S., Burles, S., Koopmans, L. V. E., Treu, T., Gavazzi, R., Moustakas, L. A., Wayth, R., and Schlegel, D. J. (2008). The Sloan Lens ACS Survey. V. The Full ACS Strong-Lens Sample. *ApJ*, 682(2):964–984.

Bolton, A. S., Burles, S., Koopmans, L. V. E., Treu, T., and Moustakas, L. A. (2006).

The Sloan Lens ACS Survey. I. A Large Spectroscopically Selected Sample of Massive Early-Type Lens Galaxies. *ApJ*, 638(2):703–724.

Bonvin, V., Courbin, F., Suyu, S. H., Marshall, P. J., Rusu, C. E., Sluse, D., Tewes, M., Wong, K. C., Collett, T., Fassnacht, C. D., Treu, T., Auger, M. W., Hilbert, S., Koopmans, L. V. E., Meylan, G., Rumbaugh, N., Sonnenfeld, A., and Spiniello, C. (2017). H0licow - v. new cosmograil time delays of he 0435-1223: H₀ to 3.8 per cent precision from strong lensing in a flat cdm model. *MNRAS*, 465:4914–4930.

Chen, G. C. F., Fassnacht, C. D., Suyu, S. H., Koopmans, L. V. E., Lagattuta, D. J., McKean, J. P., Auger, M. W., Vegetti, S., and Treu, T. (2022). SHARP - VIII. J0924+0219 lens mass distribution and time-delay prediction through adaptive-optics imaging. *MNRAS*, 513(2):2349–2359.

Chen, G. C. F., Suyu, S. H., Wong, K. C., Fassnacht, C. D., Chiueh, T., Halkola, A., Hu, I. S., Auger, M. W., Koopmans, L. V. E., Lagattuta, D. J., McKean, J. P., and Vegetti, S. (2016). SHARP - III. First use of adaptive-optics imaging to constrain cosmology with gravitational lens time delays. *MNRAS*, 462(4):3457–3475.

Chen, G. C. F., Treu, T., Fassnacht, C. D., Ragland, S., Schmidt, T., and Suyu, S. H. (2021a). Point spread function reconstruction of adaptive-optics imaging: meeting the astrometric requirements for time-delay cosmography. *MNRAS*, 508(1):755–761.

Chen, G. C. F., Treu, T., Fassnacht, C. D., Ragland, S., Schmidt, T., and Suyu, S. H. (2021b). Point spread function reconstruction of adaptive-optics imaging: meeting the astrometric requirements for time-delay cosmography. *MNRAS*, 508(1):755–761.

Clowe, D., Gonzalez, A., and Markevitch, M. (2004). Weak-lensing mass reconstruction of the interacting cluster 1e 0657-558: Direct evidence for the existence of dark matter. *ApJ*, 604(2):596–603.

Collett, T. E. (2015). The Population of Galaxy-Galaxy Strong Lenses in Forthcoming Optical Imaging Surveys. *ApJ*, 811(1):20.

Collett, T. E. and Bacon, D. J. (2016). Compound lensing: Einstein zig-zags and high-multiplicity lensed images. *MNRAS*, 456(2):2210–2220.

de Vaucouleurs, G. (1948). Recherches sur les Nebuleuses Extragalactiques. *Annales d'Astrophysique*, 11:247.

Delchambre, L., Krone-Martins, A., Wertz, O., Ducourant, C., Galluccio, L., Klüter, J., Mignard, F., Teixeira, R., Djorgovski, S. G., Stern, D., Graham, M. J., Surdej, J., Bastian, U., Wambsganss, J., Le Campion, J. F., and Slezak, E. (2019). Gaia GraL: Gaia DR2 Gravitational Lens Systems. III. A systematic blind search for new lensed systems. *A&A*, 622:A165.

Di Valentino, E., Levi Said, J., Riess, A., Pollo, A., Poulin, V., Gómez-Valent, A., Weltman, A., Palmese, A., Huang, C. D., van de Bruck, C., Shekhar Saraf, C., Kuo, C.-Y., Uhlemann, C., Grandón, D., Paz, D., Eckert, D., Teixeira, E. M., Saridakis, E. N., Colgáin, E. Ó., Beutler, F., Niedermann, F., Bajardi, F., Barenboim, G., Gubitosi, G., Musella, I., Banik, I., Szapudi, I., Singal, J., Haro Cases, J., Chluba, J., Torrado, J., Mifsud, J., Jedamzik, K., Said, K., Dialektopoulos, K., Herold, L., Perivolaropoulos, L., Zu, L., Galbany, L., Breuval, L., Visinelli, L., Escamilla, L. A., Anchordoqui, L. A., Sheikh-Jabbari, M. M., Lembo, M., Dainotti, M. G., Vincenzi, M., Asgari, M., Gerbino, M., Forconi, M., Cantiello, M., Moresco, M., Benetti, M., Schöneberg, N., Akarsu, Ö., Nunes, R. C., Bernardo, R. C., Chávez, R., Anderson, R. I., Watkins, R., Capozziello, S., Li, S., Vagnozzi, S., Pan, S., Treu, T., Irsic, V., Handley, W., Giarè, W., Murakami, Y., Poudou, A., Heavens, A., Kogut, A., Domi, A., Łukasz Lenart, A., Melchiorri, A., Vadalà, A., Amon, A., Bonilla, A., Reeves, A., Zhuk, A., Bonanno, A., Övgün, A., Pisani, A., Talebian, A., Abebe, A., Aboubrahim, A., González Morán, A. L., Kovács, A., Papatriantafyllou, A., Liddle, A. R., Paliathanasis, A., Borowiec, A., Yadav, A. K., Yadav, A., Sen, A. A., Mini Latha,

A. J. W., Davis, A. C., Shajib, A. J., Walters, A., Idicherian Lonappan, A., Chudaykin, A., Capodagli, A., da Silva, A., De Felice, A., Racioppi, A., Soler Oficial, A., Montiel, A., Favale, A., Bernui, A., Velasco, A. C., Heinesen, A., Bakopoulos, A., Chatzistavrakidis, A., Khanpour, B., Sathyaprakash, B. S., Zgirski, B., L'Huillier, B., Famaey, B., Jain, B., Marek, B., Zhang, B., Karmakar, B., Dragovich, B., Thomas, B., Correa, C., Boiza, C. G., Marques, C., Escamilla-Rivera, C., Tzerefos, C., Zhang, C., De Leo, C., Pfeifer, C., Lee, C., Venter, C., Gomes, C., Roque De bom, C., Moreno-Pulido, C., Iosifidis, D., Grin, D., Blixt, D., Scolnic, D., Oriti, D., Dobrycheva, D., Bettoni, D., Benisty, D., Fernández-Arenas, D., Wiltshire, D. L., Sanchez Cid, D., Tamayo, D., Valls-Gabaud, D., Pedrotti, D., Wang, D., Staicova, D., Totolou, D., Rubiera-Garcia, D., Milaković, D., Pesce, D., Sluse, D., Borka, D., Yusofi, E., Giusarma, E., Terlevich, E., Tomasetti, E., Vagenas, E. C., Fazzari, E., Ferreira, E. G. M., Barakovic, E., Dimastrogiovanni, E., Brinch Holm, E., Mottola, E., Özülker, E., Specogna, E., Brocato, E., Jensko, E., Antonette Enriquez, E., Bhatia, E., Bresolin, F., Avila, F., Bouchè, F., Bombacigno, F., Anagnostopoulos, F. K., Pace, F., Sorrenti, F., Lobo, F. S. N., Courbin, F., Hansen, F. K., Sloan, G., Farrugia, G., Lynch, G., Garcia-Arroyo, G., Raimondo, G., Lambiase, G., Anand, G. S., Poulot, G., Leon, G., Kouniatalis, G., Nardini, G., Csörnyei, G., Galloni, G., and Bargiacchi, G. (2025). The CosmoVerse White Paper: Addressing observational tensions in cosmology with systematics and fundamental physics. *arXiv e-prints*, page arXiv:2504.01669.

Di Valentino, E., Mena, O., Pan, S., Visinelli, L., Yang, W., Melchiorri, A., Mota, D. F., Riess, A. G., and Silk, J. (2021). In the realm of the Hubble tension-a review of solutions. *Classical and Quantum Gravity*, 38(15):153001.

Dutton, A. A., Brewer, B. J., Marshall, P. J., Auger, M. W., Treu, T., Koo, D. C., Bolton, A. S., Holden, B. P., and Koopmans, L. V. E. (2011). The swells survey - ii. breaking the disc-halo degeneracy in the spiral galaxy gravitational lens sdss j2141-0001. *MNRAS*, 417:1621–1642.

Dux, F., Millon, M., Lemon, C., Schmidt, T., and 15 colleagues (2025a). J1721+8842: The first Einstein zigzag lens. *A&A*, 694:A300.

Dux, F., Millon, M., Lemon, C., Schmidt, T., Courbin, F., Shajib, A. J., Treu, T., Birrer, S., Wong, K. C., Agnello, A., Andrade, A., Galan, A., Hjorth, J., Paic, E., Schuldt, S., Schweinfurth, A., Sluse, D., Smette, A., and Suyu, S. H. (2025b). J1721+8842: The first Einstein zigzag lens. *A&A*, 694:A300.

Eisenstein, D. J., Zehavi, I., Hogg, D. W., Scoccimarro, R., Blanton, M. R., Nichol, R. C., Scranton, R., Seo, H.-J., Tegmark, M., Zheng, Z., Anderson, S. F., Annis, J., Bahcall, N., Brinkmann, J., Burles, S., Castander, F. J., Connolly, A., Csabai, I., Doi, M., Fukugita, M., Frieman, J. A., Glazebrook, K., Gunn, J. E., Hendry, J. S., Hennessy, G., Ivezić, Z., Kent, S., Knapp, G. R., Lin, H., Loh, Y.-S., Lupton, R. H., Margon, B., McKay, T. A., Meiksin, A., Munn, J. A., Pope, A., Richmond, M. W., Schlegel, D., Schneider, D. P., Shimasaku, K., Stoughton, C., Strauss, M. A., SubbaRao, M., Szalay, A. S., Szapudi, I., Tucker, D. L., Yanny, B., and York, D. G. (2005). Detection of the Baryon Acoustic Peak in the Large-Scale Correlation Function of SDSS Luminous Red Galaxies. *ApJ*, 633(2):560–574.

Erickson, S., Wagner-Carena, S., Marshall, P., Millon, M., Birrer, S., Roodman, A., Schmidt, T., 4 colleagues, and The LSST Dark Energy Science Collaboration (2025). Lens Modeling of STRIDES Strongly Lensed Quasars Using Neural Posterior Estimation. *AJ*, 170(1):44.

Ertl, S., Schuldt, S., Suyu, S. H., Schmidt, T., Treu, T., Birrer, S., Shajib, A. J., and Sluse, D. (2023). TDCOSMO. X. Automated modeling of nine strongly lensed quasars and comparison between lens-modeling software. *A&A*, 672:A2.

Etherington, A., Nightingale, J. W., Massey, R., Cao, X., Robertson, A., Amorisco, N. C., Amvrosiadis, A., Cole, S., Frenk, C. S., He, Q., Li, R., and Tam, S.-I. (2022). Auto-

mated galaxy-galaxy strong lens modelling: no lens left behind. *arXiv e-prints*, page arXiv:2202.09201.

Faber, S. M. and Jackson, R. E. (1976). Velocity dispersions and mass-to-light ratios for elliptical galaxies. *ApJ*, 204:668–683.

Falco, E. E., Gorenstein, M. V., and Shapiro, I. I. (1985). On model-dependent bounds on H 0 from gravitational images : application to Q 0957+561 A, B. *ApJ*, 289:L1–L4.

Foreman-Mackey, D. (2016). corner.py: Scatterplot matrices in Python. *The Journal of Open Source Software*, 1:24.

Foreman-Mackey, D., Hogg, D. W., Lang, D., and Goodman, J. (2013). emcee: The MCMC Hammer. *PASP*, 125(925):306.

Gavazzi, R., Treu, T., Rhodes, J. D., Koopmans, L. V. E., Bolton, A. S., Burles, S., Massey, R. J., and Moustakas, L. A. (2007). The sloan lens acs survey. iv. the mass density profile of early-type galaxies out to 100 effective radii. *ApJ*, 667:176–190.

Glikman, E., Rusu, C. E., Djorgovski, S. G., Graham, M. J., Stern, D., Urrutia, T., Lacy, M., and O'Meara, J. M. (2018). A highly magnified gravitationally lensed red quasar at z = 2.5 with significant flux anomaly: Uncovering a missing population. *arXiv e-prints*, page arXiv:1807.05434.

Golse, G. and Kneib, J.-P. (2002). Pseudo elliptical lensing mass model: Application to the nfw mass distribution. *A&A*, 390:821–827.

Gonzalez-Buitrago, D., Barth, A. J., Edelson, R., Hernández Santisteban, J. V., Horne, K., Schmidt, T., and 39 colleagues (2025). Departures from Standard Disk Predictions in Intensive Ground-Based Monitoring of Three AGN. *MNRAS*, 542(3):2572–2596.

Goodman, J. and Weare, J. (2010). Ensemble samplers with affine invariance. *Communications in Applied Mathematics and Computational Science*, 5(1):65–80.

Greene, Z. S., Suyu, S. H., Treu, T., Hilbert, S., Auger, M. W., Collett, T. E., Marshall, P. J., Fassnacht, C. D., Blandford, R. D., Bradač, M., and Koopmans, L. V. E. (2013). Improving the Precision of Time-delay Cosmography with Observations of Galaxies along the Line of Sight. *ApJ*, 768(1):39.

Harris, C. R., Millman, K. J., van der Walt, S. J., Gommers, R., Virtanen, P., Cournapeau, D., Wieser, E., Taylor, J., Berg, S., Smith, N. J., Kern, R., Picus, M., Hoyer, S., van Kerkwijk, M. H., Brett, M., Haldane, A., del Río, J. F., Wiebe, M., Peterson, P., Gérard-Marchant, P., Sheppard, K., Reddy, T., Weckesser, W., Abbasi, H., Gohlke, C., and Oliphant, T. E. (2020). Array programming with NumPy. *Nature*, 585(7825):357–362.

Heymans, C., Grocutt, E., Heavens, A., Kilbinger, M., Kitching, T. D., Simpson, F., Benjamin, J., Erben, T., Hildebrandt, H., Hoekstra, H., Mellier, Y., Miller, L., Van Waerbeke, L., Brown, M. L., Coupon, J., Fu, L., Harnois-Déraps, J., Hudson, M. J., Kuijken, K., Rowe, B., Schrabback, T., Semboloni, E., Vafaei, S., and Velander, M. (2013). Cfhtlens tomographic weak lensing cosmological parameter constraints: Mitigating the impact of intrinsic galaxy alignments. *MNRAS*, 432(3):2433–2453.

Hezaveh, Y. D., Levasseur, L. P., and Marshall, P. J. (2017). Fast automated analysis of strong gravitational lenses with convolutional neural networks. *Nature*, 548:555–557.

Hunter, J. D. (2007). Matplotlib: A 2d graphics environment. *Computing in Science and Engineering*, 9(3):90–95.

Jones, E., Oliphant, T., Peterson, P., and Others (2001). *SciPy: Open source scientific tools for Python*.

Kluyver, T., Ragan-Kelley, B., Pérez, F., Granger, B., Bussonnier, M., Frederic, J., Kelley, K., Hamrick, J., Grout, J., Corlay, S., Ivanov, P., Avila, D., Abdalla, S., and Willing, C. (2016). Jupyter notebooks – a publishing format for reproducible computational workflows.

In Loizides, F. and Schmidt, B., editors, *Positioning and Power in Academic Publishing: Players, Agents and Agendas*, pages 87 – 90. IOS Press BV, Amsterdam, Netherlands.

Knox, L. and Millea, M. (2020). Hubble constant hunter's guide. *Phys. Rev. D*, 101(4):043533.

Koopmans, L. V. E., Bolton, A., Treu, T., Czoske, O., Auger, M. W., Barnabè, M., Vegetti, S., Gavazzi, R., Moustakas, L. A., and Burles, S. (2009). The Structure and Dynamics of Massive Early-Type Galaxies: On Homology, Isothermality, and Isotropy Inside One Effective Radius. *ApJ*, 703(1):L51–L54.

Krone-Martins, A., Delchambre, L., Wertz, O., Ducourant, C., Mignard, F., Teixeira, R., Klüter, J., Le Campion, J. F., Galluccio, L., Surdej, J., Bastian, U., Wambsganss, J., Graham, M. J., Djorgovski, S. G., and Slezak, E. (2018). Gaia GraL: Gaia DR2 gravitational lens systems. I. New quadruply imaged quasar candidates around known quasars. *A&A*, 616:L11.

Lackner, C. N. and Gunn, J. E. (2012). Astrophysically motivated bulge-disc decompositions of Sloan Digital Sky Survey galaxies. *MNRAS*, 421(3):2277–2302.

Lemon, C., Auger, M. W., McMahon, R., Anguita, T., Apostolovski, Y., Chen, G. C. F., Fassnacht, C. D., Melo, A. D., Motta, V., Shajib, A., Treu, T., Agnello, A., Buckley-Geer, E., Schechter, P. L., Birrer, S., Collett, T., Courbin, F., Rusu, C. E., Abbott, T. M. C., Allam, S., Annis, J., Avila, S., Bertin, E., Brooks, D., Burke, D. L., Carnero Rosell, A., Carrasco Kind, M., Carretero, J., Costanzi, M., da Costa, L. N., De Vicente, J., Desai, S., Eifler, T. F., Flaugher, B., Frieman, J., García-Bellido, J., Gaztanaga, E., Gerdes, D. W., Gruen, D., Gruendl, R. A., Gschwend, J., Gutierrez, G., Honscheid, K., James, D. J., Kim, A., Krause, E., Kuehn, K., Kuropatkin, N., Lahav, O., Lima, M., Lin, H., Maia, M. A. G., March, M., Marshall, J. L., Menanteau, F., Miquel, R., Palmese, A., Paz-Chinchón, F., Plazas, A. A., Roodman, A., Sanchez, E., Schubnell, M., Serrano, S.,

Smith, M., Soares-Santos, M., Suchyta, E., Tarle, G., and Walker, A. R. (2020). The STRong lensing Insights into the Dark Energy Survey (STRIDES) 2017/2018 follow-up campaign: discovery of 10 lensed quasars and 10 quasar pairs. *MNRAS*, 494(3):3491–3511.

Lemon, C., Millon, M., Sluse, D., Courbin, F., Auger, M., Chan, J. H. H., Paic, E., and Agnello, A. (2022). J1721+8842: a gravitationally lensed binary quasar with a proximate damped Lyman-α absorber. *A&A*, 657:A113.

Lemon, C. A., Auger, M. W., and McMahon, R. G. (2019). Gravitationally lensed quasars in Gaia - III. 22 new lensed quasars from Gaia data release 2. *MNRAS*, 483(3):4242–4258.

Lemon, C. A., Auger, M. W., McMahon, R. G., and Koposov, S. E. (2017). Gravitationally lensed quasars in Gaia: I. Resolving small-separation lenses. *MNRAS*, 472(4):5023–5032.

Lemon, C. A., Auger, M. W., McMahon, R. G., and Ostrovski, F. (2018). Gravitationally lensed quasars in Gaia - II. Discovery of 24 lensed quasars. *MNRAS*, 479(4):5060–5074.

Lucey, J. R., Schechter, P. L., Smith, R. J., and Anguita, T. (2018). Serendipitous discovery of quadruply imaged quasars: two diamonds. *MNRAS*, 476(1):927–932.

Luhtaru, R., Schechter, P. L., and de Soto, K. M. (2021). What Makes Quadruply Lensed Quasars Quadruple? *ApJ*, 915(1):4.

Mangat, C. S., McKean, J. P., Brilenkov, R., Hartley, P., Stacey, H. R., Vegetti, S., and Wen, D. (2021). PS J1721+8842: a gravitationally lensed dual AGN system at redshift 2.37 with two radio components. *MNRAS*, 508(1):L64–L68.

McCully, C., Keeton, C. R., Wong, K. C., and Zabludoff, A. I. (2017). Quantifying environmental and line-of-sight effects in models of strong gravitational lens systems. *ApJ*, 836:141.

Meneghetti, M. (2021). *Introduction to Gravitational Lensing; With Python Examples*, volume 956.

Michalewicz, K., Millon, M., Dux, F., and Courbin, F. (2023). STARRED: a two-channel deconvolution method with Starlet regularization. *The Journal of Open Source Software*, 8(85):5340.

Millon, M., Courbin, F., Bonvin, V., Buckley-Geer, E., Fassnacht, C. D., Frieman, J., Marshall, P. J., Suyu, S. H., Treu, T., Anguita, T., Motta, V., Agnello, A., Chan, J. H. H., Chao, D. C. Y., Chijani, M., Gilman, D., Gilmore, K., Lemon, C., Lucey, J. R., Melo, A., Paic, E., Rojas, K., Sluse, D., Williams, P. R., Hempel, A., Kim, S., Lachaume, R., and Rabus, M. (2020). TDCOSMO. II. Six new time delays in lensed quasars from high-cadence monitoring at the MPIA 2.2 m telescope. *A&A*, 642:A193.

Millon, M., Galan, A., Courbin, F., Treu, T., Suyu, S. H., Ding, X., Birrer, S., Chen, G. C. F., Shajib, A. J., Sluse, D., Wong, K. C., Agnello, A., Auger, M. W., Buckley-Geer, E. J., Chan, J. H. H., Collett, T., Fassnacht, C. D., Hilbert, S., Koopmans, L. V. E., Motta, V., Mukherjee, S., Rusu, C. E., Sonnenfeld, A., Spiniello, C., and Van de Vyvere, L. (2020). Tdcosmo. i. an exploration of systematic uncertainties in the inference of h₀ from time-delay cosmography. *A&A*, 639:A101.

Millon, M., Michalewicz, K., Dux, F., Courbin, F., and Marshall, P. J. (2024). Image Deconvolution and Point-spread Function Reconstruction with STARRED: A Wavelet-based Two-channel Method Optimized for Light-curve Extraction. *AJ*, 168(2):55.

Morgan, N. D., Caldwell, J. A. R., Schechter, P. L., Dressler, A., Egami, E., and Rix, H.-W. (2004). WFI J2026-4536 and WFI J2033-4723: Two New Quadruple Gravitational Lenses. *AJ*, 127(5):2617–2630.

Navarro, J. F., Frenk, C. S., and White, S. D. M. (1997). A universal density profile from hierarchical clustering. *ApJ*, 490:493–508.

Oguri, M. and Marshall, P. J. (2010). Gravitationally lensed quasars and supernovae in future wide-field optical imaging surveys. *MNRAS*, 405(4):2579–2593.

Oliphant, T. E. (2015). *Guide to NumPy*. CreateSpace Independent Publishing Platform, USA, second edition.

Ostrovski, F., McMahon, R. G., Connolly, A. J., Lemon, C. A., Auger, M. W., Banerji, M., Hung, J. M., Koposov, S. E., Lidman, C. E., Reed, S. L., Allam, S., Benoit-Lévy, A., Bertin, E., Brooks, D., Buckley-Geer, E., Carnero Rosell, A., Carrasco Kind, M., Carretero, J., Cunha, C. E., da Costa, L. N., Desai, S., Diehl, H. T., Dietrich, J. P., Evrard, A. E., Finley, D. A., Flaugher, B., Fosalba, P., Frieman, J., Gerdes, D. W., Goldstein, D. A., Gruen, D., Gruendl, R. A., Gutierrez, G., Honscheid, K., James, D. J., Kuehn, K., Kuropatkin, N., Lima, M., Lin, H., Maia, M. A. G., Marshall, J. L., Martini, P., Melchior, P., Miquel, R., Ogando, R., Plazas Malagón, A., Reil, K., Romer, K., Sanchez, E., Santiago, B., Scarpine, V., Sevilla-Noarbe, I., Soares-Santos, M., Sobreira, F., Suchyta, E., Tarle, G., Thomas, D., Tucker, D. L., and Walker, A. R. (2017). VDES J2325-5229 a z = 2.7 gravitationally lensed quasar discovered using morphology-independent supervised machine learning. *MNRAS*, 465(4):4325–4334.

Pearson, J., Li, N., and Dye, S. (2019). The use of convolutional neural networks for modelling large optically-selected strong galaxy-lens samples. *MNRAS*, 488(1):991–1004.

Pearson, J., Maresca, J., Li, N., and Dye, S. (2021). Strong lens modelling: comparing and combining Bayesian neural networks and parametric profile fitting. *MNRAS*, 505(3):4362–4382.

Perlmutter, S., Aldering, G., Goldhaber, G., Knop, R. A., Nugent, P., Castro, P. G., Deustua, S., Fabbro, S., Goobar, A., Groom, D. E., Hook, I. M., Kim, A. G., Kim, M. Y., Lee, J. C., Nunes, N. J., Pain, R., Pennypacker, C. R., Quimby, R., Lidman, C., Ellis, R. S., Irwin, M., McMahon, R. G., Ruiz-Lapuente, P., Walton, N., Schaefer, B., Boyle, B. J., Filippenko, A. V., Matheson, T., Fruchter, A. S., Panagia, N., Newberg, H. J. M., Couch, W. J., and Project, T. S. C. (1999). Measurements of Ω and Λ from 42 High-Redshift Supernovae. *ApJ*, 517(2):565–586.

Planck Collaboration, Aghanim, N., Akrami, Y., Ashdown, M., Aumont, J., Baccigalupi, C., Ballardini, M., Banday, A. J., Barreiro, R. B., Bartolo, N., Basak, S., Battye, R., Benabed, K., Bernard, J. P., Bersanelli, M., Bielewicz, P., Bock, J. J., Bond, J. R., Borrill, J., Bouchet, F. R., Boulanger, F., Bucher, M., Burigana, C., Butler, R. C., Calabrese, E., Cardoso, J. F., Carron, J., Challinor, A., Chiang, H. C., Chluba, J., Colombo, L. P. L., Combet, C., Contreras, D., Crill, B. P., Cuttaia, F., de Bernardis, P., de Zotti, G., Delabrouille, J., Delouis, J. M., Di Valentino, E., Diego, J. M., Doré, O., Douspis, M., Ducout, A., Dupac, X., Dusini, S., Efstathiou, G., Elsner, F., Enßlin, T. A., Eriksen, H. K., Fantaye, Y., Farhang, M., Fergusson, J., Fernandez-Cobos, R., Finelli, F., Forastieri, F., Frailis, M., Fraisse, A. A., Franceschi, E., Frolov, A., Galeotta, S., Galli, S., Ganga, K., Génova-Santos, R. T., Gerbino, M., Ghosh, T., González-Nuevo, J., Górski, K. M., Gratton, S., Gruppuso, A., Gudmundsson, J. E., Hamann, J., Handley, W., Hansen, F. K., Herranz, D., Hildebrandt, S. R., Hivon, E., Huang, Z., Jaffe, A. H., Jones, W. C., Karakci, A., Keihänen, E., Keskitalo, R., Kiiveri, K., Kim, J., Kisner, T. S., Knox, L., Krachmalnicoff, N., Kunz, M., Kurki-Suonio, H., Lagache, G., Lamarre, J. M., Lasenby, A., Lattanzi, M., Lawrence, C. R., Le Jeune, M., Lemos, P., Lesgourgues, J., Levrier, F., Lewis, A., Liguori, M., Lilje, P. B., Lilley, M., Lindholm, V., López-Caniego, M., Lubin, P. M., Ma, Y. Z., Macías-Pérez, J. F., Maggio, G., Maino, D., Mandolesi, N., Mangilli, A., Marcos-Caballero, A., Maris, M., Martin, P. G., Martinelli, M., Martínez-González, E., Matarrese, S., Mauri, N., McEwen, J. D., Meinhold, P. R., Melchiorri, A., Mennella, A., Migliaccio, M., Millea, M., Mitra, S., Miville-Deschênes, M. A., Molinari, D., Montier, L., Morgante, G., Moss, A., Natoli, P., Nørgaard-Nielsen, H. U., Pagano, L., Paoletti, D., Partridge, B., Patanchon, G., Peiris, H. V., Perrotta, F., Pettorino, V., Piacentini, F., Polastri, L., Polenta, G., Puget, J. L., Rachen, J. P., Reinecke, M., Remazeilles, M., Renzi, A., Rocha, G., Rosset, C., Roudier, G., Rubiño-Martín, J. A., Ruiz-Granados, B., Salvati, L., Sandri, M., Savelainen, M., Scott, D., Shellard, E. P. S., Sirignano, C., Sirri, G., Spencer, L. D., Sunyaev, R., Suur-Uski, A. S., Tauber, J. A., Tavagnacco, D., Tenti,

M., Toffolatti, L., Tomasi, M., Trombetti, T., Valenziano, L., Valiviita, J., Van Tent, B., Vibert, L., Vielva, P., Villa, F., Vittorio, N., Wandelt, B. D., Wehus, I. K., White, M., White, S. D. M., Zacchei, A., and Zonca, A. (2020). Planck 2018 results. VI. Cosmological parameters. *A&A*, 641:A6.

Refregier, A. (2003). Shapelets - I. A method for image analysis. *MNRAS*, 338(1):35–47.

Refsdal, S. (1964). On the possibility of determining Hubble's parameter and the masses of galaxies from the gravitational lens effect. *MNRAS*, 128:307.

Retana-Montenegro, E., Frutos-Alfaro, F., and Baes, M. (2012). Analytical shear and flexion of Einasto dark matter haloes. *A&A*, 546:A32.

Riess, A. G., Casertano, S., Yuan, W., Bowers, J. B., Macri, L., Zinn, J. C., and Scolnic, D. (2021). Cosmic Distances Calibrated to 1% Precision with Gaia EDR3 Parallaxes and Hubble Space Telescope Photometry of 75 Milky Way Cepheids Confirm Tension with ΛCDM. *ApJ*, 908(1):L6.

Riess, A. G., Filippenko, A. V., Challis, P., Clocchiatti, A., Diercks, A., Garnavich, P. M., Gilliland, R. L., Hogan, C. J., Jha, S., Kirshner, R. P., Leibundgut, B., Phillips, M. M., Reiss, D., Schmidt, B. P., Schommer, R. A., Smith, R. C., Spyromilio, J., Stubbs, C., Suntzeff, N. B., and Tonry, J. (1998). Observational Evidence from Supernovae for an Accelerating Universe and a Cosmological Constant. *AJ*, 116(3):1009–1038.

Riess, A. G., Yuan, W., Macri, L. M., Scolnic, D., Brout, D., Casertano, S., Jones, D. O., Murakami, Y., Anand, G. S., Breuval, L., Brink, T. G., Filippenko, A. V., Hoffmann, S., Jha, S. W., D'arcy Kenworthy, W., Mackenty, J., Stahl, B. E., and Zheng, W. (2022). A Comprehensive Measurement of the Local Value of the Hubble Constant with 1 km s^{-1} Mpc^{-1} Uncertainty from the Hubble Space Telescope and the SH0ES Team. *ApJ*, 934(1):L7.

Roberts-Borsani, G., Treu, T., Mason, C., Ellis, R. S., Laporte, N., Schmidt, T., and 4 colleagues (2023). Nature and Nurture? Comparing Lyα Detections in UV-bright and Fainter [O III]+Hβ Emitters at z 8 with Keck/MOSFIRE. *ApJ*, 948(1):54.

Rusu, C. E., Berghea, C. T., Fassnacht, C. D., More, A., Seman, E., Nelson, G. J., and Chen, G. C. F. (2019). A search for gravitationally lensed quasars and quasar pairs in Pan-STARRS1: spectroscopy and sources of shear in the diamond 2M1134-2103. *MNRAS*, 486(4):4987–5007.

Rusu, C. E., Fassnacht, C. D., Sluse, D., Hilbert, S., Wong, K. C., Huang, K.-H., Suyu, S. H., Collett, T. E., Marshall, P. J., Treu, T., and Koopmans, L. V. E. (2017). H0licow - iii. quantifying the effect of mass along the line of sight to the gravitational lens he 0435-1223 through weighted galaxy counts. *MNRAS*, 467:4220–4242.

Rusu, C. E. and Lemon, C. A. (2018). An Edge-on Disk in the Quadruply Lensed Quasar Cross GraL J181730853+272940139. *Research Notes of the American Astronomical Society*, 2(4):187.

Saha, P. (2000). Lensing Degeneracies Revisited. *AJ*, 120(4):1654–1659.

Saha, P., Coles, J., Macciò, A. V., and Williams, L. L. R. (2006). The Hubble Time Inferred from 10 Time Delay Lenses. *ApJ*, 650(1):L17–L20.

Schmidt, T., Treu, T., 69 colleagues, and DES Collaboration (2023a). STRIDES: automated uniform models for 30 quadruply imaged quasars. *MNRAS*, 518(1):1260–1300.

Schmidt, T., Treu, T., and 8 colleagues (2025). TDCOSMO. XVIII. Strong lens model and time-delay predictions for J1721+8842, the first Einstein zigzag lens. *A&A*, 700:A92.

Schmidt, T., Treu, T., Birrer, S., Shajib, A. J., Lemon, C., Millon, M., Sluse, D., Agnello, A., Anguita, T., Auger-Williams, M. W., McMahon, R. G., Motta, V., Schechter, P., Spiniello, C., Kayo, I., Courbin, F., Ertl, S., Fassnacht, C. D., Frieman, J. A., More,

A., Schuldt, S., Suyu, S. H., Aguena, M., Andrade-Oliveira, F., Annis, J., Bacon, D., Bertin, E., Brooks, D., Burke, D. L., Carnero Rosell, A., Carrasco Kind, M., Carretero, J., Conselice, C., Costanzi, M., da Costa, L. N., Pereira, M. E. S., De Vicente, J., Desai, S., Doel, P., Everett, S., Ferrero, I., Friedel, D., García-Bellido, J., Gaztanaga, E., Gruen, D., Gruendl, R. A., Gschwend, J., Gutierrez, G., Hinton, S. R., Hollowood, D. L., Honscheid, K., James, D. J., Kuehn, K., Lahav, O., Menanteau, F., Miquel, R., Palmese, A., Paz-Chinchón, F., Pieres, A., Plazas Malagón, A. A., Prat, J., Rodriguez-Monroy, M., Romer, A. K., Sanchez, E., Scarpine, V., Sevilla-Noarbe, I., Smith, M., Suchyta, E., Tarle, G., To, C., Varga, T. N., and DES Collaboration (2023b). STRIDES: automated uniform models for 30 quadruply imaged quasars. *MNRAS*, 518(1):1260–1300.

Schneider, P. (2019). Generalized multi-plane gravitational lensing: time delays, recursive lens equation, and the mass-sheet transformation. *A&A*, 624:A54.

Schneider, P., Ehlers, J., and Falco, E. E. (1992). *Gravitational Lenses*.

Schneider, P., Kochanek, C. S., and Wambsganss, J. (2006). *Gravitational Lensing: Strong, Weak and Micro*, volume 33 of *Saas-Fee Advanced Courses*. Springer.

Schneider, P. and Sluse, D. (2013). Mass-sheet degeneracy, power-law models and external convergence: Impact on the determination of the hubble constant from gravitational lensing. *A&A*, 559:A37.

Schneider, P. and Sluse, D. (2014). Source-position transformation: an approximate invariance in strong gravitational lensing. *A&A*, 564:A103.

Schöneberg, N., Abellán, G. F., Sánchez, A. P., Witte, S. J., Poulin, V., and Lesgourgues, J. (2022). The H_0 Olympics: A fair ranking of proposed models. *Phys. Rep.*, 984:1–55.

Schuldt, S., Suyu, S. H., Meinhardt, T., Leal-Taixé, L., Cañameras, R., Taubenberger, S., and Halkola, A. (2021). HOLISMOKES. IV. Efficient mass modeling of strong lenses through deep learning. *A&A*, 646:A126.

Sérsic, J. L. (1968). *Atlas de Galaxias Australes*.

Shajib, A. J. (2019). Unified lensing and kinematic analysis for any elliptical mass profile. *MNRAS*, 488(1):1387–1400.

Shajib, A. J., Birrer, S., Treu, T., Agnello, A., Buckley-Geer, E. J., Chan, J. H. H., Christensen, L., Lemon, C., Lin, H., Millon, M., Poh, J., Rusu, C. E., Sluse, D., Spiniello, C., Chen, G. C. F., Collett, T., Courbin, F., Fassnacht, C. D., Frieman, J., Galan, A., Gilman, D., More, A., Anguita, T., Auger, M. W., Bonvin, V., McMahon, R., Meylan, G., Wong, K. C., Abbott, T. M. C., Annis, J., Avila, S., Bechtol, K., Brooks, D., Brout, D., Burke, D. L., Carnero Rosell, A., Carrasco Kind, M., Carretero, J., Castander, F. J., Costanzi, M., da Costa, L. N., De Vicente, J., Desai, S., Dietrich, J. P., Doel, P., Drlica-Wagner, A., Evrard, A. E., Finley, D. A., Flaugher, B., Fosalba, P., García-Bellido, J., Gerdes, D. W., Gruen, D., Gruendl, R. A., Gschwend, J., Gutierrez, G., Hollowood, D. L., Honscheid, K., Huterer, D., James, D. J., Jeltema, T., Krause, E., Kuropatkin, N., Li, T. S., Lima, M., MacCrann, N., Maia, M. A. G., Marshall, J. L., Melchior, P., Miquel, R., Ogando, R. L. C., Palmese, A., Paz-Chinchón, F., Plazas, A. A., Romer, A. K., Roodman, A., Sako, M., Sanchez, E., Santiago, B., Scarpine, V., Schubnell, M., Scolnic, D., Serrano, S., Sevilla-Noarbe, I., Smith, M., Soares-Santos, M., Suchyta, E., Tarle, G., Thomas, D., Walker, A. R., and Zhang, Y. (2020). STRIDES: a 3.9 per cent measurement of the Hubble constant from the strong lens system DES J0408-5354. *MNRAS*, 494(4):6072–6102.

Shajib, A. J., Birrer, S., Treu, T., Auger, M. W., Agnello, A., Anguita, T., Buckley-Geer, E. J., Chan, J. H. H., Collett, T. E., Courbin, F., Fassnacht, C. D., Frieman, J., Kayo, I., Lemon, C., Lin, H., Marshall, P. J., McMahon, R., More, A., Morgan, N. D., Motta, V., Oguri, M., Ostrovski, F., Rusu, C. E., Schechter, P. L., Shanks, T., Suyu, S. H., Meylan, G., Abbott, T. M. C., Allam, S., Annis, J., Avila, S., Bertin, E., Brooks, D., Carnero Rosell, A., Carrasco Kind, M., Carretero, J., Cunha, C. E., da Costa, L. N., De Vicente, J., Desai, S., Doel, P., Flaugher, B., Fosalba, P., García-Bellido, J., Gerdes, D. W., Gruen,

D., Gruendl, R. A., Gutierrez, G., Hartley, W. G., Hollowood, D. L., Hoyle, B., James, D. J., Kuehn, K., Kuropatkin, N., Lahav, O., Lima, M., Maia, M. A. G., March, M., Marshall, J. L., Melchior, P., Menanteau, F., Miquel, R., Plazas, A. A., Sanchez, E., Scarpine, V., Sevilla-Noarbe, I., Smith, M., Soares-Santos, M., Sobreira, F., Suchyta, E., Swanson, M. E. C., Tarle, G., and Walker, A. R. (2019). Is every strong lens model unhappy in its own way? Uniform modelling of a sample of 13 quadruply+ imaged quasars. *MNRAS*, 483(4):5649–5671.

Shajib, A. J., Treu, T., and Agnello, A. (2018). Improving time-delay cosmography with spatially resolved kinematics. *MNRAS*, 473(1):210–226.

Shajib, A. J., Treu, T., Birrer, S., and Sonnenfeld, A. (2021). Dark matter haloes of massive elliptical galaxies at z $\sim$ 0.2 are well described by the Navarro-Frenk-White profile. *MNRAS*, 503(2):2380–2405.

Shajib, A. J., Wong, K. C., Birrer, S., Suyu, S. H., Treu, T., Buckley-Geer, E. J., Lin, H., Rusu, C. E., Poh, J., Palmese, A., Agnello, A., Auger-Williams, M. W., Galan, A., Schuldt, S., Sluse, D., Courbin, F., Frieman, J., and Millon, M. (2022). TDCOSMO. IX. Systematic comparison between lens modelling software programs: Time-delay prediction for WGD 2038−4008. *A&A*, 667:A123.

Shapiro, I. I. (1964). Fourth Test of General Relativity. *Phys. Rev. Lett.*, 13(26):789–791.

Sluse, D., Sonnenfeld, A., Rumbaugh, N., Rusu, C. E., Fassnacht, C. D., Treu, T., Suyu, S. H., Wong, K. C., Auger, M. W., Bonvin, V., Collett, T., Courbin, F., Hilbert, S., Koopmans, L. V. E., Marshall, P. J., Meylan, G., Spiniello, C., and Tewes, M. (2017). H0licow - ii. spectroscopic survey and galaxy-group identification of the strong gravitational lens system he 0435-1223. *MNRAS, submitted*, 470:4838–4857.

Sonnenfeld, A. (2021). Statistical strong lensing. II. Cosmology and galaxy structure with time-delay lenses. *A&A*, 656:A153.

Sonnenfeld, A. and Cautun, M. (2021). Statistical strong lensing. I. Constraints on the inner structure of galaxies from samples of a thousand lenses. *A&A*, 651:A18.

Spiniello, C. and Agnello, A. (2019). VEXAS: VISTA EXtension to Auxiliary Surveys. Data Release 1. The southern Galactic hemisphere. *A&A*, 630:A146.

Spiniello, C., Sergeyev, A. V., Marchetti, L., Tortora, C., Napolitano, N. R., Shalyapin, V., Agnello, A., Getman, F. I., Vaccari, M., Serjeant, S., Koopmans, L. V. E., Baker, A. J., Jarrett, T. H., Covone, G., and Vernardos, G. (2019). Spectroscopic confirmation and modelling of two lensed quadruple quasars in the Dark Energy Survey public footprint. *MNRAS*, 485(4):5086–5095.

Stern, D., Djorgovski, S. G., Krone-Martins, A., Sluse, D., Delchambre, L., Ducourant, C., Teixeira, R., Surdej, J., Boehm, C., den Brok, J., Dobie, D., Drake, A., Galluccio, L., Graham, M. J., Jalan, P., Klüter, J., Le Campion, J. F., Mahabal, A., Mignard, F., Murphy, T., Nierenberg, A., Scarano, S., J., Simon, J., Slezak, E., Spindola-Duarte, C., and Wambsganss, J. (2021). Gaia GraL: Gaia DR2 Gravitational Lens Systems. VI. Spectroscopic Confirmation and Modeling of Quadruply Imaged Lensed Quasars. *ApJ*, 921(1):42.

Stoughton, C., Lupton, R. H., Bernardi, M., Blanton, M. R., Burles, S., Castander, F. J., Connolly, A. J., Eisenstein, D. J., Frieman, J. A., Hennessy, G. S., Hindsley, R. B., Ivezić, Ž., Kent, S., Kunszt, P. Z., Lee, B. C., Meiksin, A., Munn, J. A., Newberg, H. J., Nichol, R. C., Nicinski, T., Pier, J. R., Richards, G. T., Richmond, M. W., Schlegel, D. J., Smith, J. A., Strauss, M. A., SubbaRao, M., Szalay, A. S., Thakar, A. R., Tucker, D. L., Vanden Berk, D. E., Yanny, B., Adelman, J. K., Anderson, John E., J., Anderson, S. F., Annis, J., Bahcall, N. A., Bakken, J. A., Bartelmann, M., Bastian, S., Bauer, A., Berman, E., Böhringer, H., Boroski, W. N., Bracker, S., Briegel, C., Briggs, J. W., Brinkmann, J., Brunner, R., Carey, L., Carr, M. A., Chen, B., Christian, D., Colestock, P. L., Crocker, J. H., Csabai, I., Czarapata, P. C., Dalcanton, J., Davidsen, A. F., Davis, J. E., Dehnen,

W., Dodelson, S., Doi, M., Dombeck, T., Donahue, M., Ellman, N., Elms, B. R., Evans, M. L., Eyer, L., Fan, X., Federwitz, G. R., Friedman, S., Fukugita, M., Gal, R., Gillespie, B., Glazebrook, K., Gray, J., Grebel, E. K., Greenawalt, B., Greene, G., Gunn, J. E., de Haas, E., Haiman, Z., Haldeman, M., Hall, P. B., Hamabe, M., Hansen, B., Harris, F. H., Harris, H., Harvanek, M., Hawley, S. L., Hayes, J. J. E., Heckman, T. M., Helmi, A., Henden, A., Hogan, C. J., Hogg, D. W., Holmgren, D. J., Holtzman, J., Huang, C.-H., Hull, C., Ichikawa, S.-I., Ichikawa, T., Johnston, D. E., Kauffmann, G., Kim, R. S. J., Kimball, T., Kinney, E., Klaene, M., Kleinman, S. J., Klypin, A., Knapp, G. R., Korienek, J., Krolik, J., Kron, R. G., Krzesiński, J., Lamb, D. Q., Leger, R. F., Limmongkol, S., Lindenmeyer, C., Long, D. C., Loomis, C., Loveday, J., MacKinnon, B., Mannery, E. J., Mantsch, P. M., Margon, B., McGehee, P., McKay, T. A., McLean, B., Menou, K., Merelli, A., Mo, H. J., Monet, D. G., Nakamura, O., Narayanan, V. K., Nash, T., Neilsen, Eric H., J., Newman, P. R., Nitta, A., Odenkirchen, M., Okada, N., Okamura, S., Ostriker, J. P., Owen, R., Pauls, A. G., Peoples, J., Peterson, R. S., Petravick, D., Pope, A., Pordes, R., Postman, M., Prosapio, A., Quinn, T. R., Rechenmacher, R., Rivetta, C. H., Rix, H.-W., Rockosi, C. M., Rosner, R., Ruthmansdorfer, K., Sandford, D., Schneider, D. P., Scranton, R., Sekiguchi, M., Sergey, G., Sheth, R., Shimasaku, K., Smee, S., Snedden, S. A., Stebbins, A., Stubbs, C., Szapudi, I., Szkody, P., Szokoly, G. P., Tabachnik, S., Tsvetanov, Z., Uomoto, A., Vogeley, M. S., Voges, W., Waddell, P., Walterbos, R., Wang, S.-i., Watanabe, M., Weinberg, D. H., White, R. L., White, S. D. M., Wilhite, B., Wolfe, D., Yasuda, N., York, D. G., Zehavi, I., and Zheng, W. (2002). Sloan Digital Sky Survey: Early Data Release. *AJ*, 123(1):485–548.

Suyu, S. H., Marshall, P. J., Auger, M. W., Hilbert, S., Blandford, R. D., Koopmans, L. V. E., Fassnacht, C. D., and Treu, T. (2010). Dissecting the gravitational lens b1608+656. ii. precision measurements of the hubble constant, spatial curvature, and the dark energy equation of state. *ApJ*, 711:201–221.

Suyu, S. H., Treu, T., Hilbert, S., Sonnenfeld, A., Auger, M. W., Blandford, R. D., Collett, T., Courbin, F., Fassnacht, C. D., Koopmans, L. V. E., Marshall, P. J., Meylan, G., Spiniello, C., and Tewes, M. (2014). Cosmology from gravitational lens time delays and planck data. *ApJ*, 788:L35.

Tewes, M., Courbin, F., Meylan, G., Kochanek, C. S., Eulaers, E., Cantale, N., Mosquera, A. M., Magain, P., Van Winckel, H., Sluse, D., Cataldi, G., Vörös, D., and Dye, S. (2013). COSMOGRAIL: the COSmological MOnitoring of GRAvItational Lenses. XIII. Time delays and 9-yr optical monitoring of the lensed quasar RX J1131-1231. *A&A*, 556:A22.

Treu, T., Brammer, G., Diego, J. M., Grillo, C., Kelly, P. L., Oguri, M., Rodney, S. A., Rosati, P., Sharon, K., Zitrin, A., Balestra, I., Bradač, M., Broadhurst, T., Caminha, G. B., Halkola, A., Hoag, A., Ishigaki, M., Johnson, T. L., Karman, W., Kawamata, R., Mercurio, A., Schmidt, K. B., Strolger, L. G., Suyu, S. H., Filippenko, A. V., Foley, R. J., Jha, S. W., and Patel, B. (2016). "Refsdal" Meets Popper: Comparing Predictions of the Re-appearance of the Multiply Imaged Supernova Behind MACSJ1149.5+2223. *ApJ*, 817(1):60.

Treu, T. and Koopmans, L. V. E. (2002). The internal structure and formation of early-type galaxies: The gravitational lens system mg 2016+112 at z = 1.004. *ApJ*, 575:87–94.

Treu, T. and Koopmans, L. V. E. (2004). Massive dark matter halos and evolution of early-type galaxies to z 1. *ApJ*, 611:739–760.

Treu, T. and Marshall, P. J. (2016). Time delay cosmography. *The Astronomy and Astrophysics Review*, 24(1):11.

Treu, T. and Shajib, A. J. (2024). Strong Lensing and H_0. In Di Valentino, E. and Brout Dillon, editors, *The Hubble Constant Tension*, pages 251–276.

Treu, T., Suyu, S. H., and Marshall, P. J. (2022). Strong lensing time-delay cosmography in the 2020s. *A&ARv*, 30(1):8.

Vagnozzi, S. (2023). Seven Hints That Early-Time New Physics Alone Is Not Sufficient to Solve the Hubble Tension. *Universe*, 9(9):393.

Verde, L., Treu, T., and Riess, A. G. (2019). Tensions between the early and late Universe. *Nature Astronomy*, 3:891–895.

Viola, M., Melchior, P., and Bartelmann, M. (2012). Shear-flexion cross-talk in weak-lensing measurements. *MNRAS*, 419(3):2215–2225.

Virtanen, P., Gommers, R., Oliphant, T. E., Haberland, M., Reddy, T., Cournapeau, D., Burovski, E., Peterson, P., Weckesser, W., Bright, J., van der Walt, S. J., Brett, M., Wilson, J., Millman, K. J., Mayorov, N., Nelson, A. R. J., Jones, E., Kern, R., Larson, E., Carey, C. J., Polat, İ., Feng, Y., Moore, E. W., VanderPlas, J., Laxalde, D., Perktold, J., Cimrman, R., Henriksen, I., Quintero, E. A., Harris, C. R., Archibald, A. M., Ribeiro, A. H., Pedregosa, F., van Mulbregt, P., and SciPy 1.0 Contributors (2020). SciPy 1.0: Fundamental Algorithms for Scientific Computing in Python. *Nature Methods*, 17:261–272.

Waskom, M. (2021). seaborn: statistical data visualization. *The Journal of Open Source Software*, 6(60):3021.

Wertz, O., Stern, D., Krone-Martins, A., Delchambre, L., Ducourant, C., Gråe Jørgensen, U., Dominik, M., Burgdorf, M., Surdej, J., Mignard, F., Teixeira, R., Galluccio, L., Klüter, J., Djorgovski, S. G., Graham, M. J., Bastian, U., Wambsganss, J., Boehm, C., LeCampion, J. F., and Slezak, E. (2019). Gaia GraL: Gaia DR2 gravitational lens systems. IV. Keck/LRIS spectroscopic confirmation of GRAL 113100-441959 and model prediction of time delays. *A&A*, 628:A17.

Williams, D. M., Treu, T., Birrer, S., Shajib, A. J., Wong, K. C., Morishita, T., Schmidt, T., and Stiavelli, M. (2025). TDCOSMO. XX. WFI2033–4723, the First Quadruply-Imaged

Quasar Modeled with JWST Imaging. *Submitted to MNRAS (2025) and arXiv e-prints*, page arXiv:2503.00099.

Williams, P., Agnello, A., and Treu, T. (2017). Population mixtures and searches of lensed and extended quasars across photometric surveys. *MNRAS*, 466(3):3088–3102.

Williams, P. R., Agnello, A., Treu, T., Abramson, L. E., Anguita, T., Apostolovski, Y., Chen, G. C. F., Fassnacht, C. D., Hsueh, J. W., Lemaux, B. C., Motta, V., Oldham, L., Rojas, K., Rusu, C. E., Shajib, A. J., and Wang, X. (2018). Discovery of three strongly lensed quasars in the Sloan Digital Sky Survey. *MNRAS*, 477(1):L70–L74.

Wong, K. C., Suyu, S. H., Chen, G. C. F., Rusu, C. E., Millon, M., Sluse, D., Bonvin, V., Fassnacht, C. D., Taubenberger, S., Auger, M. W., Birrer, S., Chan, J. H. H., Courbin, F., Hilbert, S., Tihhonova, O., Treu, T., Agnello, A., Ding, X., Jee, I., Komatsu, E., Shajib, A. J., Sonnenfeld, A., Blandford, R. D., Koopmans, L. V. E., Marshall, P. J., and Meylan, G. (2020). H0LiCOW - XIII. A 2.4 per cent measurement of H_0 from lensed quasars: 5.3σ tension between early- and late-Universe probes. *MNRAS*, 498(1):1420–1439.

Wucknitz, O. (2002). Degeneracies and scaling relations in general power-law models for gravitational lenses. *MNRAS*, 332(4):951–961.